



HAL
open science

Electron-Triggered Metamorphism in Viologen Based Self-Assembled Supramolecular Materials

Shagor Chowdhury

► **To cite this version:**

Shagor Chowdhury. Electron-Triggered Metamorphism in Viologen Based Self-Assembled Supramolecular Materials. Coordination chemistry. Université de Lyon, 2020. English. NNT : 2020LYSEN051 . tel-03917513

HAL Id: tel-03917513

<https://theses.hal.science/tel-03917513>

Submitted on 2 Jan 2023

HAL is a multi-disciplinary open access archive for the deposit and dissemination of scientific research documents, whether they are published or not. The documents may come from teaching and research institutions in France or abroad, or from public or private research centers.

L'archive ouverte pluridisciplinaire **HAL**, est destinée au dépôt et à la diffusion de documents scientifiques de niveau recherche, publiés ou non, émanant des établissements d'enseignement et de recherche français ou étrangers, des laboratoires publics ou privés.



Numéro National de
Thèse : 2020LYSEN051

THESE de DOCTORAT DE L'UNIVERSITE DE LYON

opérée par

l'Ecole Normale Supérieure de Lyon

Ecole Doctorale N° 206

Ecole Doctorale de Chimie (Chimie, Procédés, Environnement)

Discipline : Chimie

Soutenue publiquement le 9/10/2020, par :

Shagor CHOWDHURY

**Electron-Triggered Metamorphism in Viologen Based
Self-Assembled Supramolecular Materials**

**Métamorphisme (Supra)moléculaire Induit par Stimulation Électrique de
Tectons à Base de Motifs 4,4'-Bipyridium**

Devant le jury composé de :

M. Guillaume Vives	Maître de Conférences Sorbonne Université	Rapporteur
Mme Corinne Lagrost	Directrice de Recherche CNRS Université de Rennes 1	Rapporteuse
M. Charles Devillers	Maître de Conférences Université de Bourgogne Franche-Comté	Examineur
M. Eric Saint-Aman	Professeur des Universités Université Grenoble Alpes	Examineur
Mme Chantal Andraud	Directrice de Recherche CNRS ENS de Lyon	Examinatrice
M. Christophe Bucher	Directeur de Recherche ENS de Lyon	Directeur
M. Floris Chevallier	Maître de Conférences ENS de Lyon	Co-encadrant

Acknowledgment

I would like to thank Dr. Corinne Lagrost and Dr. Guillaume Vives for accepting to be my thesis referees and for the time they spent on qualifying my work. My warm thanks to Dr. Chantal Andraud, Dr. Charles Devillers and Prof. Eric Saint-Aman for accepting to be a part of my thesis jury.

I would like also to thank the members of the committee de thèse Dr. Jean-Pierre Dutasta and Dr. Maurice Medebielle for evaluating the work during my thesis and for their fruitful advices.

Profound appreciation and sincere gratitude goes to my thesis advisor Dr. Christophe Bucher. Thank you for offering me the thesis that is rich in diversity and creativity. Thank you for being a fantastic mentor, and for the valuable experiences and skills that you have given me throughout the way. I am really fortunate to have you as a supervisor.

Special thanks to Dr. Floris Chevallier, Dr. Denis Frath, Dr. Andrea Mulas and Dr. Guillaume George for their resolute support, discussions and comments that helped me look at things from different perspectives.

Huge thanks to Jean-Christophe and Delphine for their daily presence and helping me with their advices. Thanks also to Sandrine for all her help with the NMR measurements, and Christian for resolving the computer issues.

I would like to thank also my colleagues in the lab Janah, Sylvan, Amandine, Mathieu, Jean, Carolin, Jeremy, lulu, Maher, Damien, Quentin, Martin, Alix, Junchao, Shaymaa, Gaston and Hussein. Deep “Thank you” to Orsola for being there all the way, and helping me with your experience and advices.

Not to forget my friends with whom I share some of the best moments in life Hagop, Mohammad Jamal, Al-Mouatasem, Yousef and Sary.

Last but not the least, I would like to thank deeply my parents, for their love and unconditional support and without them I would not have made it this far.

Table of Contents

List of Abbreviations and Symbols.....	6
Résumé de la Thèse:	8
General Introduction	9
CHAPTER I: General Aspects of π-Dimerization – Towards Redox-Controllable Molecular Motions	10
I.1. Introduction	11
I.2. Viologens	13
I.3. π -Dimerization of Viologen Derivatives.....	14
I.4. Strategies to Promote Dimerization	16
I.4.1. Covalently Linked Bis-Viologens	16
I.4.2. Confinement Strategies.....	23
I.4.2.1. Cyclodextrin-Based Inclusion Complexes.....	23
I.4.2.2. Cucurbituril-Based Inclusion Complexes	25
I.5. Conclusion, Perspectives and Objectives.....	29
CHAPTER II: Redox-Responsive Supramolecular Assemblies Built From Cucurbit[8]uril and Viologen–Based Tectons	30
II.1. Introduction.....	31
II.1.1. Background on Viologen/Cucurbituril-Based Assemblies	32
II.1.2. Objectives.....	34
II.2. Redox-Responsive 2D-Assemblies built from a Star-Shaped Porphyrin-Based Tecto	36
II.2.1. Synthesis of the Targeted Tecton $11M^{8+}$	36
II.2.2. 1H -NMR Characterization.....	37
II.2.3. Characterization of the Association Between CB[n]	38
II.2.3.1. Threading of CB[7] on $11M^{8+}$	38

II.2.3.2. Threading of CB[8] on 11M ⁸⁺	39
II.2.4. Electrochemistry and Spectro-Electrochemistry in Organic Medium	41
II.2.5. Electrochemistry and Spectro-Electrochemistry in Aqueous Medium	44
II.2.6. Computational Analysis	54
II.2.7. Conclusion.....	55
II.3. Redox-Responsive 1D-Assemblies built from a Linear Porphyrin-based Tecton.....	56
II.3.1. Synthesis of the Targeted Tecton 17Zn ⁴⁺	56
II.3.2. ¹ H-NMR Characterization.....	57
II.3.3. UV-visible Absorbance Characterisation.....	62
II.3.4. Characterization of the Association between CB[n].....	65
II.3.5. Electrochemistry and Spectro-Electrochemistry in Organic Media.....	69
II.3.6. Photoreduction of 17Zn ⁴⁺ in Organic Media.....	72
II.3.7. Electrochemistry and Spectro-Electrochemistry in Aqueous Medium	73
II.3.8. Conclusion.....	80
II.4. Redox- Responsive Assembly involving Tetraphenyl Ethylene Based Tecton.....	81
II.4.1. Synthesis of the Targeted Tecton 21 ⁸⁺	81
II.4.2. ¹ H-NMR Characterization	82
II.4.2.1. Threading of 21 ⁸⁺ through CB[7].....	82
II.4.2.2. Threading of 21 ⁸⁺ through CB[8]	83
II.4.3. Electrochemistry and Spectro-Electrochemistry in Organic Medium	84
II.4.4. Electrochemistry and Spectro-Electrochemistry in Aqueous Medium	87
II.4.5. Conclusion.....	90
Chapter III: Redox Responsive Clips and Tweezers	91
III.1. Introduction	92
III.1.1. Flexible Tweezer.....	94
III.1.2. Clips	96

III.1.3. Stimuli-Responsive Tweezers.....	99
III.1.3.1. Chemically Responsive Molecular Tweezers	99
III.1.3.2. Light-Responsive Molecular Tweezers.....	101
III.1.3.3. pH-Responsive Molecular Tweezers	102
III.1.3.4. Redox-Responsive Molecular Tweezers	103
III.1.4. Objectives of this Chapter.....	104
III.2 . Flexible Tweezers Incorporating a 2,6- <i>Bis</i> (phenyl)pyridine Spacer	106
III.2.1: Synthesis of the Targeted Tectons	106
III.2.2. NMR Characterization	107
III.2.3. Electrochemical Characterization	109
III.2.4: Spectro-Electrochemical Characterization.....	112
III.2.5. Computational Analysis.....	117
III.2.6. Molecular Recognition Properties	118
III.2.7: Conclusion	123
III.3. Flexible Tweezers Incorporating a Terpyridine Spacer.....	124
III.3.1: Synthesis of the Targeted Tectons	124
III.3.2. NMR Characterization	125
III.3.3. Electrochemical and Spectro-Electrochemical Characterizations	126
III.3.4. Metallation of the Terpyridine Spacer	129
III.3.5. Electrochemistry of the Coordination Complexes	133
III.3.6. Conclusion	134
III.4. Rigid Viologen-Based Clips Incorporating Dibenzoacridine Linker	135
III.4.1. Synthesis of the Targeted Tectons	135
III.4.2. ¹ H-NMR Characterization	138
III.4.3. Electrochemical and Spectro-electrochemical Characterizations	140
III.4.4. Computational Analysis.....	142
III.4.5. Conclusion	143

Chapter IV: Viologen Based Redox Responsive Coordination Polymer	144
IV.1. Introduction	145
IV.1.2. Synthesis of the Targeted Tecton.....	148
IV.1.3. ¹ H-NMR Characterization	148
IV.1.4. Complexation with Palladium	149
IV.1.5. Electrochemical Characterization	154
IV.1.6. Spectro-Electrochemical Measurements.....	161
IV.1.7. Conclusion	166
General Conclusion	167
V: Experimental Part.....	169
V.1. General Synthesis	170
V.1.1. Solvents and Reagents	170
V.1.2. Apparatus and Spectroscopic Characterizations	170
V.2. Electrochemical studies	171
V.2.1. Solvents and Electrolytes	171
V.2.2. Apparatus and Spectroelectrochemical Characterization.....	171
V.3. Synthetic procedures.....	172
V.3.1. Synthetic procedures related to chapter II.....	172
V.3.2. Synthetic procedures related to chapter III	175
V.3.3. Synthetic procedures related to chapter IV	186
References	188

List of Abbreviations and Symbols

K_{dim} : dimerization constant

K_{a} : association constant

K_{disp} : disproportionation constant

ESR: electron spin resonance spectroscopy

SOMO: singly occupied molecular orbital

VRDE: voltammetry with rotating disc electrode

CV: cyclic voltammetry

ΔE_{p} : potential separation ($= E_{\text{pa}} - E_{\text{pc}}$)

E_{pc} : cathodic peak potential

E_{pa} : anodic peak potential

$E_{1/2}$: half-wave potential ($= (E_{\text{pa}} + E_{\text{pc}})/2$)

E_{app} : fixed applied potential at electrolysis

DMF: dimethylformamide

ACN: acetonitrile

DMSO: dimethyl sulfoxide

CB[7]: cucurbit[7]uril

CB[8]: cucurbit[8]uril

DOSY: diffusion ordered spectroscopy

COSY: correlation spectroscopy

ROESY: rotating frame Overhauser effect spectroscopy

HRMS-ESI: high resolution mass spectrometry-electrospray ionization

CBPQT⁴⁺: cyclobis(paraquat-*p*-phenylene)

DNP: 1,5-dihydroxynaphthalene

TBAP: tetra-*n*-butylammonium perchlorate

NIR: near infrared

Vis: visible

M: mol.l⁻¹

equiv.: molar equivalent

en : ethylenediamine
δ: chemical shift
d: doublet
ε: Molar absorptivity
J: coupling constant
K: association constant
λ: wavelength
m: multiplet
NMR: nuclear magnetic resonance
NOE: nuclear Overhauser effect
PEG: polyethylene glycol
ppm: part per million
TLC: thin layer chromatography
V: volume
Å : Ångström (10^{-10} m)
cm : centimeter (10^{-2} m)
Boc : Tert-butyl carbonate
EtOH : ethanol
Et₃N : triethylamine
Fc : ferrocene
DMV²⁺: 1,1'-diméthyl-4,4'-bipyridinium
THF : tetrahydrofuran
TTF : tetrathiafulvalene
CT : charge-transfer
DLS : Dynamic Light Scattering
K : Kelvin
SCE : saturated calomel electrode
CD : cyclodextrin
SAM : self-assembled monolayer

Résumé de la Thèse

L'objectif de mon travail de thèse était de développer de nouvelles approches vers des objets moléculaires et vers des assemblages supramoléculaires stimulables par transferts d'électrons. Au cours de ce travail, nous avons conçu, synthétisé et caractérisé de nombreux systèmes (supra)moléculaires dont la structure peut être bouleversée par le déclenchement de processus de π -dimérisation impliquant des radicaux π -conjugués électrogénérés à base de motifs 4,4'-bipyridiums, plus connu sous le nom de viologène. Le contrôle rédox des phénomènes d'auto-association est abordé dans un premier temps avec des tectons porphyriniques électroactivables capables de s'assembler, en présence de cucurbit[8]uril, sous l'effet d'une stimulation électrique centrée sur des substituants de type viologène. Nous avons notamment démontré que l'augmentation du nombre d'unités viologène sur un tecton donné permet de favoriser les phénomènes de réorganisation intramoléculaires impliqués dans les assemblages, une découverte qui ouvre de larges perspectives dans le domaine des assemblages commutables. Dans une seconde approche, nous avons développé des pinces et des clips moléculaires électro-activables susceptibles de former des matériaux auto-assemblés via l'établissement d'interactions supramoléculaires (type donneur/accepteur) entre des motifs auto-complémentaires introduits sur chaque tecton. Nos travaux ont permis de montrer l'influence de la taille et de la flexibilité de la plateforme organique choisie pour relier les motifs viologène sur les propriétés de reconnaissance et de dimérisation de ce type de molécule. Dans une dernière partie, nous décrivons la formation de polymères de coordination construits par assemblage d'un ligand ditopique à base de 4,4'-bipyridium avec du palladium, utilisé à la fois comme vecteur de la polymérisation et comme charnière inorganique favorisant la dimérisation intramoléculaire des formes réduites. Les résultats présentés révèlent que la formation de polymères / oligomères de coordination en solution peut être contrôlée par une stimulation électrique appropriée.

General Introduction

One of the most fascinating aspect of supramolecular chemistry is the opportunity to control the organization of molecules within so-called self-assembled materials. In recent years, the use of metamorphic molecular systems, capable of undergoing large amplitude molecular motions in response to an external stimulus (temperature, light, electrons, chemicals, magnetic field...), has emerged as a promising approach for the development of switchable supramolecular assemblies. Heat, pH, pressure and light are the most common stimuli used so far to trigger changes in the organization of simple molecular building blocks that eventually leads to macroscopic changes. Among all the stimuli investigated so far, responsiveness to electrical stimuli remains almost unexplored, despite being particularly attractive to ensure the implementation of such materials in devices.

The work presented in this thesis deals with the development of new approaches towards “smart” redox responsive molecular and/or supramolecular systems involving viologen units as key redox responsive elements. In all cases, the molecular or supramolecular-level metamorphic processes have been actuated by changing the redox state of the viologen units from their dicationic to their cation radical states, the driving force of the reorganization being the non-covalent and fully reversible dimerization occurring between viologen cation radicals.

In a first bibliographic chapter, we describe the main characteristics of viologen derivatives and their interest as active components in redox-switchable molecular and supramolecular systems.

The second chapter is devoted to the synthesis of redox-responsive supramolecular assemblies obtained in aqueous medium by self-assembly of carefully designed poly-viologen tectons and cucurbit[n]uril cavitands.

The third chapter deals with the development of viologen-based redox-responsive molecular clips and tweezers with detailed investigations of their molecular recognition and π -dimerization properties.

The last chapter describes another concept of redox-responsive assembly involving palladium and a viologen-based ditopic ligand as building elements. The self-association between the metal ions and the ligand leads to the formation of coordination polymers/oligomers which can be dissociated by reduction of the viologen centers.

**CHAPTER I: General Aspects of π -Dimerization –
Towards Redox-Controllable Molecular Motions**

I.1. Introduction

Supramolecular assemblies are ubiquitous in living systems. The most common example found in nature is DNA, wherein simple molecular building blocks are organized into functional structures.¹⁻² Therefore, in order to understand and predict the formation of supramolecular assemblies, it is necessary to have an overview of the non-covalent bonds available in the supramolecular toolbox. In particular, planar π -conjugated molecules are known for their ability to interact with their environment in many different ways. In most cases, the stabilization energy arises either from interactions between the quadrupolar moments of individual π -systems (best known as “ π - π stacking”) or from charge transfer processes occurring between electron-rich and electron-deficient π -units.³⁻⁷

In rare circumstances, when π -radicals are involved, stacking might be promoted by π -dimerization or pimerization processes. Both, the pimer and the π -dimer complexes exhibit sandwich-like, multicenter-bonded structures involving two planar π -conjugated units held together at sub-Van der Waals intra-dimer separation distances.

In π -dimers, the non-covalent “chemical bonding” arises from orbital overlaps occurring between two SOMOs centered on two identical radical ions or neutral species, whereas pimers, which are in essence the mixed-valence analogues of π -dimers, involve orbital overlaps between an organic π -conjugated system with its own radical (Figure 1).⁸

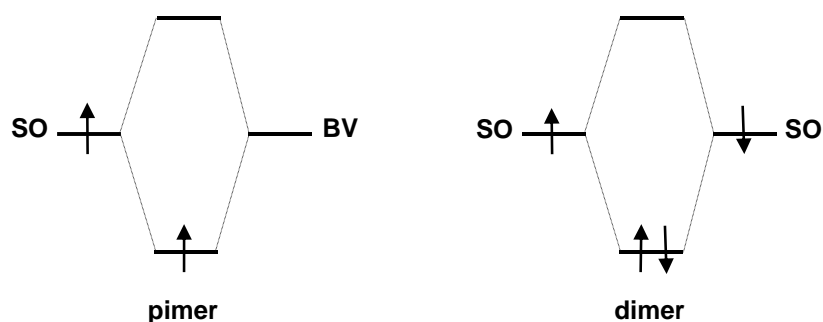


Figure 1: Schematic representation of the bonding orbitals involved in the formation of pimers and π -dimers.

Another salient feature of π -dimers is their metastable character, inherent to the quite weak stabilizing bonding energy. The latter eventually adds up to significant solvophobic and/or attractive electrostatic interactions with counter ions to overcome the electrostatic repulsion between both π -conjugated building elements bearing the same charge (positive or negative).⁹⁻¹⁰ The association is also fully reversible and the equilibrium between free radicals

and dimers can be readily displaced with standard physical parameters like temperature and concentration. A wide range of planar organic radicals, featuring different sizes and charges, have been shown to form such dimers. The most common ones are represented in Figure 2.

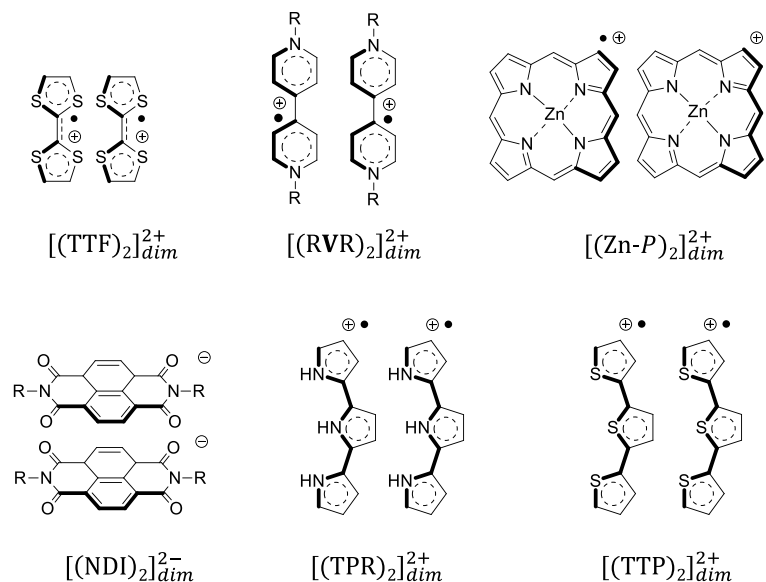


Figure 2: General representation of π -dimers obtained from tetrathiafulvalene (TTF), viologen (RVR)²⁺, porphyrine (Zn-P), naphthalenediimide (NDI), terpyrrole (TPR) and terthiophen-based radicals (TTP).

Tetrathiafulvalenes (TTF) are non-aromatic compounds but their one-electron oxidation ($E_{ox}^0 = 0.37$ vs. SCE) leads to the formation of aromatic/stable radical cations (TTF^{•+}). These species are quite often isolated as a π -dimers at the solid state.¹¹ In solution, the formation of π -dimers $[(TTF)_2]_{dim}^{2+}$ can be revealed by UV-visible spectroscopy measurements, with an absorption band observed in the 730 - 750 nm range depending on the solvent used.¹²

Metalloporphyrins, in particular zinc porphyrins (Zn-P) has been shown to form π -dimer both at the solid state and in solution.¹³ Oxidation of the porphyrin ring produces a radical cation that can eventually dimerize in concentrated solutions. The π -dimer $[(Zn-P)_2]_{dim}^{2+}$ shows an absorption band in the near-infrared region at 930 nm.

The one-electron reduction of naphthalenediimide (NDI) derivatives also lead to the observation of π -dimers. For instance, the electrochemical reduction of a sulphonated NDI (R= phenyl sulphonate) at -0.42 V vs SCE in aqueous solution has been shown to produce a radical anion (NDI^{•-}) which spontaneously dimerizes into $[(NDI)_2]_{dim}^{2-}$ which usually shows a broad absorption band at 1140 nm.

The dimerization of terpyrrole derivatives is also well documented. For instance, the one-electron oxidation of a phenyl substituted terpyrrole was shown to produce a stable radical cation ($E_{1/2}^1 = 0.28V$ vs. Fc/Fc^+) whose π -dimerization was revealed from variable temperature absorption spectroscopy measurements with the observation of a diagnostic absorption bands at 752 nm.¹⁴

All the concepts that we have developed in this thesis work involve the π -dimerization of viologen-cation radicals as the driving force of molecular motions. Emphasis will thus be given in the following sections to the reversible and noncovalent interactions arising between viologen radical cations.

I.2. Viologens

1,1-Di(hydrocarbyl)-4,4'-bipyridinium salts, best known as viologen (RVR^{2+}), can be readily formed by *N*-quaternization of 4, 4' -bipyridine. Use of methyl iodide as a reactant leads to the formation of 1,1'-diméthyl-4,4'-bipyridinium $MeVMe^{2+}$, most commonly known as paraquat. From an electrochemical point of view, this dicationic compound exhibits two consecutive Nernstian electron transfers attributed to the successive formation of the cation radical $MeVMe^{+\bullet}$ and of the neutral quinonic forms $MeVMe^0$ (Figure 3).¹⁵⁻¹⁶

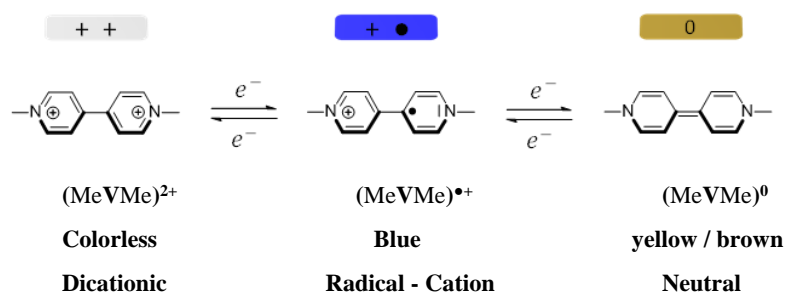


Figure 3: The three redox states of $MeVMe^{2+}$.

The dication salt $MeVMe^{2+}$ is colorless and its solubility in organic or aqueous media can be tuned with the two surrounding anions. Addition of one electron produces the paramagnetic blue-colored radical cation $MeVMe^{+\bullet}$,¹⁷ which is quite sensitive to the presence of oxidizing agents like molecular oxygen. The stability of the radical cation state is mainly governed by the delocalization of the single electron along the π -framework of the bipyridyl unit, wherein part of the charge is weakly carried by the 1 and 1' substituents.¹⁸ Another key feature of viologens is that the potential shift measured between both successive reduction processes is

large enough (> 400 mV) to ensure the stability of the π -radical cation $\text{MeVMe}^{+\bullet}$ state toward disproportionation.¹⁵ Further reduction of $\text{MeVMe}^{+\bullet}$ affords the diamagnetic neutral quinone-like MeVMe^0 which appears as a yellow-brown compound in solution. The latter is extremely reactive, and often referred to as the quinonic or biradical form.¹⁹

I.3. π -Dimerization of Viologen Derivatives

Spectroscopic studies carried out on RVR^{2+} (Figure 2) reveal the absence of absorption bands in the visible range due to the fact that the two pyridinium rings which are connected through a C–C single bond at 4,4'-positions are electronically independent.²⁰ The radical cation species ($\text{RVR}^{+\bullet}$) conversely shows an intense absorption band in the visible region associated to the delocalization of the unpaired electron throughout an extended π -framework of two pyridyl groups arranged in a fully coplanar conformation.²¹

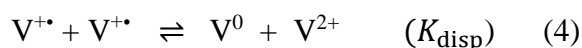
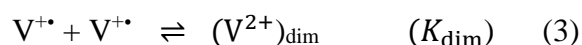


Figure 4: Successive one-electron reductions of a generic viologen derivative RVR^{2+} ((1) and (2)), and their potential coupled reactions (dimerization (3) and disproportionation (4)).

In aqueous solution, the color of the $\text{RVR}^{+\bullet}$ species ranges from blue to purple depending on concentration. The color of a 2×10^3 mM solution of $\text{MeVMe}^{+\bullet}$ was found to turn from violet at low temperature ($T < -196^\circ\text{C}$) to blue at room temperature.²²⁻²³ Schwarz and coll. have examined the spectroscopic signature of solutions of MeVMe^{2+} produced electrochemically over the concentration range in which an obvious color change occurs. As part of these studies, they have shown that the π -dimerization of $\text{MeVMe}^{+\bullet}$ ($K_{\text{dim}} = 385 \text{ M}^{-1}$) (eqn. 3, Figure 4) is the only process that can explain the change in color of the solution as a function of concentration and/or temperature.²⁴

The absorption spectrum of the dimer $[(\text{MeVMe})_2]_{\text{dim}}^{2+}$ features a broad absorption band at 850 nm and an intense signal in the visible region at 540 nm, blue shifted by about 60 nm compared to that observed for the non-associated radical.²⁵ This blue shift (Davidoff shift) is

attributed to the interactions between the transition dipole moments on adjacent molecules in the dimer. The most characteristic signal observed in the near IR region is due to the formation of bonding and non-bonding molecular orbitals from a pair of equivalent SOMO'S (scheme 1).^{8, 23, 26} The transition energy can be assessed as $h\nu_L = (\Delta^2 + 4H_{ab}^2)^{1/2}$, where Δ is the energy difference between the interacting orbitals (Ψ_a and Ψ_b) and the electronic-coupling element H_{ab} is equated to the resonance integral $\int \Psi_b H^{\text{eff}} \Psi_a$. In the case of π -dimerization, $\Delta=0$. Then the transition energy $h\nu_L$ in π -bonded dimers is directly related to the electronic-coupling term H_{ab} .⁸

The dimerization efficiency can also be readily assessed from ESR spectroscopy measurements as the singlet state electronic configuration of viologen-based π -dimers gives a silent ESR spectrum. The presence of non-dimerized paramagnetic viologen radicals in solution is thus revealed at room temperature by the observation of an intense signal close to the free electron g-value at 2.0023. For instance, temperature dependent ESR experiments have been implemented to determine the dimerization constant of 1,1'-ethyl-4, 4'-bipyridinium mono-radical cation in methanol ($K_{\text{dim}} = 1203 \text{ M}^{-1}$ for $\text{EtV}^{+\cdot}\text{Et}$ at 10^{-4} M).²⁷⁻²⁸

The radical cation of 1,1'-dimethyl-4,4'-bipyridinium ($\text{MeVMe}^{+\cdot}$) was isolated and characterized at the solid state in 1989.²⁹ The first π -dimer of viologen cation radicals ($\text{R} = \text{Et}$) has been characterized at the solid state in 2007 with $[\text{Fe}_4\text{Pt}(\text{CO})_{16}]^{2-}$ as a counter ion. Within each dimer, the radical moieties are perfectly eclipsed with a mean sub van der Waals distance of 3.275 Å measured between the planes defined by the two viologen units (Figure 5).³⁰



Figure 5: A) Crystal structure $[\text{EtV}^{+\cdot}\text{Et}]_2$ π -dimer. B) Chemdraw representation of the dimer.³⁰

Unfortunately, due to their low stability, the vast majority of dimers and in particular most viologen based π -dimers reported so far in literature involve intermolecular overlaps imposed either at the solid state by packing effects or favoured in solution by temperature effects or by use of unusually high concentrations of radicals. To cope with this problem, one strategy

which has proved quite effective in promoting the formation of non-covalent long bonded dimers in standard temperature and concentration ranges relies on the use of container molecules, such as the cyclodextrins or cucurbit[n]urils, capable of hosting and stabilizing such self-assembled dimeric entities.³¹⁻³² Alternatively, their formation can also be greatly improved through the introduction of both dimerizable partners on a suitable rigid scaffold or through their connection with covalent linkers of appropriate size and flexibility.

I.4. Strategies to Promote Dimerization

I.4.1. Covalently Linked Bis-Viologens

One of the most efficient and widely used strategy to promote the dimerization of viologen-based cation radicals rely on a molecular engineering approach enabling to link two monomers through a flexible covalent linker of appropriate size and flexibility. Early developments in this field involve the use of flexible alkyl linkers such as the propyl chain which has been found in agreement with the $n=3$ rule defined in the sixties by Hirayama³³, to yield the highest dimerization binding constant ($K_{dim} = 515 \text{ M}^{-1}$).³⁴⁻⁴⁰

A systematic electrochemical/spectroscopic study has been carried out by Tazuki and coll. on a series of alkyl linked bis- and tris viologens (Figure 6).⁴¹

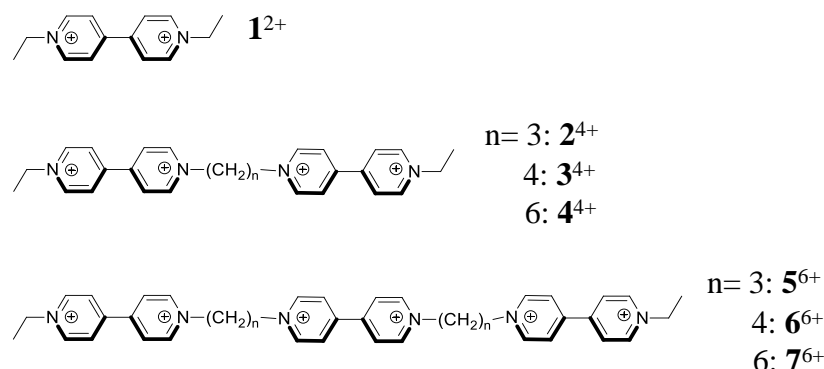


Figure 6: Bis- and tris-viologen compounds with flexible alkyl chains investigated by Tazuki and coll.⁴¹

The absorption spectra of the viologen-based cation radicals produced *in situ* by electrolysis are shown in Figure 7. The radical cations 1^+ , $\text{4}^{2(+\bullet)}$ and $\text{7}^{3(+\bullet)}$ show similar absorption bands observed between 400 nm and 600 nm (Figure 7A) attributed to the spectroscopic signature of free, non-dimerized, viologen radicals.⁴²

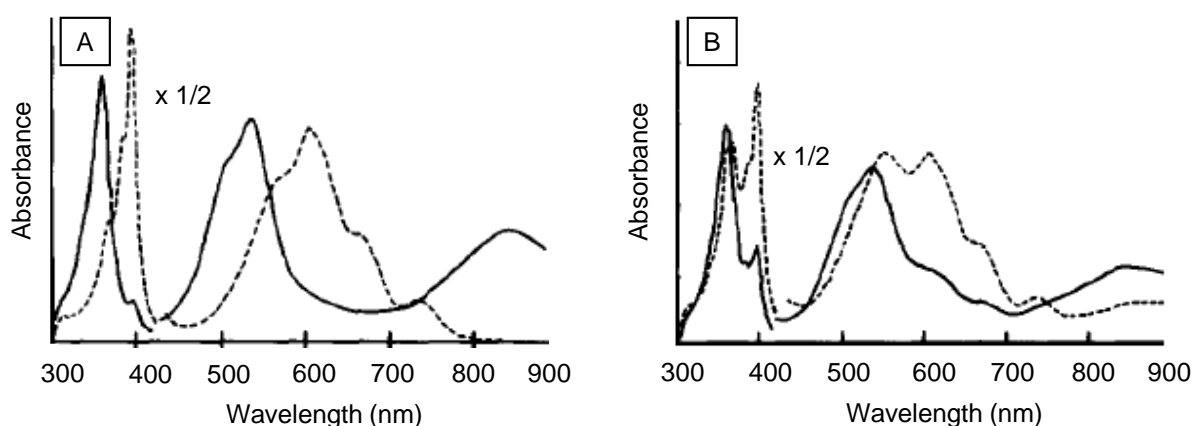


Figure 7: Absorption spectra recorded for a series of viologen-based radical cations (1.1mM) in DMF containing 0.1 M TBAP. A) 1^{+} , 4^{2+} , 7^{3+} (dashed line), and 2^{2+} (solid line), B) 3^{2+} , 6^{3+} (dashed line), and 5^{3+} (solid line).⁴¹

The radical cation of the propyl-linked derivative 2^{4+} shows a fully different absorption spectrum with intense bands centered at $\lambda_{\max} = 360$ nm and 533 nm as well as a broad diagnostic π -dimer band at 850 nm. The radical cations generated from the butyl- and hexyl-linked derivative 3^{4+} and 6^{6+} were found to exhibit similar absorption bands centered at 360 nm, 533 nm, 600 nm and a weak π -dimer band at 850 nm while the propyl-linked derivative 5^{6+} shows an absorption spectrum similar to that obtained in the same conditions upon reduction of 2^{4+} (one electron/viologen).⁴¹ These results demonstrate that a mixture of free radical and of π -dimerized species is systematically obtained upon reduction of all the alkyl-linked bis-viologens. Hence this pioneer work, and many more recent ones, have thus revealed that the value of the dimerization constant K_{dim} is tuned to a large extent by the length of the alkyl linker, and the propylene spacer being the most suitable one to promote the face-to-face dimerization between viologen-based radicals.²⁷

It needs to be mentioned that the photoreduction of alkyl-linked bis viologens has also been reported.⁴³ It has for instance been established that irradiating an oxygen-free solution of 1,1'-trimethylene-bis-4-bipyridinium bromide (5×10^{-4} M) and 2-propanol (0.65 M) in water with a 300 W medium pressure mercury arc lamp ($\lambda > 300$ nm) results in the formation of viologen-based π -dimers showing absorption maxima at 850, 533, and 360 nm.

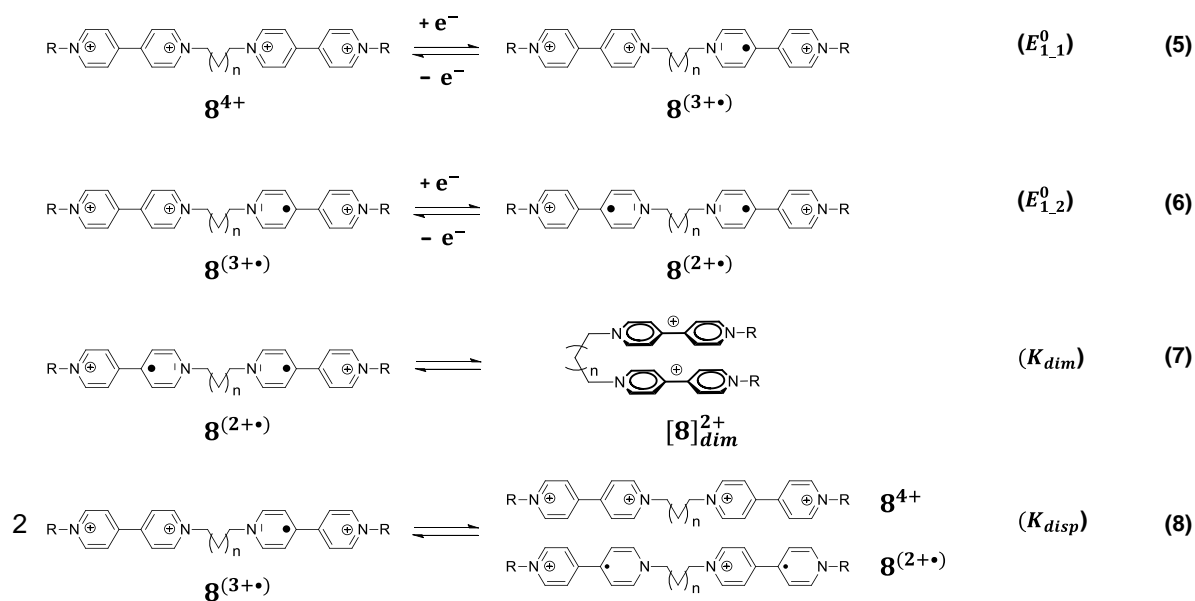


Figure 8 : Decomposition of the first reduction processes in linked bis-viologen species and their potential coupled reactions.

From an electrochemical point of view, such poly-viologen compounds featuring multiple chemically equivalent redox centers,^{44, 45} show an interesting behaviour in solution. Therefore, based on the electrochemical and spectroscopic investigations conducted over the past years on alkyl-linked viologen derivatives,^{34, 43, 46-50} the following conclusions can be drawn:

- The intramolecular dimerization of viologen-based cation radicals leads to a shift of the viologen-centered reduction potential toward less negative values. In other words, viologen centers are more easily reduced in compounds capable of π -dimerization.
- The dimerization constant K_{dim} (Figure 8), corresponding to the formation of $[\mathbf{g}]_{dim}^{2+}$ from $\mathbf{g}^{(2+•)}$, decreases as the number of carbon atoms in the chain increases from $n = 1$ to $n = 4$.
- The disproportionation constant (K_{disp}) of the one-electron reduced species, that is, $\mathbf{g}^{(3+•)} \leftrightarrow \mathbf{g}^{(4+)} + \mathbf{g}^{(2+•)}$ is favored by the consumption of the doubly reduced species in the dimerization reaction (K_{dim}). The efficiency of the π -dimerization and the value of the disproportionation constant (K_{disp}) can be readily assessed by cyclic voltammetry, most notably from the anodic shift of the first viologen-centered reduction wave and from the associated ΔE_p value (peak to peak potential shift; $\Delta E_p = E_{pa} - E_{pc}$), the fact that the second electron becomes easier to transfer than the first one ($K_{disp} > 1$ if

$E_2^\circ > E_1^\circ$) implying that ΔE_p gets lower than the expected 58 mV shift predicted from theory for a one-electron Nernstian process.

- The signature of intramolecular dimers is independent of concentration, anion and solvent. The typical π -dimer band appears around 840-860 nm and increasing the chain length from 3 to 4 carbon atoms only leads to a small red-shift of about 5-10 nm.
- In the presence of a flexible linker like in $\mathbf{8}^{(4+)}$ the stabilization energy involved in the intramolecular dimerization is about -9 Kcal/mol while for $[(\text{MeVMe})_2]_{\text{dim}}^{2+}$ the stabilization energy associated to the intermolecular dimerization is about 4 to 5 Kcal/mol.^{39, 51}

Another interesting feature of the tetra-cationic propyl-linked bis-viologen $\mathbf{8}^{4+}$ is that it adopts an elongated (unfolded) conformation at the ground state due to repulsive forces arising from the electrostatic repulsion between both dicationic viologens, while at the reduced state, the attractive forces between both cation radicals leads to the formation and stabilization of a π -dimerized folded conformation.

This situation is hardly seen with any other π -systems where attractive forces, such as those leading to the so-called π -stacking processes, are already involved at the ground state. This ability of $\mathbf{8}^{4+}$ ($n=3$) to oscillate between an “open” and a “closed” conformation under the effect of a two-electron transfer has been exploited in the past to develop a wide range of switchable systems like the redox responsive porphyrin-based molecular tweezer $\mathbf{9}^{4+}$ (Figure 9).³⁶

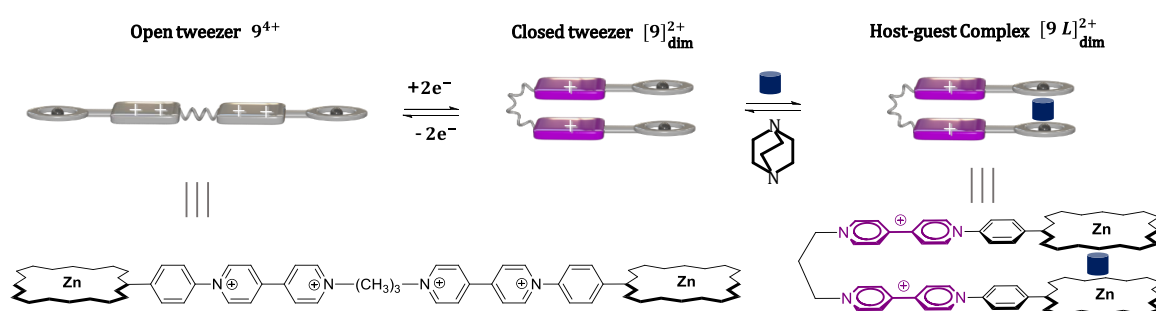


Figure 9: Redox-responsive porphyrin-based molecular tweezers.³⁶

This flexible molecule features two porphyrin rings covalently-linked through a flexible tetra-cationic bipyrindinium-based linker used as a redox-responsive molecular hinge, the reversible

conversion between the open (charge-repelled) and closed (face-to-face) forms relies on the ability of both bipyridinium subunits to dimerize in their reduced forms. Electrochemistry, spectroelectrochemistry and ESR spectroscopy measurements supported by computational analyses have shown that $\mathbf{9}^{4+}$ can be efficiently and reversibly converted from an “open” charge-repelled conformation into a “closed” cofacial arrangement resulting from the formation of the intramolecular π -dimer $[\mathbf{9}]_{dim}^{2+}$. This open/closed molecular motion, triggered by electron-transfers centred on π -dimerizable bipyridinium subunits, has furthermore been shown to allow the complexation of a bidentate heterocyclic ligand pinched between both metallo-porphyrins as revealed by the modulation of the porphyrin-based exciton coupling phenomena (Figure 9).

A similar principle has been used to devise the first ferrocene-based redox-responsive molecular carousel $\mathbf{10}^{4+}$ whose rotating motion is triggered by simple electron transfers centred on bipyridinium fragments introduced on both Cp's. Detailed electrochemical, theoretical, and spectroscopic analyses reveal that formation of the intramolecular π -dimer $[\mathbf{10}]_{dim}^{2+}$ requires the introduction of rigid, conjugated organic linkers between the rotating metallocene module and the electron motive π -dimerizable drivers. Evidence for intramolecular dimerization came from electrochemistry data, supporting the existence of chemical steps coupled to the electron transfer processes, and from ESR and UV-vis spectroscopy with the observation of diagnostic absorption bands in the near-infrared region (Figure 10).⁵²

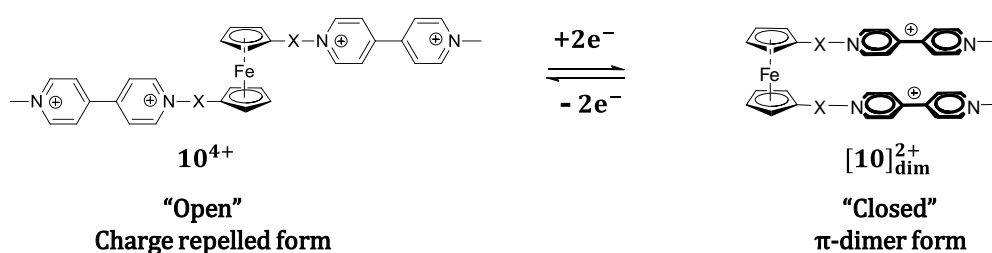


Figure 10: Redox-responsive carousel (X=organic linker : -CH₂-, -CH₂-CH₂-, -Ph-, -ethyne-).⁵²

It has also been reported that bipyridinium radicals can be reversibly π -dimerized under the combined effects of chemical and electrochemical stimuli.⁵³

A series of investigations carried out on viologen appended calixarenes that led to the discovery that the π -dimer $[\mathbf{11H}_2]_{dim}^{2+}$ can be produced from $\mathbf{11}^{2+}$ following two different

pathways involving either the CE or EC activation sequences, where C and E stand for the protonation (Chemical) and reduction (Electrochemical) processes, respectively (Figure 11).

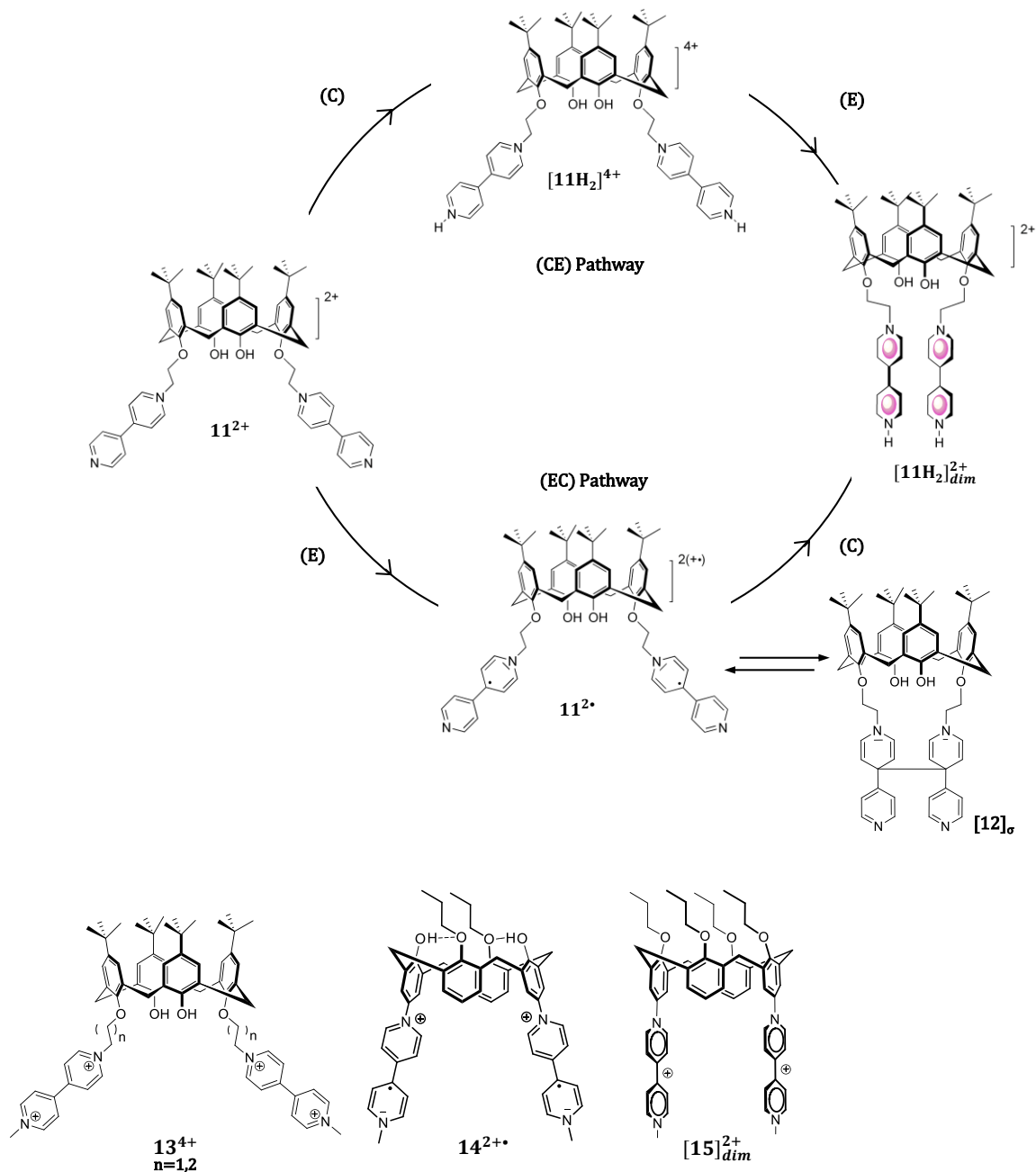


Figure 11: Schematic representation of different viologen-appended calixarenes ^[53]

It has even been established that the EC pathway involves an equilibrium between the σ -dimer $[12]_{\sigma}$ and the π -dimer $[11H_2]^{2+}_{dim}$. Experimental and theoretical data collected with the *N*-methylated and *N*-protonated compounds $11H_2$ and 13 ($n = 1, 2$) also support the existence of multivariant orientations in π -bonded dimers of viologen cation-radicals.⁵³⁻⁵⁵ For each

species investigated, it has been found that two different π -dimers, designated as the parallel and perpendicular isomers, stand as local minima on the potential energy surface and that the length of the linker ($n=1$ or 2 in **13**) as well as the nature of the substituents introduced on the terminal pyridine rings (H vs. Me) determine the most stable, parallel vs. perpendicular, conformation. Theoretical calculations carried out in the same conditions on the two-electron reduced forms of **11H₂** and **13** ($n = 2$) suggest that the most stable π -dimers are the perpendicular ($[\mathbf{11H}_2]_{dim}^{2+}$ and parallel $[\mathbf{13}]_{dim}^{2+}$ isomers, respectively).

Further investigations involving the linker-free viologen-calixarenes **14⁴⁺** and **15⁴⁺** revealed that the formation of an intramolecular π -dimer involving both pending viologen cation radicals requires the alkylation of the phenolic oxygen atoms at the lower rim of the calixarene skeleton. The conformational flexibility of the per-alkylated compound **15⁴⁺** allows for the formation of the intramolecular π -dimer $[\mathbf{15}]_{dim}^{2+}$ which is precluded in the case of the partially alkylated compound **14²⁽⁺⁾** as a result of the rigidity imposed by the hydrogen-bond network involving the remaining phenolic OHs.⁵⁶

The nature of the linkage separating the two bipyridinium units determines the efficiency of the dimerization. For instance, xylylene-linked bis-bipyridinium molecules have been shown to form long-bonded dimers in their reduced states. The aryl moiety has been introduced in the linker mainly for the purpose of rigidification.⁵⁷⁻⁵⁸ Spectro-electrochemical measurements revealed that the most efficient intramolecular π -dimerization is observed with the two-electron reduced forms of the ortho-substituted isomers *o*-**16⁴⁺** and *o,o*-**17⁴⁺** (Figure 12), which have been found to exist exclusively as π -dimers in their dicationic redox states $[o\text{-}\mathbf{16}]_{dim}^{2+}$ ($K_{dim} = 3.45 \text{ M}^{-1}$) and $[o\text{-}\mathbf{17}]_{dim}^{2+}$ ($K_{dim} = 20 \text{ M}^{-1}$).



Figure 12: Schematic presentation for bis-viologen species with flexible xylyl linkage.⁵⁷⁻⁵⁸

The viologen-based cyclophane known as the “blue box” has been exploited by Stoddart since the early 70th to devise a wide range of responsive catenanes and rotaxanes.⁵⁹ The presence of two viologen units provide the macrocyclic host with strong π -electron deficiency. These systems have been widely investigated because of their ability to form inclusion complexes with planar electron-rich organic molecules.⁶⁰⁻⁶¹

Recent works revealed that the close proximity of the two viologen units in $\mathbf{18}^{4+}$ may also facilitates the formation of π -dimerized complexes. In line with this comment, It has been shown that the doubly reduced species $\mathbf{18}^{2(+\bullet)}$ (Figure 13) forms an inclusion complex with various 4,4-bipyridinium cation radicals (RVR $^{+\bullet}$) yielding an equilibrium between the triradicals species [RVR $^{+\bullet}$ \subset $\mathbf{18}^{2(+\bullet)}$] and the corresponding π -dimer [RVR \subset $\mathbf{18}$] $_{dim}^{2+(+\bullet)}$ ($K_a = 5 \times 10^4 \text{ M}^{-1}$) featuring a pair of singlet state dimerized radicals and a single non-associated radical.⁶²

The formation of the tricationic triradical inclusion complexes between the radical state of dimethyl viologen MeVMe $^{+\bullet}$ and $\mathbf{18}^{2(+\bullet)}$ shows a binding energy around $-12.7 \text{ kcal/mol}^{-1}$.

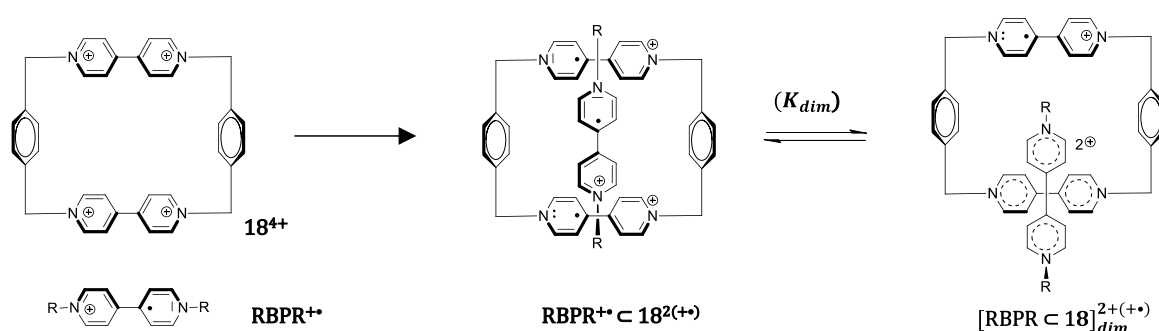


Figure 13: Schematic representation for the dimerization process of 4,4-bipyridinium cation radicals and doubly reduced "blue box".⁶⁰⁻⁶¹

I.4.2. Confinement Strategies

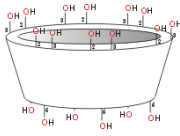
Another strategy to promote the dimerization of viologen-based radicals involves use of container-shaped cavitands, like cyclodextrin or cucurbit[8]uril, capable of hosting viologen-based π -dimers within their cavity.

I.4.2.1. Cyclodextrin-Based Inclusion Complexes

Cyclodextrins (CDs), also known as Schardinger dextrans, and cycloamyloses, comprise a family of cyclic oligosaccharides obtained by enzymatic degradation of starch.⁶³ These compounds are of great interest because of their ability to form inclusion complexes with a variety of organic molecules. The size/diameter/hydrophobicity of the inner cavity play important roles in their recognition abilities (Table 1).⁶⁴⁻⁶⁶

Previous reports have clearly demonstrated that the dimerization of viologens is enhanced upon addition of γ -CD, while the addition α -CD and β -CD inhibit the dimerization.⁶⁷⁻⁶⁹ In addition to that, the formation of inclusion complexes between viologens and CD has been

shown to depend on the substituents introduced on the viologen unit, on the size of the cavity, and on the redox state of the viologens. For instance, α -CD proved unable to stabilize the dimer of $\text{MeVMe}^{+\bullet}$, while β -CD led to an equilibrium between the dimer $[(\text{MeVMe})_2]_{\text{dim}}^{2+}$ and the free radical $\text{MeVMe}^{+\bullet}$ but the largest dimerization constant was obtained in the presence of γ -CD ($K_{\text{dim}} = 530 \text{ M}^{-1}$). On the other hand, reduction of the hexyl-substituted derivative $\text{HexV}^{2+}\text{Hex}$ alone or in the presence of γ -CD led to the observation of $[(\text{HexVHex})_2]_{\text{dim}}^{2+}$, While only the free radical $\text{HexV}^{+\bullet}\text{Hex}$ could be observed in the presence of α -CD and β -CD.



	Outer Diameter (Å)	Cavity Diameter inner rim (Å)	Cavity Diameter outer rim (Å)	Height (Å)	Cavity volume, (mL/g)	Solubility, g/kg H ₂ O
α , (glucose) ₆	15.2	4.5	5.3	7.8	0.1	129.5
β , (glucose) ₇	16.6	6	6.5	7.8	0.14	18.4
γ , (glucose) ₈	17.7	7.5	8.5	7.8	0.2	249.2

Table 1: Main physicochemical properties of cyclodextrins.⁶⁴⁻⁶⁶

It has also been demonstrated on the ground of CV and NMR data that viologens bearing short alkyl chains (methyl and ethyl) do not form inclusion complexes with α -CD, neither as dications nor as radical cations. This however proved not true with β -CD and γ -CD leading to the formation of inclusion complexes with $\text{RVR}^{+\bullet}$, as revealed by the positive shift of E_{pc} accompanied with significant changes in the UV-vis absorption spectra induced upon addition of CDs.

Viologens bearing long alkyl chains (like hexyl and heptyl) form 1:1 inclusion complexes with both α - and β -CD. In the oxidized state of viologen, both the α - and β -CD lies within the alkyl chain. While in the reduced state the β -CD moves toward bipyridine ring position and the α -CD remains in the alkyl chain (Figure 14A).⁷⁰

Finally γ -CD does not form an inclusion complex with the viologens in the oxidized state. Whereas it forms 1:2 complex with viologens in the reduced state that are stabilized as a π -dimer within the cavity of CD (Figure 14B).

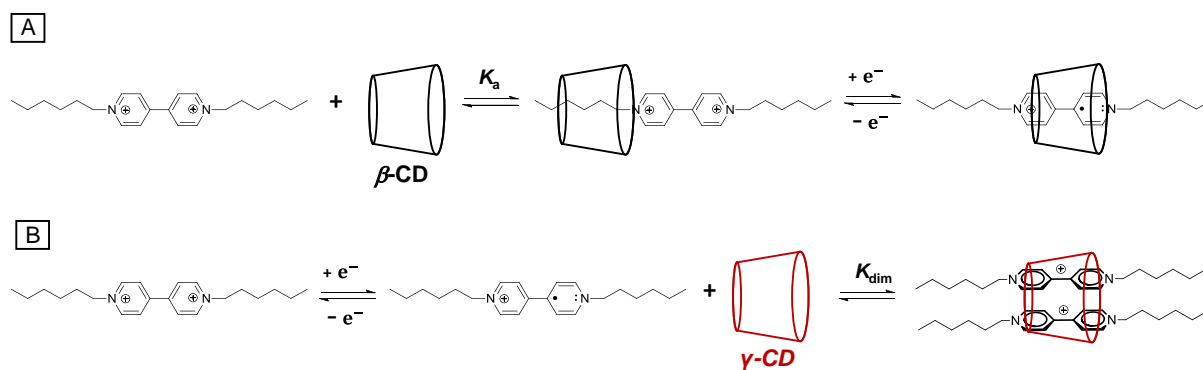


Figure 14: Schematic illustration of the inclusion of HexV²⁺Hex in CDs.⁷⁰

I.4.2.2. Cucurbituril-Based Inclusion Complexes

Cucurbit[n]urils (abbreviated henceforth as CB[n]) are pumpkin-shaped macrocyclic compounds composed of n glycoluril units interconnected with methylene bridges. They are obtained by condensation of glycoluril (Figure 15) with formaldehyde under high acidic conditions.⁷¹⁻⁷⁶

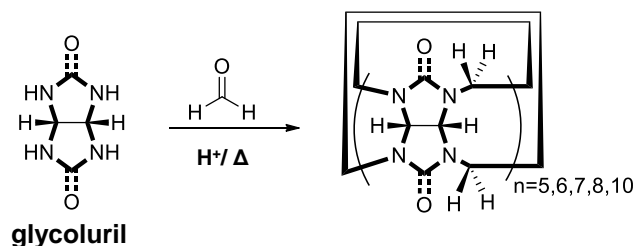
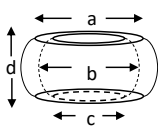


Figure 15: Preparation of CB[n]s from glycoluril and formaldehyde under acidic conditions.

CB[n]s replace advantageously cyclodextrins for most applications both in terms of cavity size and properties. They are also cheap, not toxic, resistant to microorganisms but only fairly to poorly soluble in aqueous media (see solubility values in Table 2).⁷⁴ The size and diameter of CB[n]s play an important role in their recognition abilities (Table 2).⁷⁷⁻⁸¹

A wide range of guest molecules can be stabilized within the cavity of CB[n]s *via* non-covalent interactions involving their hydrophilic carbonyl portals and/or the hydrophobicity of the cavity. CB[n]s have a high affinity for positively charged “hydrophobic” water-soluble organic molecules. The hydrophobic part of the guest can fit within the hydrophobic cavity of CB[n]s while the positively charged head of the guest is usually found in interaction with the hydrophilic, carbonylated part of the host.^{75, 82} It is worth mentioning that the strongest

binding affinity ever reported so far for host-guest complexes involves CB[7] and avidin as host and guest, respectively (10^{15} M^{-1}).⁸²⁻⁸³



	External Diameter (Å)	Portal Diameter (Å)	Cavity Diameter (Å)	Height (Å)	Volume (Å ³)	Solubility in H ₂ O at 25°C (mM)	Highest Binding Affinity (K_a) (M ⁻¹)
CB[5]	13.1	2.4	4.4	9.1	82	20-30	---
CB[6]	14.4	3.9	5.8	9.1	164	0.018	5.4×10^{10}
CB[7]	16	5.4	7.3	9.1	279	20-30	5.0×10^{15}
CB[8]	17.5	6.9	8.8	9.1	479	<0.01	4.3×10^{11}
CB[10]	20-21.1	9.5-10.6	11.3-12.4	9.1	870	<0.05	---

a: Portal Diameter b: Cavity Diameter c: Total Depth d: External Diameter

Structural parameters are calculated from the X-ray crystal structures.

Cavity depth determined from electrostatic potential minima.

Table 2: Main Physicochemical properties of CB[n]s.

CB[n]s featuring relatively small cavity sizes ($n = 5, 6$ and 7) usually form 1/1 inclusion complexes while larger CB[n]s ($n = 8, 9, 10$) can potentially accommodate two or even three guests. CB[n]s and viologens derivatives forms very stable host-guest complexes. The size, structure, symmetry and dicationic nature of viologens makes them perfect guests for CB[n]s.

I.4.2.2.1. Inclusion of Viologen Derivatives in Cucurbit[7]uril

The inclusion behavior of 1,1'-dimethyl-4,4'-bipyridinium (MeVMe^{2+}) in cucurbit[7]uril (CB[7]) has been investigated by Kim and coll.⁸⁴ Based on mass spectrometry and ¹H-NMR spectroscopy analyses, they found that (MeVMe^{2+}) forms a stable 1:1 host-guest complex with CB[7] in water ($K_1 = 2 \times 10^5 \text{ M}^{-1}$) (Figure 16). They have also established from cyclic voltammetry data that CB[7] has a stronger affinity for the cationic species MeVMe^{2+} ($K_1 = 2 \times 10^5 \text{ M}^{-1}$) and $\text{MeVMe}^{+\bullet}$ ($K_2 = 8.5 \times 10^4 \text{ M}^{-1}$) than for the neutral species MeVMe^0 ($K_3 = 2.5 \times 10^2 \text{ M}^{-1}$).

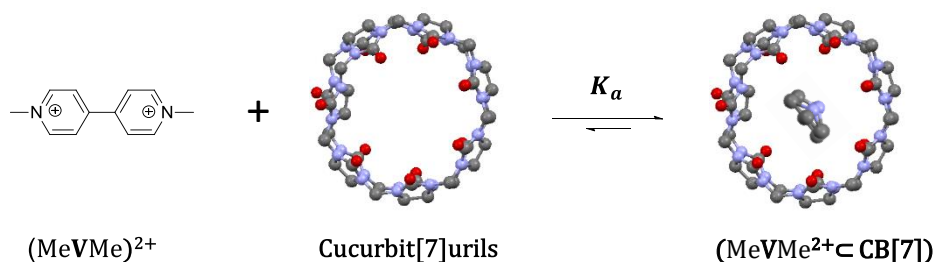


Figure 16: Schematic illustration of the inclusion of MeVMe^{2+} in CB[7].

As can be seen in Figure 17A, MeVMe²⁺ undergoes two reversible one-electron reductions attributed to the formation of MeVMe^{+•} ($E_{1/2}^1 = -0.704\text{ V}$, MeVMe²⁺/MeVMe^{+•}) followed by a second viologen-centered reduction yielding the neutral quinonic state MeVMe⁰ ($E_{1/2}^2 = -1.014\text{ V}$, MeVMe^{+•}/MeVMe⁰). Addition of CB[7] leads to a small negative shift in the half wave potential measured for the first CV wave, which suggests that CB[7] has a stronger affinity for MeVMe²⁺ than for MeVMe^{+•}. On the other hand, the large negative shift of the second CV wave indicate that CB[7] has a very weak affinity for the electrogenerated neutral species MeVMe⁰ (Figure 17A).⁸⁴

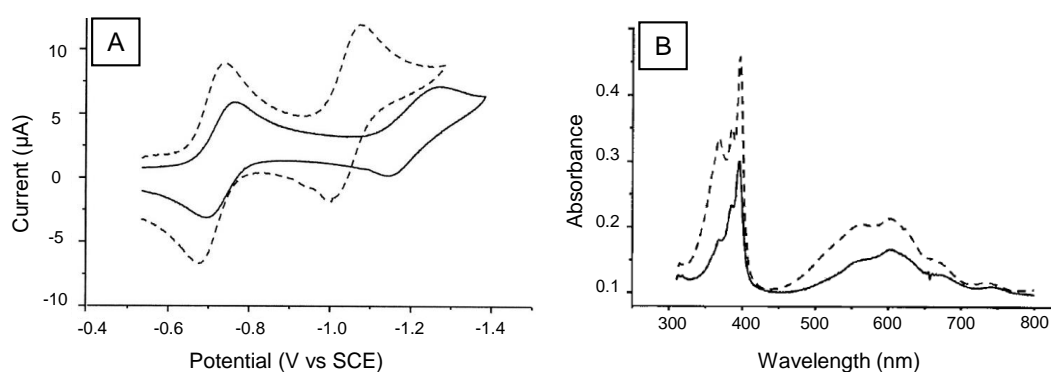


Figure 17: A) Cyclic voltammograms ($0.1\text{ V}\cdot\text{s}^{-1}$) of MeVMe²⁺ (0.5 mM in phosphate buffer solutions (pH 7.0)) recorded in the presence (solid line) of 3 molar equivalents of CB[7] and in the absence (dashed line) of CB[7]. B) Absorption spectra recorded in the presence (solid line) of 1 molar equivalent of CB[7] and in the absence of CB[7] (dashed line) after an exhaustive one-electron-reduction of MeVMe²⁺ (1.5 mM in phosphate buffer at pH 7.0) carried out at an indium tin oxide glass electrode whose potential was set to -0.8 V vs. SCE .⁸⁴

Further analyses involving spectro-electrochemical measurements demonstrated that CB[7] prohibits the π -dimerization of MeVMe^{+•}, as revealed by the fact that the UV-visible absorption spectrum recorded in the presence of CB[7] after reduction of the viologens is identical to that of the monomeric MeVMe^{+•} (Figure 17B).

1.4.2.2.2. Inclusion of Viologen Derivatives in Cucurbit[8]uril

Cucurbit[8]uril (CB[8]) has a wider cavity than CB[7] (see Table 2). It has nevertheless been shown to form 1:1 inclusion complex with MeVMe²⁺ ($K_a = 1.1 \times 10^5\text{ M}^{-1}$) (Figure 18).⁸⁵

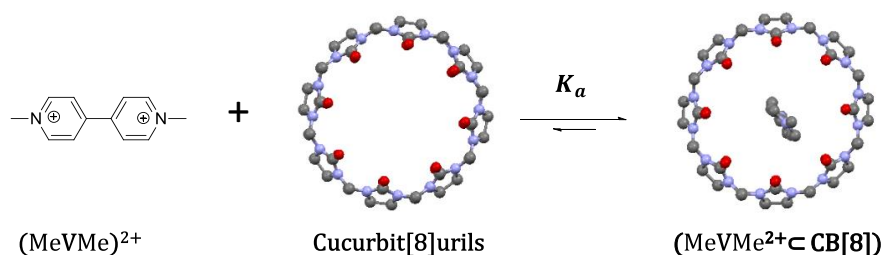


Figure 18: Schematic illustration of the inclusion of MeVMe²⁺ in CB[8].

The redox behavior of MeVMe^{2+} in the presence of CB[8] has been studied by electrochemical methods.⁸⁶ The presence of CB[8] was found to induce drastic changes in the electrochemical signature of MeVMe^{2+} . As can be seen in Figure 19A, the first and second reduction waves are shifted by about + 200 mV and – 250 mV, respectively, upon addition of 1 molar equivalent of CB[8]. These changes have been attributed to the formation of the 2/1 inclusion complex $[(\text{MeVMe})_{\text{dim}}^{2+} \subset \text{CB}[8]]$ ($K_{\text{dim}} = 2 \times 10^7 \text{ M}^{-1}$) wherein the cation radical state $\text{MeVMe}^{+\bullet}$ is stabilized as a π -dimer within the cavity of CB[8] (Figure 19A).

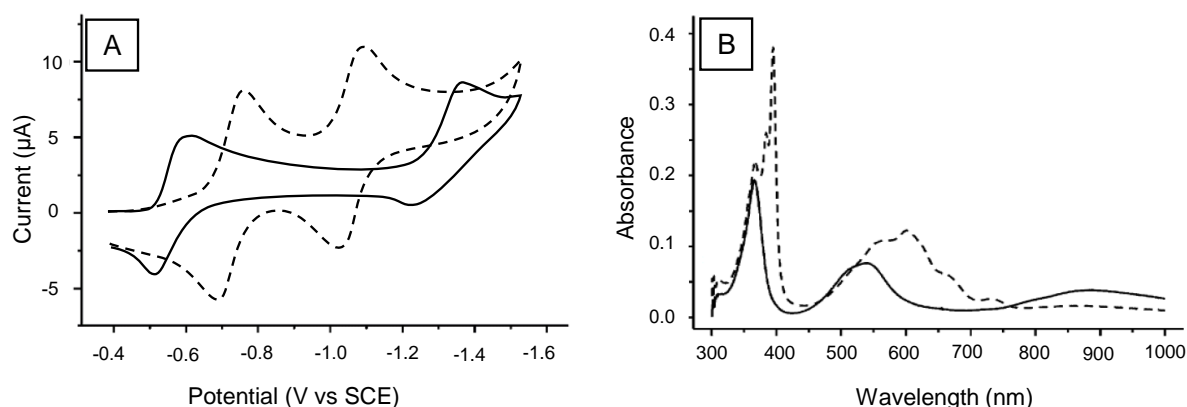


Figure 19 : A) Cyclic voltammograms ($0.1 \text{ V}\cdot\text{s}^{-1}$) of MeVMe^{2+} (0.5 mM in phosphate buffer (pH = 7.0)) recorded in the presence (solid line) of 3 molar equivalents of CB[8] and in the absence (dashed line) of CB[8]. B) Absorption spectra recorded in the presence (solid line) of 1 molar equivalent of CB[8] and in the absence of CB[8] (dashed line) after an exhaustive one-electron-reduction of MeVMe^{2+} (1.5 mM in phosphate buffer at pH 7.0) carried out at an indium tin oxide glass electrode whose potential was set to -0.8 V vs. SCE .⁸⁶

This conclusion is further supported by the spectro-electrochemical data depicted in Figure 19B showing that the characteristic absorption of the radical $\text{MeVMe}^{+\bullet}$ turns into that of the dimer upon addition of CB[8].

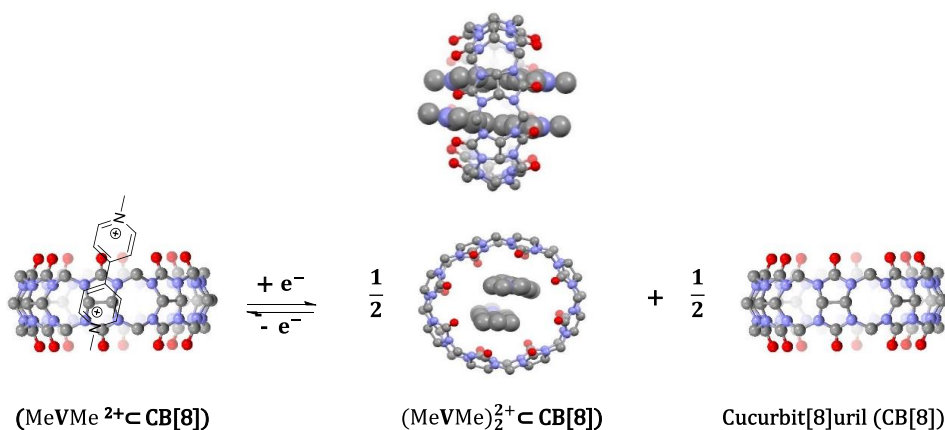


Figure 20: Schematic representation showing the conversion of the 1:1 inclusion complex ($\text{MeVMe}^{2+} \subset \text{CB}[8]$) into the 2:1 inclusion complex ($(\text{MeVMe})_2^{2+} \subset \text{CB}[8]$).

All these data support the conclusion that the mechanism shown in Figure 20 is involved in solution after reduction of the 1/1 inclusion complex $[\text{MeVMe}^{2+} \subset \text{CB}[8]]$. Accumulation of $\text{MeVMe}^{+\bullet}$ in solution triggers the inclusion of π -dimers in CB[8] together with a release of free CB[8]. The extensive stabilization of the dimer within CB[8] accounts for the potential shifts observed on the CV curves leading in the end to a large increase of the stability domain of the radical state, which gets much easier to form and harder to consume in the presence of CB[8].

I.5. Conclusion, Perspectives and Objectives

We have discussed in this chapter the general characteristics of π -dimers, paying particular attention to those derived from 4,4'-bipyridinium salts. In solution, the π -dimerization requires specific experimental conditions (low temperature, high concentrations...), which greatly limits the utility of these systems. These limitations could however be overcome by molecular engineering, upon introduction of suitable covalent hinges between the two partners or by encapsulating the partners inside the cavity of container-shaped cavitands. These strategies can be exploited to develop new switchable (supra)molecular architectures and materials.

In this context, the objective of this project is to develop new approaches towards “smart” redox responsive molecular and/or supramolecular materials containing π -dimerizable viologen units. This strategy has been used during my thesis to achieve an electronic control over the assembled and disassembled states of molecular systems.

**CHAPTER II: Redox-Responsive Supramolecular
Assemblies Built From Cucurbit[8]uril and
Viologen-Based Tectons**

II.1. Introduction

Supramolecular chemistry is known as “the chemistry beyond molecules”. One key objective in this field is to design and develop supramolecular architectures combining multiple components held together through non-covalent interactions. These interactions are reversible and usually weaker than covalent bonds.⁸⁷ The most well-known are the so-called hydrogen bonds, the electrostatic or van der Waals forces and the donor-acceptor interactions. As an inspiration, nature presents classical prototypes for the design and synthesis of supramolecular systems, since for many biological processes inter- and intra-molecular non-covalent interactions are crucial.⁸⁸ An archetypal example of such supramolecular systems found in nature is the DNA molecule, wherein a self-assembled helical structure is due to the association of complementary base-pairs interacting through multiple hydrogen-bonds.⁸⁹⁻⁹⁰

Inspired by such complex and efficient systems, chemists have focused on the development of supramolecular systems capable of performing specific tasks and functions in a controlled manner. This has been achieved through the introduction of stimuli-responsive moieties. A wide range of stimuli have already been considered to operate responsive-molecular systems including heat, pH, electric fields, magnetic fields, mechanical forces, sound, light, microwaves and chemical reactions.

Compared to other stimuli, the use of electrons is particularly attractive as it can simultaneously alter the charge, the properties and the spin states of a molecule. The oxidation or reduction of key responsive elements can be achieved electrochemically, by application of suitable potential values at a working electrode, photochemically or by addition of chemical oxidants/reductants. There are many redox-active molecular units available for the construction of redox-responsive supramolecular systems. The most widely used ones are the viologen derivatives (**RVR**)²⁺,⁷⁴ the tetrathiafulvalene derivatives (**TTF**),⁹¹ and the naphthalene diimide derivatives (**NDI**).⁹² Interest for these compounds mostly stems from the fact that they can be easily oxidized and/or reduced to yield stable radicals featuring intense and easily identified spectroscopic signatures.

In this chapter, we will focus on redox-switchable supramolecular assemblies involving viologen-based organic tectons and cucurbit[8]uril (CB[8]) cavitands as building blocks. We will first present and discuss a few relevant examples taken from literature then report on our own contribution in the field.

II.1.1. Background on Viologen/Cucurbituril-Based Assemblies

As mentioned in the first chapter, CB[n]s can form 1:1 inclusion complexes with a wide range of water-soluble positively charged organic species. This specific property has been exploited over the past decade to provide access to a wide range of self-assembled supramolecular assemblies.⁹³ Much efforts in this field have focused on CB[8], due to its ability to accommodate two different π -conjugated guests (electron-rich/electron-deficient) yielding 1:1:1 hetero-ternary inclusion complexes^{85, 94} stabilized through charge-transfer (CT) processes (π donors to π acceptors).

Various supramolecular assemblies have been developed over the past decade from CB[8] and covalently linked donor-acceptor molecules.⁷⁴ The type of assembly obtained from such building blocks greatly depends on the length and flexibility of the linker introduced between the donor and acceptor moieties. For instance, long and flexible linkers tend to favour the formation of intramolecular 1:1 CT complexes⁹⁵, while short and/or rigid linkers favour the formation of intermolecular 2:2 CT complexes or polymers.⁹⁶ In rarer cases, the use of rigid linker featuring specific angles has been shown to yield well defined “molecular necklaces” (cyclic oligomers) stabilized through intermolecular CT processes (Figure 21).⁹⁷

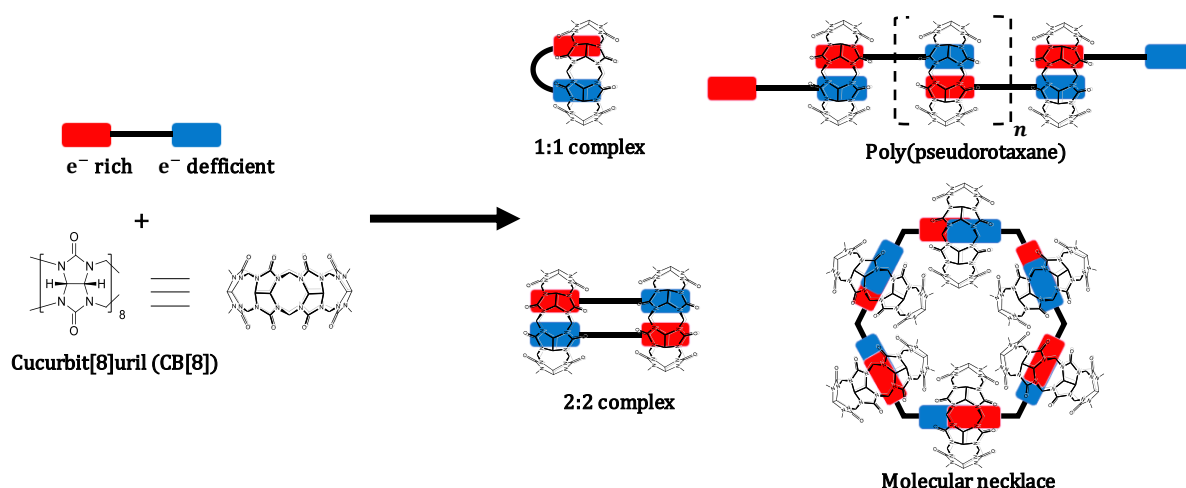


Figure 21: Different supramolecular assemblies built from CB[8] and D-A molecules containing a π -donor (in red) and a π -acceptor (in blue) connected through different covalent linkers.⁹⁷

The formation of a host-stabilized self-assembled polymers has first been achieved by Kim's group in 2004.⁹⁶ The concept that has been developed involves growing poly(pseudorotaxane) chains on a gold surface using host-stabilized CT interactions (Figure 22). The idea was to graft the pseudorotaxane $1^{2+} \subset \text{CB}[8]$ on the gold surface and to use it as an initiator. The targeted supramolecular polymerization was achieved by immersing the resulting gold-

modified SAM into a solution of $2^{2+} \subset \text{CB}[8]$. The growth of the poly(pseudorotaxane) was monitored by reflectance FT-IR spectroscopy measurements.

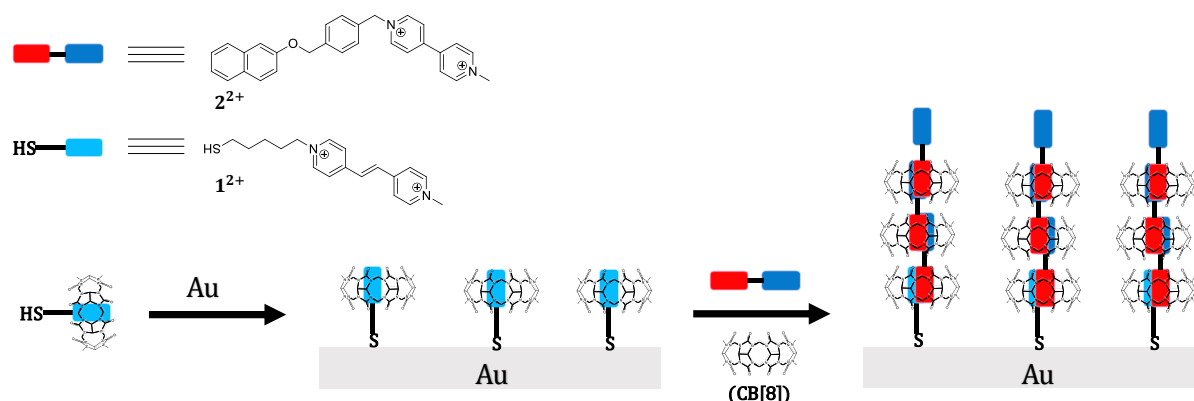


Figure 22: Formation of poly(pseudorotaxane) on a gold surface.⁹⁶

A similar supramolecular ‘bottlebrush’ polymer has been constructed from two separated rigid bis-donor and bis-acceptor units in water (Figure 23). The self-assembled supramolecular polymer formed in the presence of CB[8] was mainly characterized by DLS and DOSY NMR.⁹⁸

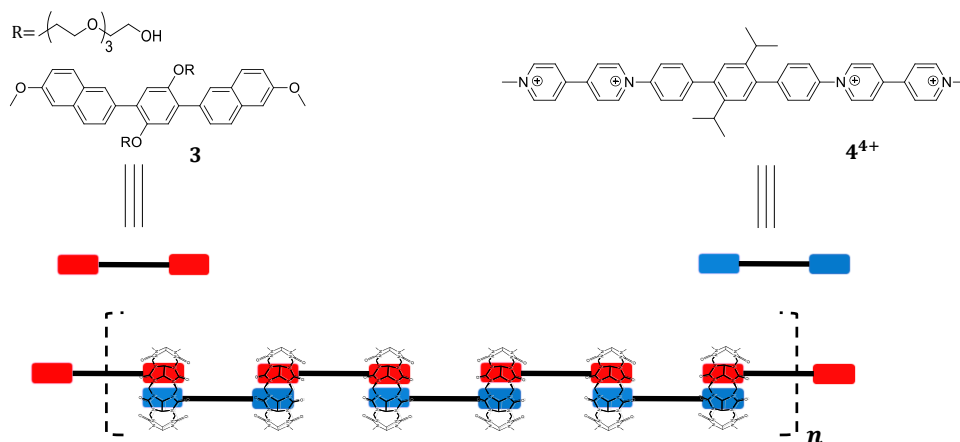


Figure 23: Supramolecular ‘bottlebrush’ polymer constructed from rigid monomers **3** and 4^{4+} .⁹⁸

Another approach that has been developed toward viologen-based stimuli-responsive supramolecular assemblies takes advantages of the redox properties of viologens and of their ability to dimerize in the presence of CB[8] to form 1D or 2D polymers.⁹⁹⁻¹⁰⁰ For instance, the group of Li and Zhao have reported beautiful examples of redox-switchable assemblies built from a series of linear π -conjugated compounds incorporating viologen units connected through phenyl (5^{4+}) or biphenyl linkers (6^{4+}). They first found that these oligomers spontaneously self-assemble in aqueous media, even in quite diluted conditions (5×10^{-4} M)

upon addition of sodium dithionite, used as a reducing agent, to form linear 1D polymers. They also established that the π -dimer-based self-assembly proceeds even more efficiently in the presence of one molar equivalent of CB[8]. The aggregation of the 1D polymers into bundles was also proposed to account for the micrometric diameter of linear molecular wires observed by cryo-transmission electron microscopy measurements. (Figure 24)¹⁰¹

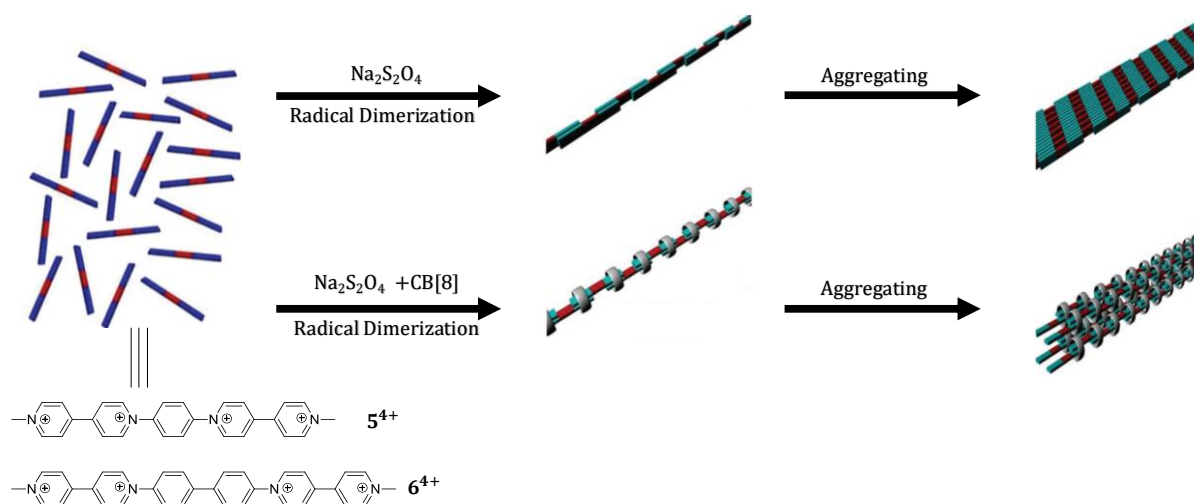


Figure 24 : Cartoon representation of the rigid linear 1D polymer structures generated by chemical reduction of **1** or **2** in the presence or in the absence of CB[8].¹⁰¹

II.1.2. Objectives

The concepts that were developed during my PhD thesis are mainly inspired by the works described in the previous section. The idea was to achieve an electrochemical control over the formation of supramolecular assemblies (Figure 25A) by exploiting the high affinity of CB[8] cavitands for viologen based π -dimers (Figure 25B); the underlying idea being that the dimensionality of the assemblies (1D or 2D) could be tuned with the number and relative orientation of the viologen units introduced on a given organic scaffold. The studies detailed below involve monomers incorporating either a porphyrin ring or a tetraphenyl ethylene unit used as structuring elements (Figure 25C) as readout molecular tools and as a functional units that could provide the resulting supramolecular materials with unique sensing, catalytic or photochemical properties.

According to the concept pictured in Figure 25A, the reversible association/dissociation of 1D or 2D viologen-based self-assembled polymers is expected to be triggered upon controlling the redox state of the viologen subunits (V^{2+} vs. $V^{+\bullet}$), the self-assembly process is being

driven by the formation of CB[8]-stabilized intermolecular π -dimers ($[\text{CB}[8]\text{C}(\text{V}^{\bullet+})_2]_{\text{dim}}$. We will first focus on the results obtained with porphyrin derivatives bearing either four or only two viologen units and then in more simple ethylene-linked tetra-viologen derivative (Figure 25C)

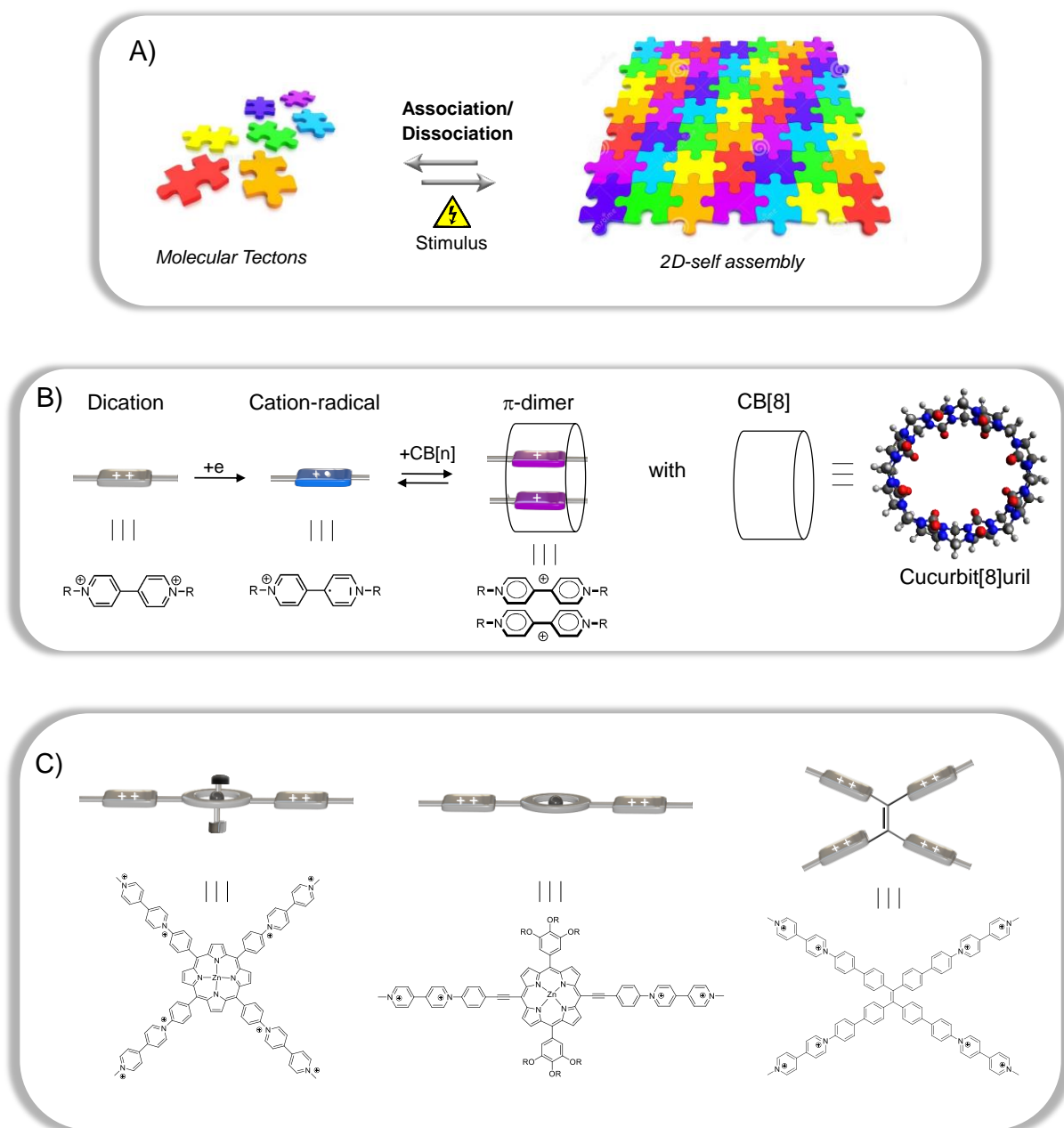


Figure 25: Schematic representation of A) the targeted stimuli-responsive 2D self-assembly process, B) the electron-triggered π -dimerization of two viologen-based cation radicals in the presence of CB[8] C). The schematic structure of the targeted viologen-based tectons.

II.2. Redox-Responsive 2D-Assemblies built from a Star-Shaped Porphyrin-Based Tecton

II.2.1. Synthesis of the Targeted Tecton $11M^{8+}$

The multi-step synthesis of the targeted molecule $11M^{8+}$ ($M = H_2$ or Zn), is summarized in Figure 26. This synthesis is actually the result of an improvement of a previously reported procedure.¹⁰² The starting point is a standard Rothmund condensation of pyrrole with 4-nitrobenzaldehyde carried out in a propionic acid/acetic anhydride mixture yielding the corresponding 5,10,15,20-*tetrakis*(4'-nitrophenyl)porphyrin **7** in 30% yield. Reduction of the nitro group in the presence of $SnCl_2 \cdot 2H_2O$, led with quite good yield to 5,10,15,20-*tetrakis*(4'-aminophenyl)porphyrin intermediate **8**, obtained as dark-blue crystals. The latter compound was then metalated with an excess of zinc (II) acetate at room temperature to afford **9** in quantitative yield. The targeted compounds $11H_2^{8+}$ and $11Zn^{8+}$ have *in fine* been obtained through multiple Zincke coupling reactions¹⁰³ involving the activated Zincke salt 10^{2+} as a reactant.¹⁰⁴

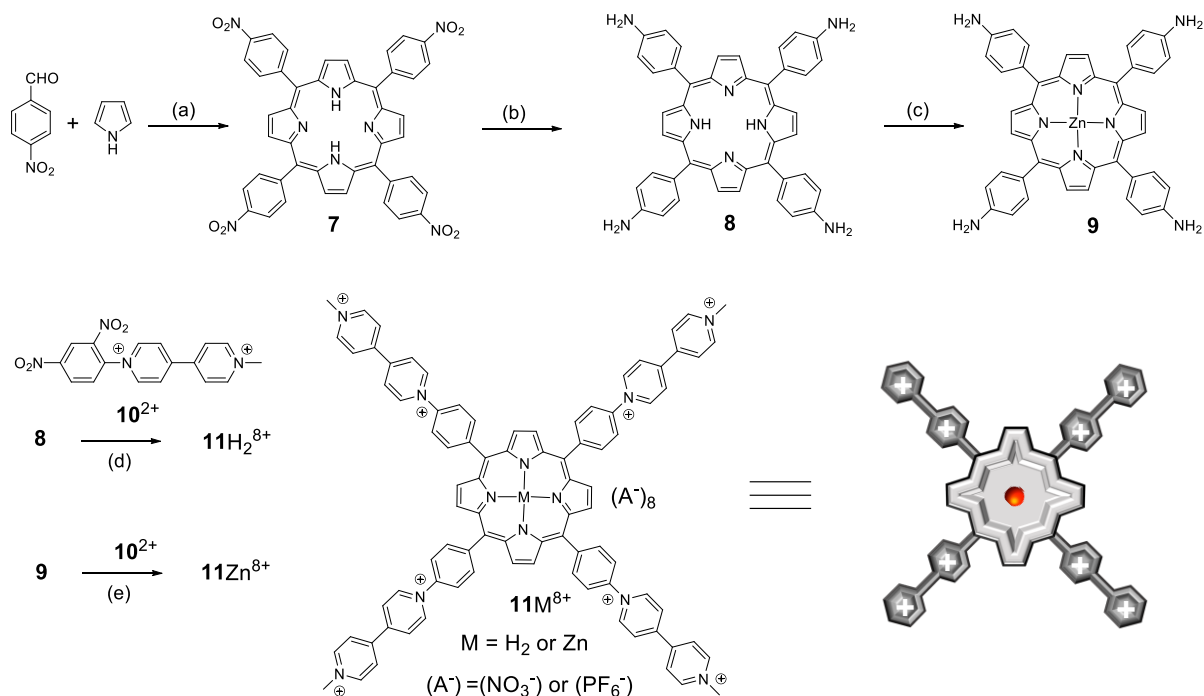


Figure 26: Synthesis of the targeted porphyrins. (a) $EtCO_2H$, Ac_2O , reflux, 4 h, 30%; (b) $SnCl_2 \cdot 2H_2O$, conc. aq. HCl , reflux, 16 h, 62%; (c) $Zn(OAc)_2$, DMF , $25^\circ C$, 30 min, > 99%; (d) $10(PF_6)_2$, $EtOH$, H_2O , reflux, 18 h, 29%; (e) $10(PF_6)_2$, $EtOH$, H_2O , reflux, 18 h, 32%.

II.2.2. $^1\text{H-NMR}$ Characterization

The $^1\text{H-NMR}$ spectra of $11\text{Zn}(\text{X})_8$ recorded in deuterated water ($\text{X} = \text{NO}_3^-$) and in DMSO ($\text{X} = \text{PF}_6^-$) are shown in Figure 27. The exact assignment of all these signals was achieved from the careful analyses of 1D- and 2D-NMR spectroscopy data. The spectrum of 11Zn^{8+} exhibits 6 doublets at low field attributed to the hydrogen atoms located on the viologen (b,c,d,e) and phenyl (f,g) units, as well as two singlets attributed to the hydrogens of the porphyrin and $\text{N}^+\text{-Me}$ moieties. The spectra recorded in water and in DMSO exhibit very similar features but with significant differences in the chemical shifts of the signals attributed to the viologens and to the porphyrin ring. The electron-withdrawing effect of the viologen units is brought to light through the low-field shift of the signals attributed to the β -hydrogen atoms of the porphyrin ring going from 9.17 ppm in the spectrum of the reference ZnTPP complex ($\text{TPP} = 5,10,15,20$ -tetraphenylporphine) to 8.95 ppm in that of 11Zn^{8+} . The presence of the zinc metal within the cavity of the porphyrin ring was confirmed by the absence of signal at $\delta < 0$ ppm.

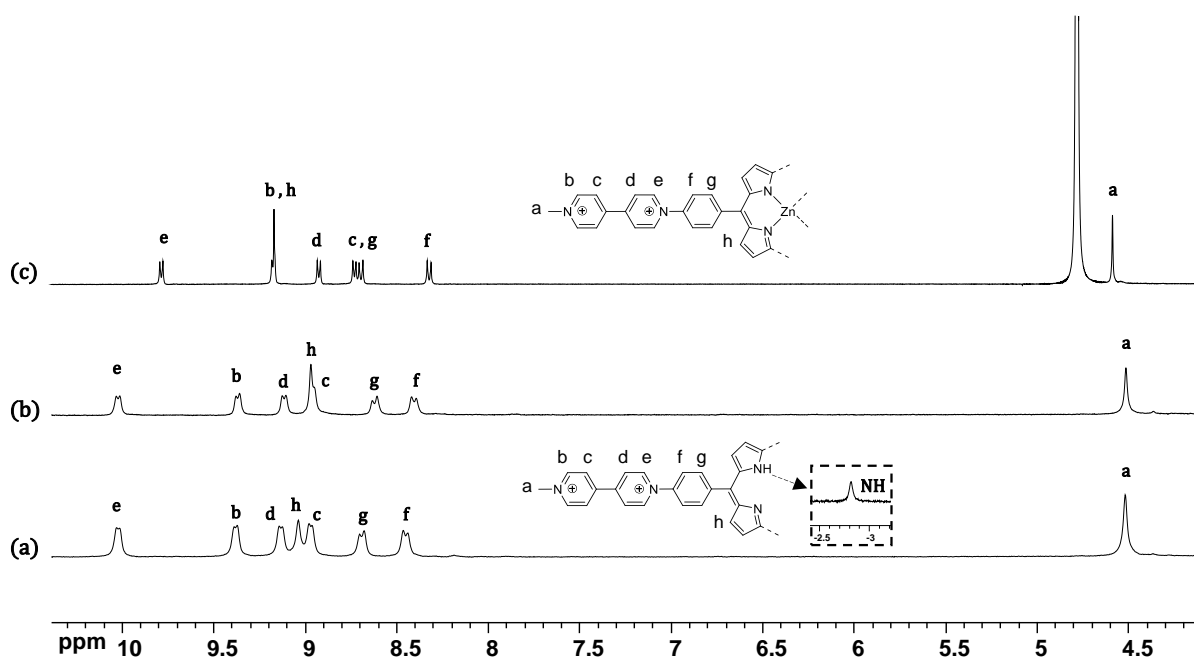


Figure 27: $^1\text{H-NMR}$ spectra of (a): $11\text{H}_2(\text{PF}_6)_8$ (DMSO, 400MHz), (b): $11\text{Zn}(\text{PF}_6)_8$ (DMSO, 400MHz), and (c): $11\text{Zn}(\text{NO}_3)_8$ (D_2O , 400MHz).

II.2.3. Characterization of the Association Between CB[n]

II.2.3.1. Threading of CB[7] on $11M^{8+}$

As mentioned before, both the CB[7] and CB[8] hosts have the ability to form [1:1] inclusion complexes with viologen-based guests (noted as RVR^{2+} , see Chapter:1, Figure 16, Figure 18). 1H -NMR titration experiments have been performed in deuterated water to get accurate and reliable information on the binding mode (stoichiometry, structure) between our star-shaped guest ($11Zn^{8+}$) and those barrel-shaped hosts (CBs).

As observed in Figure 28, the progressive addition of CB[7] (0 to 4 molar equivalents) led to the disappearance of all the signals corresponding to the free guest $11Zn(NO_3)_8$ at the expense of new signals attributed to the formation of different inclusion complexes.

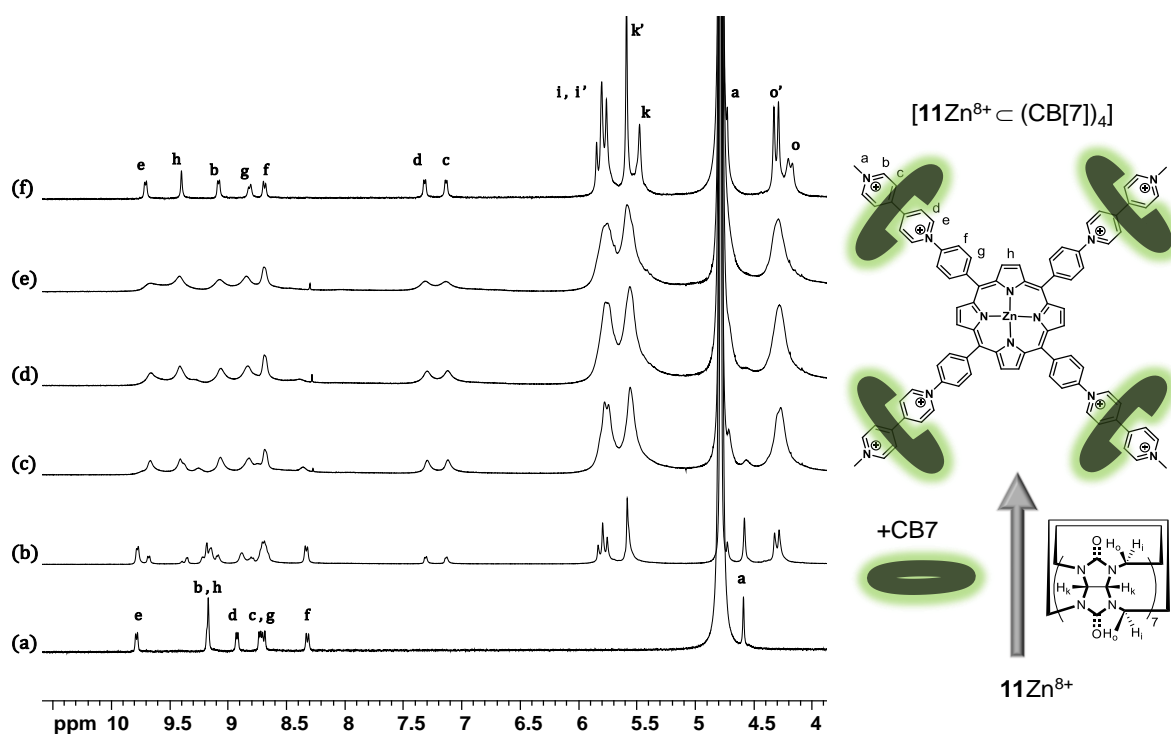


Figure 28 : 1H -NMR spectra (400 MHz, D_2O) of $11Zn(NO_3)_8$ (a) at 1.0 mM in the absence and in the presence of (b) 1.0 molar equiv. of CB[7] at 1.0 mM, (c) 2.0 molar equiv. of CB[7] at 1.0 mM, (d) 4.0 molar equiv. of CB[7] at 1.0 mM, (e) 8.0 molar equiv. of CB[7] at 1.0 mM, (f) 8.0 molar equiv. of CB[7] at 0.1 mM.

The first thing to notice is that the host-guest equilibria are kinetically slow at the NMR time scale. Another key information is that the maximum number of CB[n] hosts ($n=7$) that can be threaded onto the viologen-appended porphyrin is four, as revealed by the amount of CBs (in molar equivalents) needed to reach completion of the titration experiment. This result is consistent with the complexation of one viologen per CB to yield the inclusion complex $[11Zn^{8+} \cdot (CB[7])_4]$. Then, the largest shift is observed for signals attributed to the viologen

units (H_c , H_d), with upfield shifts reaching 1.6 ppm by the end of the titration. This large amplitude stands in contrast with the limited shifts of about 0.1-0.2 ppm monitored for the other protons of the viologens (H_b , H_e). These shifts thus reveal that the threaded CB[7] rings lie in between both pyridinium rings. Inclusion of the viologen units within the cavity of CB[7] has also a significant impact on the chemical shift of the signals attributed to the CB hosts. In the absence of guest, CB[7] displays one singlet at 5.53 ppm attributed to H_k and two doublets at 4.23 and 5.80 ppm attributed to the hydrogens of the methylenic bridge pointing outside (H_o) or inside (H_i) the cavity of CB[7], respectively.¹⁰⁵ As can be seen in the early stage of the titration (Figure 28), threading of a non-symmetrical viologen-based axle through a CB[7] ring also results in the splitting of the signal attributed to H_i , which ends up being observed as two partially overlapped doublets (pseudo triplet at 5.80 ppm) in the spectrum of the inclusion complex. The effect of the viologen-based guests on the CB[7] hosts is further revealed on the spectrum recorded at low concentration of $\mathbf{11Zn}^{8+}$ (0.1 mM) in the presence of 8 equivalents of CB[7] (top spectrum in Figure 28) through the observation of different sets of signals corresponding to the free (H_i' , H_o' , H_k') and complexed (H_i , H_o , H_k) CB[7]s.

Formation of the self-assembled host-guest complex $[\mathbf{11Zn} \subset (\text{CB}[7])_4]^{8+}$ has been further demonstrated by mass spectrometry measurements. The spectrum obtained with a Q-TOF instrument equipped with an electrospray ionization source in the presence of a formate buffer indeed showed a base peak at $m/z=865$ attributed to $[\mathbf{11Zn} \subset (\text{CB}[7])_4, (\text{HCO}_2)]^{7+}$.

II.2.3.2. Threading of CB[8] on $\mathbf{11M}^{8+}$

A similar investigation has then been carried out with the less soluble CB[8] host, featuring a wider inner cavity but still capable of forming 1/1 inclusion complexes with viologen derivatives.^{82, 106-107} The stoichiometry and structure of the assembly formed in solution were also deduced from the titration data depicted in Figure 29. As observed with CB[7], the largest chemical shifts involve the protons H_c/H_d and the titration reaches completion after addition of 4 molar equivalents of CB[8]. These results thus support the conclusion that four CB[8] rings can be threaded on $\mathbf{11Zn}^{8+}$ and that each CB ring lies in between both pyridinium rings. The impact of binding on the chemical shifts of the host is also found to be less pronounced for CB[8] than for CB[7]. This size effect is for instance revealed in the spectra of $[\mathbf{11Zn} \subset (\text{CB}[7])_4]^{8+}$ and $[\mathbf{11Zn} \subset (\text{CB}[8])_4]^{8+}$ through the observation of H_i as a broad singlet for CB[8] and as two singlets for CB[7].

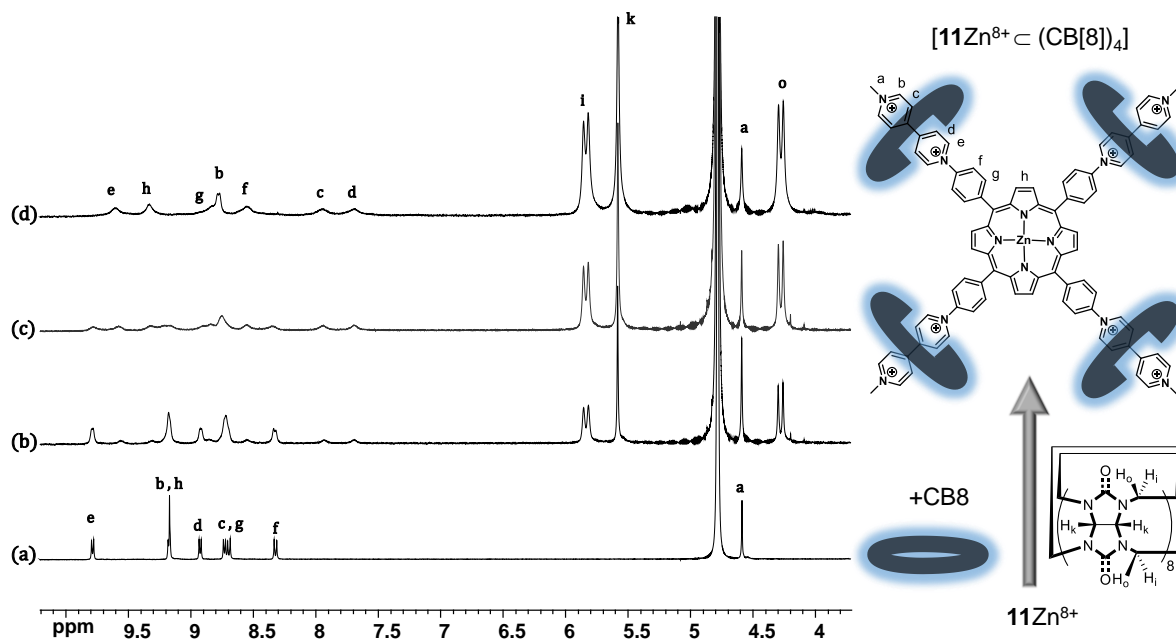


Figure 29: $^1\text{H-NMR}$ spectra (400 MHz, D_2O , 0.1 mM, 293 K) of $11\text{Zn}(\text{NO}_3)_8$ (a) in the absence and in the presence of (b) 1.0 molar equiv. of CB[8], (c) 2.0 molar equiv. of CB[8], (d) 4.0 molar equiv. of CB[8].

DFT calculations have been carried out by Dr. Elise Dumont at ENS-Lyon on the inclusion complex $[11\text{Zn} \subset (\text{CB}[8])_4]^{8+}$. The minimized structure (Figure 30) shows the absence of steric clashes of any sort, neither between the threaded macrocycles nor between the porphyrin skeleton and the CBs. It also confirms that the CB ring indeed lies right in between both pyridinium rings, with both positively charged nitrogens located close to the oxygen atoms at the cucurbituril portals.

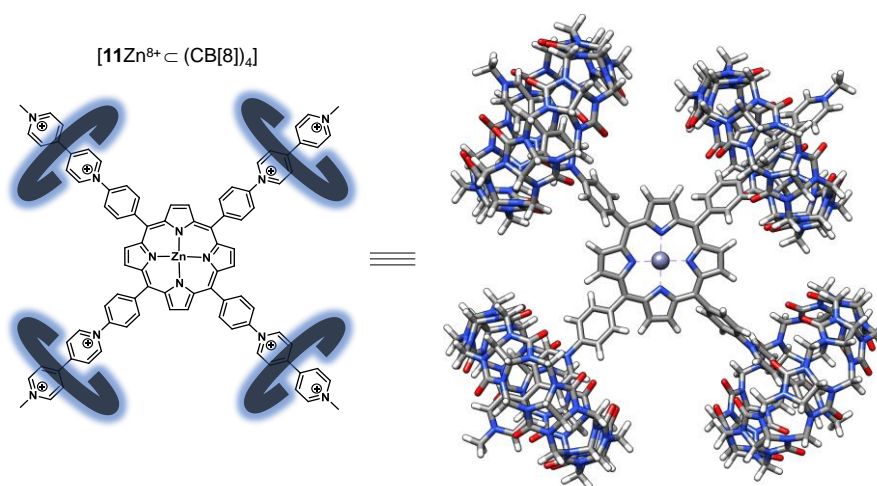


Figure 30: Left) Schematic representation of the inclusion complex $[11\text{Zn} \subset (\text{CB}[8])_4]^{8+}$ formed in solution upon mixing 11Zn^{8+} with an excess of CB[8]; Right) Structure of the complex optimized at the GGA hybrid Truhlar's density functional DFT/M06-2X level of theory, with a basis set 6-31G(d,p) using the Gaussian 16 revision B.01 suite of programs.

These data discussed above thus support the effective inclusion of the four viologen units available on the porphyrin platform in the cavity of CB[7] or CB[8] to yield the caviplex compounds [**11**Zn⁸⁺⊂(CB[n])₄]⁸⁺ (n = 7 or 8).

II.2.4. Electrochemistry and Spectro-Electrochemistry in Organic Medium

The electrochemical signatures of the title compounds **11**H₂(PF₆)₈ and **11**Zn(PF₆)₈ have first been investigated in DMF using tetra-*n*-butylammonium perchlorate (TBAP) as an electrolyte. Both compounds display similar signatures featuring four consecutive reductions (noted E^{1c} , E^{2c} , E^{3c} and E^{4c}) and one oxidation (noted E^{1a}) in the accessible potential window (Table 3).

The first reversible wave at $(E_{1/2})^{1c} = -0.762$ mV is attributed to the one-electron reduction of the four viologens units (one electron *per* viologen) yielding the tetra-cationic compound **11**Zn⁴⁽⁺⁾. The shape of this wave, featuring a standard ΔE_p value of about 63 mV reveals the absence of “communication” between each viologen introduced at the *meso*-positions of the π -conjugated porphyrin ring. Savéant has established in the early seventies that electron transfers to or from molecules containing n identical, non-interacting, redox centers should yield simple CV curves similar to that observed with a single electroactive center ($\Delta E_p \approx 58$ mV at 25°C) but with current values determined by the total number of redox centers.¹⁰⁸ When each center is characterized by the same formal potential and adheres to the Nernst equation independently of the oxidation state of any of the other centers in the molecule, it is possible to calculate the formal potentials corresponding to each pair of n successive oxidation states of the molecules. Considering fully non-interacting centers, the theoretical shift between the first viologen-based formal reduction potentials in **11**Zn⁸⁺ ($E^{0'}_{1-1}$, $E^{0'}_{1-2}$, $E^{0'}_{1-3}$, $E^{0'}_{1-4}$ in Figure 31) should thus equal $\Delta E^{0'}_1 = E^{0'}_{1-n} - E^{0'}_{1-(n-1)} = 23.7$ mV, although the overall four electron reduction appear *in fine* as a single four-electron reversible wave with peak potentials satisfying $\Delta E_p \approx 60$ mV.

The second one electron reduction of the viologen units (one electron *per* viologen) is observed at $(E_{1/2})^{2c} = -1,087$ V as a reversible wave. Here again, there is no experimental evidence supporting the existence of intramolecular “interactions” between the redox centers and the comments raised above when discussing the four-electron reduction **11**Zn⁸⁺ → **11**Zn⁽⁴⁺⁾ apply for **11**Zn⁽⁴⁺⁾ → **11**Zn⁰. It is worth mentioning here that the stability domain measured for the viologen cation state in **11**Zn⁽⁴⁺⁾ [$\Delta E = (E_{1/2})^{2c} - (E_{1/2})^{1c} = 325$ mV],

falling within the range of that measured in the same conditions with MeVMe²⁺ ($\Delta E = 336$ mV, Table 3) used as a reference, is a first evidence suggesting the absence of intermolecular interactions between the viologen cation radicals in solution.¹⁰⁹

The porphyrin ring is also submitted to two consecutive one-electron reduction at $(E_{1/2})^{3c} = -1.827$ V and $(E_{1/2})^{4c} = -2.236$ V, seen in Figure 31 as two reversible waves of low intensity yielding successively the porphyrin-based anion radical **11**Zn^{•-} and the dianion **11**Zn²⁻. On the anodic side, the weakly intense and poorly reversible wave observed at $E^{1a} = 0.682$ V is attributed to the oxidation of the porphyrin ring, shifted by more than +300 mV compared to that of TPPZn (TPP:5,10,15,20-*tetrakis*(phenyl)porphyrin)¹¹⁰ due to the presence of four electron-withdrawing viologen substituents.

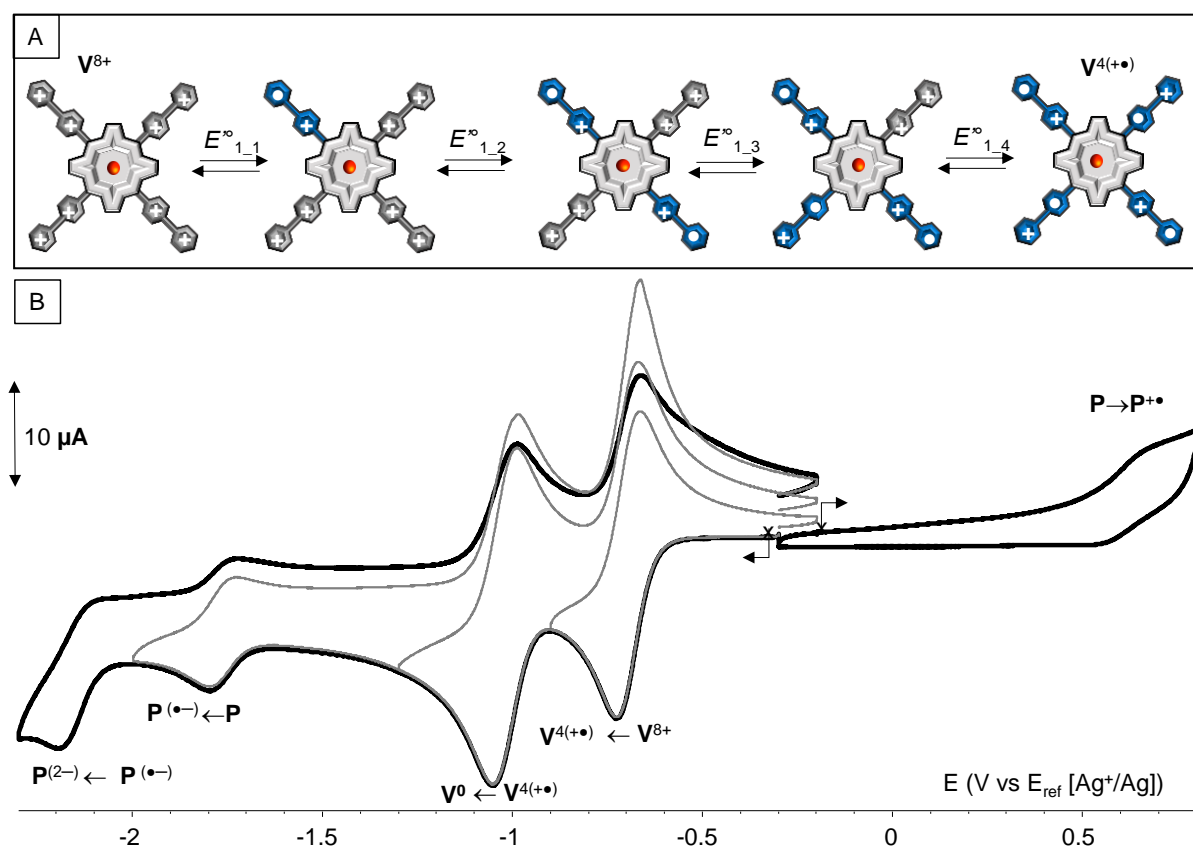


Figure 31: CV curves of a DMF (TBAP 0.1M) solution of **11**Zn(PF₆)₈ (5×10^{-4} M) recorded at a carbon working electrode ($\varnothing = 3$ mm, E vs. Ag⁺/Ag (10^{-2} M), $\nu = 0.1$ V.s⁻¹).

The free base porphyrin **11**H₂⁸⁺ was also studied in the same experimental conditions. Selected key values recorded with this compound are collected in Table 3. We found that the four electron-reduced species **11**H₂^(4+•) is more prone to adsorption than the metalated analog. These phenomenon were revealed on the CV curves by the observation of Gaussian-shaped

redissolution peaks on the backward scan, and could be readily circumvented upon dilution (below 2×10^{-4} M). The absence of metal in the porphyrin rings is also found to result in a significant anodic shift of the porphyrin-centered reduction waves and in the observation of a fully irreversible oxidation wave at $E^{1a} = 0.728$ V, which is in agreement with the known stabilizing effect of the zinc atom on the porphyrin-based π -system. The values collected in Table 3 also reveal that the viologen-based reduction potentials are only weakly affected by the presence of the zinc ion in the cavity of the porphyrin ring.

	Solvent	E^{4c} (n, ΔE_p) P^{••}/P²⁻	E^{3c} (n, ΔE_p) P/P[•]	E^{2c} (n, ΔE_p) V^{••}/V⁰	E^{1c} (n, ΔE_p) V²⁺/V^{••}	E^{1a} (n, ΔE_p) P[•]/P^{••}
MeVMe(PF ₆) ₂	DMF	na	na	-1.163 ^b (1,62)	-0.774 ^b (1,60)	na
11 H ₂ (PF ₆) ₈	DMF	-2.011 ^b (1,84)	-1.613 ^b (1,84)	-1.115 ^b (4,77)	-0.785 ^b (4,60)	0.728 ^c (1)
11 Zn(PF ₆) ₈	DMF	-2.236 ^b (1)	-1.827 ^b (1,75)	-1.087 ^b (4,67)	-0.762 ^b (4,63)	0.682 ^c (1)
MeVMe(Cl) ₂	H ₂ O	na	na	-0.99 (1,77) ^b	-0,654(1,60)	na
11 Zn(Cl) ₈	H ₂ O	na	na	-0.638 (4,24)	-0,389 ^{c,d}	0,861 ^c (1)

Table 3: Measured by CV, $2 \cdot 5 \cdot 10^{-4}$ M in DMF/TBAP (0.1 M, $E(V)$ vs. Fc/Fc⁺), or in an aqueous phosphate buffer (0.1M, pH = 7, $E(V)$ vs. AgCl/Ag (KCl sat)) at a vitreous carbon working electrode $\varnothing = 3$ mm, 298 K, $\nu = 0.1$ V·s⁻¹. na : Not available / ^b : Half wave potential / ^c : Peak potential / ^d : Adsorption phenomena

As discussed in chapter 1, the ability of viologen cation radicals to form non-covalent intermolecular π -dimers¹¹¹ in solution can be readily inferred from absorption spectroscopy measurements, most notably through the observation of a diagnostic broad absorption bands in the near infra-red region.¹¹²

Spectro-electrochemical measurements have therefore been conducted in the absence and in the presence of CBs. The absorption spectra recorded during an exhaustive electrolysis ($1e^-$ /viologen) of **11**Zn⁸⁺ (5.7×10^{-5} M) carried out in DMF at a platinum electrode led to a slight broadening of the porphyrin-based Soret band coming along with a significant bathochromic shift, of about 7 nm, of its maximum wavelength (from 426 to 433 nm) with a clean isosbestic point at 429 nm (Figure 32A). The extent of these modifications is fully compatible with electron transfers centered on the peripheral viologens having a minor impact on the electron density of the porphyrin-based π -system. This attribution is further supported by the emergence of intense absorption bands between 500 and 800 nm, overlying with the porphyrin-based Q bands, attributed to a series of transitions centered on a viologen cation-radicals, as revealed by the good match with the spectrum of the radical electrogenerated from the reference MeVMe^{•+} (dash-dotted line in Figure 32).

The main findings of this preliminary studies are thus that the conversion $\mathbf{11Zn}^{8+} \rightarrow \mathbf{11Zn}^{(4+\bullet)}$ is fully reversible at the electrolysis time scale (30 min) and that the electrogenerated species $\mathbf{11Zn}^{(4+\bullet)}$ do not form π -dimers in these experimental conditions, as revealed by the absence of diagnostic absorption bands in the near IR region (~ 900 nm) and by the standard ΔE_p value of about 60 mV measured on the first viologen-based CV wave.

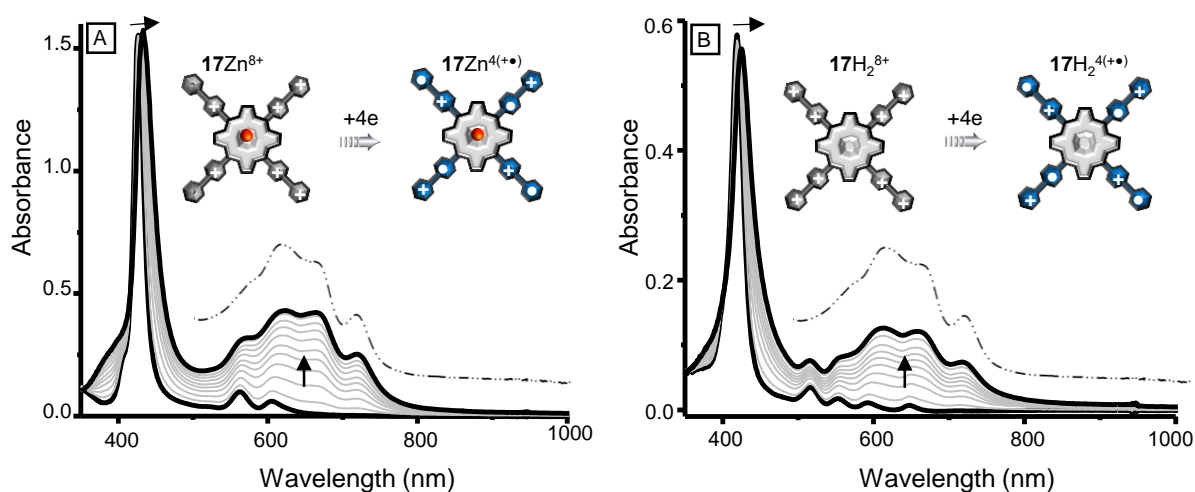


Figure 32: UV-vis spectra recorded during the exhaustive one-electron reduction (per viologen) of A) $\mathbf{11Zn}(\text{PF}_6)_8$ (5.7×10^{-5} M) and B) $\mathbf{11H}_2(\text{PF}_6)_8$ (2×10^{-5} M) in DMF (0.1 M TBAP) using a platinum plate working electrode whose potential was fixed at $E_{\text{app}} = -0.85$ V vs. $E_{\text{Ag}^+/\text{Ag}}$ (10 mL, $l = 1$ mm, $t \approx 30$ min).

Further investigations carried out on the free base $\mathbf{11H}_2^{8+}$ led to similar findings with a spectroscopic signature recorded after bulk electrolysis at $E_{\text{app}} = -0.85$ V (vs. $E_{\text{ref}} [\text{Ag}^+/\text{Ag}]$) in agreement with the formation of non-interacting tetra-radical species $\mathbf{11H}_2^{(4+\bullet)}$ (Figure 32B).

II.2.5. Electrochemistry and Spectro-Electrochemistry in Aqueous Medium

All the studies described below have been conducted on the metalated compound $\mathbf{11Zn}^{8+}$ only, as its signature and stability in aqueous medium proved to be the best suited for reaching the targeted objectives.

The idea here was to investigate the ability of CB[8] to promote the intermolecular dimerization of the four-electron reduced species $\mathbf{11Zn}^{(4+\bullet)}$ in water to yield 2D self-assemblies, as opposed to CB[7] expected to form only discrete host-guest caviplaxes with $\mathbf{11Zn}^{(4+\bullet)}$ (Figure 33).

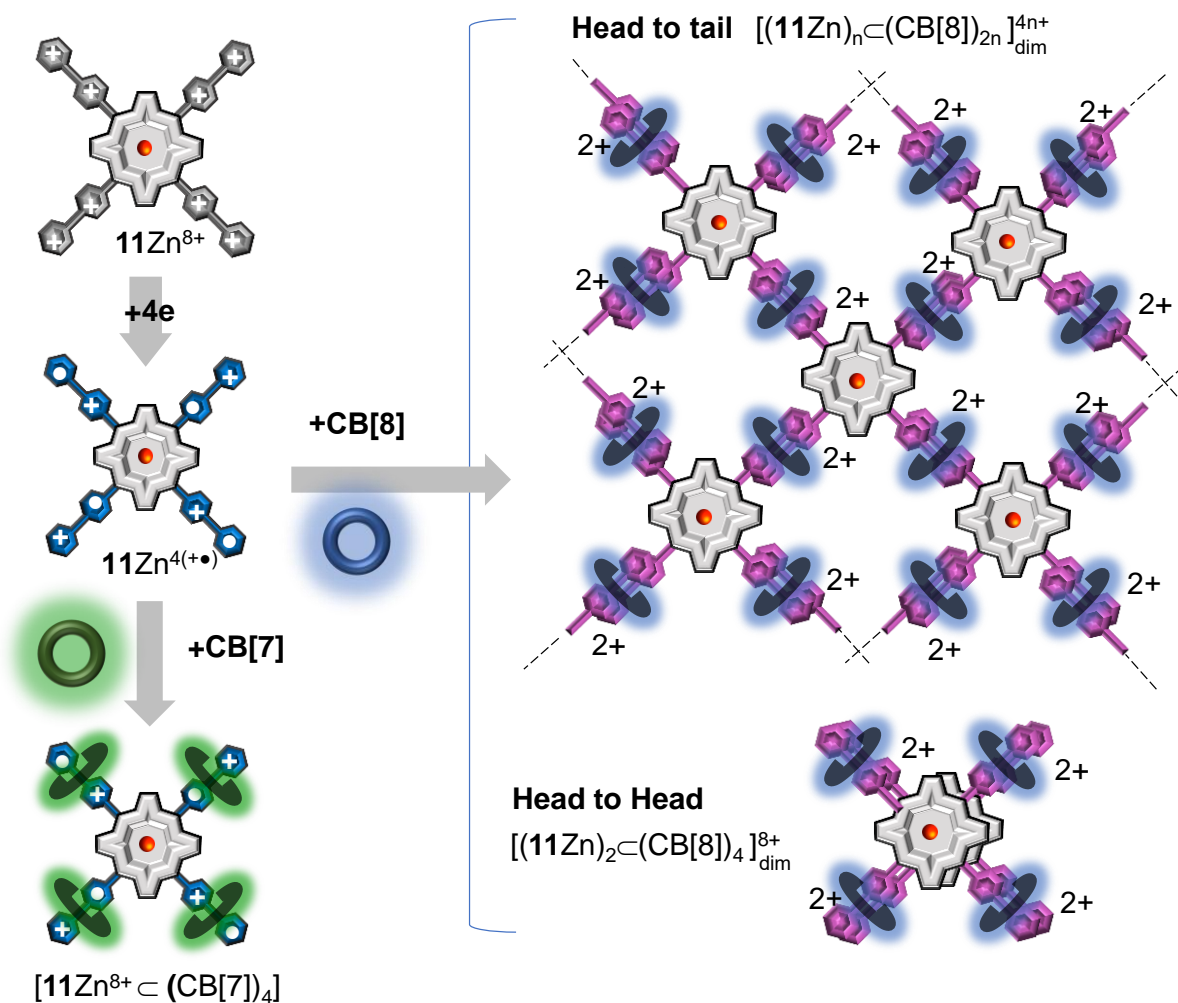


Figure 33: Schematic drawing showing the expected binding modes between the four-electron reduced species **11Zn^{4(+)•}** and **CB[n]**, with $n = 7$ or 8 .

11Zn⁸⁺ has been investigated in a phosphate buffer ($\text{pH} = 7$, 0.1 M) at a vitreous carbon electrode. The CV curve displays an irreversible oxidation wave centered at $E^{1a} = 0.861 \text{ V}$ attributed to the one-electron oxidation of the porphyrin. It also shows two consecutive viologen-based reduction waves centered at $E^{1c} = -0.389$ and $E^{2c} = -0.638 \text{ V}$ (Table 3). The reduction waves are found to be associated on the reverse scan to Gaussian-shaped reoxidation peaks attributed to the anodic redissolution of physisorbed species. As expected, such phenomenon was found to be particularly important for the neutral and hydrophobic porphyrin-based complex **11Zn⁰**, involving quinonic **V⁰** substituents, electrogenerated at $E^{2c} = -0.638 \text{ V}$. A systematic study carried out with different electrolytes allowed us to establish that the adsorption of the first tetra-cationic compound **11Zn^{4(+)•}** can be significantly reduced upon lowering the concentration of **11Zn⁸⁺** down to $2 \times 10^{-4} \text{ M}$ and upon increasing the scan rate of the CV measurement, as revealed by the linear $I_{\text{peak}} = f(v^{1/2})$ plot recorded on the first reduction wave for $v \geq 400 \text{ mV/s}$.

The interaction of 11Zn^{8+} with CB[8] has been investigated in these experimental conditions using electrochemical methods. As can be seen in Figure 34, the progressive addition of CB[8] results in the progressive disappearance of the initial reduction wave at -0.389 V at the expense of a new reduction wave emerging at a less negative potential. This trend prevails up to the end of the titration, when reaching the maximum concentration of CB[8] (2 molar equivalents, full red line in Figure 34), with the observation of a new wave attributed to the reduction of the inclusion complex $[11\text{Zn}^{8+} \subset (\text{CB}[8])_2]$ at $E_p = -0.354\text{ V}$.

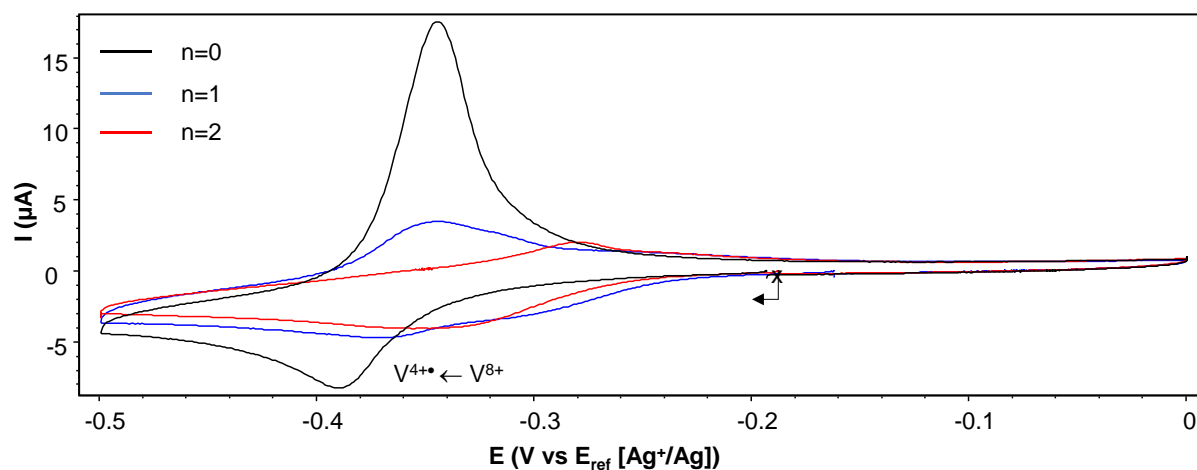


Figure 34: CV curves recorded for $11\text{Zn}(\text{Cl})_8$ ($2 \times 10^{-4}\text{ M}$) in aqueous phosphate buffer ($\text{pH} = 7$, 0.1 M) ($\text{VC } \varnothing = 3\text{ mm}$, $\nu = 0.1\text{ V}\cdot\text{s}^{-1}$, E vs. AgCl/Ag) in the presence of n molar equivalents of CB[8].

These changes are moreover seen to come along with a significant loss in the peak-current values measured on the forward and backward scans, which is in agreement with the formation of much larger species featuring lower diffusion coefficients. It needs to be mentioned here that the upper value of the molar ratio reached towards the end of the titration, $\text{CB}[8]: 11\text{Zn}^{8+} = 2$, not only corresponds to the ratio needed to form the ideal 2D arrangement shown in figure 30, it was also found to be the solubility limit of CB[8] in our experimental conditions. The formation of host-guest complexes involving both the V^{2+} and V^{+} redox states of the appended viologen is further revealed by the ability of CB[8] to prevent the physisorption of the four-electron reduced species, as demonstrated by the progressive loss of the Gaussian character associated to the reoxydation peak observed prior the addition of CB[8]. Such evolution is indeed consistent with the formation of inclusion species with limited affinity for the electrode surface at the CV time scale, as demonstrated by the linearity of the $I_{\text{peak}} = f(\nu^{1/2})$ curve recorded after addition of 2 molar equivalents of CB[8] (Figure 35B). The stabilization of the viologen cation radical as dimers included in CB[8] is further revealed by the large shift, reaching -400 mV by the end of the titration, of the second

viologen-centered reduction leading the neutral quinonic form of the viologens ($V^{+•} \rightarrow V^0$, Figure 34). As mentioned in the introduction,¹¹³ such effect of CB[8] is consistent with an extension of the stability domain of the cation radicals state on account of π -dimerization, which end up being easier to produce (anodic shift of the first reduction potential) and harder to consume (cathodic shift of the second reduction potential).

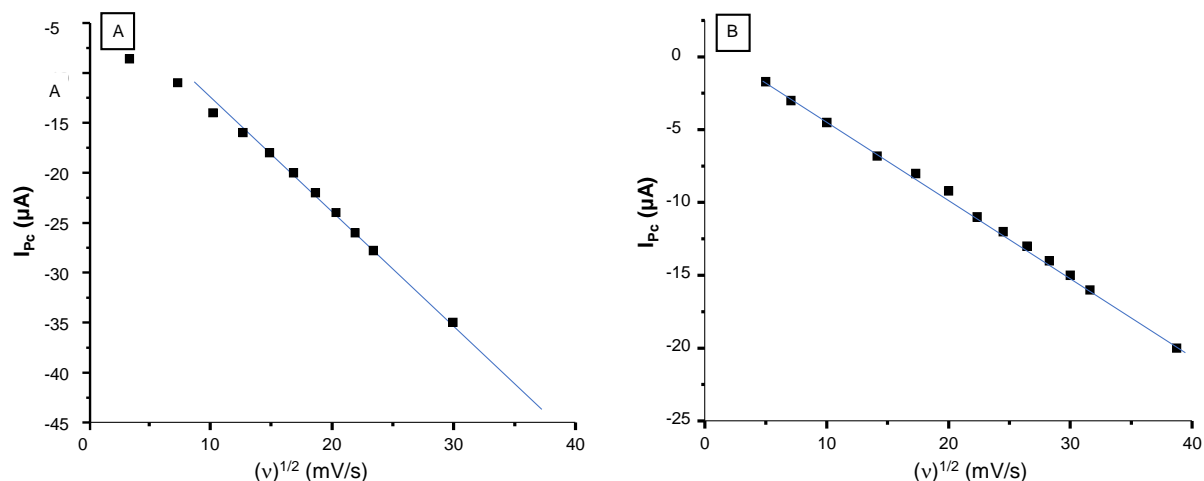


Figure 35: Peak current as a function of scan rate recorded for $11Zn^{8+}$ (2×10^{-4} M) in the absence (A) and the presence (B) of 2 molar equivalents of CB[8] (3 mm carbon working electrode, phosphate buffer (0,1 M, pH=7)).

The formation of self-assembled supramolecular architectures $[(11Zn)_n \subset (CB[8])_{2n}]^{4n+}$ through iterative CB[8]-assisted π -dimerization of the viologen cation radicals in $11Zn^{4(+)}$ has been further demonstrated upon carrying out the same investigations with CB[7], whose cavity dimension precludes the formation of such dimers. The CV curves recorded after addition of increasing amounts of CB[7] are collected in Figure 36.

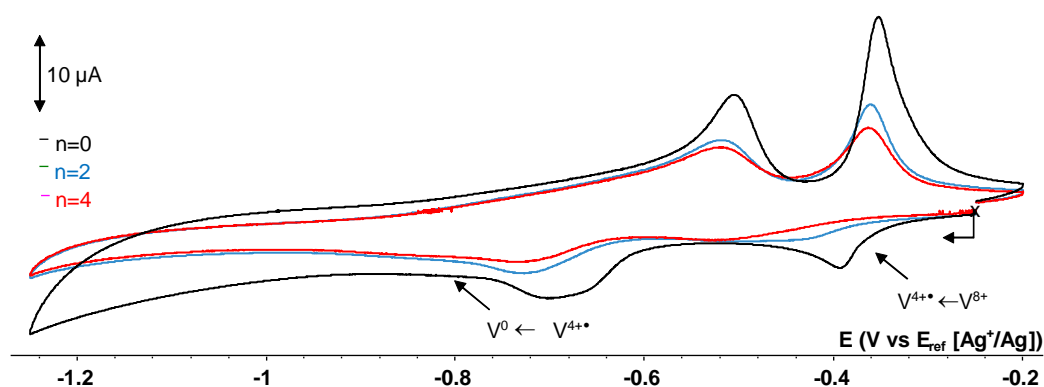


Figure 36: Voltammetric curve (CV) recorded for $11Zn(Cl)_8$ (2×10^{-4} M) in aqueous phosphate buffer (pH= 7, 0.1 M) ($VC \text{ } \varnothing = 3 \text{ mm}$, $v = 0.1 \text{ V.s}^{-1}$, E vs. $AgCl/Ag$) in the presence of n molar equivalents of CB[7].

As opposed to what was found with CB[8], the formation of $[(11Zn) \subset (CB[7])_n]^{8+}$ ($1 \leq n \leq 4$) results in the progressive shift of the reduction potential towards more negative potential

values along with a drop of the current levels. Such behavior is here again fully consistent with previous studies carried out with MeVMe^{2+} showing that such cathodic shift can be attributed to the similar affinity of CB[7] for the dication MeVMe^{2+} ($K_1 = 2 \times 10^5 \text{ M}$) and for the electrogenerated cation radical $\text{MeVMe}^{+\bullet}$ ($K_1 = 8.5 \times 10^4 \text{ M}$)⁸⁴. Hence, a similar conclusion can thus be put forward to account for the modification of the CV data recorded in the presence of $\mathbf{11Zn}^{8+}$ and CB[7].

Spectroscopic measurements have been carried out in water to confirm the CB[8]-promoted π -dimerization of the 4-electron-reduced species $\mathbf{11Zn}^{4(+\bullet)}$ into self-assembled supramolecular systems conforming to the general formula $[(\mathbf{11Zn})_n \subset (\text{CB}[8])_{2n}]_{dim}^{4n+}$ (see Figure 33). Preliminary attempts to generate the reduced species by bulk electrolysis at reticulated vitreous carbon foam electrodes failed due to the significant adsorption of the reduction products, even though no such process was observed at much shorter time scales over the course of CV analyses. The one-electron reduction of the viologen units in $\mathbf{11Zn}^{8+}$ was thus carried out in phosphate buffer (pH = 7) using sodium dithionite $\text{Na}_2\text{S}_2\text{O}_4$ as a reductant.¹¹⁴ The UV-vis absorption spectra recorded over time in the presence of CB[8] after addition of $\text{Na}_2\text{S}_2\text{O}_4$ in excess are shown in Figure 37A. These curves reveal that the chemical reduction has very little impact on the main porphyrin-based Soret band centered at 421 nm, as expected for electron transfers centered on the peripheral viologens ($\text{V}^{2+} \rightarrow \text{V}^{+\bullet}$) and not on the porphyrin ring. The curves show however the development of two intense absorption bands at $\lambda_{\text{max}} = 560$ and 634 nm coming along with a less intense broad signal centered at 918 nm. The attribution of those signals could be achieved through comparison with the spectra of structurally related reference compounds, namely the viologen-based radical $\mathbf{12}^{+\bullet}$ and the pure π -dimer $[(\mathbf{13})_2]_{dim}^{2+}$ (blue and purple drawings and curves in Figure 37A).¹¹⁵ One key conclusion drawn from this analysis, and more particularly from the perfect matching between the spectrum of $[(\mathbf{13})_2]_{dim}^{2+}$ and that recorded after reduction of $[\mathbf{11Zn} \subset (\text{CB}[8])_2]^{8+}$ with $\text{Na}_2\text{S}_2\text{O}_4$, is that the viologen radicals in the chemically-reduced species $\mathbf{11Zn}^{4(+\bullet)}$ are involved in the formation of intermolecular π -dimers. Both spectra indeed feature an intense charge-resonance absorption band observed in the NIR region, at $\lambda_{\text{max}} = 918 \text{ nm}$, which is a typical feature of viologen-based π -dimers.

In solution, such long-bonded dimers are most of the time found in equilibrium with the non-associated cation radicals. In our case, the presence of free cation radicals in solution is revealed by the third signal growing at $\lambda_{\text{max}} = 634 \text{ nm}$, which is similar to the signature of the

“free radical” reference compound $\mathbf{12}^{2+}$ (Figure 37A). The spectroscopic data collected over the four-electron reduction of $\mathbf{11Zn}^{8+} \subset (\text{CB}[8])_2$ with $\text{Na}_2\text{S}_2\text{O}_4$ are thus consistent with the formation of self-assembled supramolecular structure $[(\mathbf{11Zn})_n \subset (\text{CB}[8])_{2n}]_{dim}^{4n+}$ built from a CB[8]-promoted intermolecular π -dimerization of the viologen cation radicals present in $\mathbf{11Zn}^{4(++)}$. Another key feature of the proposed supramolecular assembly is its fully dynamic and reversible nature, since the slow re-oxidation of the viologen-based radicals with compressed air led to the regeneration of initial spectrum (Figure 37B).

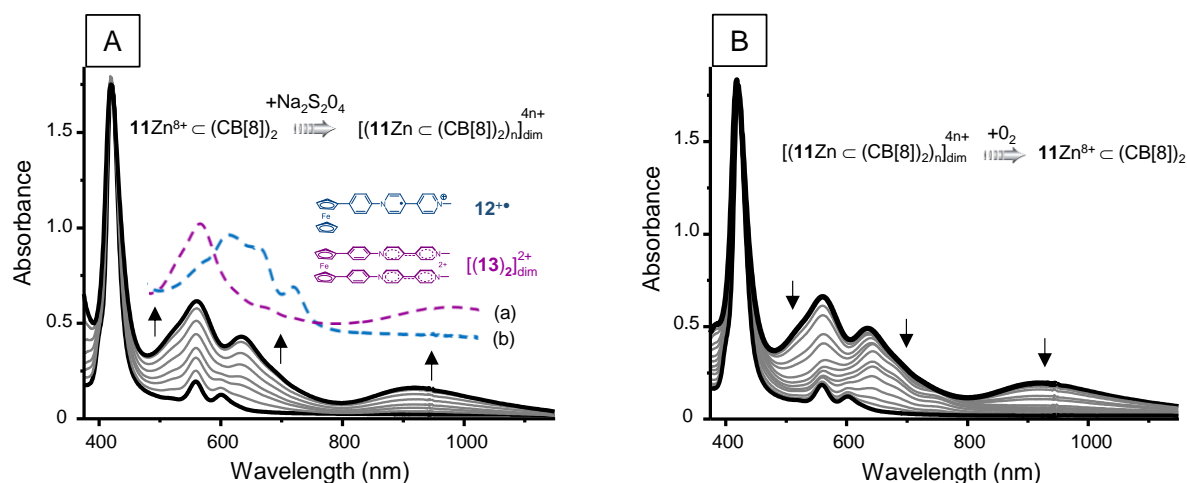


Figure 37: UV-vis spectra of $\mathbf{11Zn}(\text{Cl})_8$ (1.1×10^{-5} M) and CB[8] (2 molar equivalents) in phosphate buffer (pH=7, 0.1 M) recorded over time after addition of $\text{Na}_2\text{S}_2\text{O}_4$ in excess (A) and followed by gentle bubbling of compressed air (B). The spectrum of $\mathbf{12}^{2+}$ and $[(\mathbf{13})_2]_{dim}^{2+}$ are shown as dotted lines.

Similar experiments have then be carried out in the absence (Figure 38A, B) and in the presence of CB[7] (Figure 38C, D). In both experiments we observed that the reduction $\mathbf{11Zn}^{8+}$ has a major impact on the Soret band, as revealed by a loss of about 1/3 of its initial intensity accompanied with a blue shift of about 13 nm of the maximum wavelength, going from 420 to 407 nm with a well-defined isosbestic point at 413 nm. There is also emergence of a series of new bands centered at 518 (sh), 550 and 622 nm coming along with a very broad and weakly intense signal at $\lambda_{max}=1050$ nm. Another key output is that the reduction/oxidation cycle is fully reversible.

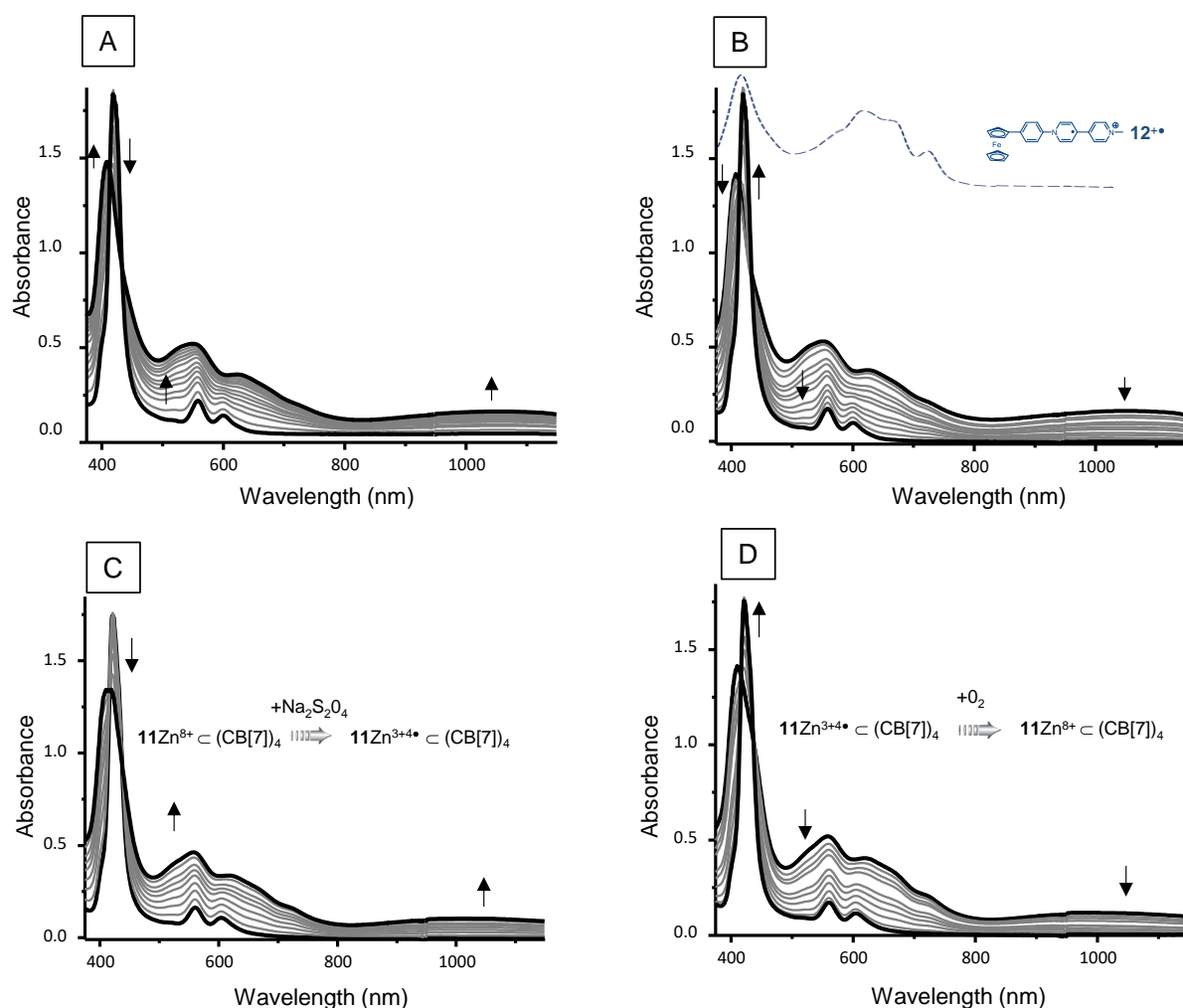


Figure 38: UV-vis spectra of $11\text{Zn}(\text{Cl})_8$ (1.1×10^{-5} M) in phosphate buffer (pH=7, 0.1 M) recorded over time, (A) after addition of $\text{Na}_2\text{S}_2\text{O}_4$ in excess and followed by gentle bubbling of compressed air (B) / UV-vis spectra of $11\text{Zn}(\text{Cl})_8$ (1.1×10^{-5} M) and CB[7] (4 molar equivalents) in phosphate buffer (pH=7, 0.1 M) recorded over time after addition of $\text{Na}_2\text{S}_2\text{O}_4$ in excess (C) and followed by gentle bubbling of compressed air (D).

Several interpretations can be put forward to account for these important changes observed upon reduction. The first one involves the aggregation of the four-electron reduced species $11\text{Zn}^{4(+)}$. The ability of positively or negatively charged porphyrins to form so called J- or H-aggregates in aqueous solution is well documented. In H-aggregates, the molecules stack predominantly face-to-face, while in J-aggregates, the molecules are made up from monomers adopting brickstone-type slipped cofacial arrangements. When porphyrins are involved, the formation of H- vs. J-aggregates can be revealed by the hypso- vs. batho-chromic shift of the Soret band, respectively. In most cases, excitonic coupling between chromophores indeed lead to blue shifts for H-aggregate and to red shifts for J-aggregates.

Formation of co-facial stacks from the four-electron reduced species $11\text{Zn}^{4(+)}$ is thus mainly supported by the blue shift of the Soret absorption, from $\lambda_{\text{max}} = 420$ nm to 407 nm, observed

upon addition of $\text{Na}_2\text{S}_2\text{O}_4$ to $\mathbf{11Zn}^{8+}$ or $[\mathbf{11Zn}\subset(\text{CB}[7])_4]^{8+}$. The fact that the same spectra could be obtained in the presence or in the absence of CB[7] suggest that the stabilization of $\mathbf{11Zn}^{4(++)}$ through aggregation leads to the dissociation of $[\mathbf{11Zn}\subset(\text{CB}[7])_4]^{(++)}$. The stoichiometry of the association (n in Figure 39) is still unknown but the observation of a well-defined isosbestic point at 416 nm supports the formation of a discrete species (dimer, trimer). Another key feature of the spectra displayed in Figure 38 is the weak and broad absorption band stretching over a quite broad wavelength range suggesting the formation of ill-defined π -dimers. Formation of such species can in fact be readily envisioned from the arrangements proposed in Figure 39 bringing to light the spatial proximity of the viologen cation radicals, the unusual broadness and low energy shift of the π -dimer band being potentially attributed to the number of interacting radicals and to the steric constraints prohibiting the formation of perfectly stacked dimers.

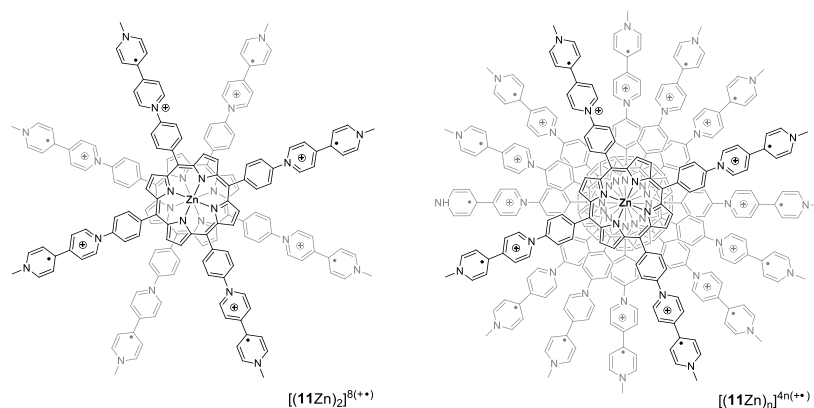


Figure 39: Chemdraw representation of the possible types of aggregate.

The second hypotheses considered to explain the experimental results collected in the presence of CB[7] involves an electron transfer centered on the porphyrin ring. The data shown in Figure 38 could indeed support the conclusion that the chemical reduction of $\mathbf{11Zn}^{8+}$ or $[\mathbf{11Zn}^{8+}\subset(\text{CB}[7])_4]$ with an excess of $\text{Na}_2\text{S}_2\text{O}_4$ results in the concomitant reduction of the viologen substituents ($\text{V}\rightarrow\text{V}^{++}$) and of the porphyrin ring ($\text{P}\rightarrow\text{P}^{\bullet-}$). There is limited literature on porphyrin anion radicals and porphyrin dianions but some studies conducted in aqueous media on the parent 5,10,15,20-*tetrakis*(*N*-methyl pyridinyl)porphyrin (TPyPZn^{+4}) proved useful to put forward a global interpretation of the observed phenomena. The latter have for instance established that the π -anion radical ($\text{P}^{\bullet-}$) of TPyPZn^{+4} ($\lambda_{\text{max}} \approx 700\text{-}750\text{ nm}$)¹¹⁶⁻¹¹⁸ is unstable in solution and quickly evolves, through a bimolecular disproportionation process occurring at the millisecond time scale, into a porphyrin dianion (P^{2-}) which is in turn readily transformed at neutral pH into a protonated species termed phlorin (PH^-) featuring one sp^3 -

hybridized *meso* carbon atom.^{116, 119-123} It should also be mentioned that the driving force of this overall EC₂ process ($P \rightarrow P^{\bullet-} \rightarrow P^{2-} \rightarrow PH^-$) is so strong that it can also be observed in aprotic polar organic solvent polluted with water molecules. Another specific feature relevant to the experimental data shown in Figure 38 and Figure 39 is that the formation of phlorin anions from porphyrins is a reversible process, the latter being usually fully regenerated ($PH^- \rightarrow P$) by simple electrochemical or chemical re-oxidation of the sample.^{119, 124-125, 126, 127} In terms of characterization, phlorins are known to be more easily reduced than porphyrins ($E^\circ[PH/PH^-] > E^\circ[P/P^{\bullet-}]$). Their formation is most of the time revealed by absorption spectroscopy through the observation of a broad absorption band developing in the near IR region (>700 nm, with feature depending on the central metal and on the *meso*-substituents) and by the disappearance of the initial Soret band at the expense of a much weaker and broader signal developing at longer wavelengths ($\Delta\lambda \approx +30$ nm and $\epsilon_P/\epsilon_{PH} \approx 7$ for ZnTPP).¹²⁷

All this literature demonstrating the instability of porphyrin anions radicals in protic media thus suggests that the unexpected behavior recorded with $11Zn^{8+}$ and $[11Zn^{8+} \subset (CB[7])_4]$ could be attributed to the formation of a phlorin product (noted $11Zn^{3+4\bullet}$ in Figure 40), incorporating four viologen cation radicals and a negatively charged *meso*-protonated phlorin ring (Figure 40).

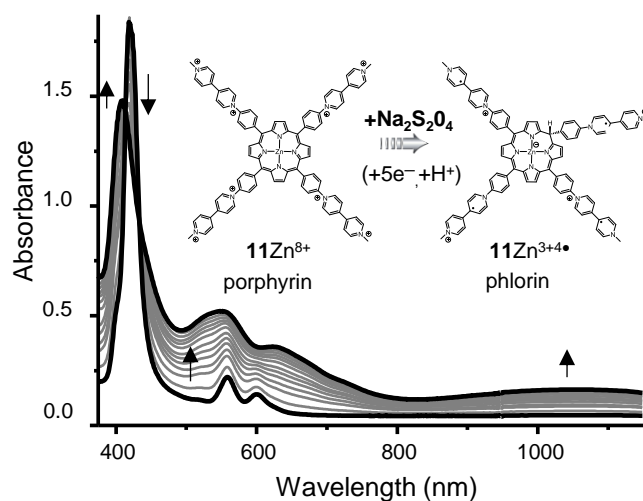


Figure 40 : UV-vis spectra of $1Zn(Cl)_8$ (1.1×10^{-5} M) in phosphate buffer (pH=7, 0.1 M) recorded over time, (A) after addition of $Na_2S_2O_4$ in excess in phosphate buffer (pH=7, 0.1 M).

Such finding implies that, in our experimental conditions, $Na_2S_2O_4$ is capable of reducing the viologen cation radical and the porphyrin ring. The main evidence supporting the involvement of the porphyrin ring in the electron transfer is provided in (Figure 40) by the disappearance of the initial Soret band at the expense of a less intense and blue shifted signal centered at 407

nm, whose features are reminiscent of that observed in the same range on the spectrum of the reference viologen cation radical $\mathbf{12}^{+\bullet}$ (shown as a blue curve in Figure 38B). The presence of viologen cation radicals is thus clearly revealed in Figure 40 and Figure 38C by the emergence of a signal centered at 407 nm together with multiple signals above 600 nm. Formation of a phlorin-type product is conversely demonstrated by i) the disappearance of the initial Soret band, ii) by the development of a broad band in the NIR region; iii) by the observation of a shoulder at ~ 450 nm and by iii) the full regeneration of the initial porphyrin by simple re-oxygenation of the reduced sample.

The two hypotheses discussed above can be put forward to account for the peculiar results collected with CB[7] only. No such behavior was observed upon reduction of the inclusion complex formed with CB[8]. As demonstrated above, the formation of 2D supramolecular assemblies is unambiguously revealed by the observation well defined absorption bands attributed to intermolecular π -dimerization processes. This interpretation was further confirmed with additional experiments showing that similar signatures can be obtained when using *tetrakis*(dimethylamino)ethylene¹²⁸ as a reducing agent or using light in the presence of a suitable electron donor.¹²⁹⁻¹³⁰ The latter procedure involve irradiation at $\lambda_{\text{ex}} = 455$ nm of the investigated solutions containing *tris*(bipyridine) ruthenium chloride as a photosensitizer (0.1 mM) and ethylenediaminetetraacetic acid (EDTA, 0.1mM) as a sacrificial electron donor.¹³¹

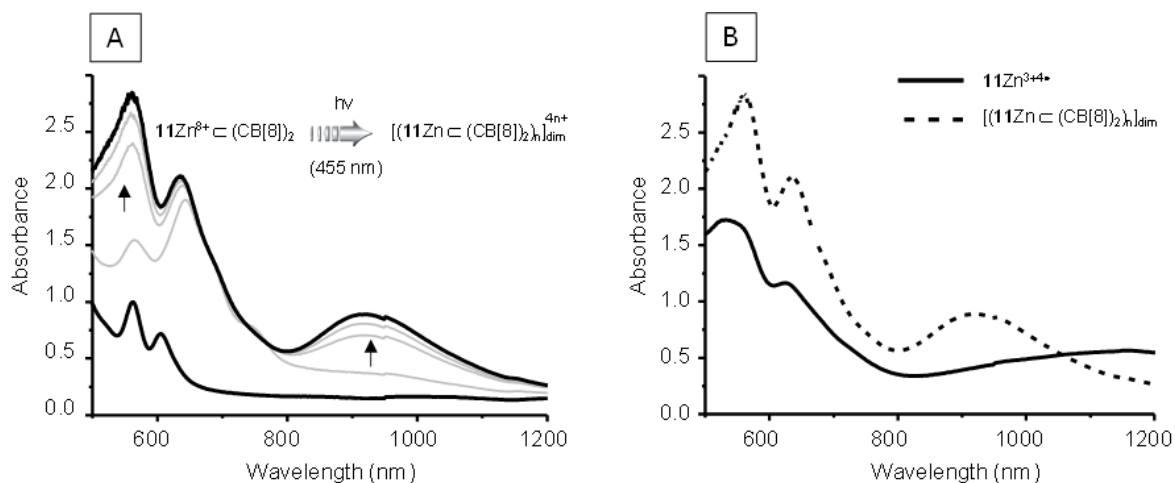


Figure 41:(A) UV-vis spectra of $11\text{Zn}(\text{Cl})_8$ (1×10^{-4} M) and CB[8] (2×10^{-4} M) in phosphate buffer (pH= 7, 0.1 M) recorded during irradiation at $\lambda_{\text{ex}} = 455$ nm in the presence of *tris*(bipyridine) ruthenium chloride (0,1 mM) and (EDTA, 0,1mM) (B) Comparison of UV-vis spectra of $11\text{Zn}(\text{Cl})_8$ (1×10^{-4} M) in absence (plain line) and presence of CB[8] (2×10^{-4} M) (dotted line) in phosphate buffer (pH 7, 0.1 M) recorded during irradiation at $\lambda_{\text{ex}} = 455$ nm.

The absorption spectra recorded during irradiation are shown in Figure 41. Here again the signal centered at ~ 900 nm, attributed to the formation of intermolecular viologen-based π -dimers, is observed only in the presence of CB[8] (Figure 41A), the photoreduction of 11Zn^{8+}

and $11\text{Zn}^{8+\ominus}(\text{CB}[7])_4$ leading to the observation of different signals matching those obtained in the presence of $\text{Na}_2\text{S}_2\text{O}_4$ (Figure 41B). It should be noted that all our attempts to reduce the viologen units using the porphyrin ring as the photosensitizer ($\lambda_{\text{ex}} = 365$ or 455 nm) have failed, most probably due to the efficient and fast recombination of the charge separated intermediates.

Overall, the photo or chemical reduction experiments discussed above lead to the same experimental data consistent with the conclusion that CB[8] *i*) promotes the intermolecular dimerization of the viologen cation radicals and *ii*) prevents the aggregation and the reduction of the porphyrin ring.

II.2.6. Computational Analysis

The ability of CB[8] to promote the π -dimerization of $11\text{Zn}^{4(+\bullet)}$ has been investigated by quantum chemistry (collaboration with Dr. Elise Dumont). These calculations have been carried out on a simple model featuring only one viologen unit linked to a zinc porphyrin ring (Figure 42). A geometry optimization has been conducted on the self-assembled π -dimers formed at the reduced state (one electron per viologen) in the presence of CB[8] to evaluate the structural and energetical impacts of the CB[8] cavitand on the dimer, to gain insights into its stabilization energy and into the relative position of the porphyrin and viologen subunits. Geometries have been optimized at the GGA hybrid Truhlar's density functional DFT/M06-2X level of theory,¹³² with a basis set 6-31G(d,p) using the Gaussian 16 revision B.01 suite of programs. This density functional is best suited to account for the dispersion interactions involved in π -dimers and comes with a high percentage of exact exchange which is a needed feature to describe π -radicals.¹³³ Preliminary calculations carried out on the two possible head to tail and head to head conformers shown Figure 42 led to the conclusion that the head to head conformation is disfavored by steric clashes arising between the phenyl linkers. A detailed optimization has thus been carried out starting from an ideal "head to tail" π -dimer model (two viologen cation-radicals perfectly aligned sitting on top of each other at a contact distance of 3.4 \AA) stabilized within the cavity of a CB[8] host. The structure obtained after optimization is shown in Figure 42 (a, b). The phenyl ring ends up being tilted with respect to the porphyrin and viologen-based mean planes (44°) as a result of the steric repulsion occurring between the hydrogen atoms of the phenyl ring (H_f , H_g in Figure 42) and those located on the porphyrin (H_h) and viologen units (H_e). This optimized structure also reveals that both viologen radicals adopt a slightly staggered conformation with a twist angle of about

36° imposed by the steric hindrance between the *N*-Methyl substituent and the phenyl linker. It should however be mentioned that the energy difference calculated between this partially “staggered” optimized conformation and the perfectly aligned structure does not exceed 3 kcal.mol⁻¹. Such small difference suggests that the inclusion complex oscillates at room temperature between the two absolute minima centered at -36° and +36°. Similar calculations carried out on the twisted (36°) vs. parallel conformers of a less bulky dimer, involving two *N,N'*-dimethyl-4,4'-bipyridinium radical cation (MeVMe⁺) bound within a CB[8] host, led to a higher energetic difference reaching 6.4 kcal.mol⁻¹ (-10.0 kcal.mol⁻¹ vs. -16.4 kcal.mol⁻¹).

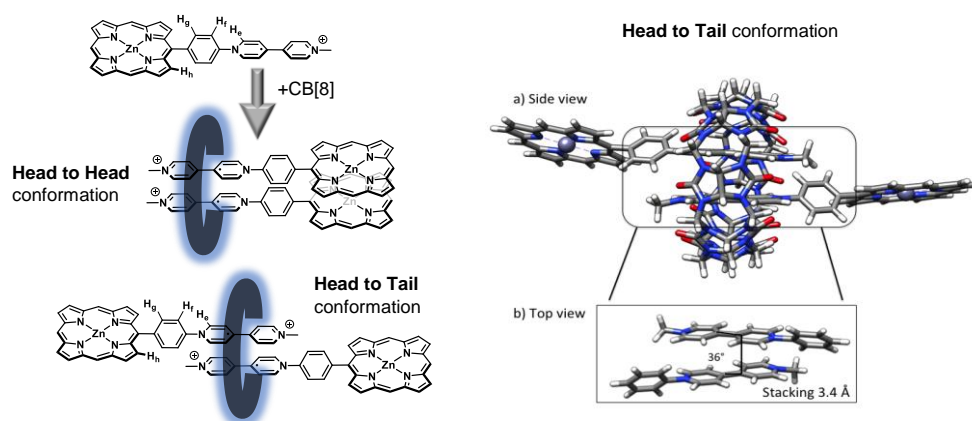


Figure 42 : Left) Schematic representation of the face to face or head to tail conformations of the selected π -dimer model complex formed in the presence of cucurbit[8]uril (shown as a blue ring). Right) Structure of the head to tail conformer optimized at DFT/M06-2X level of theory.

II.2.7. Conclusion

Formation of discrete 4:1 pseudo-rotaxane-like caviplexes, involving threading of 4 CB[n] rings on a viologen-based four-pointed star-shaped guest molecule, has been demonstrated by NMR, MS and electrochemical measurements. Detailed electrochemical, theoretical and spectroscopic analyses revealed that formation of intramolecular π -dimers requires the presence of cucurbit[8]uril acting as an assembling element. Evidences for intermolecular dimerization came from electrochemistry data, supporting the existence of chemical steps coupled to the electron transfer processes, and from UV-vis spectroscopy data collected after exhaustive chemical or photochemical reduction of the samples, with the observation of diagnostic absorption bands, most notably in the near infra-red region. The CB[8] hosts not only proved useful to promote the redox-triggered formation of supramolecular assemblies in solution, but it was also found to prevent the aggregation or chemical reduction of the porphyrin ring in aqueous media.

II.3. Redox-Responsive 1D-Assemblies built from a Linear Porphyrin-based Tecton

The second approach that has been developed toward redox-responsive supramolecular assemblies involves CB[8] and the ditopic bis-viologen porphyrin $17Zn^{4+}$ as building elements (Figure 43). This strategy aimed at decreasing the dimensionality of the assembly, from 2D to 1D, upon introducing only two viologen units at the 5 and 15 positions of a porphyrin ring, the two remaining *meso* positions being occupied by water solubilizing TEG (triethylene glycol) substituted phenyl groups.

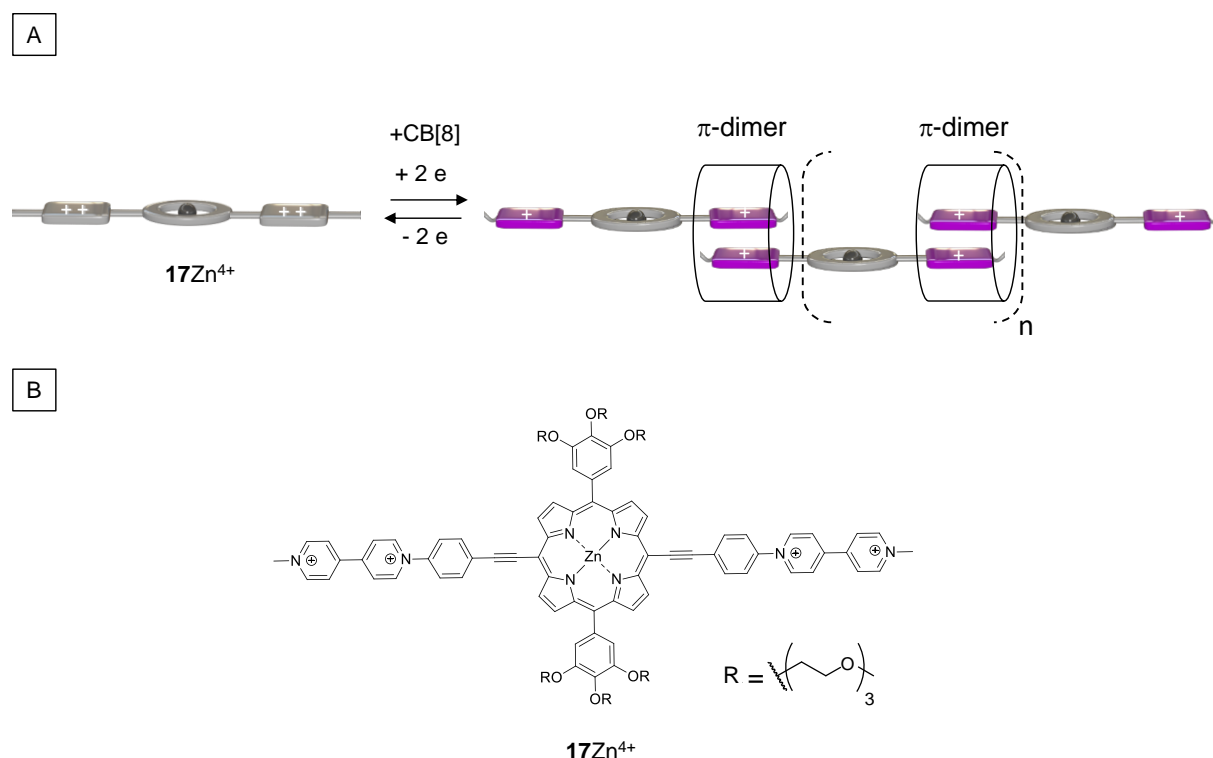


Figure 43: Schematic representation of A) a stimuli-responsive 1D self-assembly process, B) Chemdraw structure of the porphyrin based tectons

II.3.1. Synthesis of the Targeted Tecton $17Zn^{4+}$

Part of this work has been achieved by Paul Hennequin PhD (2015-2016) with the help of J.C Mulatier (ENS). The multi-step synthesis of the targeted ditopic tecton $17Zn^{4+}$ is summarized in Figure 44. The key intermediate **14** was prepared according to a procedure reported by Kuroda and coll.¹³⁴ The latter was subjected to a Sonagashira cross-coupling reaction with ethynylaniline to yield the aniline substituted porphyrin **15**. This intermediate was reacted with the activated viologen **16**²⁺¹⁰⁴ to afford $17H_2^{4+}$ in 58 % yield. The final step involves

metalation of $17H_2^{4+}$ with zinc acetate to afford $17Zn^{4+}$ isolated as a green solid. The latter species could be easily isolated as a chloride or hexafluorophosphate salt by simple anion metathesis. The chloride anions proved necessary to reach a suitable solubility in aqueous medium while $17Zn(PF_6)_4$ was found to be soluble in most polar organic solvents (DMF, DMSO, ACN).

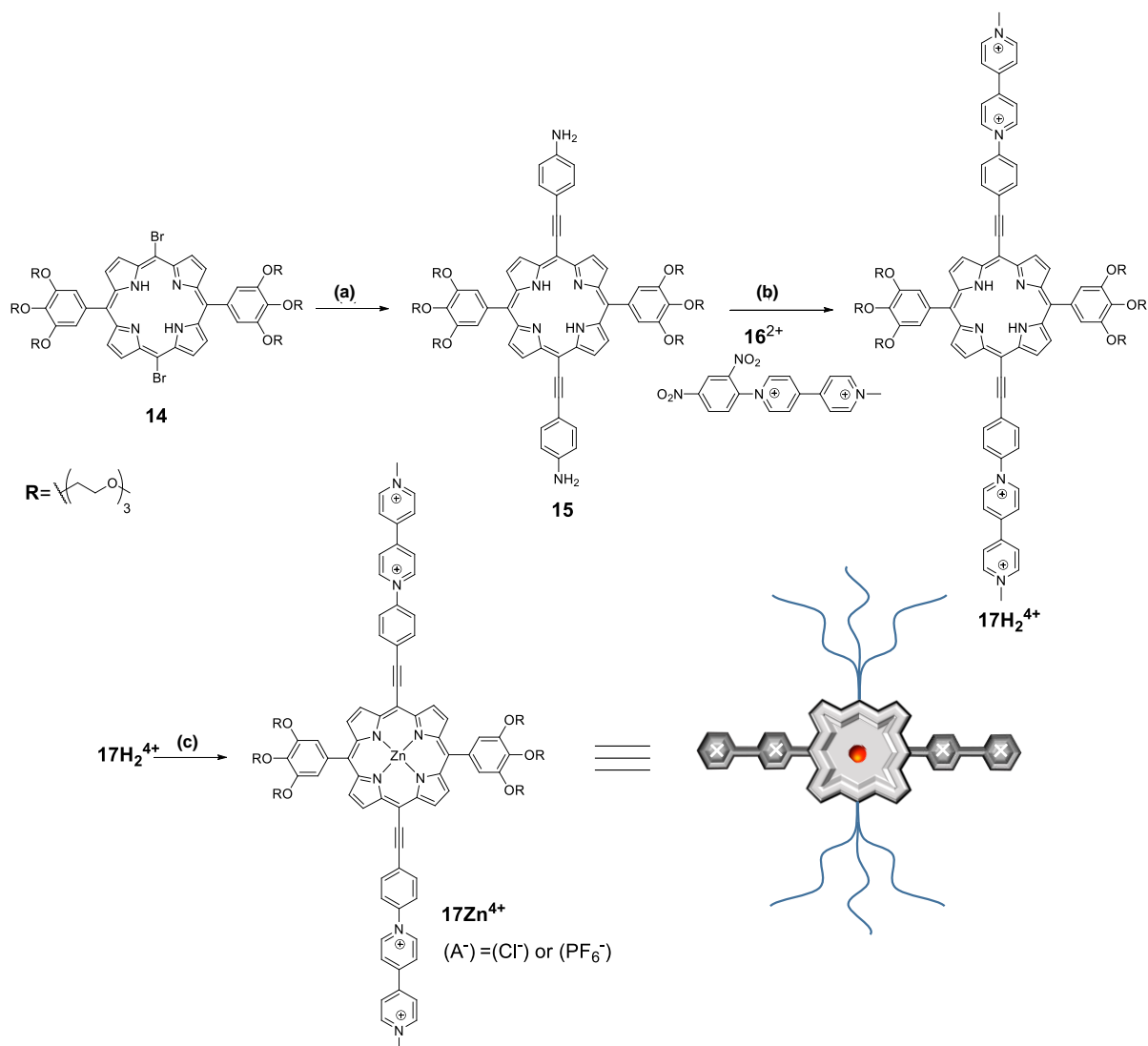


Figure 44: (a) ethynylaniline, $Pd_2(dba)_2$, Et_3N , THF, reflux, 24 h, 90%; (b) $16(PF_6)_2$, EtOH, CH_3CN , reflux, 18 h, 58%; (c) $Zn(OAc)_2$, CH_3CN , 25 °C, 16 h, >99%.

II.3.2. 1H -NMR Characterization

The 1H -NMR spectra of $17Zn(PF_6)_4$ and $17H_2(PF_6)_4$ recorded in deuterated DMSO is shown in Figure 45. The accurate attribution of the aromatic signals was achieved from careful analyses of the 1H -NMR spectrum and of the associated COSY map. The most deshielded signal in the spectrum of the freebase $17H_2(PF_6)_4$ and of the metalated $17Zn(PF_6)_4$ porphyrin

is attributed to the β -hydrogen H_h . The presence of zinc induces a slight upfield shift of the aromatic protons, more specifically the protons located at the β position (H_h and H_i) and those located on the TEGylated phenyl ring H_j . This is in agreement with the known electron-donating effect of the zinc atom on the porphyrin-based π -system.¹³⁵ The presence of the zinc metal within the cavity of the porphyrin ring was also confirmed by the absence of signal at $\delta < 0$ ppm.

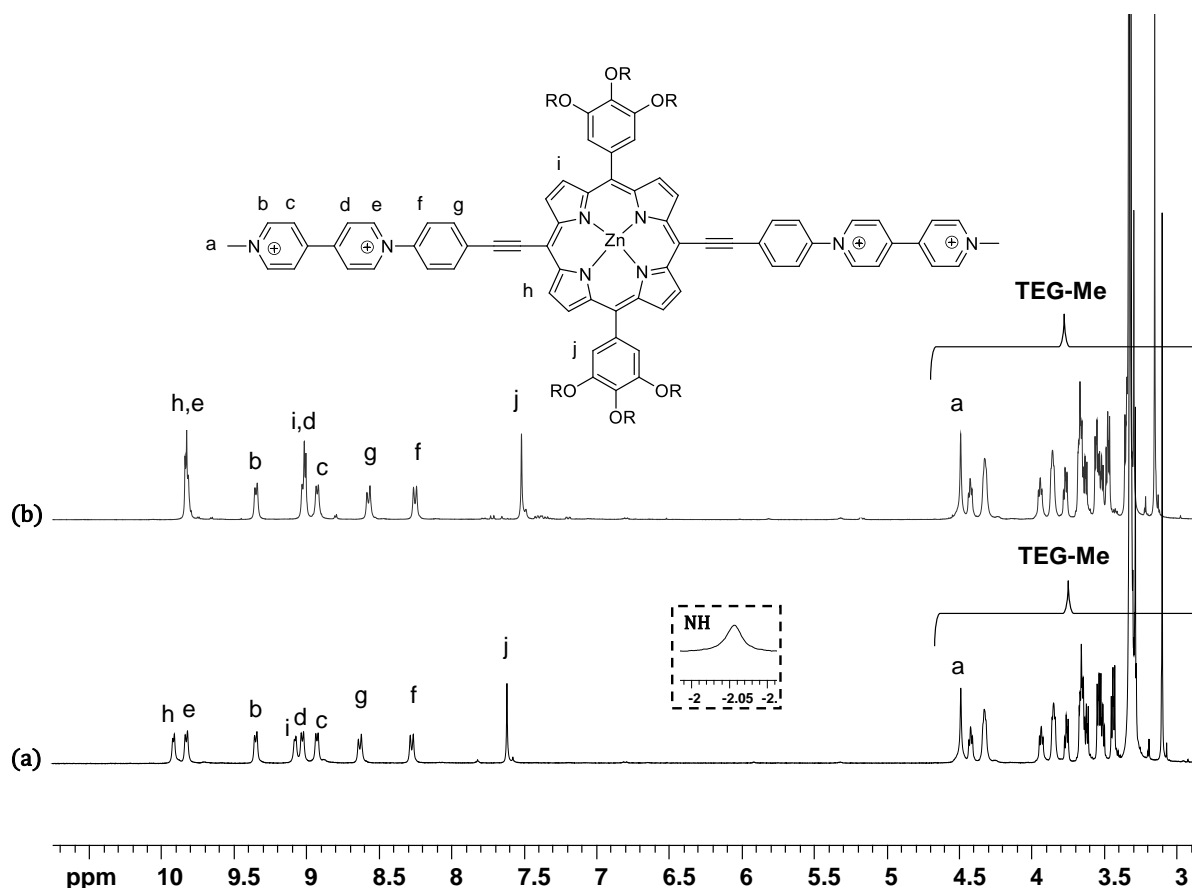


Figure 45: ¹H-NMR Spectra of (a):**17**H₂(PF₆)₄ (DMSO-d₆, 400MHz) and (b): **17**Zn(PF₆)₄(DMSO-d₆, 400MHz).

The chloride salt **17**Zn(Cl)₄ was also characterized by ¹H-NMR spectroscopy in deuterated water and DMSO. In D₂O, the spectrum displays up to nineteen signals in the aromatic region, which is about twice the number of signals observed in DMSO (Figure 46). The signals were also found to appear on a much wider window in water, from 5 to 11.5 ppm compared to that in DMSO. The major role of the solvent and the minor role of the anion in the complexity of the data recorded in water were eventually confirmed upon showing that the spectra of **17**Zn(PF₆)₄ and of **17**Zn(Cl)₄ are identical in DMSO (Figure 46).

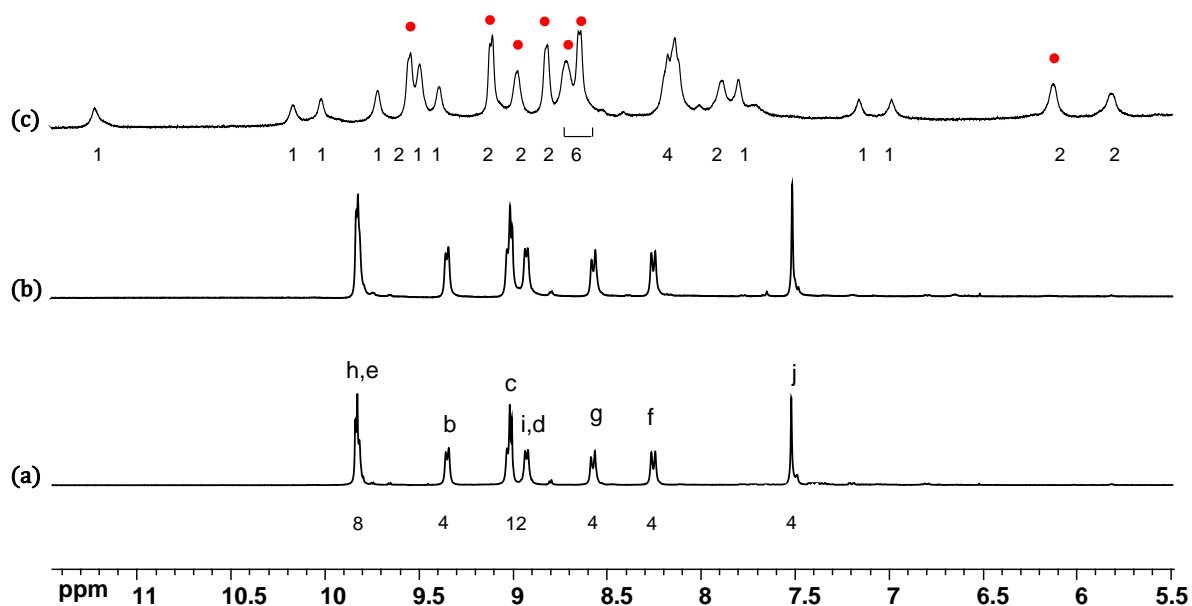


Figure 46: $^1\text{H-NMR}$ Spectra of $17\text{Zn}(\text{X})_4$ ($5 \times 10^{-4} \text{ mol.l}^{-1}$, 400MHz) recorded at different solvents: a) $\text{X} = \text{PF}_6^-$ (DMSO), b) $\text{X} = \text{Cl}$ (DMSO), c) $\text{X} = \text{Cl}$ (D_2O) red spots correspond to the signals attributed to the viologen units and the numbers below corresponds to the integration value.

All attempts to fully attribute the signals observed in $^1\text{H-NMR}$ spectrum recorded in water have failed so far. The signals attributed to the viologen moieties (red spots in Figure 46) could nevertheless be identified from careful analyses of the $^1\text{H-NMR}$ data (coupling constants of about 5/6 Hz) and of the COSY, ROESY maps. Most of these signals appear between 8.5 and 10 ppm except for 1 signal resonating at 6.15 ppm. The main conclusion drawn from the number of signals monitored in water, and from their relative intensities, is that 17Zn^{4+} aggregates in water to yield a discrete and poorly symmetric self-assembled architecture. Similar differences were observed with the free base $17\text{H}_2(\text{Cl})_4$ yielding a well-resolved spectrum in DMSO but a broad and ill-defined one in water (Figure 47).

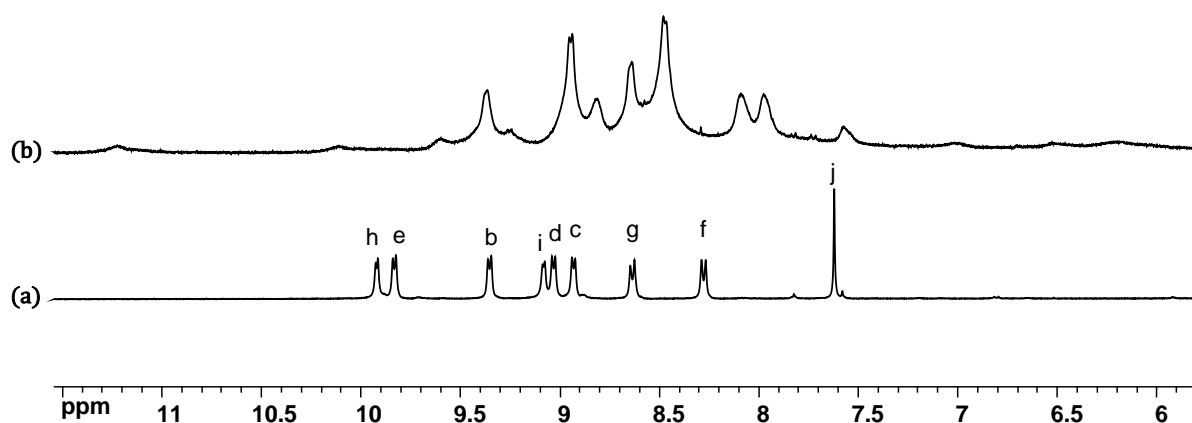


Figure 47: $^1\text{H-NMR}$ Spectra of $17\text{H}_2(\text{X})_4$ ($5 \times 10^{-4} \text{ mol.l}^{-1}$, 400MHz) recorded in different solvents: a) $\text{X} = \text{PF}_6^-$ (DMSO), b) $\text{X} = \text{Cl}^-$ (D_2O).

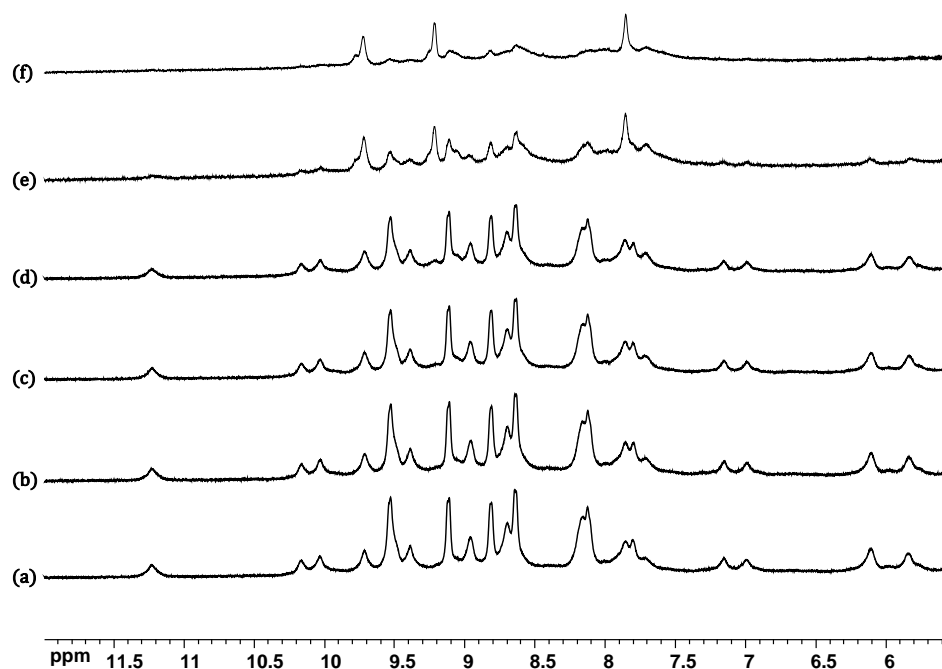


Figure 49: $^1\text{H-NMR}$ Spectra of $^{17}\text{Zn}(\text{Cl})_4$ (D_2O , 400MHz) recorded at different concentrations: a) 1 mM, b) 0.8 mM, c) 0.6 mM, d) 0.4 mM, e) 0.2 mM and f) 0.1 mM.

We also checked the influence of temperature on the aggregation process upon recording the $^1\text{H-NMR}$ spectrum of a 1mM aqueous solution of $^{17}\text{Zn}(\text{Cl})_4$ at different temperature. This study revealed that increasing the temperature of the sample from 298 K to 348 K induces a significant simplification of the spectrum (Figure 50), the most important ones being a large drop in the number of signals and of the chemical shift window (7.5 to 10.5 ppm) .

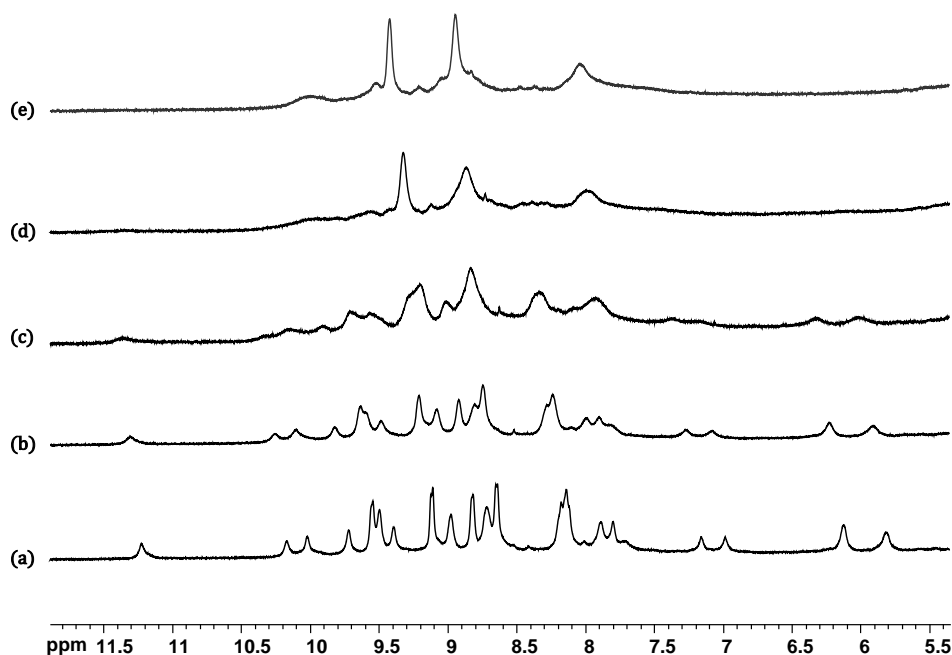


Figure 50: $^1\text{H-NMR}$ Spectra of $^{17}\text{Zn}(\text{Cl})_4$ ($10^{-3} \text{ mol.l}^{-1}$, D_2O , 400MHz) recorded as a function of temperature: a) 298 K, b) 308 K, c) 318 K, d) 328 K, e) 348 K.

As a conclusion, both the concentration and temperature-dependent experimental data discussed above support the conclusion that the self-assembled species formed in aqueous media get dissociated at low temperature or at concentrations below 0.1 mM.

II.3.3. UV-visible Absorbance Characterisation

As mentioned above, the formation of J- or H- aggregates can be identified from their UV-vis absorption spectroscopic signatures. When porphyrins are involved, the Soret band of J-aggregates (“side-by-side” arrangement) gets red-shifted with respect to that of the monomer while that of H-aggregates (face-to-face arrangement) is blue shifted. J-aggregation also result in the formation of intense narrow absorption bands while formation of H-aggregates lead to bands of similar or of lower intensities than the monomer.¹⁴¹

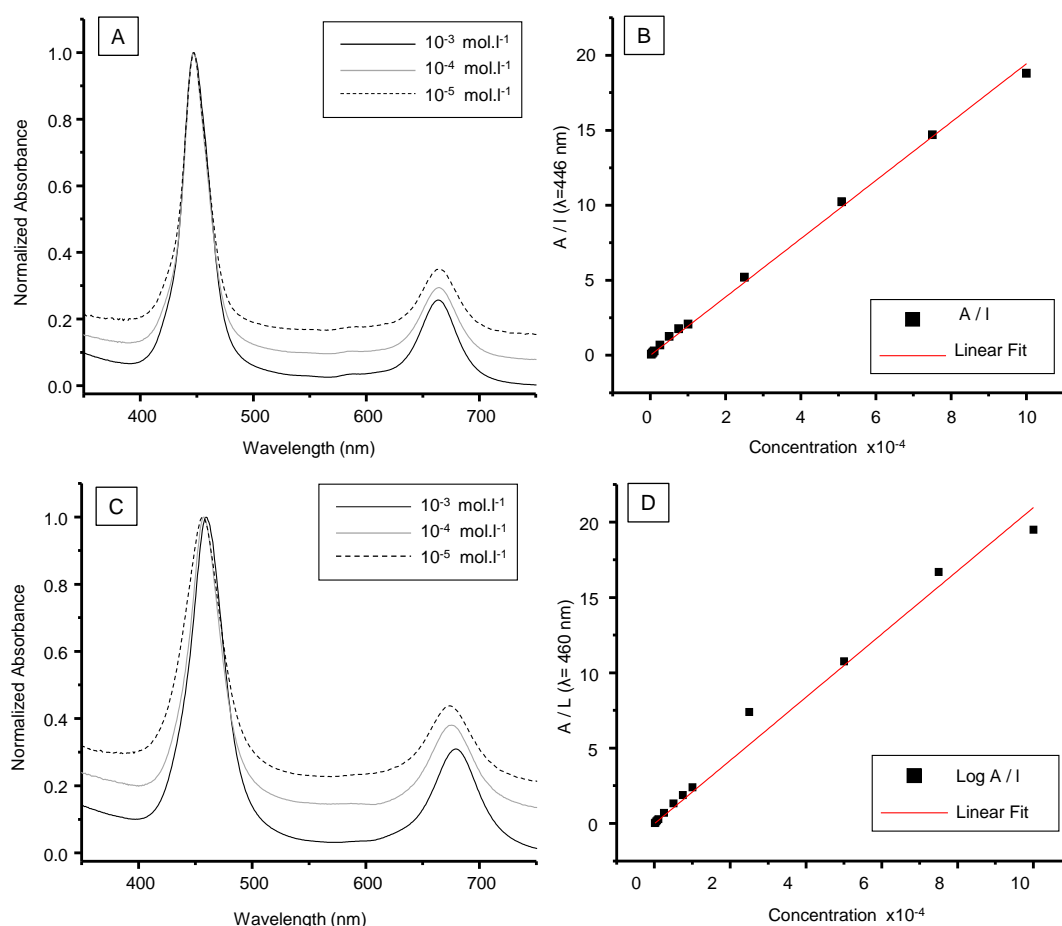


Figure 51: Normalized UV-visible absorption spectra of $17\text{Zn}(\text{X})_4$ recorded at different concentrations in (A) CH_3CN ($\text{X} = \text{PF}_6^-$) and in (C) H_2O ($\text{X} = \text{Cl}^-$). Plot of the absorbance measured (B) at $\lambda_{\text{max}} = 446$ nm as a function of the concentration of $17\text{Zn}(\text{PF}_6)_4$ in CH_3CN and (D) at $\lambda = 460$ nm as a function of the concentration for $17\text{Zn}(\text{Cl})_4$ in H_2O .

Further insights into the aggregation mode of $17\text{Zn}(\text{Cl})_4$ have thus been provided by UV-vis absorption measurements. The UV-vis absorption spectrum of $17\text{Zn}(\text{PF}_6)_4$ in CH_3CN exhibits one main (Soret band) signal centred at $\lambda_{\text{max}} = 446$ nm ($208000 \text{ M}^{-1} \cdot \text{cm}^{-1}$) and a much weaker

one (Q band) at $\lambda_{\text{max}} = 663 \text{ nm}$ ($54000 \text{ M}^{-1}.\text{cm}^{-1}$). The absence of aggregation in these conditions is revealed by the linear evolution of the intensity measured at $\lambda_{\text{max}} = 446 \text{ nm}$ as a function of concentration ($10^{-3} \text{ mol.l}^{-1}$ to $10^{-6} \text{ mol.l}^{-1}$) (Figure 51B). This conclusion is also further supported by the curves shown in Figure 51A revealing that the shape and max wavelengths of the porphyrin-based signals do not change with concentration.

The UV-Visible absorption spectrum of $\mathbf{17Zn(Cl)}_4$ (10^{-4} to $10^{-5} \text{ mol.l}^{-1}$) in water features two absorption bands, at $\lambda_{\text{max}} = 456 \text{ nm}$ ($194000 \text{ M}^{-1}.\text{cm}^{-1}$ calculated at 1 mM) and at $\lambda_{\text{max}} = 674 \text{ nm}$ ($63000 \text{ M}^{-1}.\text{cm}^{-1}$ calculated at 1 mM). The curves in Figure 51C show that increasing the concentration of $\mathbf{17Zn(Cl)}_4$ from 10^{-5} to $10^{-3} \text{ mol.l}^{-1}$ leads to a (+4) nm bathochromic shift of both the Soret (456 to 460 nm) and Q-bands (674 to 679 nm). The effect of concentration on the spectroscopic signature of $\mathbf{17Zn}^{4+}$ in water was then further revealed by the significant deviation from the Beer Lambert law in the $10^{-3} \text{ mol.l}^{-1}$ to $10^{-6} \text{ mol.l}^{-1}$ range (Figure 51D).

Overall, these concentration-dependent data are consistent with the self-aggregation of $\mathbf{17Zn(Cl)}_4$ in water. This conclusion is also supported by the known propensity of cationic porphyrins to self-assemble in water producing either extended J- or H-aggregates or discrete dimers.¹⁴² One first conclusion that can be drawn by putting these literature data in perspective with the limited magnitude of the modifications observed in the UV-vis spectra of $\mathbf{17Zn}^{4+}$ recorded at different concentrations is that the porphyrin rings remain fairly distant from each other in the aggregated form.

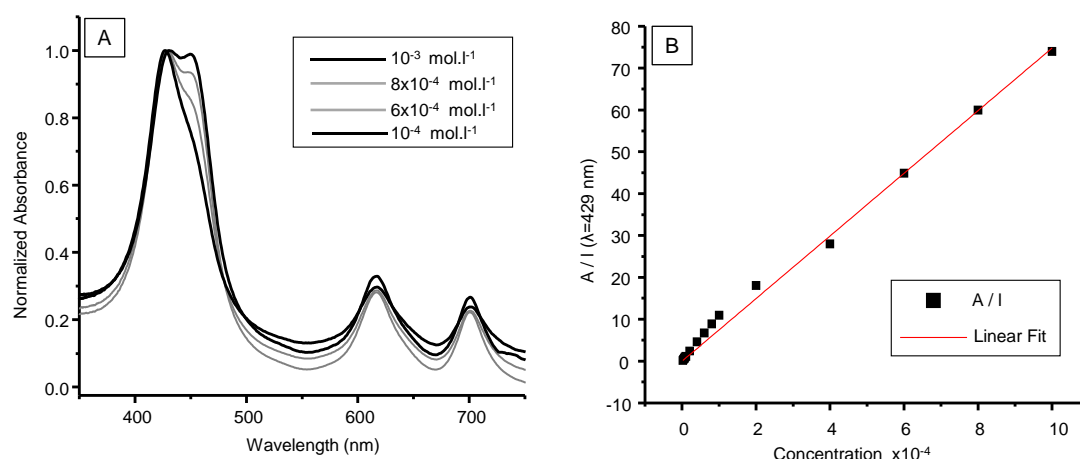


Figure 52: (A) Normalized UV-visible absorption spectra recorded at different concentrations of $\mathbf{17H_2(Cl)}_4$ in H_2O . (B) Variation of the absorbance measured at $\lambda = 429 \text{ nm}$ for $\mathbf{17Zn(Cl)}_4$ in H_2O as function of concentration.

Similar investigations have been carried out with the free base $\mathbf{17H_2(Cl)}_4$. The UV- visible absorption spectrum recorded in water from 10^{-3} to $10^{-6} \text{ mol.l}^{-1}$ display three absorption bands centred at $\lambda_{\text{max}} = 429 \text{ nm}$ ($21000 \text{ M}^{-1}.\text{cm}^{-1}$), 617 nm ($40000 \text{ M}^{-1}.\text{cm}^{-1}$) and 701 nm ($20000 \text{ M}^{-1}.\text{cm}^{-1}$).

$^1.\text{cm}^{-1}$) (see Figure 52). The concentration-induced self-aggregation of the free base was in this case readily revealed by a significant deviation from the Beer Lambert law (Figure 52B) and by the emergence of a new absorption band developing at $\lambda_{\text{max}} = 452 \text{ nm}$ ($70000 \text{ M}^{-1}.\text{cm}^{-1}$, $C=10^{-3} \text{ mol.l}^{-1}$).

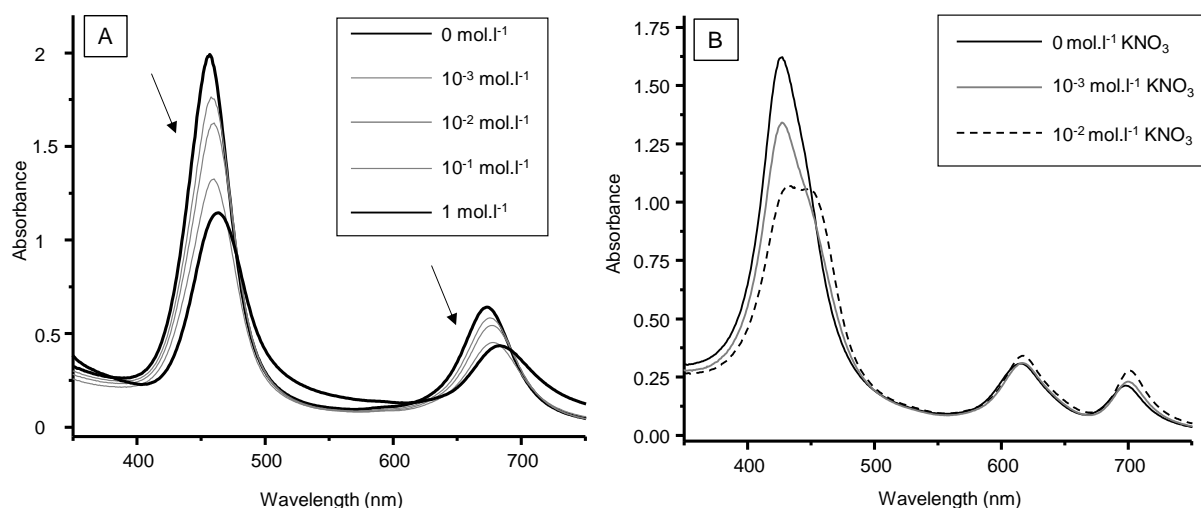


Figure 53: Changes in the UV-Visible absorption spectrum recorded for $17\text{M}(\text{Cl})_4$ in H_2O at different concentration of KNO_3 (A) [$17\text{Zn}(\text{Cl})_4$] $=10^{-5} \text{ mol.l}^{-1}$] and (B) [$17\text{H}_2(\text{Cl})_4$] $=10^{-5} \text{ mol.l}^{-1}$.

Increasing the ionic strength of the aqueous medium was found to have an effect similar to concentration. As can be seen in Figure 53A, the progressive addition of KNO_3 (up to 1M) to an aqueous solution of $17\text{Zn}(\text{Cl})_4$ ($10^{-5} \text{ mol.l}^{-1}$) led to a red shift of the Soret (456 to 464 nm) and Q bands (673 to 683 nm) associated to a loss of half of their intensities. It needs to be mentioned that a similar behaviour was observed upon addition of MeVMe^{2+} (up to 0.1 M) leading to a large loss in intensity and red shift of the Soret and Q bands (+ 4 nm and +13 nm). As observed upon varying the concentration in monomer, addition of KNO_3 to an aqueous solution of the free base $17\text{H}_2(\text{Cl})_4$ ($10^{-5} \text{ mol.l}^{-1}$) led to the emergence of a second band centred at 450 nm and to a weak red shift of both Q bands ($4 \geq \Delta\lambda \geq 2 \text{ nm}$) (Figure 53B).

All these data recorded at different concentrations or at different ionic strengths are consistent with the aggregation of both $17\text{H}_2(\text{Cl})_4$ and $17\text{Zn}(\text{Cl})_4$ in water. As a general statement, a red-shift of the Soret band is indicative of a slipped parallel (head-to-tail, J-aggregate) arrangement of the porphyrin units while a blue shift results from a face to face (head-to-head, H-aggregates) arrangement of the porphyrin units.

The red shift of the Soret band observed upon increasing the concentration in 17Zn^{4+} and 17H_2^{4+} or the ionic strength of the medium thus suggest the formation of J-aggregates. The much larger changes observed with the free base 17H_2^{4+} than with the zinc complex 17Zn^{4+}

presence of CB[7]. It is thus assumed that the structure of the pseudo-rotaxane formed with CB[7] is similar to that of the dimer $(\mathbf{17Zn})_2^{8+}$.

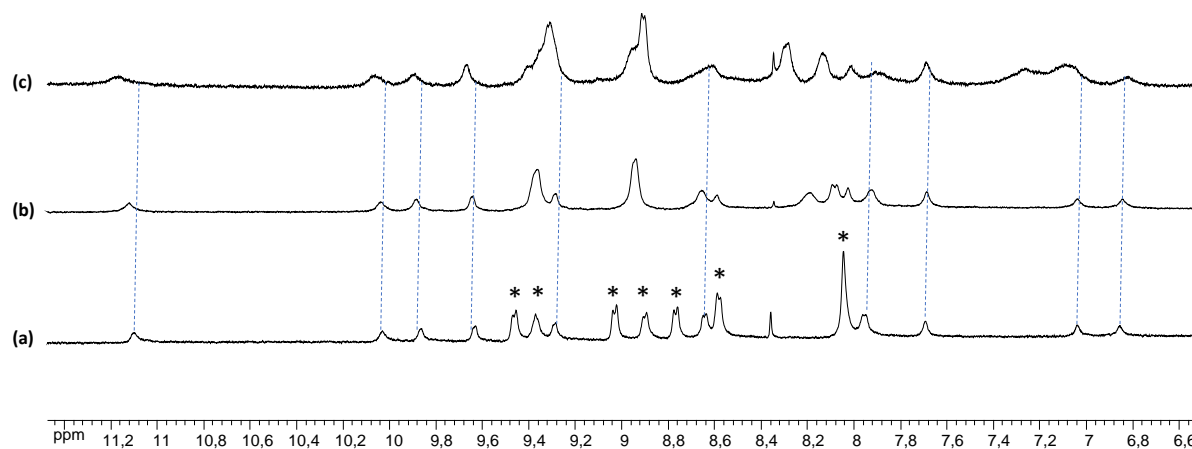


Figure 55: $^1\text{H-NMR}$ Spectra of $\mathbf{17Zn}(\text{Cl})_4$ (5×10^{-4} M in D_2O , 0.1 M phosphate buffer pH=7, 400MHz) recorded after addition: a) 0, b) 1 and c) 2 molar equivalents of CB(7). All the signals impacted by the addition are signaled by a star.

Similar analyses have been conducted in the presence of CB[8]. The progressive addition of CB[8] led in the early stage of the experiment to the broadening and disappearance of all the signals attributed to the dimer $(\mathbf{17Zn})_2^{8+}$. Further addition (>1 molar equivalents) led to the observation of the well-defined spectrum shown in Figure 56b/c featuring up to 17 signals in the aromatic region.

These evolutions reveal that the dimeric assembly $(\mathbf{17Zn})_2^{8+}$ is dissociated in the presence of CB[8] but that the resulting inclusion complex remains poorly symmetric. Careful analyses of the $^1\text{H-NMR}$, 2D-COSY and ROESY correlation maps led us to conclude that the [1:1] inclusion complex $[\mathbf{17Zn}^{4+} \subset \text{CB}[8]]$ shown in Figure 56 is the only product formed in solution in the presence of CB[8]. The latter features one single CB[8] ring interacting on one side of the porphyrin ring with one viologen unit and two TEG chains.

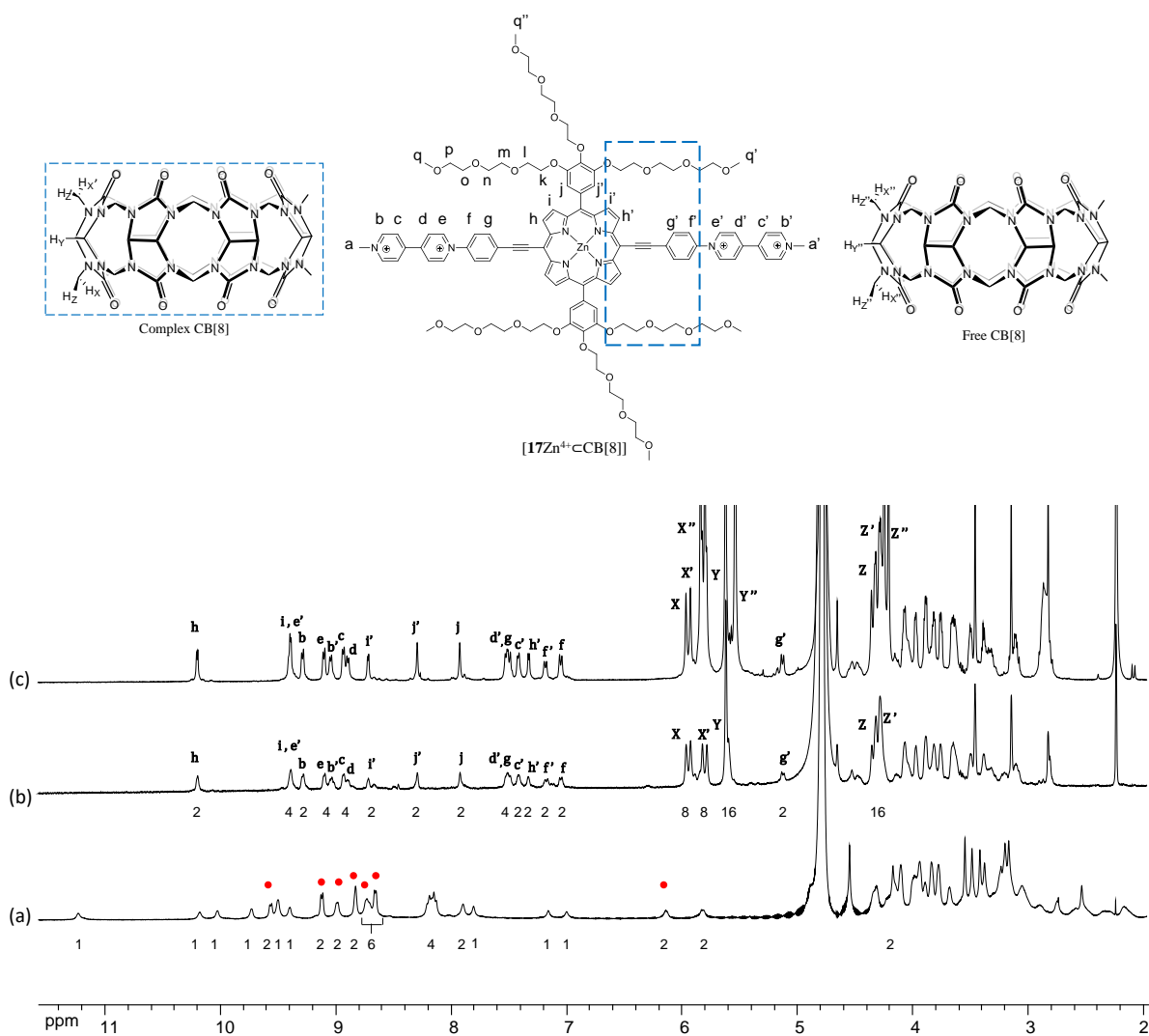


Figure 56: $^1\text{H-NMR}$ Spectra of $17\text{Zn}(\text{Cl})_4$ (D_2O , 400MHz) recorded in D_2O after the addition of different molar equivalents of $\text{CB}[8]$: a) 0, b) 1.1 and c) 2.2. The numbers below the spectrum corresponds to its integration value.

The proposed structure is supported by the following evidences:

- i) The [1:1] species $[17\text{Zn}^{4+}\cdot\text{CB}[8]]$ ($m/z=841$ with $z = 4$) is the main inclusion complex observed on the MS spectrum (ESI^+) recorded in the presence of an excess $\text{CB}[8]$ (4 molar equivalents)
- ii) The integration values measured on the $^1\text{H-NMR}$ spectrum shown in Figure 56b are consistent with the presence of 1 $\text{CB}[8]$ host *per* molecules of 17^{4+} . Addition of $\text{CB}[8]$ in excess (>2 molar equivalents) has no effect on the signals observed at $\text{M:L}=1$ (Figure 56c).
- iii) Both viologen-based substituents are not magnetically equivalent and give rise to 12 different signals attributed to $\text{H}_{\text{b-g}}$ and $\text{H}_{\text{b'-g'}}$.

- iv) Both phenyl rings carrying the TEG chains are magnetically equivalent but locked in the same conformation, as revealed by the fact H_j and H_j' are not equivalent and give rise to two different, albeit scalarly coupled, signals.
- v) The large up-field shift of H_g' (~ 5 ppm) compared to H_g (~ 7.5 ppm) suggest that only one phenyl ring lies within the cavity of a CB host.
- vi) One side of the porphyrin ring, the one bearing the shielded phenyl ring mentioned above, also happens to be much more impacted by the complexation than the other one, as revealed by the observation of signals attributed to H_h and H_h' at 10.25 and 7.25 ppm, respectively.
- vii) The three TEG chains from the same phenyl ring are not magnetically equivalent. This conclusion is based on the observation of three distinct singlets attributed to three different terminal methyl substituents resonating at ~ 2.8 , 3.1 and 3.5 ppm.

Further insights into the association between CB[n] and $17Zn^{4+}$ have been obtained from UV-vis absorption measurements. As can be seen in Figure 57, addition of CB[7] or CB[8] (up to 3 molar equiv.) led to a similar blue shift of the Soret band reaching $\Delta\lambda = -3$ nm (458 to 455 nm) in the presence of 3 molar equivalents of CB, while the Q bands experienced in the same conditions a 9 nm red shift (678 to 687 nm) and a 5 nm blue shift (678 to 673 nm) upon addition of CB[8] and CB[7], respectively. In both cases the slight blue shift of the Soret band is reminiscent of the changes observed upon dilution, attributed to the dissociation of the dimer $(17Zn^{4+})_2 \rightarrow 2(17Zn^{4+})$.

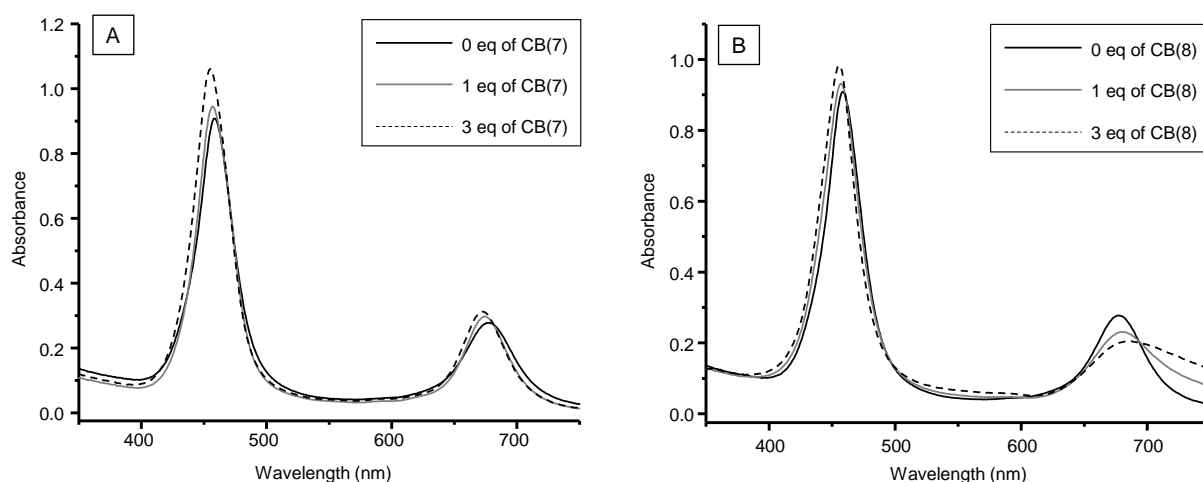


Figure 57: Absorbance spectra of $17Zn(Cl)_4$ (5×10^{-4} mol.l $^{-1}$) in H_2O recorded in the presence of n molar equivalents of A) CB[7] / B) CB[8]: black (n=0), grey (n=1), dashed (n=3) lines.

Although some results remain poorly understood, the spectroscopic data collected with CB[8] and CB[7] are consistent with the conclusion that the viologen units get threaded in the

cucurbiturils rings. Formation of pseudorotaxanes with CB[8] also triggers the dissociation of the dimeric self-assembled species (17Zn^{4+})₂ to yield a well-defined non-symmetric inclusion complex.

II.3.5. Electrochemistry and Spectro-Electrochemistry in Organic Media

The electrochemical signatures of the title compounds $17\text{H}_2(\text{PF}_6)_4$ and $17\text{Zn}(\text{PF}_6)_4$ have first been investigated in DMF using tetra-*n*-butylammonium perchlorate (TBAP) as an electrolyte. Both compounds display similar signatures featuring four consecutive reduction waves and one oxidation wave in the accessible potential window (Table 4).

The first reversible reduction wave centered at $(E_{1/2})^{1c} = -0.763$ V is attributed to the one-electron reduction of the two viologens units (one electron *per* viologen) in 17Zn^{4+} yielding the di-cationic compound $17\text{Zn}^{2(+)}$. The Nernstian character ($I_{pa} / I_{pc} \approx 1$, $\Delta E_p \approx 60$ mV, $I_p = \alpha v^{1/2}$, see Figure 58 and Figure 59) of the reduction wave indicates the absence of chemical reactions coupled to the electron transfer in our experimental conditions (1 mM in DMF).

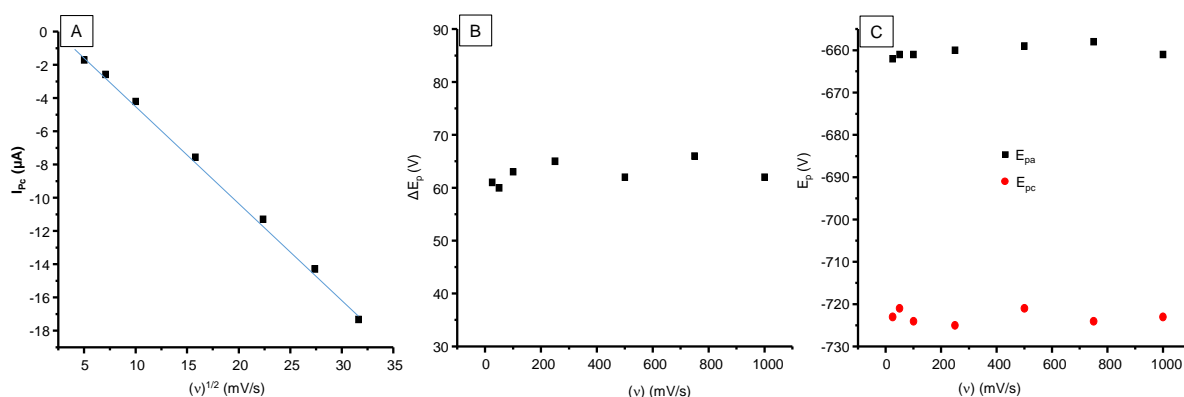


Figure 58: Variations of the (A) peak current, (B) anodic (E_{pa}) and cathodic (E_{pc}) peak potentials values and of the (C) peak to peak potential shift (ΔE_p) (C) as a function of scan rate (v in mV/s) (measured for $17\text{Zn}(\text{PF}_6)_4$ by CV in DMF (0.1 M TBAP) at a glassy carbon working electrode ($\varnothing = 3$ mm, E in volts vs. Ag^+/Ag 10^{-2} M).

The second reversible reduction wave centered at $(E_{1/2})^{2c} = -1,076$ V is attributed to the second one-electron reduction of the viologen units (one electron *per* viologens) leading to the neutral quinonic species 17Zn^0 . Here again, the ΔE_p value of about 64 mV suggests the absence of communication/interactions between the viologen centers. Another evidence supporting this assumption is the rather short stability domain of the cation-radical state in $17\text{Zn}^{(2+)}$, $\Delta E = (E_{1/2})^{2c} - (E_{1/2})^{1c} = 313$ mV, the latter value being similar to the one measured in the same conditions for the reference molecule MeVMe^{2+} ($\Delta E = 336$ mV).

The two remaining reversible reduction waves of low intensities observed at $(E_{1/2})^{3c} = -1.547$ V and $(E_{1/2})^{4c} = -2.065$ V have been attributed to the one-electron reduction of the porphyrin skeleton yielding successively the anion radical $17Zn^{\bullet-}$ and the dianion $17Zn^{2\bullet-}$, respectively. On the anodic side, the weakly intense and poorly reversible wave observed at $E^{1a} = 0.484$ V is attributed to the one electron oxidation of the porphyrin ring.

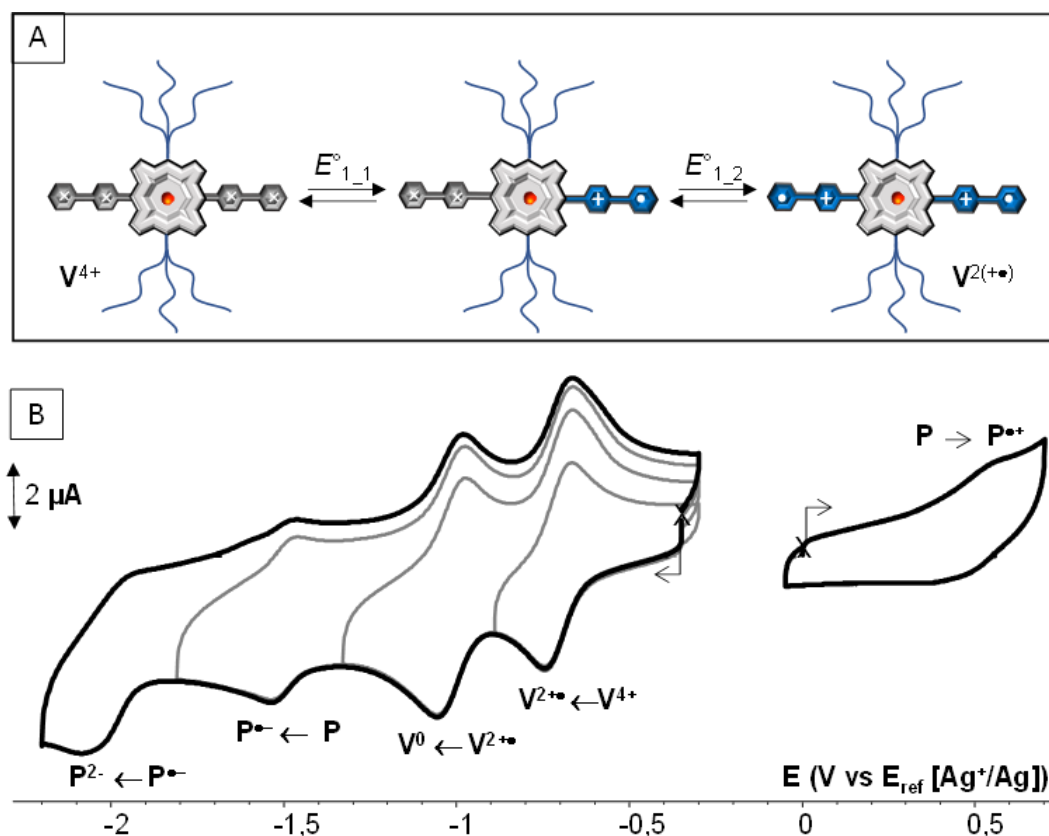


Figure 59: CV curves of a DMF (TBAP 0.1M) solution of $21Zn(PF_6)_4$ (1×10^{-3} M) recorded at a glassy carbon working electrode ($\varnothing = 3$ mm, E vs. Ag^+/Ag (10^{-2} M), $v = 0.1$ V.s $^{-1}$).

The free base porphyrin $17H_2^{4+}$ has been also studied in the same experimental conditions. Selected values recorded with this compound are collected in Table 4. These data reveal that the metal has a significant effect on the porphyrin-centered redox processes with potential shifts ($\Delta E \sim -200$ mV) in agreement with the known stabilizing effect of the zinc atom on the porphyrin-based π system. The values collected in Table 4 also bring to light that the viologen-based reduction potentials are only weakly affected by the presence of the zinc ion in the cavity of the porphyrin ring.

The influence of the viologen substituents on the redox activity of the porphyrin ring is further provided by the comparison of key figures obtained with $11Zn^{8+}$ and $17Zn^{4+}$ in DMF electrolytes (Table 4). The porphyrin ring surprisingly found to be easier to reduce in $17Zn^{4+}$

than in **11Zn**⁸⁺ despite the lower number of viologen units. This shift can nevertheless be understood based on conjugation issues upon considering that the ethynyl linkers could lead to an improved “communication” between the viologens and the porphyrin.

	Solvent	E^{4c} (n, ΔE_p) P•/ P²⁻	E^{3c} (n, ΔE_p) P/ P•	E^{2c} (n, ΔE_p) V²⁺/ V⁰	E^{1c} (n, ΔE_p) V²⁺/ V^{•+}	E^{1a} (n, ΔE_p) P⁺/P^{•+}
MeVMe(PF ₆) ₂	DMF	na	na	-1.163 ^b (1,62)	-0.774 ^b (1,60)	na
17H₂ (PF ₆) ₄	DMF	-1.816 ^c	-1.304(1, 64)	-1.051(2, 62)	-0.743(2, 55)	0.686 ^a
17Zn (PF ₆) ₄	DMF	-2.065 ^c	-1.547(1, 66)	-1.076 (2, 64)	-0.763 (2, 63)	0.484 ^a
11H₂ (PF ₆) ₈	DMF	-2.011 ^b (1,84)	-1.613 ^b (1,84)	-1.115 ^b (4,77)	-0.785 ^b (4,60)	0.728 ^c (1)
11Zn (PF ₆) ₈	DMF	-2.236 ^b (1)	-1.827 ^b (1,75)	-1.087 ^b (4,67)	-0.762 ^b (4,63)	0.682 ^c (1)
MeVMe(Cl) ₂	H ₂ O	na	na	-0.99 (1,77) ^b	-0,654(1,60)	na
17Zn (Cl) ₄	H ₂ O	na	na	-0.645 (2,157)	-0.402 (2,119)	na
11Zn (Cl) ₈	H ₂ O	na	na	-0.638 (4,24)	-0,389 ^{c,d}	0,861 ^c (1)

Table 4: Measured by CV, 2-5·10⁻⁴ m in DMF/TBAP (0.1 M, $E(V)$ vs. Fc⁺/Fc), or in an aqueous phosphate buffer (0.1M, pH = 7, $E(V)$ vs. AgCl/Ag (KCl sat) at a vitreous carbon working electrode \varnothing = 3 mm, 298 K, ν = 0.1 V·s⁻¹. na : Not available / ^b : Half wave potential / ^c : Peak potential / ^d : Adsorption phenomena

Both the free base **17H₂**⁴⁺ and the zinc complex **17Zn**⁴⁺ have been submitted to spectro-electrochemical characterizations to provide further insights into the fate of the reduced species. These studies have been carried out in a glove box using a conventional three-electrode setting and an all quartz immersion probe. The exhaustive two-electron reduction (1e⁻/viologen) of **17Zn**(PF₆)₄ (1.66x10⁻⁴ M) in DMF (0.1 M TBAP) solution has been performed in a potentiostatic regime involving setting the potential of the platinum working electrode at -0.94 V vs. E_{ref} [Ag⁺/Ag (0.01M)]. The advancement/completion of the electrolysis was checked by steady-state voltammetry measurements carried out at a rotating disk electrode.

As can be seen in Figure 60, the exhaustive 2-electrons reduction of **17Zn**⁴⁺ led to a slight broadening of the porphyrin-based Soret band coming along with a significant bathochromic shift, of about 6 nm, of its maximum wavelength (from 451 to 457 nm) accompanied with a weak hyperchromic effect (Figure 60A). These minor changes indicate that the electron transfer centered on the viologens has a limited impact on the electron density of the porphyrin-based π -system. The novel set of absorption bands developing between 500 and 800 nm, overlapping with the porphyrin-based Q band, is attributed to a series of transitions centered on the electrogenerated viologen cation-radical. Our experiments also revealed that the electrochemical conversion of **17Zn**⁴⁺ into **17Zn**^(2•+) is fully reversible at the electrolysis

time scale (30 min) and that the electrogenerated species $17\text{Zn}^{(2+)}$ do not form π -dimers in these experimental conditions, as revealed by the absence of diagnostic absorption bands in the near IR region (~ 900 nm) and by the standard ΔE_p value of about 60 mV measured on the first viologen-based CV wave.

Further investigations carried out on the free base 17H_2^{4+} led to similar findings with a spectroscopic signature recorded after bulk electrolysis at $E_{\text{app}} = -0.94\text{V}$ (vs. $E_{\text{ref}}[\text{Ag}^+/\text{Ag}]$) in agreement with the formation of the di-radical species $17\text{H}_2^{(2+)}$ (Figure 60B).

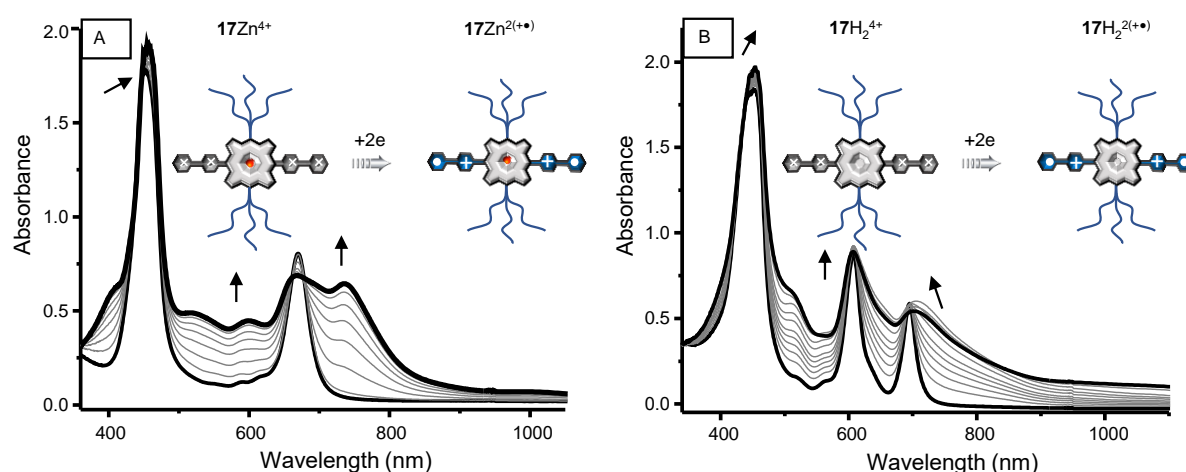


Figure 60: UV-vis spectra recorded during the exhaustive one-electron reduction (per viologen) of A) $17\text{Zn}(\text{PF}_6)_4$ (1.66×10^{-4} M) and B) $17\text{H}_2(\text{PF}_6)_4$ (1.11×10^{-4} M) in DMF (0.1 M TBAP) using a platinum plate working electrode whose potential was fixed at $E_{\text{app}} = -0.94\text{V}$ vs. $E_{\text{Ag}^+/\text{Ag}}$ (10 mL, $l = 1$ mm, $t \approx 30$ min)

II.3.6. Photoreduction of 17Zn^{4+} in Organic Media

We investigated the effect of continuous irradiation of 17Zn^{4+} with visible light in solution. It was expected that upon excitation of the porphyrin core, a photo-induced electron transfer (PET) would result in the formation of viologen radical cations. Based on the electrochemical and spectroscopic results described above, it is possible to calculate the driving force of this photo-induced process. In order to do that, the value of the redox potential for 17Zn^{4+} in the excited state E^* has to be determined. It was obtained by subtracting the energy needed to reach the excited state from the redox potential measured at the ground state. The excited state energy $E_{0,0}$ was estimated at 1.77 eV ($\pm 5\%$) from the tangent of the low energy side of the absorption Q-band of 17Zn^{4+} ($\Delta E(\text{eV}) \approx 1240/\lambda$ (nm)). Using the data collected in Table 4, the redox potentials of the excited states ($\text{P}^*/\text{P}^{+\bullet}$) has been estimated at -1.29 V ($E^* = E^{1a} - E_{0,0}$). After applying the Rehm-Weller equation¹⁴³⁻¹⁴⁴ to our system and neglecting Coulombic factors, we obtain the simplified equation: $\Delta G = E^* - E^{1c}$ giving us a free energy value of *ca.*

–550 meV. The thermodynamic driving force thus clearly favors a PET mechanism from the porphyrin core to the viologen fragments.

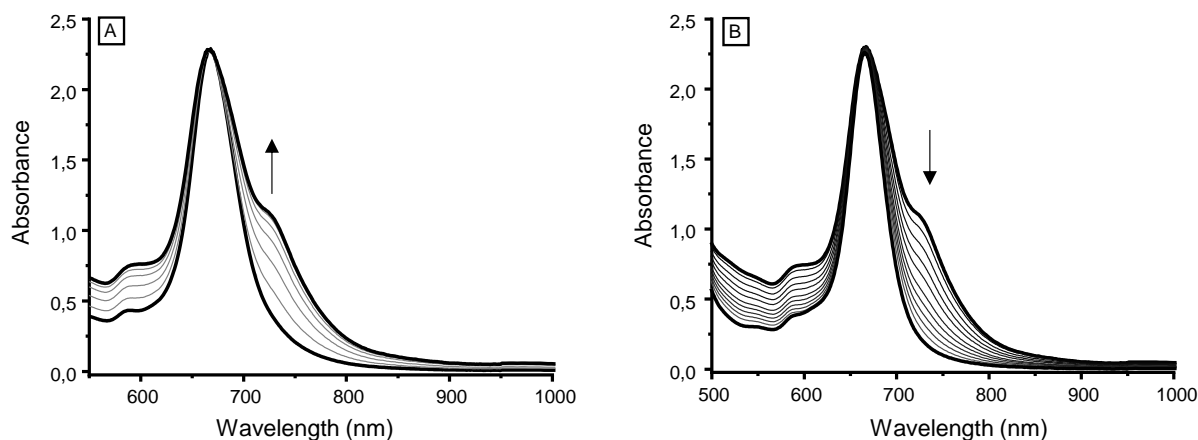


Figure 61: A) UV-vis spectra of $17\text{Zn}(\text{PF}_6)_4$ (5×10^{-5} M) in anaerobic MeCN in presence of TEOA (5×10^{-3} M) recorded during irradiation at $\lambda_{\text{exc}} = 660$ nm (B) Reoxydation under air.

A solution of 17Zn^{4+} (5×10^{-5} M) and triethanolamine (5×10^{-3} M) in DMF was irradiated under anaerobic conditions with visible light using a monochromatic LED lamp ($\lambda_{\text{exc}} = 660$ nm). This irradiation led to the emergence of the characteristic signature of the viologen radical cation developing progressively over 35 minutes and overlapping with the porphyrin Q-bands (Figure 61A). Bubbling oxygen through the cell then led to the disappearance of these signals at the expense (Figure 61B) of the initial spectrum, a result which demonstrates the photochemical stability of 17Zn^{4+} . As for the spectro-electrochemical experiments, π -dimers do not form in these experimental conditions as attested by the lack of band in the near infrared region.

II.3.7. Electrochemistry and Spectro-Electrochemistry in Aqueous Medium

The objective here was to check the ability of CB[8] to promote the intermolecular π -dimerization of the two-electron reduced species $17\text{Zn}^{(2+\bullet)}$ in water to yield the targeted 1D self-assembled polymers (Figure 62). These studies have also been conducted with CB[7], used here as a reference only capable of yielding discrete host-guest caviplaxes with $17\text{Zn}^{(2+\bullet)}$.

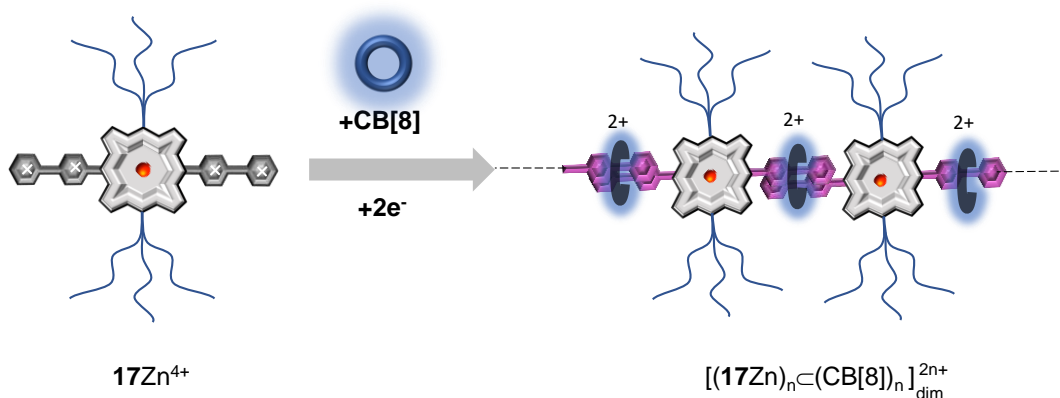


Figure 62: Schematic drawing showing the expected binding modes between the two-electron reduced species $17\text{Zn}^{(2+\bullet)}$ and CB[8].

As a preliminary experiment, the electrochemistry of $17\text{Zn}(\text{Cl})_4$ has been investigated by CV measurements carried out in a phosphate buffer (pH=7, 0.1 M) at a vitreous carbon electrode. The CV curve display two consecutive reduction waves at $E^{1c} = -0.402$ and $E^{2c} = -0.645$ V (E vs. Ag^+/Ag) attributed to the successive formation of $17\text{Zn}^{(2+\bullet)}$ and 17Zn^0 , respectively (Table 4). The data depicted in Figure 63 reveal that the main characteristics of the first reduction wave evolve to a great extent with scan rate. The current remains limited by diffusion but the peak potential measured in the forward scan happens to shift quite significantly towards more negative values with increasing scan rates. The cause of this irreversibility is not well understood but the most likely hypothesis is that it is linked to the aggregation of 17Zn^{4+} in aqueous medium.

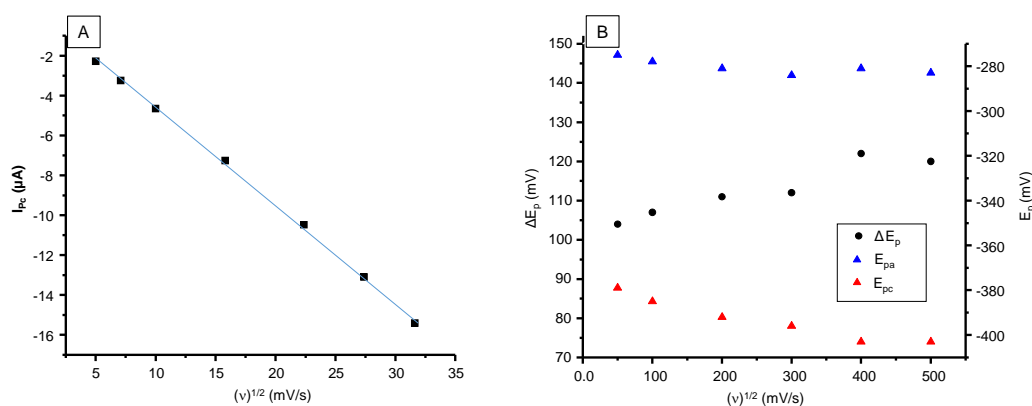


Figure 63 : Variations of the (A) Peak current , (B) the anodic (E_{pa}) and cathodic (E_{pc}) peak potentials and peak to peak potential shift (ΔE_p) as a function of scan rate (v) (measured for $17\text{Zn}(\text{Cl})_4$ by CV in a phosphate buffer (0.1 M, pH=7) at a glassy carbon working electrode ($\varnothing = 3\text{mm}$, E in volts vs. AgCl/Ag).

The relative affinity of CB[8] for 17Zn^{4+} and $17\text{Zn}^{(2+\bullet)}$ was assessed from CV data focusing on the first viologen-centered reduction wave. The data shown on Figure 64 reveal the addition of CB[8] leads to the disappearing of the initial reduction wave ($E_p = -0.426$ V) at the expense of a new wave developing at a less negative potential value ($E_p = -0.345$ V)

attributed to the reduction of the inclusion complex formed between 17Zn^{4+} and CB[8]. Both waves are still clearly observed on the CV curve recorded in the presence of 0.5 molar equivalent of CB[8] (blue line in Figure 64) while only the second wave developing at $E_p = -0.345\text{ V}$ remains visible after addition of one molar equivalent of CB8 (red line in Figure 64).

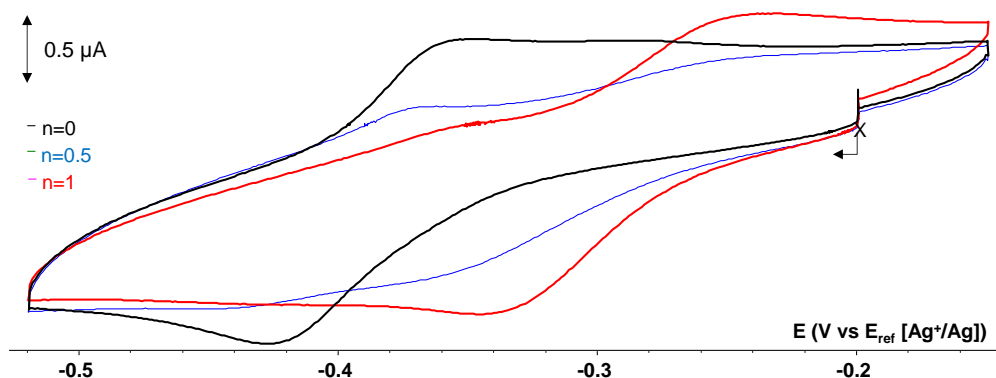


Figure 64: Voltametric curve (CV) recorded for $17\text{Zn}(\text{Cl})_4$ ($5 \times 10^{-4}\text{ M}$) in aqueous phosphate buffer ($\text{pH} = 7$, 0.1 M) in the presence of 0 (red line), 0.5 (blue line) and 1 (black line) molar equivalents of CB[8] ($\text{VC } \varnothing = 3\text{ mm}$, $v = 25\text{ mV}\cdot\text{s}^{-1}$, E vs. AgCl/Ag).

The peak potential of the second viologen-centered reduction is found to shift to a much greater extent upon addition of CB[8], the wave initially observed at $E_p = -0.724\text{ V}$ undergoes a negative shift reaching -1.07 V in the presence of one molar equivalence of CB[8] (red line in Figure 65). It is worth to mention that the upper value of the molar ratio reached towards the end of the titration, $\text{CB}[8]:17\text{Zn}^{4+} = 1$, not only match the ratio needed to form the ideal 1D arrangement shown in Figure 62, it also happens to correspond to the solubility limit of CB[8] in our experimental conditions (0.1 M phosphate buffer $\text{pH} = 7$).

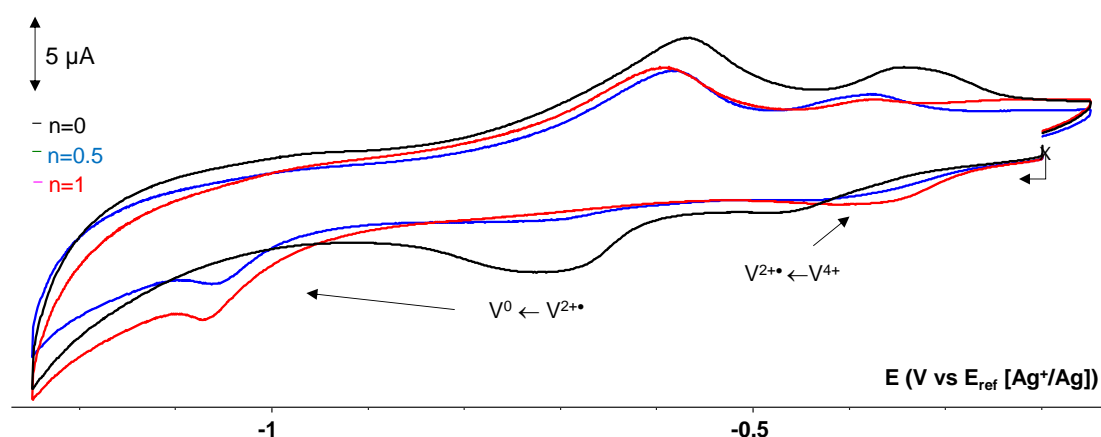


Figure 65: CV curves recorded for $17\text{Zn}(\text{Cl})_4$ ($5 \times 10^{-4}\text{ M}$) in aqueous phosphate buffer ($\text{pH} = 7$, 0.1 M) ($\text{VC } \varnothing = 3\text{ mm}$, $v = 0.1\text{ V}\cdot\text{s}^{-1}$, E vs. AgCl/Ag) in the presence of n molar equivalents of CB[8].

Altogether, these electrochemical data are consistent with the conclusion that the viologen based cation radicals in $17\text{Zn}^{2+(\bullet)}$ are stabilized in the presence of CB[8],^{74, 113, 135} the most striking evidence being that the viologen cation radicals are more easily formed and harder to reduce in the presence than in the absence of CB[8]. Based on relevant scientific literature and on previous results collected with the parent compound 11Zn^{8+} , we attribute the extensive stabilization of the viologen cation radicals in $17\text{Zn}^{2+(\bullet)}$ to the formation of intramolecular π -dimers included within the cavity of CB[8] hosts, *i. e.* to the redox triggered transformation of the 1:1 inclusion complex $[17\text{Zn}^{4+}\subset\text{CB}[8]]$ into the targeted 1D self-assembled architecture fitting the general formula $[(17\text{Zn}\subset\text{CB}[8])_n]_{dim}^{2n+}$.

This hypothesis has been further confirmed upon carrying out similar investigations with CB[7], used as a control prohibiting the formation of π -dimers.^{84, 135}

Selected CV curves recorded during the progressive addition of CB[7] to a solution of 17Zn^{4+} in water are displayed in Figure 66. In contrast to what was observed with CB[8], the presence of CB[7] is found to induce the simultaneous shift of both viologen-centered reduction waves towards more negative potential values, coming along with a significant drop of the current levels. In agreement with previous report on CB[7]-viologen inclusion complexes, such behavior is here consistent with the idea that CB[7] has a weaker affinity for the viologen cation radicals in $17\text{Zn}^{2+(\bullet)}$ than for the dicationic viologens in 17Zn^{4+} .⁸⁴ The stability domain of $17\text{Zn}^{2+(\bullet)}$ is indeed not significantly modified while both the viologen dication and cation radicals end-up being harder to reduce in the presence of CB[7].

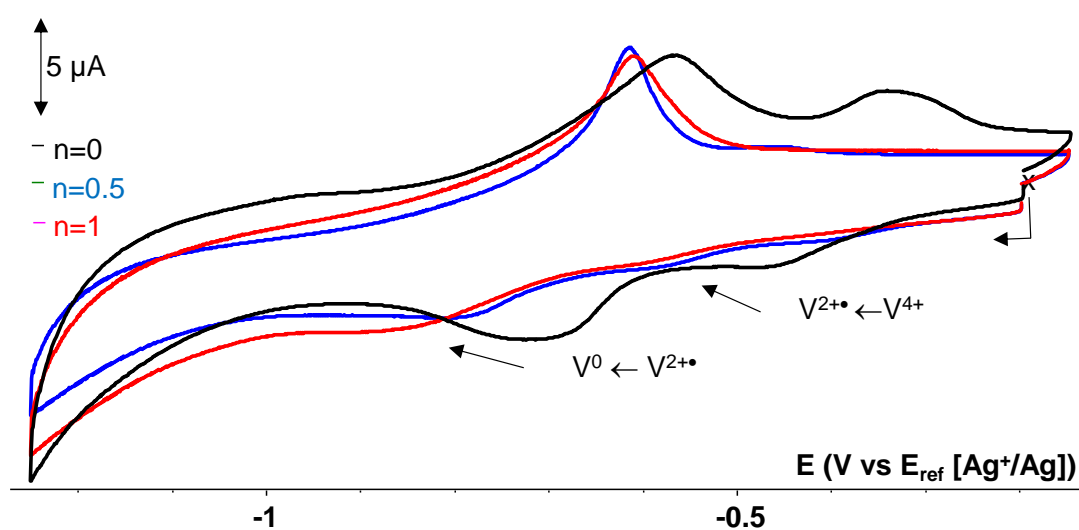


Figure 66: CV curves recorded for $17\text{Zn}(\text{Cl})_4$ (5×10^{-4} M) in aqueous phosphate buffer (pH= 7, 0.1 M) (VC \varnothing = 3 mm, v = 0.1 $\text{V}\cdot\text{s}^{-1}$, E vs. AgCl/Ag) in the presence of n molar equivalents of CB[7].

As a conclusion, the electrochemical data discussed above are quite similar to those recorded with the star shaped porphyrin 11Zn^{8+} in the presence of CBs (see part II.2). As revealed by the NMR data discussed in section II.3.4, the initial chemical step is a threading of CB[8] or CB[7] onto the porphyrin axles to yield $[17\text{Zn} \subset (\text{CB}[n])_x]^{4+}$ ($n=7$ or 8 , $x=1$ or 2). When $n=7$, all the evidence support the conclusion that the two consecutive reduction of both viologen units lead to the successive formation of the reduced inclusion complexes $[17\text{Zn} \subset (\text{CB}[7])_2]^{2(+)}$ and $[17\text{Zn} \subset (\text{CB}[7])_2]^0$.

When $n=8$, the anodic shift of the first reduction wave coming along with a cathodic shift of the second reduction wave are attributed to a CB[8]-driven stabilization of intermolecular π -dimers leading to the formation of 1D assemblies. These assumptions have been further confirmed by UV-vis absorption spectrophotometric measurements conducted in water on the *in-situ* generated 2-electron-reduced species $17\text{Zn}^{2(+)}$ in the absence or in the presence of CBs.

The one-electron reduction of both viologen units in 17Zn^{4+} has been carried out in phosphate buffer (pH=7) using sodium dithionite $\text{Na}_2\text{S}_2\text{O}_4$ as a reductant.¹¹⁴ Selected UV-vis absorption spectra collected during the progressive addition of $\text{Na}_2\text{S}_2\text{O}_4$ to an aqueous solution of 17Zn^{4+} are shown in Figure 67.

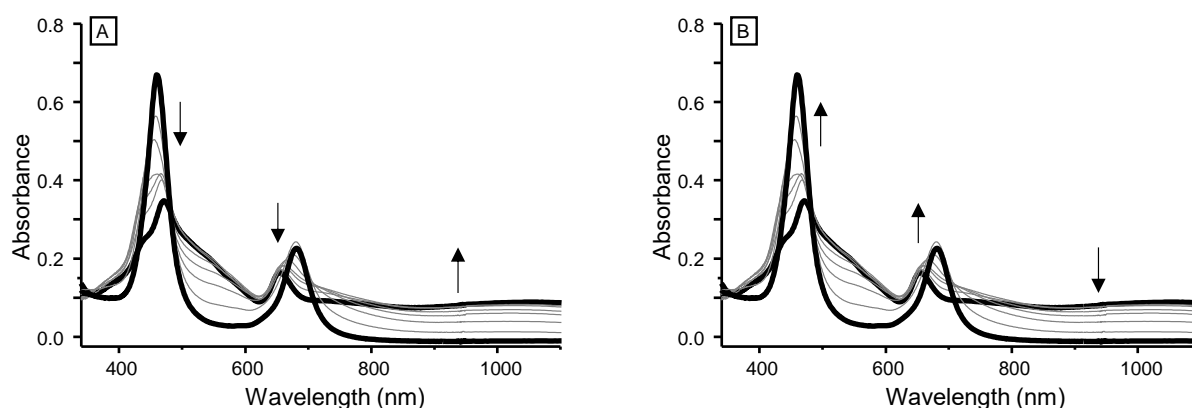


Figure 67: UV-vis spectra of $17\text{Zn}(\text{Cl})_4$ (1.1×10^{-4} M) in phosphate buffer (pH=7, 0.1 M) recorded over time after addition of $\text{Na}_2\text{S}_2\text{O}_4$ in excess (A) and followed by gentle bubbling of compressed air (B).

These curves reveal that the chemical reduction of 17Zn^{4+} leads to a large drop (about 50%) in the intensity of the Soret band and to a blue shift (27 nm) of the single Q band coming along with a large increase of the baseline signal. Most interestingly, these drastic changes proved to be perfectly reversible, as revealed by the fact that the initial spectrum of 17Zn^{4+} could be fully recovered after gentle bubbling of compressed air through the chemically reduced sample (Figure 67B). The curves recovered after addition of $\text{Na}_2\text{S}_2\text{O}_4$ are nevertheless

consistent with the existence of chemical steps coupled to the electron transfer. The redox and chemical processes involved in solution upon reduction of 17Zn^{4+} are still poorly understood but the large increase of the base signal, the unusual broadness, splitting and red shift of the initial Soret band strongly suggest the formation of mixtures of J aggregates in solution.¹³⁹ Such supramolecular assembly could indeed potentially be formed as a result of the reduction of both viologens (one electron/viologen) in 17Zn^{4+} leading to the much less water soluble species $17\text{Zn}^{2(+\bullet)}$, prone to stacking. The spectroscopic signature recorded in the presence of reducing agent are moreover reminiscent of data reported by different authors with various pyridium-substituted porphyrins where splitting, hypochromicity, broadening and red shifts or blue shifts of Soret bands reveal the formation of mixtures of J- and H-aggregates, respectively.^{138, 145}

Similar studies have been carried out in the presence of CB[8]. Figure 68A shows the UV-vis absorption spectra of $[17\text{Zn}\subset\text{CB}[8]]^{4+}$ (formed in situ from a 1:1 mixture of 17Zn^{4+} and CB[8]) after progressive addition of $\text{Na}_2\text{S}_2\text{O}_4$. These curves reveal that the chemical reduction of $[17\text{Zn}\subset\text{CB}[8]]^{4+}$ leads to a slight broadening of the porphyrin-based Soret band accompanied with a hypsochromic shift (blue shift) of about 13 nm of its maximum wavelength (from 455 to 442 nm with a clean isosbestic point at 450 nm). These modifications are fully compatible with electron transfers centered on the peripheral viologens having a minor impact on the electron density of the porphyrin-based π -system. This attribution is further supported by the emergence of absorption bands between 500 and 800 nm, overlying with the porphyrin-based Q bands, attributed to a series of transitions centered on a viologen cation-radical. Another diagnostic absorption bands emerged in the near IR region centered at 960 nm. The latter is attributed to the viologen-based π -dimers whose energy is proportional to the electronic coupling term arising from frontier-orbital interactions between a pair of equivalent SOMOs.

One key conclusion drawn from this analysis, is that the viologen radicals in the chemically reduced pseudo-rotaxane $[17\text{Zn}\subset\text{CB}[8]]^{4+}$ is involved in the formation of self-assembled intermolecular π -dimers. The experimental data also demonstrate that the proposed supramolecular self-assembly process is fully reversible, as revealed by the fact that a gentle bubbling of compressed air through the sample leads to the regeneration of the initial inclusion complex (Figure 68B).

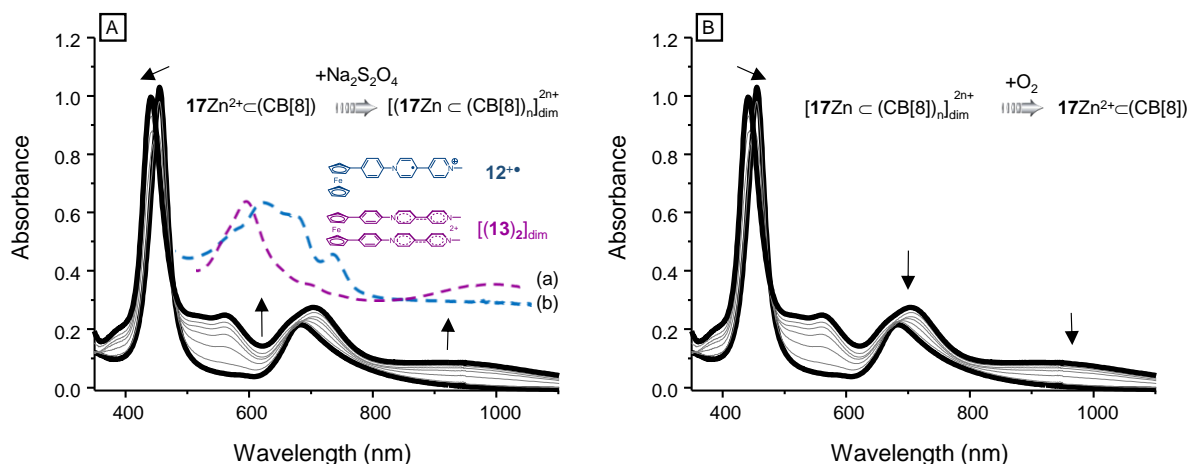


Figure 68: UV-vis spectra of $17\text{Zn}(\text{Cl})_4$ (7×10^{-5} M) and CB[8] (1 molar equivalents) in phosphate buffer (pH=7, 0.1 M) recorded over time after addition of $\text{Na}_2\text{S}_2\text{O}_4$ in excess (A) and followed by gentle bubbling of compressed air (B).

Controlled experiments have then be carried out in the presence of CB[7], mostly to confirm the hypotheses raised above (Figure 69). The reduction of 17Zn^{4+} carried out in the presence of 2 molar equivalents of CB[7] upon addition of $\text{Na}_2\text{S}_2\text{O}_4$ in excess led to a 15 % loss of the initial intensity of the Soret band centered at 455nm and to the development of a new signals between 500 and 800 nm, overlying with the porphyrin-based Q bands (Figure 69). These results support the conclusion that the electron transfers are centered on the peripheral viologens and that they have minor impact on the electron density of the porphyrin-based π -system. Most importantly, the lack of clear diagnostic absorption bands in the near IR region (≈ 900 nm) demonstrate that the formation of pseudorotaxane with CB[7] inhibits the formation of intermolecular π -dimers.

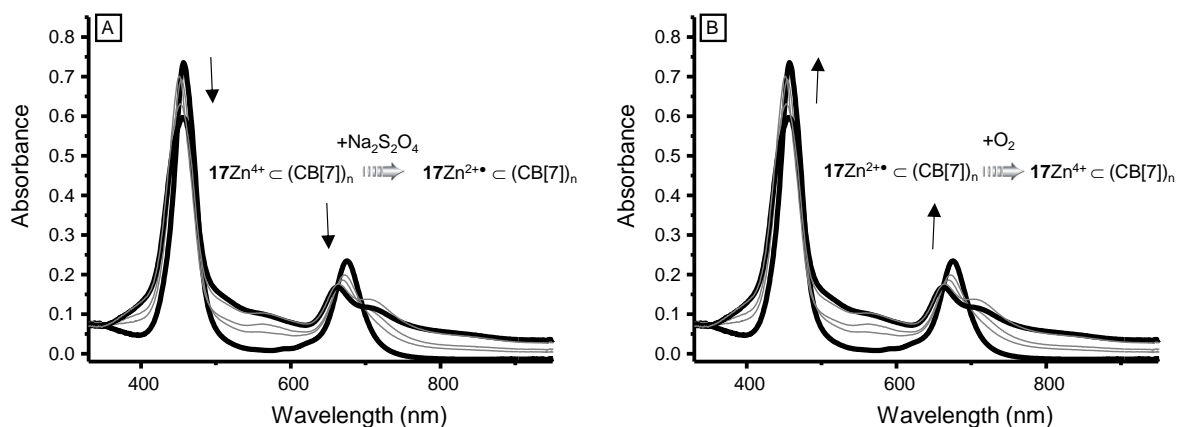


Figure 69 : UV-vis spectra of $17\text{Zn}(\text{Cl})_4$ (8.5×10^{-5} M) and CB[7] (2 molar equivalents) in phosphate buffer (pH=7, 0.1 M) recorded over time after addition of $\text{Na}_2\text{S}_2\text{O}_4$ in excess (A) and followed by gentle bubbling of compressed air (B).

II.3.8. Conclusion

All the experiments carried out with $\mathbf{17Zn(X)_4}$ ($X = \text{Cl}^-$ or PF_6^-) in aqueous and organic media support the conclusions that $\mathbf{17Zn^{4+}}$ self assembles in water to form a non-symmetric dimeric species $(\mathbf{17Zn^{4+}})_2$. Addition of CB[8] in excess was then shown to trigger a dissociation of $(\mathbf{17Zn^{4+}})_2$ to yield a pseudorotaxane derivative $[\mathbf{17Zn} \subset \text{CB}[8]]^{4+}$ wherein one of the rigid viologen-containing arms is threaded through the CB[8] ring. Reduction of the latter species (one electron/viologens) using sodium dithionite was then found to trigger a CB[8]-mediated intermolecular π -dimerization of the porphyrin-viologen tectons leading to the formation of a 1D self-assembled species $[(\mathbf{17Zn}^{2(+\bullet)} \subset \text{CB}[8])_n]_{\text{dim}}$. Support for these assumptions came from detailed NMR, electrochemical and spectroelectrochemical measurements and from controlled experiments involving CB[7].

II.4. Redox- Responsive Assembly involving Tetraphenyl Ethylene Based Tecton

The third approach that has been developed toward redox-responsive supramolecular assemblies involves the use of a tetraphenyl-ethylene (TPE) linker (Figure 43). The objective here was to exploit and investigate the ability of the TPE scaffold to promote the intermolecular dimerization of viologen radical cation in solution.

II.4.1. Synthesis of the Targeted Tecton 21^{8+}

The multi-step synthesis of the targeted viologen-TPE 21^{8+} is summarized in Figure 70. The key intermediate compound **20** was prepared according to a procedure reported by Yaghi and coll,¹⁴⁶ starting with the bromination of tetraphenyl ethylene (TPE) **18**¹⁴⁷ in acidic condition to obtain compound **19** in a quantitative yield. The latter was subjected to a Suzuki cross-coupling reaction with 4-Aminophenylboronic acid to yield the aniline substituted TPE **20**.¹⁴⁶ This intermediate was reacted with the activated viologen **16**²⁺¹⁰⁴ to afford 21^{8+} in 40 % yield. This final product could be easily isolated as a chloride or hexafluorophosphate salt through anion metathesis. The minimized structure shown in Figure 70 reveals that the four phenyl rings cannot be coplanar and thus remain tilted with respect to the ethylene unit.

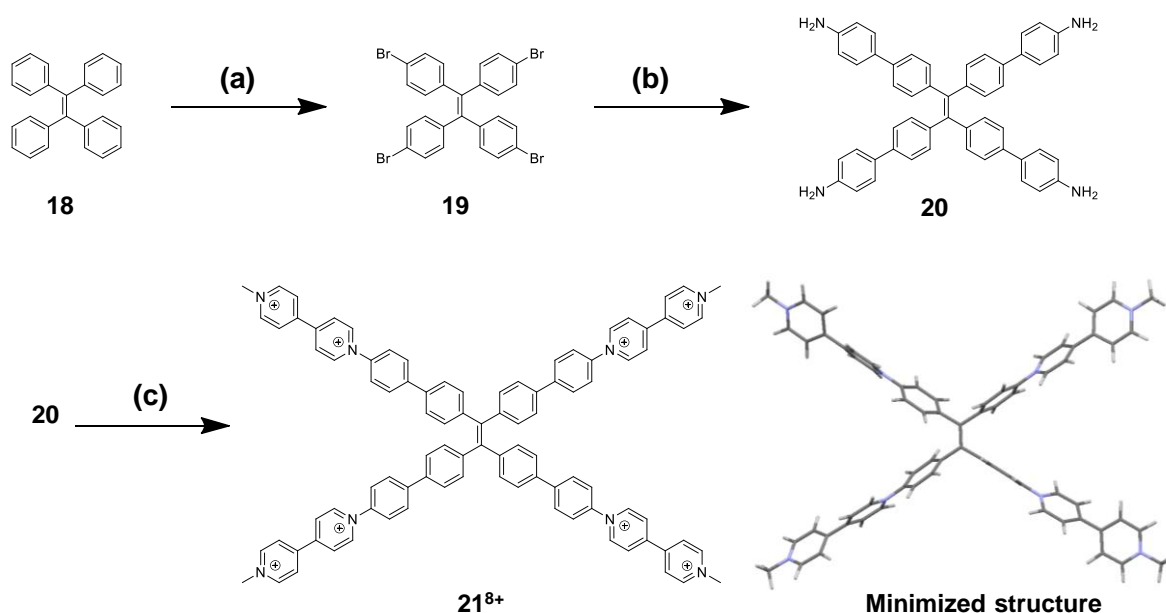


Figure 70 : (a) Br_2 , AcOH, quantitative; (b) 4-Aminophenylboronic acid, $\text{Pd}(\text{PPh}_3)_4$, Toluene/ H_2O , 90°C , 24h, 70% (c) **16**(PF_6)₂, EtOH/ CH_3CN , reflux, 18 h, 40%.

II.4.2. ^1H -NMR Characterization

The ^1H -NMR spectra of $\mathbf{21}(\text{Cl})_8$ recorded in deuterated water is shown in Figure 71. The accurate attribution of the aromatic signals was achieved from careful analyses of the ^1H spectrum and of the associated ^1H - ^1H 2D cosy map. In the aromatic range, the four most deshielded doublets (8H, $J = 6.7$ Hz), observed between 8.5 and 9.5 ppm, are attributed to the bipyridinium units. The hydrogen atoms H_f and H_g (8H) located on the phenyl rings adjacent to the viologens appear as two doublets ($J = 7.2$ Hz) between 7.9 and 8.05 ppm. while the protons of the phenyl ring corresponding to the TPE unit (H_h , H_i) resonate between 7.5 and 7.7 ppm as two doublets ($J = 8.1$ Hz). Finally, the methyl group attributed to H_a (12H) is observed as a singlet at 4.5 ppm.

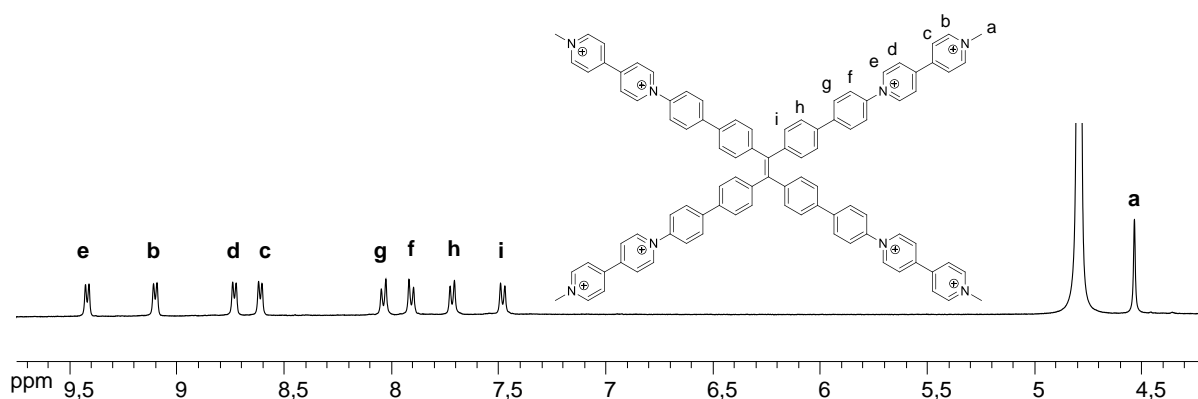


Figure 71: ^1H NMR spectra of $\mathbf{21}(\text{Cl})_8$ (D_2O , 400MHz) .

II.4.2.1. Threading of $\mathbf{21}^{8+}$ through $\text{CB}[7]$

As can be seen in Figure 72, the gradual addition of $\text{CB}[7]$ led to the disappearance of the signals corresponding to $\mathbf{21}(\text{Cl})_8$ at the expense of new signals attributed to the formation of different pseudo-rotaxane derivatives. The host-guest equilibria are kinetically slow at the NMR time scale and four molar equivalents of $\text{CB}[7]$ were needed to complete the titration experiment. This result indicates that the maximum number of $\text{CB}[n]$ hosts ($n=7$) that can be threaded on the TPE platform is four, which is in agreement with the complexation of one viologen *per* CB to yield the pseudo rotaxane $[\mathbf{21}^{8+} \subset (\text{CB}[7])_4]$.

The largest shift is observed for signals attributed to the viologen units (H_c , H_d), with upfield shifts reaching 1.3 ppm by the end of the titration. Here again, this large amplitude stands in contrast with the limited shift of about 0.1-0.3 ppm monitored the inclusion for the signals of

the other protons located on the viologens (H_b , H_c). These shifts thus reveal that the CB[7] rings lie in between both pyridinium rings. Inclusion of the viologen units within the cavity of CB[7] has also a significant impact on the chemical shift of the signals attributed to the CB host. In the absence of guest, CB[7] displays one singlet at 5.53 ppm attributed to H_k and two doublets at 4.23 and 5.80 ppm, attributed to the hydrogens of the methylenic bridge pointing outside (H_o) or inside (H_i) the cavity of CB[7], respectively.¹⁰⁵ As can be seen in the early stage of the titration (Figure 72), threading of a non-symmetrical viologen-based axle through a fully symmetric ring-shaped cavitand CB[7] results in the splitting of the signal attributed to H_i , which end-up being observed as two doublets centered at 5.71 ppm in the spectrum of the 4:1 inclusion complex $[21^{8+} \subset (CB[7])_4]$.

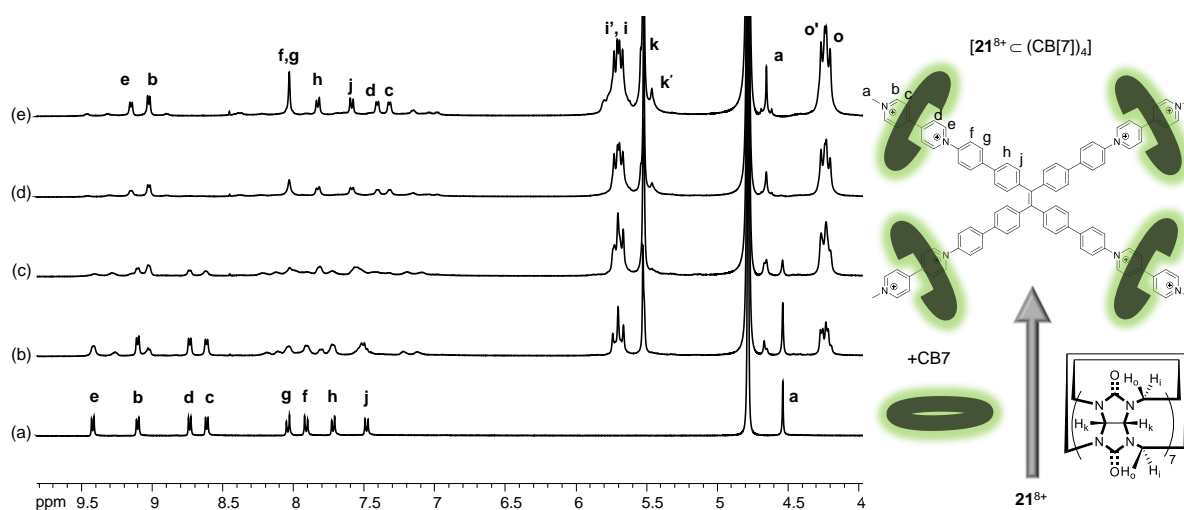


Figure 72 : ^1H -NMR spectra (400 MHz, D_2O , $5 \times 10^{-4} \text{ mol.l}^{-1}$) of $21(\text{Cl})_8$ recorded in the presence of (a) 0, (b) 1, (c) 2, (d) 3 and (e) 4 molar equivalents of CB[7].

II.4.2.2. Threading of 21^{8+} through CB[8]

A similar investigation has then been carried out with the less soluble CB[8] host.^{82, 106-107} The stoichiometry and structure of the assembly was similarly assessed from the titration data depicted in Figure 73. As observed with CB[7], the largest chemical shifts involve the protons H_c and H_d and the titration reaches completion after addition of 4 molar equivalents of CB[8]. These results thus support the conclusion that four CB[8] rings can be threaded onto 21^{8+} and that the macrocyclic guest lies in between both pyridinium rings

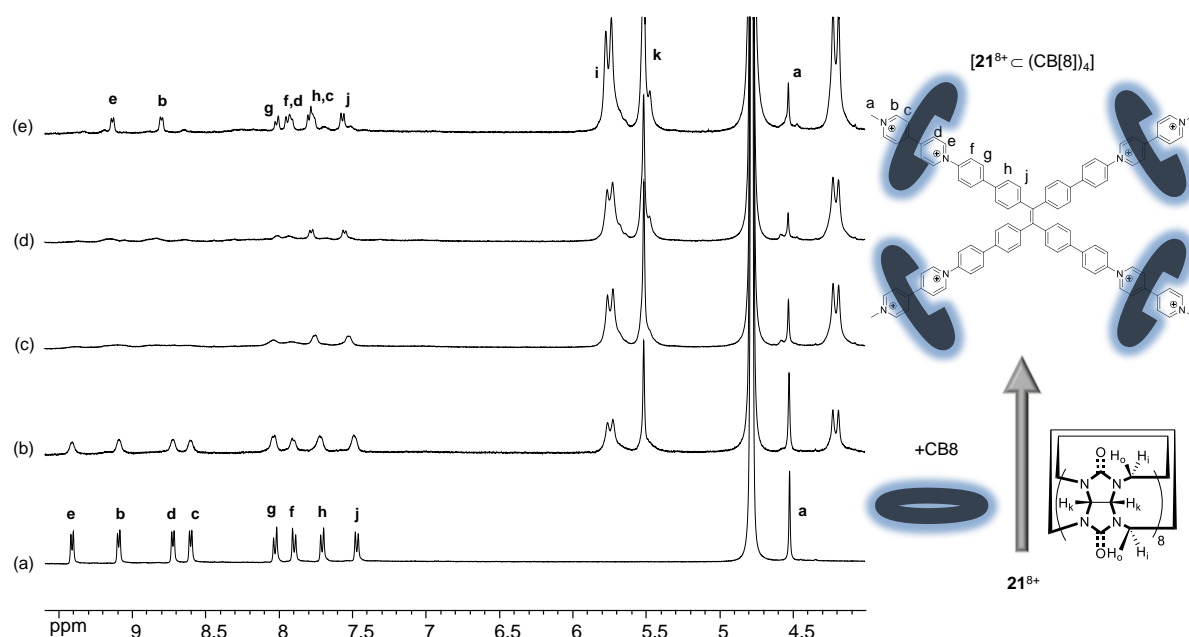


Figure 73 : $^1\text{H-NMR}$ spectra (400 MHz, D_2O , $1 \times 10^{-4} \text{ mol.l}^{-1}$) of $\mathbf{21}(\text{Cl})_8$ recorded in the presence of (a) 0, (b) 1, (c) 2, (d) 3, (e) 4 molar equivalents of CB[8].

II.4.3. Electrochemistry and Spectro-Electrochemistry in Organic Medium

The electrochemical signature of $\mathbf{21}(\text{PF}_6)_8$ has first been investigated in DMF using tetra-*n*-butylammonium perchlorate (TBAP) as an electrolyte.

The CV curve displays two consecutive reductions (noted E^{1c} and E^{2c}) in the accessible potential window (Table 5 and Figure 74). The first reduction wave leading to the formation of the tetra(radical-cation) species $\mathbf{21}^{4(+\bullet)}$, is observed at $(E_{1/2})^{1c} = -0.776 \text{ mV}$ ($\Delta E_p^1 = 44 \text{ mV}$ at $\nu = 0.1 \text{ V.s}^{-1}$), while the second ill-defined reduction wave corresponding to the formation of the quinonic species $\mathbf{21}^0$ appears at $E_{pc}^2 = -1.047 \text{ V}$. The unusual shape of the second reduction wave is attributed to the adsorption of the neutral reduction product onto the electrode surface, a process which is revealed by the intense desorption peak observed on the reverse scan at $E_{pa} = -0.936 \text{ V}$. It should be noted that the unexpectedly low ΔE_p value measured on the first reduction wave is a first indication suggesting the existence of intermolecular π -dimerization processes involving the tetra cationic reduced species $\mathbf{21}^{4(+\bullet)}$, the intramolecular association between the viologen cations radicals being here precluded for obvious steric reasons (see minimized structure obtained with Avogadro[®] in Figure 70)

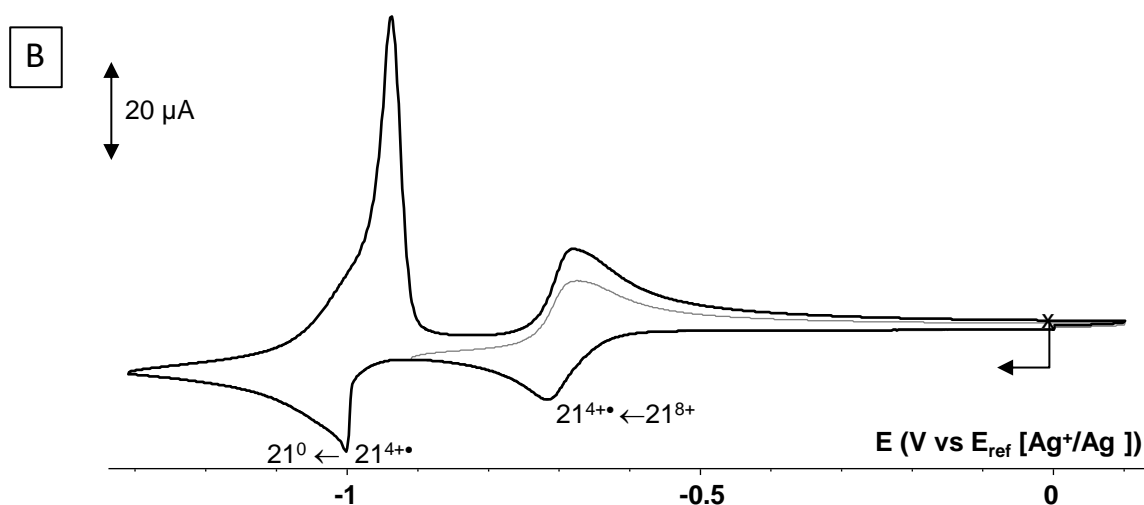
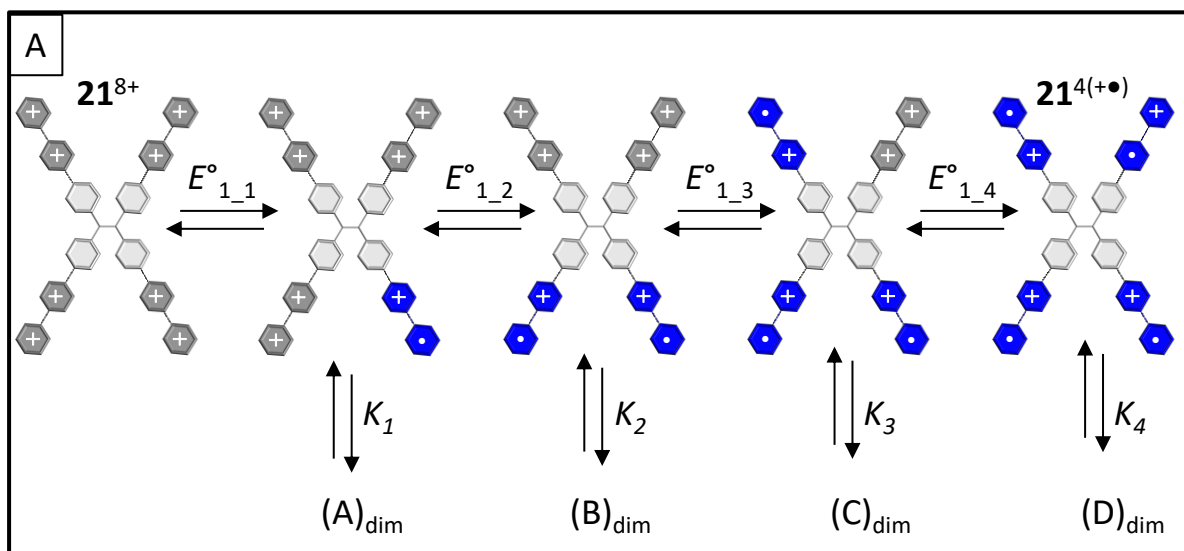


Figure 74: CV curves of $21\text{Zn}(\text{PF}_6)_4$ (1×10^{-3} M) recorded in DMF (TBAP 0.1M) at a carbon working electrode ($\varnothing = 3$ mm, E vs Ag^+/Ag (10^{-2} M), $\nu = 0.1$ V.s $^{-1}$).

The ability of 21^{8+} to form π -dimers in solution upon reduction has been further demonstrated by spectro-electrochemical analyses (Figure 75B); $E_{app} = -0.91$ V, 1 electron *per* viologen subunit, $C = 0.16$ mM), through the growth of diagnostic absorption bands centered at 425 nm (70625 M $^{-1}$.cm $^{-1}$), 577 nm (39375 M $^{-1}$.cm $^{-1}$) and 945 nm (5500 M $^{-1}$.cm $^{-1}$). This signature contrasts with that recorded in the same experimental conditions, at the same or higher concentration in viologen units, with the reference compounds PhVMe $^{2+}$ or MeVMe $^{2+}$ leading to the observation of absorption bands centred at 415 nm (19000 M $^{-1}$.cm $^{-1}$), 612 nm (8450 M $^{-1}$.cm $^{-1}$), and 713 nm (3550 M $^{-1}$.cm $^{-1}$) attributed to the non-associated viologen based cation radical (Figure 75D and Figure 75E).

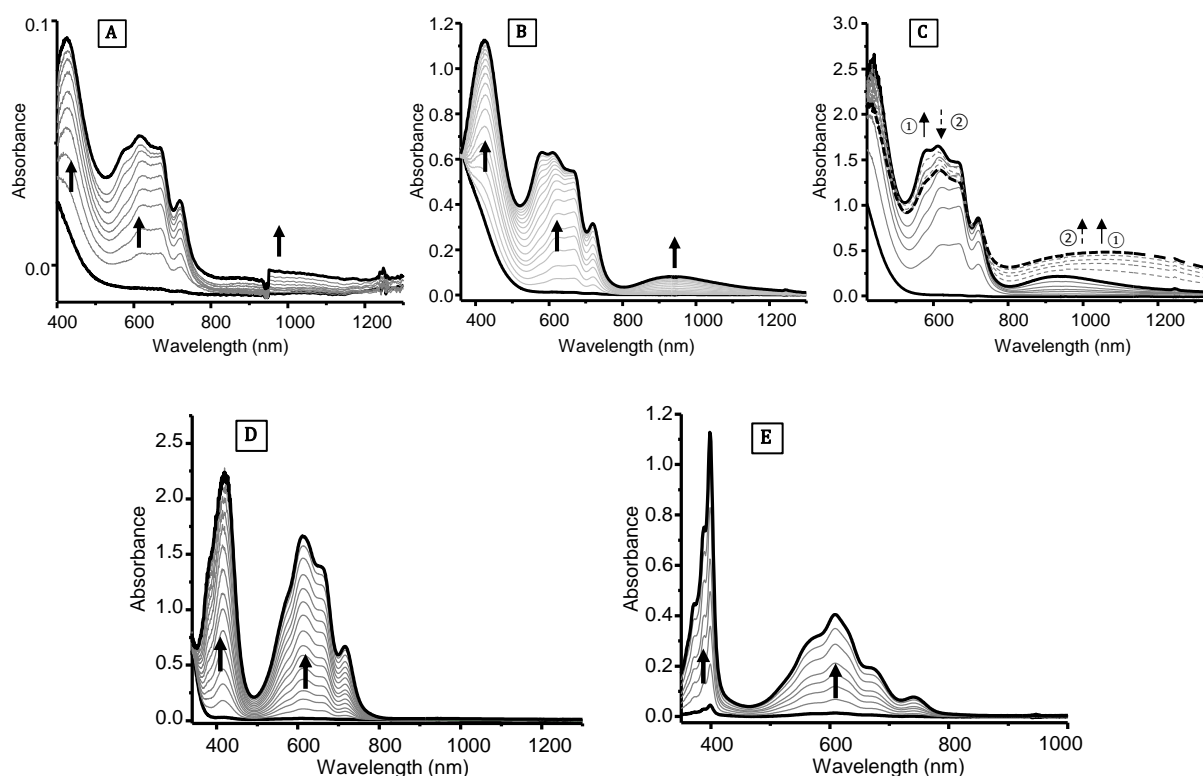


Figure 75: Superposition of UV-vis absorption spectra recorded during the exhaustive one electron reduction (one electron per viologen) of (A) $\mathbf{21}(\text{PF}_6)_8$ (0.01 mM, $E_{\text{app}} = -0.91$ V), (B) $\mathbf{21}(\text{PF}_6)_8$ (0.16 mM, $E_{\text{app}} = -0.91$ V), (C) $\mathbf{21}(\text{PF}_6)_8$ (0.5 mM, 10 mL, $E_{\text{app}} = -0.91$ V), (D) $\text{PhVMe}(\text{PF}_6)_2$ (2 mM, 10 mL, $E_{\text{app}} = -0.91$ V) and (E) $\text{MeVMe}(\text{PF}_6)_2$ (0.5 mM, 10 mL, $E_{\text{app}} = -1$ V). [DMF + 0.1 M TBAP, $l = 1$ mm, $t \approx 30$ min, working electrode = Pt].

The differences between the absorption spectra shown in Figure 75 B, C and D confirm that the one-electron reduction per viologen of $\mathbf{21}^{8+}$ leads to the formation of intermolecular π -dimers in solution and that no such process is observed for simple viologen derivatives in the investigated concentration range (up to 2mM).

Concentration-dependent spectroelectrochemical studies have also been undertaken to confirm the intermolecular nature of the association involving the reduced forms (1 to 4 electron/viologen) of $\mathbf{21}^{8+}$. As can be seen in Figure 75, the exhaustive reduction of $\mathbf{21}^{8+}$ at $5 \times 10^{-4} \text{ mol.l}^{-1}$ to $1 \times 10^{-5} \text{ mol.l}^{-1}$ led to the development of similar absorption bands centred at 577 nm and 613 nm coming along with a broad signal centered at 945 nm (solid line in Figure 75C). We also found that the more concentrated solution of $\mathbf{21}^{4(+\bullet)}$ ($5 \times 10^{-4} \text{ mol.l}^{-1}$) evolves toward the end of electrolysis with a progressive drop in the intensity of the initial signals observed between 540 nm and 700 nm, while the band in the NIR region gained both in intensity and broadness (dashed lines in Figure 75C). This complex behavior reveals the existence of multiple equilibria involving dimerized and non-dimerized viologen radicals consistent with the formation of aggregates in solution. The most important conclusion is that $\mathbf{21}^{4(+\bullet)}$ can form intermolecular π -dimers in the absence of cucurbiturils.

II.4.4. Electrochemistry and Spectro-Electrochemistry in Aqueous Medium

The electrochemistry of the titled compound **21**⁸⁺ has been investigated in a phosphate buffer (pH 7, 0.1 M) at a vitreous carbon electrode. The CV curve displays the expected consecutive viologen-based reduction waves centered at $E^{1c} = -0,413\text{V}$ and $E^{2c} = -0,698\text{ V}$ (Table 5).

	Solvent	$E^{2c}(n, \Delta E_p)$ v^{2+}/v^0	$E^{1c}(n, \Delta E_p)$ v^{2+}/v^{2+}
MeVMe(PF ₆) ₂	DMF	-1.163 ^b (1,62)	-0.774 ^b (1,60)
PhVMe(PF ₆) ₂	DMF	-1.101 ^b (1,58)	-0.772 ^b (1,58)
21 (PF ₆) ₈	DMF	-1.047 ^{c,d} (4,na)	-0.776 ^b (4,44)
MeVMe(Cl) ₂	H ₂ O	-0.99 ^b (1,77)	-0,654(1,60)
21 (Cl) ₈	H ₂ O	-0.698 ^b (4,201)	-0.413 ^d (4,145)

Table 5: Measured by CV, 1-5·10⁻⁴ M in DMF/TBAP (0.1 M, $E(\text{V})$ vs. Fc/Fc⁺), or in an aqueous phosphate buffer (0.1M, pH = 7, $E(\text{V})$ vs. AgCl/Ag (KCl sat)) at a vitreous carbon working electrode $\varnothing = 3$ mm, 298 K, $v = 0.1\text{ V}\cdot\text{s}^{-1}$. na : Not available / ^b : Half wave potential / ^c : Peak potential / ^d : Adsorption phenomena

The plots depicted in Figure 76 reveal that the first reduction wave remains limited by diffusion but the unusual shape of the re-oxidation wave (see the black curve shown in Figure 77) and the large ΔE_p value (~130 mV) suggest the existence of coupled processes which have not yet been identified (adsorption, aggregation, communication...).

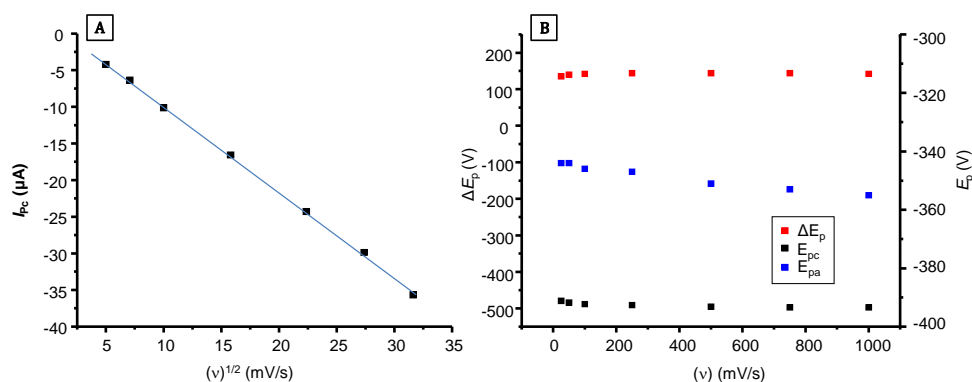


Figure 76: Variations of the (A) peak current value, of the (B) anodic (E_{pa}) and cathodic (E_{pc}) peak potential values and of the peak to peak potential shift (ΔE_p) as a function of scan rate (v) (measured for **21**(Cl)₈ by CV in a phosphate buffer (0.1 M, pH=7) at a glassy carbon working electrode ($\varnothing = 3\text{mm}$, E in volts vs. AgCl /Ag).

The interaction of **21**⁸⁺ and of its reduced forms with CB[8] has nevertheless been investigated using electrochemical methods. As can be seen in Figure 77, the progressive addition of CB[8], up to 4 molar equivalents, resulted in a significant loss in the peak-current values measured on the forward and backward scans. The peak potential values measured on the first and second reduction waves did not change significantly upon addition of CBs, a result stands

in a sharp contrast with what has been observed before with $11\text{Zn}(\text{Cl})_8$ and $17\text{Zn}(\text{Cl})_4$. One preliminary conclusion that can be drawn from the negligible shift in the E^{1c} value measured in the presence of CB[8] is that 21^{8+} and $21^{4(++)}$ have similar affinities toward CB[8] and that CB[8] does not promote the π -dimerization of $21^{4(++)}$.

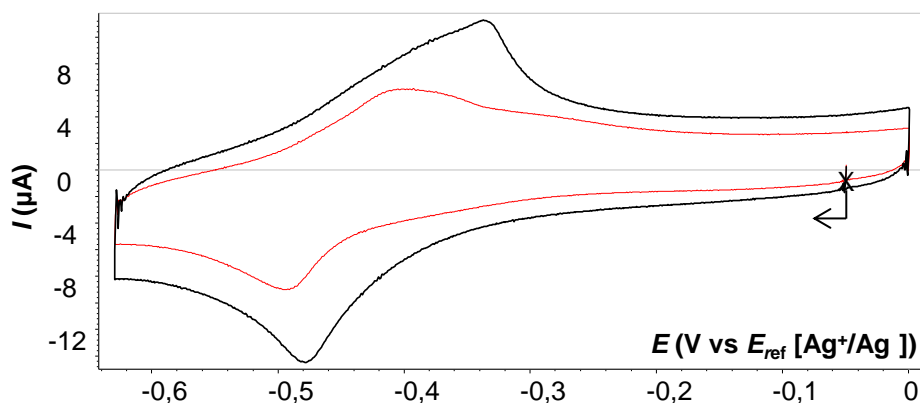


Figure 77: CV curves recorded for $21(\text{Cl})_8$ (1×10^{-4} M) in aqueous phosphate buffer (pH= 7, 0.1 M) (VC $\varnothing = 3$ mm, $v = 0.1$ V.s $^{-1}$, E vs. Ag/AgCl) in the presence of n molar equivalents of CB[8] [$n=0$ (black), $n=4$ (red)].

A control experiment has been carried out with CB[7], that is known to prohibit the formation of π -dimers.^{84, 135} The CV curves recorded before and after addition of four molar equivalents of CB[7] to a solution of 21^{8+} in water are displayed in Figure 78. The presence of CB[7] is found to induce a significant shift ($\Delta E = 84$ mV) of the first viologen-centered reduction wave towards more negative potential values coming along with a significant drop of the current levels. In agreement with literature, such behavior is here consistent with the idea that CB[7] has a weaker affinity for the viologen cation radicals in $21^{4(+\bullet)}$ than for the dicationic viologens in 21^{8+} .⁸⁴

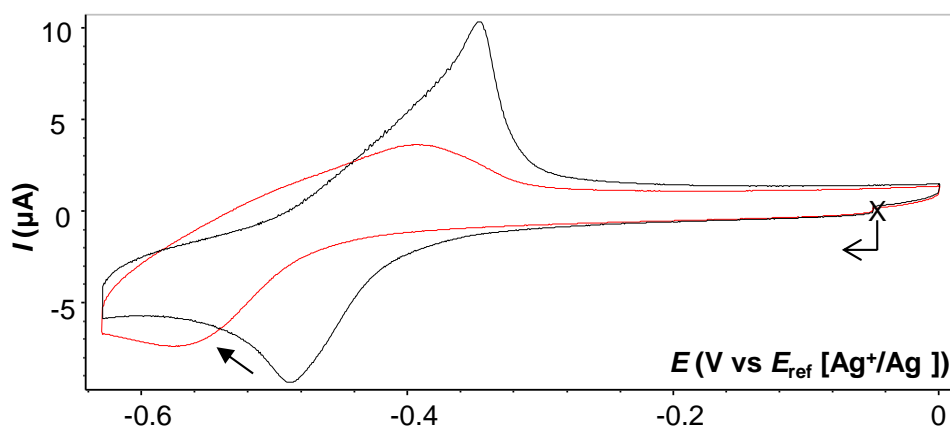


Figure 78 :CV curves recorded for $21(\text{Cl})_8$ (5×10^{-4} M) in aqueous phosphate buffer (pH= 7, 0.1 M) (VC $\varnothing = 3$ mm, $v = 0.1$ V.s $^{-1}$, E vs. AgCl/Ag) in the presence of n molar equivalents of CB[7] [$n=0$ (black), $n=4$ (red)].

Spectroscopic measurements have been carried out in water to determine whether the 4-electron-reduced species $\mathbf{21}^{4(+)}$ can dimerize in aqueous media. The one-electron reduction of the viologen units in $\mathbf{21}^{8+}$ was thus carried out in phosphate buffer (pH =7) using sodium dithionite $\text{Na}_2\text{S}_2\text{O}_4$ as the reductant.¹¹⁴ The UV-Vis absorption spectra recorded over time after addition of $\text{Na}_2\text{S}_2\text{O}_4$ in excess in the absence or presence of CB[8] are shown in Figure 79A and B.

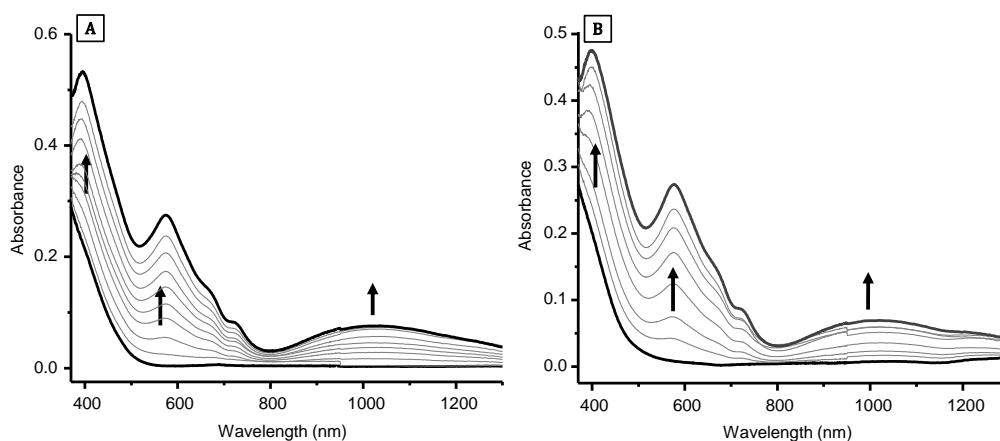


Figure 79: UV-vis spectra of $\mathbf{21}(\text{Cl})_8$ (1×10^{-4} M) in H_2O recorded over time after addition of $\text{Na}_2\text{S}_2\text{O}_4$ in excess in the presence of (A) 0 or (B) 4 molar equivalents of CB[8].

What strikes at first sight is the great similarities between these data, both featuring the development of two intense absorption bands at $\lambda_{\text{max}} = 394$ and 572 nm coming along with a less intense broad diagnostic signal centered at 1025 nm attributed to the formation of viologen-based π -dimers. The E_nC_n coupled process involved in solution was also found to be fully reversible, as revealed by the fact that the signature of the initial inclusion complex can be recovered upon bubbling compressed air through the solution. These data suggest that the reduction of $\mathbf{21}^{8+}$ leads to the same species in the absence or the presence of CB[8] and thus the latter is not needed to achieve the intermolecular π -dimerization of $\mathbf{21}^{4(+)}$.

Similar experiments have then be carried out in the presence of CB[7] to prohibit the CB-assisted dimerization and to provide support for the proposal that $\mathbf{21}^{4(+)}$ could form supramolecular dimers in solution in the absence of CBs.

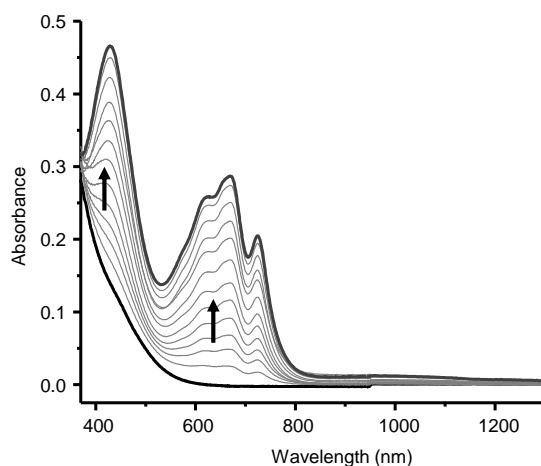


Figure 80: UV-vis spectra of $\mathbf{21}(\text{Cl})_8$ (1×10^{-4} M) in H_2O recorded over time after addition of $\text{Na}_2\text{S}_2\text{O}_4$ in excess in the presence of 4 molar equivalents of CB[7].

The chemical reduction of $\mathbf{21}^{8+}$ with $\text{Na}_2\text{S}_2\text{O}_4$ in the presence of 4 molar equivalents of CB[7] led to the emergence of intense bands readily attributed to non-associated viologen based cation radical (Figure 80), which support the conclusion that the formation of intermolecular π -dimers is prohibited by the inclusion of CB[7] yielding $[\mathbf{21}^{8+} \subset (\text{CB}[7])_4]$. In these condition, the chemical reduction indeed leads to the accumulation of frees radicals revealed by the bands growing in the visible range and by absence of diagnostic absorption bands in the near IR region.

II.4.5. Conclusion

Detailed NMR analysis revealed that four CB[7] and CB[8] rings can be threaded on the tetra-viologen derivative $\mathbf{21}^{8+}$. The presence of CB[7] prohibits the intermolecular dimerization of $\mathbf{21}^{4(+)}$, while the presence of CB[8] has not significant impact on the dimerization ability of $\mathbf{21}^{4(+)}$. Reduction of $\mathbf{21}^{8+}$ into $\mathbf{21}^{4(+)}$ lead to the formation of same intermolecular π -dimers as in the presence of cucurbiturils in aqueous medium.

Chapter III: Redox Responsive Clips and Tweezers

III.1. Introduction

Built on the shoulders of classical synthetic organic chemistry and inspired from nature, supramolecular chemistry has paved its own way toward understanding and mimicking biological processes.¹⁴⁸ Over the years, the supramolecular chemistry tool box has proved extremely useful in many fields from material science¹⁴⁹ to catalysis.¹⁵⁰ Recent efforts have been devoted to the construction of supramolecular assemblies or discrete molecular hosts displaying switchable properties. Molecular tweezers and clips have proved to be particularly relevant to the development of molecular hosts whose substrate recognition ability can be tuned by external stimuli.¹⁵¹

The term tweezer was initially introduced by Whitlock.¹⁵² These molecules are characterized by an open cavity (substrate binding site) bordered by two interaction sites that are linked to the spacer (Figure 81).¹⁵³

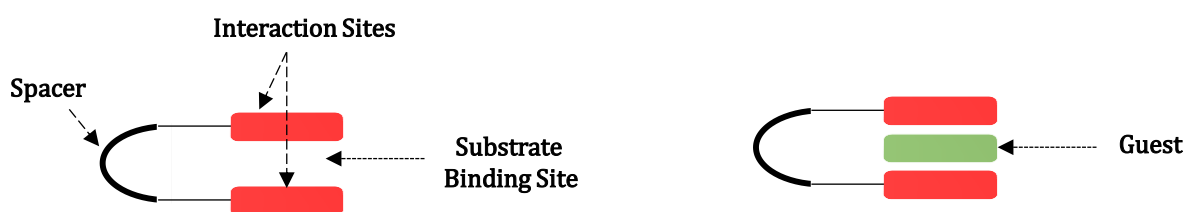


Figure 81: Schematic representation of the key components of molecular tweezers and the binding of a guest by a tweezer in its folded conformation.

The mode of action of tweezers can be understood from a direct analogy with the conventional mechanical ones, where the hold-and-release mechanism involves an external force. In molecular tweezers, the two interaction sites (sometimes called “tip”) pinch a guest molecule through various non-covalent interactions including metal coordination, hydrogen bonding, hydrophobic forces, van der Waals forces, electrostatic effects and/or π - π interactions (Figure 81). In most cases, binding involves attractive π -interactions between two π -conjugated organic moieties adopting a sandwich-like arrangement around a guest molecule. π - π interactions are however often too weak to ensure an effective binding. Donor/acceptor-type interactions supplemented by hydrogen bonds and hydrophobic effects are thus frequently employed to enhance the interactions between the host and the guest. Incorporating additional functional groups on the backbone of tweezers has also been shown to improve the selectivity/efficiency of binding. It should be mentioned that these improvements through multiple binding sites go beyond a simple sum of all the interactions

involved in the host-guest complex. These issues are referred to as “complex additivity in binding energies”.¹⁵⁴

The recognition process is also influenced by the structure of the spacer (length, rigidity, bulkiness...). The latter can be either flexible, rigid or have a switchable shape (Figure 82). Its importance has been for instance brought to light by the work of Colquhoun and co-workers showing that the ability of tweezer molecules to detect long-range sequence information in chain-folding aromatic copolyimides depends to a large extent on the structure of the spacer.¹⁵⁵

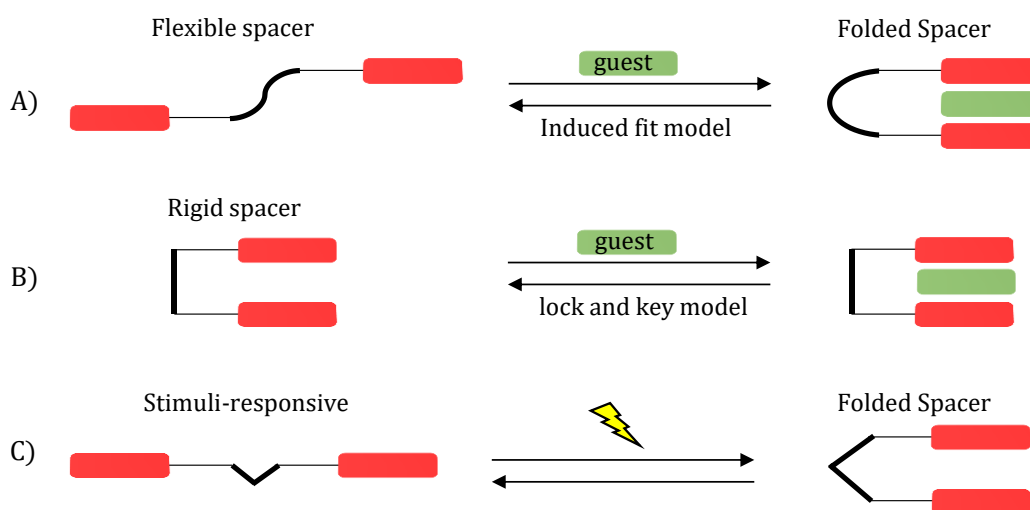


Figure 82 : Schematic representation of A). flexible tweezers, B). Clip (incorporating rigid spacer) and C). stimuli-responsive tweezers.¹⁵³

Tweezers and clips are considered as two different systems that can be distinguished by specific features. These features were not clear until 2004, when F.G Klärner developed a series of di- to tetramethylene-bridged compounds, these compounds were defined as molecular clips and tweezers, respectively (Figure 83).¹⁵⁶

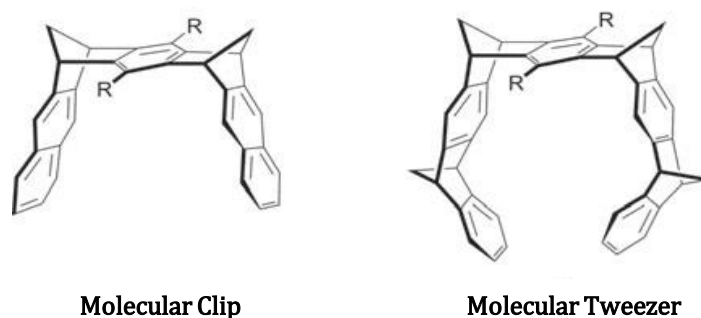


Figure 83: Molecular clip to molecular tweezer with di-, tri- and tetramethylene-bridged polyaromatic systems.¹⁵⁶

Clips exhibit U-shape locked conformations defining a cavity wherein guest molecules can be complexed. All the molecules incorporating rigid spacer with no or very little, structural flexibility are thus named clips. Tweezers incorporate flexible, eventually stimuli-responsive, linkers and can thus adopt different conformations (folded/unfolded) which can eventually be controlled by an external stimulus.

The main features and applications of molecular clips and tweezers will be discussed in the following sections on the basis of relevant examples.

III.1.1. Flexible Tweezer

In such molecules, flexibility is provided by the covalent spacer linking both “interaction sites”. The latter are not necessarily arranged in a folded (also called *syn*) conformation at all times and the folding process (anti \rightarrow syn) can be triggered by an external stimulus (light, electron...) or by a binding event. In terms of energy, the stabilization energy associated to the folding process should compensate the entropy loss.¹⁵³

One of the first tweezers reported in literature is a system made up of two caffeine units interconnected by a diacetylene spacer (**1**) (Figure 84A).¹⁵⁷ The flexibility is provided by the free rotation of both caffeine subunits around the diacetylene axle and the presence of guests like the naphthoate anion ($K_a = 10^4 \text{ M}^{-1}$, in phosphate buffer pH=7) forces the interaction sites to align in a parallel orientation. Such binding process illustrates the “induced-fit” model, where the host adopts the most appropriate conformation for binding.

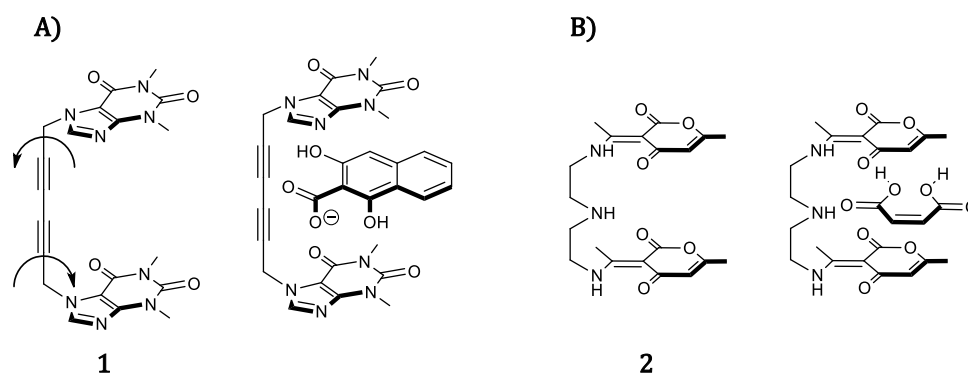


Figure 84: Early examples of molecular tweezers incorporating A) diacetylene¹⁵⁷ or B) polyamine¹⁵⁸ linker.

The selectivity and guest-binding affinity can be improved by functionalisation of the flexible spacers with suitable functional moieties. It is the case of molecule **2** featuring a polyamine

spacer capable of forming hydrogen bonds with various dicarboxylic acids (phthalic or maleic) (Figure 84B).¹⁵⁸

Many systems reported in literature exhibit two electron rich π -conjugated units connected through a flexible isophthaloyl linker. Williams and coll.¹⁵⁹ have for instance reported a series of tweezers incorporating an isophthalic linker and two pyrene-based recognition sites (Figure 85).

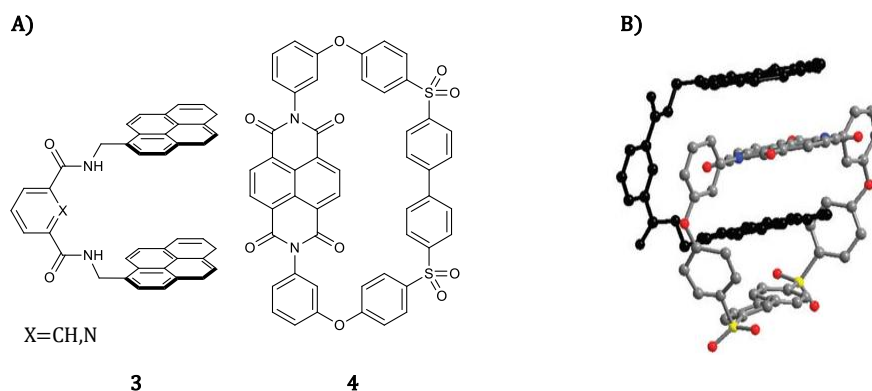


Figure 85: A) Pyrene-based tweezer **3** developed by Williams and Coll and the targeted guest molecule **4** B) X-ray crystal structure of the 1:1 complex formed between tweezer **3** ($X = CH$) and the macrocyclic guest **4**.¹⁵⁹

The drastic color change, from yellow to red, observed in solution upon addition of the electron-poor naphthalenediimide-based macrocycle **4** was attributed to the formation of the host guest complex **3**⊂**4** stabilized by a charge transfer from the electron-rich pyrene units to the electron-deficient guest ($K_a = 24300 \text{ M}^{-1}$ in CHCl_3).¹⁵⁹

Tetrathiafulvalene (TTF) derivatives have also been widely used as electron-rich moieties in the construction of flexible tweezers capable of binding electron deficient π -conjugated guests.

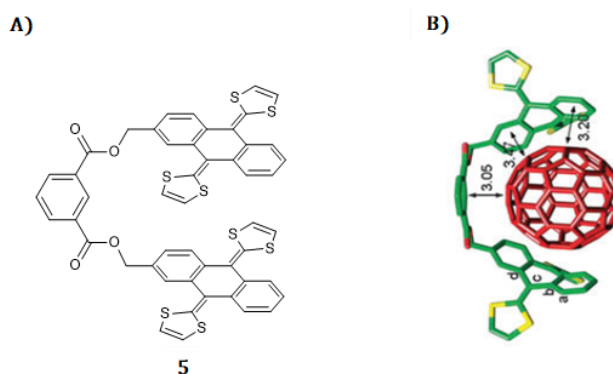


Figure 86: A) Molecular tweezer incorporating tetrathiafulvalene-like interaction sites. B) calculated host-guest complex formed between **5** and C_{60} (BH&H/6-31G** level).¹⁶⁰

The tweezer shown in Figure 86, exhibits an isophthalic spacer and two TTF-like units. The later was found to be large/flexible enough to accommodate a C_{60} guest pinched between both TTF units ($K_a \approx 3000 \text{ M}^{-1}$ in chlorobenzene).¹⁶⁰

Following these discoveries, the authors have devised a second generation of tweezers incorporating both the TTF donors and the C_{60} acceptor. Detailed investigations carried out in organic media have revealed the ability of (**6**) to self-assemble in a head to tail fashion through donor-acceptor interactions into a linear supramolecular architecture (Figure 87).¹⁶¹

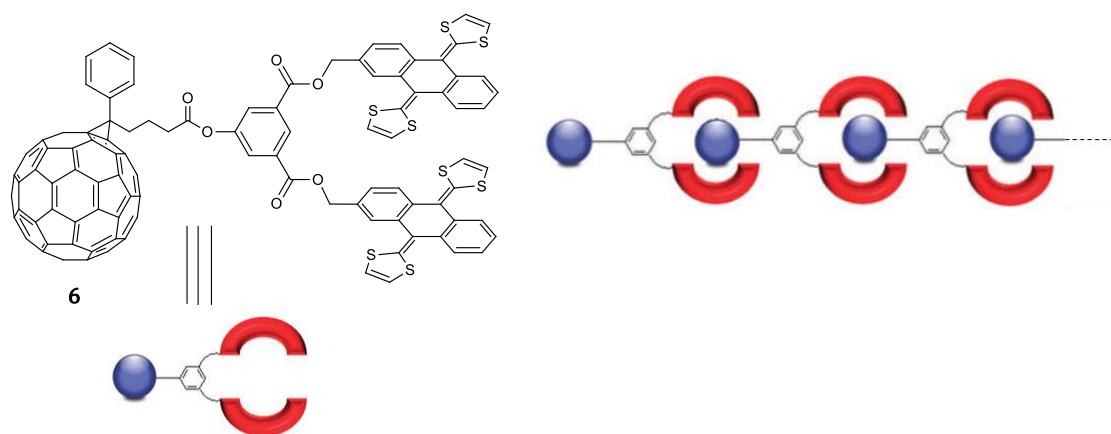


Figure 87: Chemical structure of tweezer **6** and schematic representation of the associated supramolecular donor-acceptor polymer.¹⁶¹

III.1.2. Clips

Rigid spacers have mainly been considered as a way to improve the recognition ability of the tweezers through fixing the two interaction sites in more suitable “U-shaped” conformations. The rigidity that is obtained at the expense of flexibility leads to a transition from an “induced-fit” model to a “lock and key” model, where the substrate acts as a 'key' and the active site as the 'lock', as introduced by Fischer in the late 19th.¹⁶² This locked structure of the host minimizes the entropic cost associated to the binding event, and hence improves both the binding strength and the selectivity.

One example of conformationally restricted host considered as a molecular clip is shown in Figure 88A.¹⁶³ It is made of a very rigid polyaryl spacer allowing to freeze both acridines in a cofacial arrangement. The distance between the interaction sites is 7.24 \AA , which is slightly larger than the 6.8 \AA that is required for sandwiching an aromatic guest through van der Waals interactions (π - π stacking). The association constant has been shown to increase as the electron density of the acridine groups increases. For instance, the association constants

recorded between host **7** and the guest TNF (2,4,7-Trinitrofluoren-9-one) increases from 150 M^{-1} to 358 M^{-1} by changing the R substituent from H to *tert*-butyl group.¹⁶⁴⁻¹⁶⁵

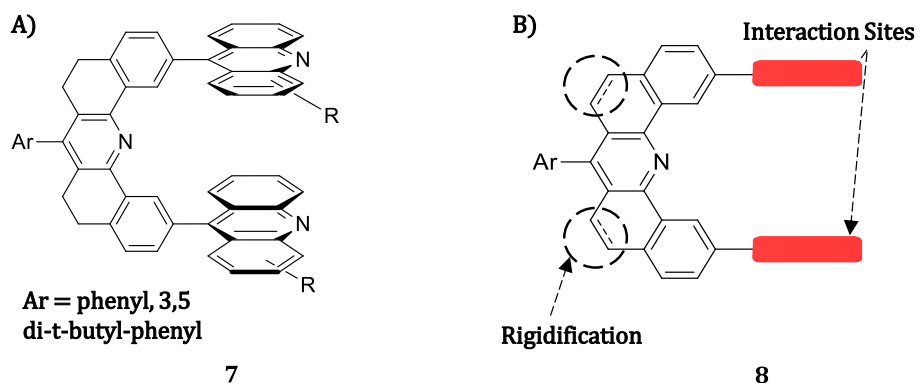


Figure 88: A) Chemical structure of Zimmerman's fused aromatic clip (**7**)¹⁶³; B) Rigidification of Zimmerman's clip by oxidation of the aromatic bridge.¹⁶⁶

Different planar coordination complexes have also been introduced on such spacer as interaction sites. It is the case for instance of the dicationic clip **9** featuring two square planar terpyridyl-Pd(II) acting as electron-deficient binding moieties (Figure 89). This clip has been found to form a stable complex in acetonitrile with 9-methylanthracene ($K_a = 650 \text{ M}^{-1}$, 1:1 complex in CD_3CN).¹⁶⁷

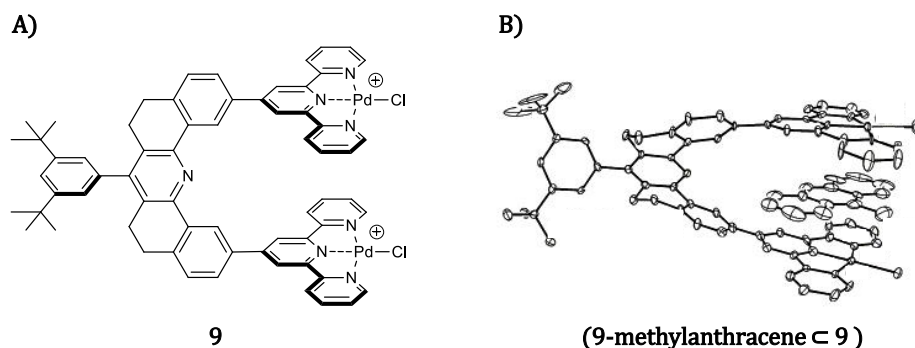


Figure 89: A) Chemical structure of clip **9** incorporating two [chloro(2,2',2''-terpyridine)palladium(II)]⁺ units; B) complex formed between **9** and 9-methylanthracene.¹⁶⁷

Such fused spacer can be further rigidified by oxidation of the methylene bridges (Figure 89B). These modifications were found to promote a significant increase in the free binding energy estimated to 3.8 KJ.mol^{-1} per C-C bond.¹⁶⁸ Such fully rigid linker is a key component of the tweezer shown in Figure 90, featuring two metalloporphyrin rings as interaction sites. The later has been shown to form strong complexes with various electron rich ligands, such as DABCO ($K_a = 1.1 \times 10^8 \text{ M}^{-1}$), and with electron-deficient guests, such as the acridinium cation to form the host-guest complex (**10**) ($K_a = 1.6 \times 10^7 \text{ M}^{-1}$ in CHCl_3).¹⁶⁹

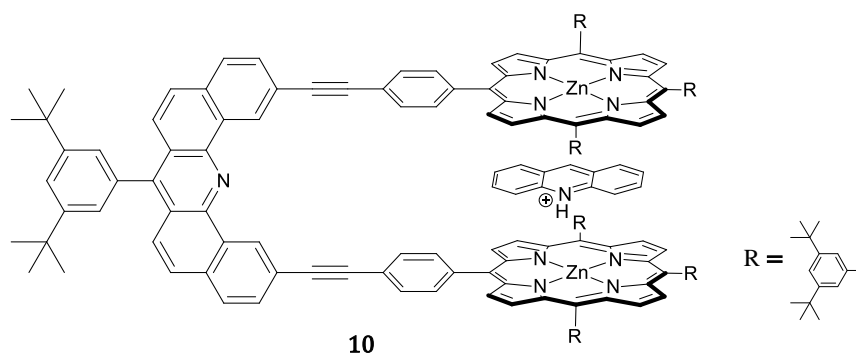


Figure 90: Chemical structure of the HG complex formed between the porphyrin based clip **10** and the acridinium cation.¹⁶⁹

In another example, the spacer has been functionalized with a carboxylic acid substituent oriented towards the inner cavity of the clip. Such modification was found to induce an increase of the distance between both interaction sites up to 8.2 Å and to enhance the binding affinity and selectivity toward various nucleotide-based guests ($K_a \approx 1.2 \times 10^5 \text{ M}^{-1}$ with adenine, Figure 91).¹⁶⁶ Computational studies have also revealed that the hydrogen bonding and π -stacking equally contribute to the stabilization of such guests in the cavity of **11**.

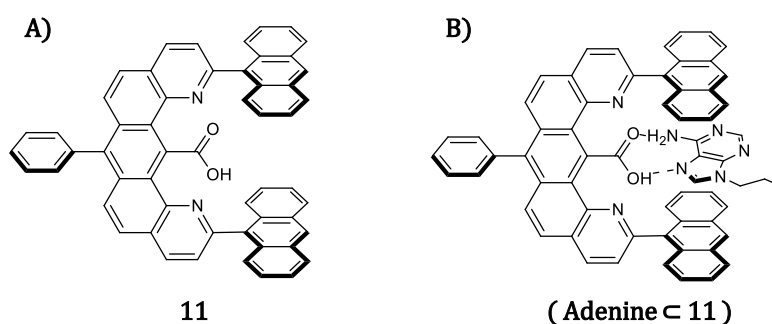


Figure 91: A) Chemical structure of clip **11** featuring a functionalized linker B) Chemical structure of the complex formed between **11** and 9-propyladenine.

Another type of highly rigid clip based on polyarenes has been developed in 2004 by the group of Klarner (Figure 92).¹⁷⁰

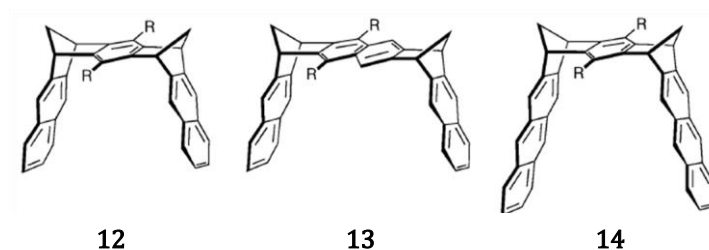


Figure 92: Chemical structures of rigid molecular clips involving a bicyclic connection.¹⁷⁰

The conformation of **12**, **13** and **14** is locked by the presence of a methylene bridge leading to the formation of a rigid bicyclic connection. These interesting compounds exhibit a convex

structure which proved suitable to achieve an efficient complexation of various aromatic guest stabilized in the cavity through π - π and CH- π interactions. The size of the cavity can moreover be tuned upon varying the number of benzene rings in the spacer (see for instance **12** and **13** in Figure 92).¹⁷⁰

III.1.3. Stimuli-Responsive Tweezers

Stimuli-responsive tweezers are able to undergo conformational changes in response to external stimuli such as pH, light or in the presence of a suitable chemical species. The prospect of controlling their binding/recognition properties with a given input signal opens up particularly exciting perspectives for the development of sensors, molecular machines and in material science.

III.1.3.1. Chemically Responsive Molecular Tweezers

Most chemically responsive molecular tweezers reported so far in literature involve a terpyridine linker. Terpyridine ligands exhibit very high binding affinity towards transition metals due to $d\pi^*$ - $p\pi^*$ back bonding of the metal to the pyridine rings and to chelate effects.¹⁷¹ The complexation can induce an isomerization of the ligand from a W shape to a U shape. This specific feature has been widely used in the development of switchable molecular tweezers capable of binding or releasing a given guest molecule (Figure 93).¹⁷²

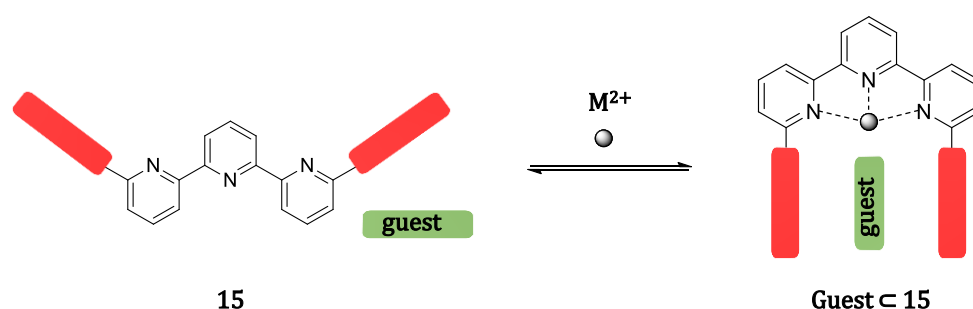


Figure 93 : Metal-induced folding of a terpyridine-based molecular tweezer.

The group of J. M. Lehn has reported the recognition of various aromatic derivatives (pyrene, anthracene, or naphthalene derivatives) by a series of molecular tweezers made up of a terpyridine-like pentadentate spacer. The U-shaped conformation of the spacer is imposed by the complexation of Zn^{2+} and Pb^{2+} . These seminal works bring to light the importance of the metal in determining the size of the cavity available for binding (Figure 94).¹⁷³

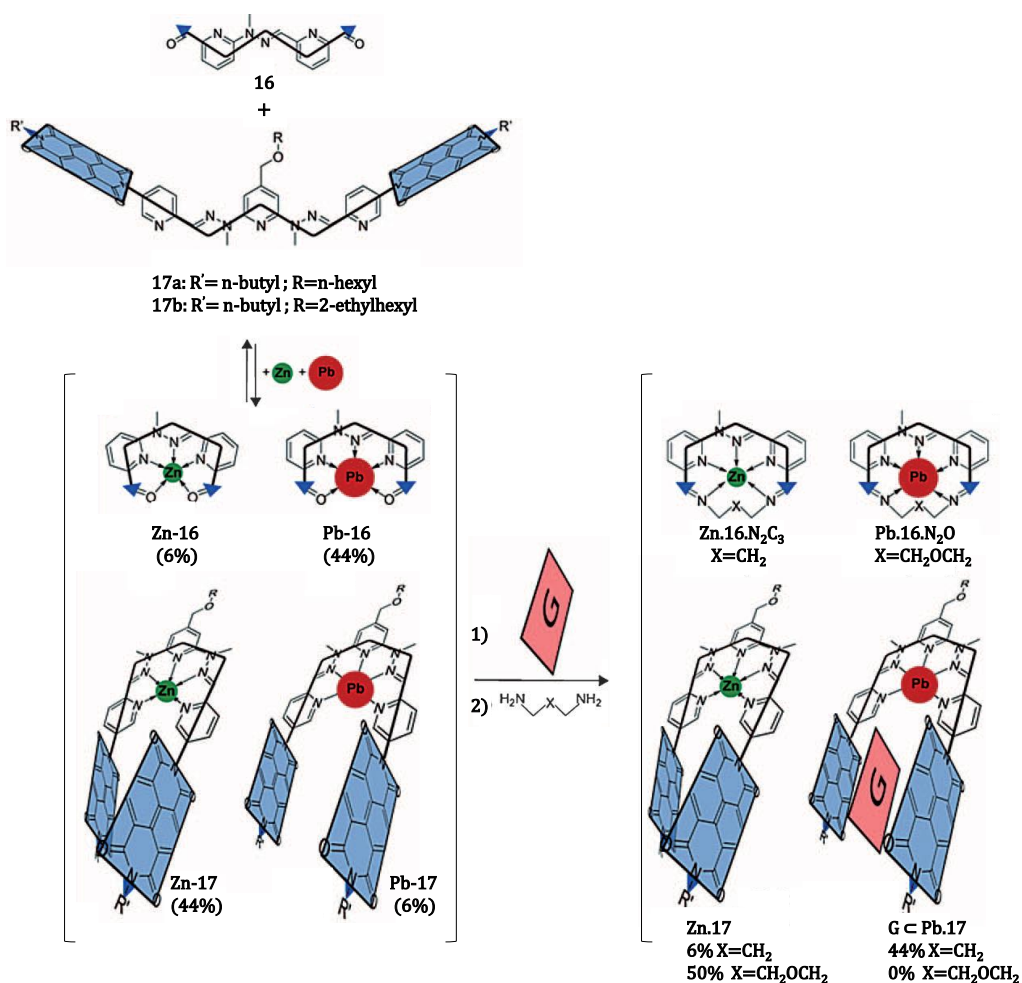


Figure 94: Representation of the processes occurring in a dynamic system of constituents, ligands **16** and **17** and their zinc(II) and lead(II) complexes, undergoing both shape changes and metal ion exchange and their evolution that is driven by double condensation of **16** with a diamine, towards the generation of the metal complex constituent that cannot (**Zn-17**) or can (**Pb-17**) form a supramolecular intercalation complex with a guest **G**.¹⁷³

The switchable terpyridine-based tweezer **18**, featuring pendant porphyrin arms, has been reported in 2006.¹⁷⁴ Here again the U-Shape is imposed by a complexation of the terpyridine linker (Figure 95). Converting the open “W”-shaped isomer into the closed “U”-shaped one has also been achieved upon binding of diamine guests such as DABCO and 1,2-ethylenediamine between both metalloporphyrin centers.

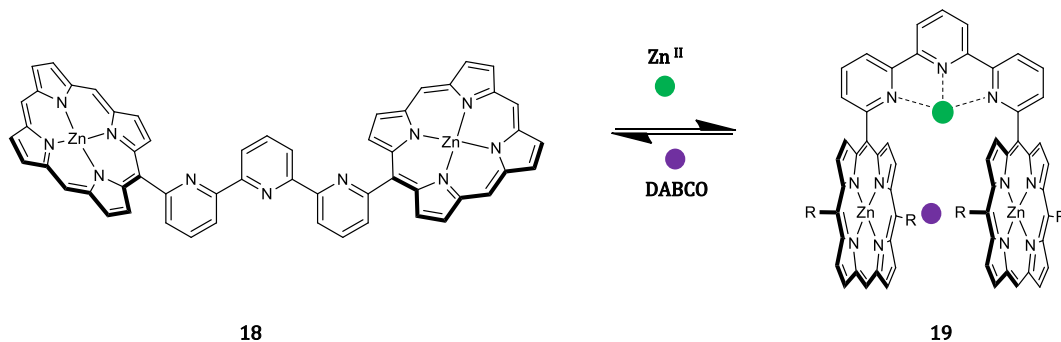


Figure 95 : Representation of the W-U isomerization triggered by complexation of a terpyridine linker.¹⁷⁴

Recently, the group of Vives have developed a series of terpyridine-based molecular tweezers incorporating peripheral salphen units. Here again, the addition of metal ions has been shown to trigger a W→U shape isomerization of the polypyridine spacer.¹⁷⁵⁻¹⁷⁶ The author also established that the nickel complex **20** behaves as a six level molecular switch responding to three orthogonal stimuli: complexation of the linker, oxidation of the salphen units and binding to pyrazine (Figure 96).

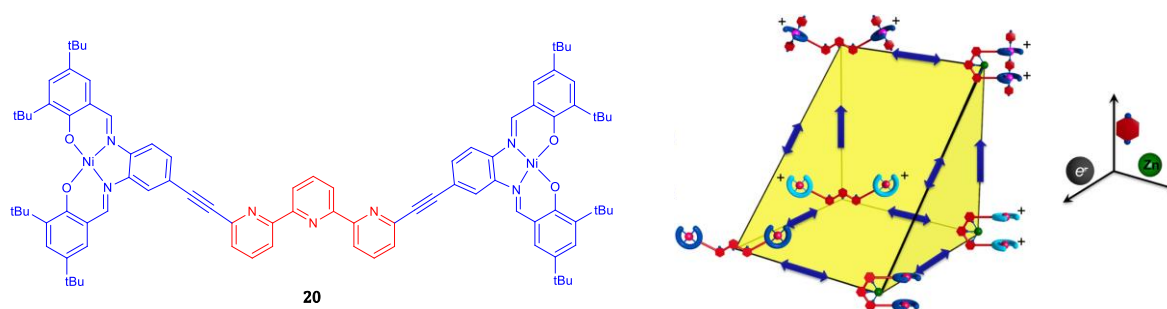


Figure 96: Representation of a six-level switching process involving 3 orthogonal stimuli (complexation of the linker, oxidation of the salphen units and binding to pyrazine).¹⁷⁵⁻¹⁷⁶

III.1.3.2. Light-Responsive Molecular Tweezers

Light has been widely used to trigger conformational changes. Most light-responsive systems reported in literature involve a diazobenzene unit capable of undergoing *trans/cis* isomerization in response to UV irradiation. This concept has for instance been exploited to achieve trans-membrane ion transport with tweezer **21**, wherein complexation of potassium between two crown-ether units introduced on a diazobenzene platform takes place only under UV light when **22-cis** is formed (Figure 97). These studies have also revealed that the release of potassium conversely takes place in the dark upon formation of the **21-trans**.¹⁷⁷

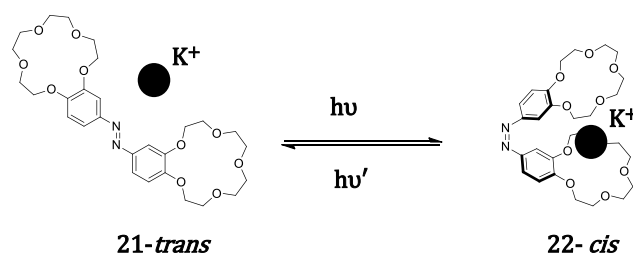


Figure 97: Chemical representation of the azo-based tweezer and its conformational changes upon irradiation to light.¹⁷⁷

Kato and his group have reported the synthesis of photoisomerizable thioindigo derivatives bearing ethylene-glycol side chains (Figure 98).¹⁷⁸ Experimental results revealed that the *trans* form (**22**) had no binding ability towards any of the metal ions, whereas the *cis* form binds to sodium, rubidium and potassium.

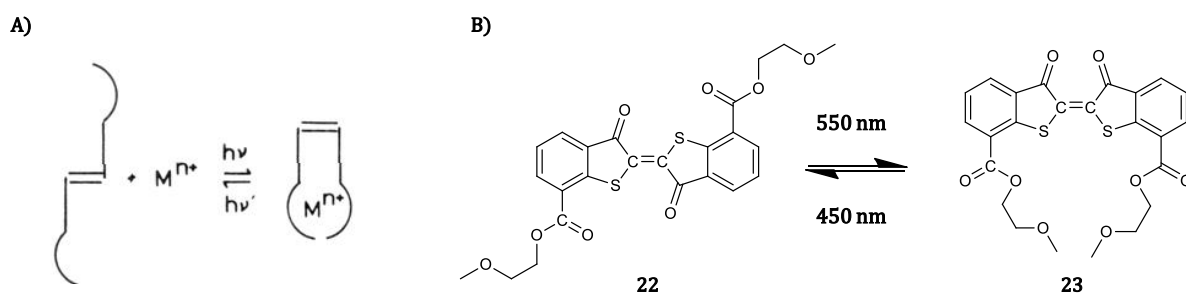


Figure 98: A) Concept of photo-responsive molecular tweezer displaying switchable metal binding affinities. B) Photo isomerization of a thioindigo derivative.¹⁷⁸

In 2009, Jayawickramarajah and his group have developed a stilbene-tethered bis(porphyrin) tweezer (Figure 99)¹⁷⁹ which can be obtained as two different isomers (Z and E). It has been demonstrated that the Z isomer **25** has a higher affinity towards both C₆₀ ($2.9 \pm 0.4 \times 10^4 \text{ M}^{-1}$) and C₇₀ ($8.2 \pm 0.8 \times 10^4 \text{ M}^{-1}$) compared to the E isomer **24** [C₆₀ ($7.1 \pm 0.2 \times 10^3 \text{ M}^{-1}$) and C₇₀ ($1.7 \pm 0.1 \times 10^4 \text{ M}^{-1}$)].

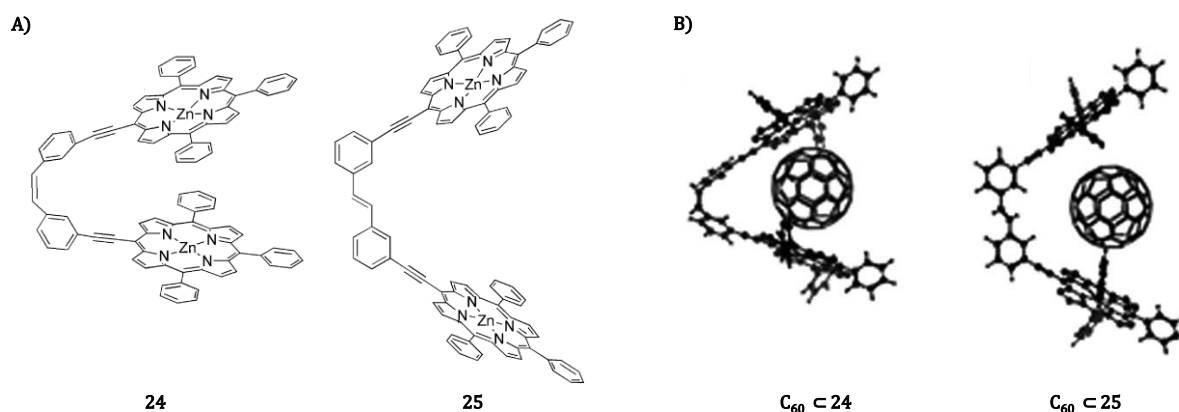


Figure 99: A) Schematic representation of photo-responsive bis(porphyrin) tweezers in both *cis* (**24**) and *trans* (**25**) conformation. B) Representation of the proposed binding modes of the tweezers with fullerene C₆₀.¹⁷⁹

III.1.3.3. pH-Responsive Molecular Tweezers

Proton exchanges are widely used by nature to trigger specific biological functions. In a biomimetic approach, much effort has been devoted over the years to develop artificial pH-sensitive molecular hosts capable of binding or releasing a given guest molecule at specific pH values. A beautiful example of water soluble, pH-responsive molecular tweezer has been reported by Leroux and Petitjean in 2010 (Figure 100).¹⁸⁰ The authors have established that the affinity for quinizarin and mitoxantrone depends on the conformation of the host which can be controlled upon adjusting the pH of the solution. In acidic media, protonation of the central pyridine ring leads to a loss of the recognition properties (release of the guest) resulting from the extended conformation imposed by two intramolecular hydrogen-bonds.

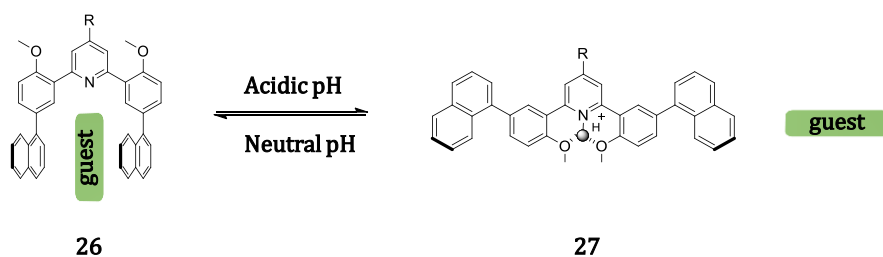


Figure 100: Chemical representation of the pH-responsive molecular tweezer developed by Leroux and Petitjean.¹⁸⁰

III.1.3.4. Redox-Responsive Molecular Tweezers

The charge and the recognition properties of the binding sites involved in molecular tweezers can be modified through electron transfer. This stimulus can also trigger the isomerization of the tweezer.

Such phenomenon has been reported by the group of Stelten with a tweezer incorporating two redox-responsive TTF units (Figure 101).¹⁸¹ In its neutral state, **28** adopts a folded conformation but the one-electron oxidation of both TTF triggers the formation of the *open* tweezer **29** whose conformation is imposed by the electrostatic repulsion between the oxidized TTF moieties.

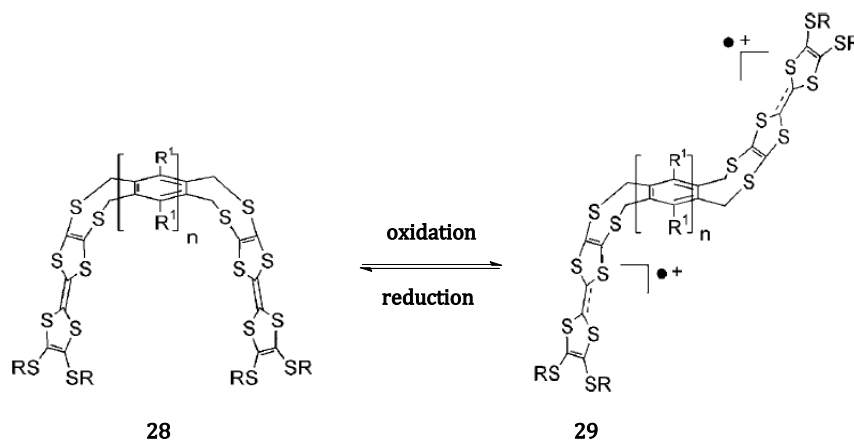


Figure 101: Chemical representation redox responsive tweezer developed by Stelten.¹⁸²

Two TTF units have also been incorporated on a glycoluril-based platform by Hudhomme and coll.¹⁸³ These authors have established that **30** self-assembles in *o*-dichlorobenzene with C₆₀ to yield the 2:1 (**31**) complex shown in Figure 102 ($K = 10^9 \text{ M}^{-1}$).

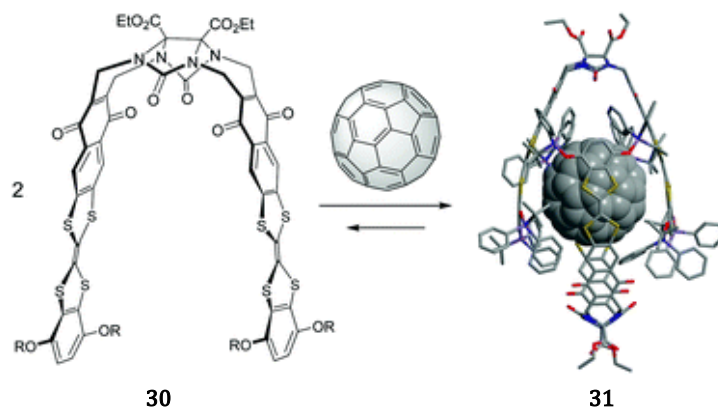


Figure 102 : Formation of the complex **31** (the optimized geometry was obtained through Molecular Mechanics calculations).

The redox-responsive porphyrin-based molecular tweezers **32**⁴⁺ has been previously developed in our group (Figure 103).³⁵ These studies have shown that **32**⁴⁺ can be efficiently and reversibly converted from an “open” charge-repelled conformation into a “closed” cofacial arrangement. This open/close molecular motion, triggered by electron-transfer centered on π -dimerizable bipyridinium subunits, has been shown to allow the complexation of a bidentate heterocyclic ligand pinched between both metallo-porphyrins as revealed by the modulation of the porphyrin-based exciton coupling phenomena. The reduction of both bipyridiniums in the open “charge repelled” conformer thus leads to a large reorganization triggered by the formation of an intramolecular π -dimer, the driving force of this molecular motion being the stabilization of both organic radicals in a sandwich-like structure.

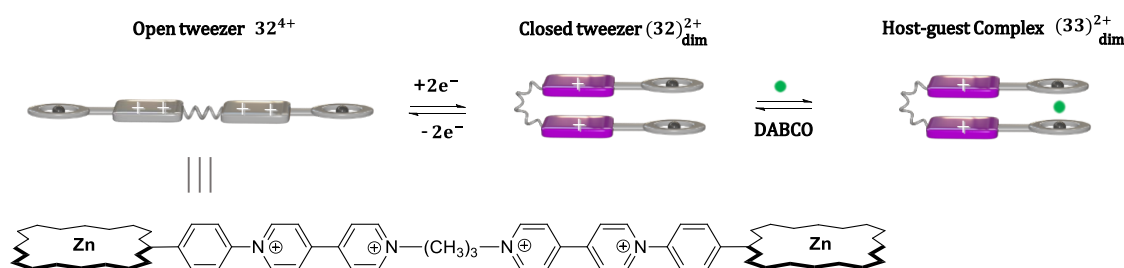


Figure 103: Redox-Responsive Porphyrin-Based Molecular Tweezers.³⁵

III.1.4. Objectives of this Chapter

This chapter reports on the synthesis and characterization of various tweezers and clips incorporating viologen units as redox-responsive and binding elements. It includes detailed investigations on their recognition, π -dimerization and self-assembling properties using NMR / UV-Visible absorption spectroscopy and (spectro)electrochemical methods supported by

III.2 . Flexible Tweezers Incorporating a 2,6-Bis(phenyl)pyridine Spacer

This choice of spacer was mainly inspired by the work of Wang and coll.¹⁸⁴ The latter exhibits structural features compatible with the objectives discussed above, most notably a suitable distance between both terminal phenyl rings enabling to envision the formation of Acceptor/Donor/Acceptor (ADA) sandwich-like complexes (Figure 104B). The choice was also driven by the synthetic availability and versatility of the precursors and intermediates involved in the synthesis of the targeted compounds **38**⁴⁺, **42**⁴⁺, **44**⁴⁺ and **48**⁴⁺ (Figure 105).

III.2.1: Synthesis of the Targeted Tectons

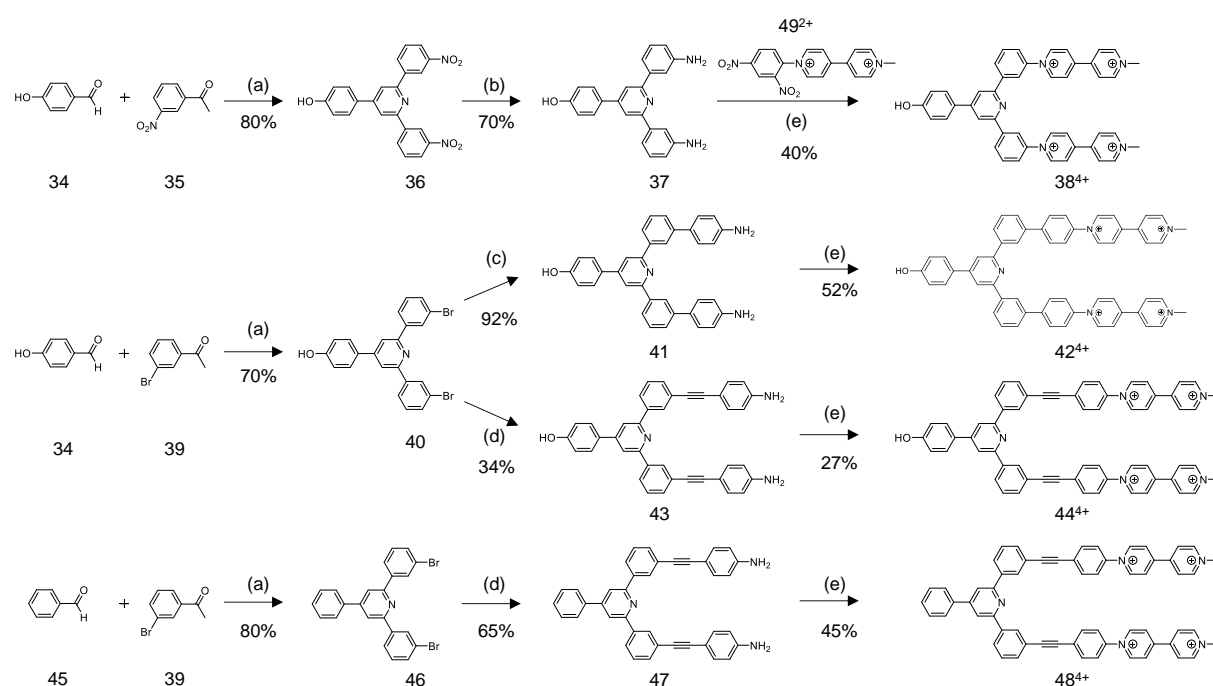


Figure 105: (a) NH_4OAc , Acetic acid, reflux, 14h; (b) $\text{N}_2\text{H}_4\cdot\text{H}_2\text{O}$, Pd/C, K_3PO_4 , DMF/ETOH, 16h; (c) 4-Aminophenylboronic acid pinacol ester, $\text{Pd}(\text{PPh}_3)_4$, K_3PO_4 , THF, reflux; (d) 4-Ethynylaniline, $\text{Pd}(\text{PPh}_3)_2\text{Cl}_2$, CuI, piperidine, THF, reflux; (e) **49**(PF_6)₂, EtOH/ CH_3CN , 70 °C, 18h.

The multi-step syntheses of the targeted tweezers are shown in Figure 105. They involve a sequence of three reactions starting with a condensation reaction between two suitable aldehyde and ketone yielding the key intermediates **36**, **40** and **46** in 70-80% yields.¹⁸⁵ The aniline terminated product **37**¹⁸⁵ was then obtained by reduction of **36** with hydrazine,¹⁸⁵ while **41**, **43** and **47** featuring additional phenyl or phenylethynyl linkers could be obtained from **40** and **46** through either Suzuki or Sonagashira coupling reactions. Introduction of the terminal 4,4'-bipyridinium units to obtain the desired compounds **38**⁴⁺, **42**⁴⁺, **44**⁴⁺ and **48**⁴⁺ was

ultimately achieved through a Zincke reaction involving 49^{2+} as a key reactant. The structure and purity of the tectons was mainly established on the ground of mass spectrometry and NMR spectroscopy measurements.

III.2.2. NMR Characterization

These tweezers were characterized by $^1\text{H-NMR}$ (1D/2D) and $^{13}\text{C-NMR}$ spectroscopy measurements. The exact attributions of the $^1\text{H-NMR}$ spectra is shown in Figure 106.

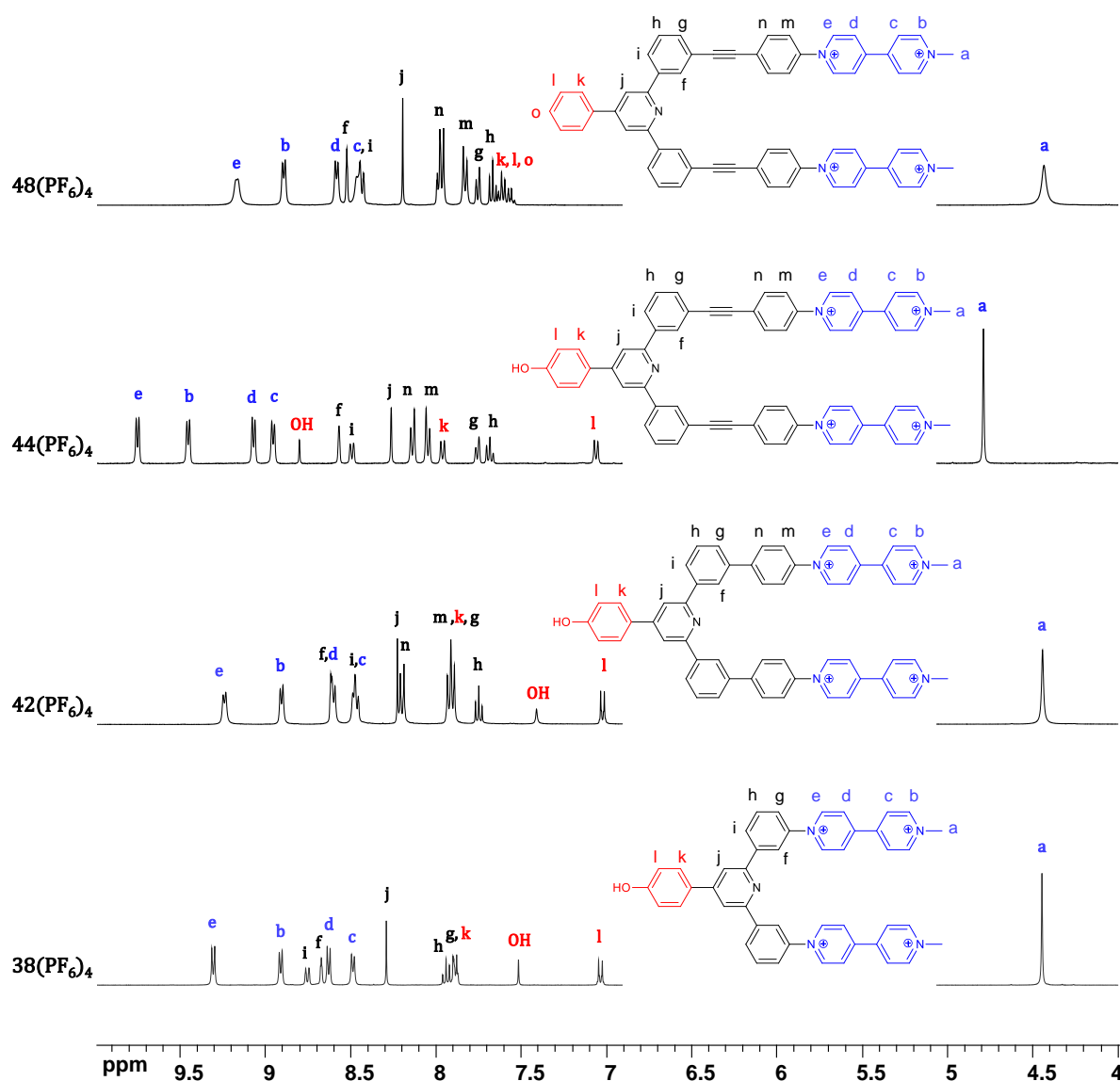


Figure 106: $^1\text{H-NMR}$ spectrum of the viologen based tweezers $38(\text{PF}_6)_4$ (5 mM, $\text{CD}_3\text{CN-}d_3$), $42(\text{PF}_6)_4$ (5 mM, $\text{CD}_3\text{CN-}d_3$), $44(\text{PF}_6)_4$ (3 mM, acetone- d_6), and $48(\text{PF}_6)_4$ (5 mM, $\text{CD}_3\text{CN-}d_3$) recorded in (295 K, 400 MHz).

All these compounds have been characterized as PF_6 salts in deuterated acetone (44^{4+}) or in acetonitrile (38^{4+} , 42^{4+} and 48^{4+}). In the aromatic region, the most de-shielded signals observed between 8.4 and 9.5 ppm are attributed to the bipyridinium units, the signal of H_e

being systematically observed above 9 ppm. The low field shift of these signals is even found to be larger in acetone where the resonance of H_e in **44**(PF₆)₄ reaches 9.75 ppm. The terminal phenol rings are observed on all spectra as two doublets resonating at 7.03 and 7.96 ppm. The hydrogen atoms on the two phenyl ring adjacent to the central pyridine (H_f, H_g, H_h and H_i) appear as three multiplets and one singlets around 8.32 ppm. Then, the protons of the phenyl rings linked to the bipyridinium moieties (H_m and H_n) are observed as doublets resonating around 7.9 and 8.2 ppm.

The differences observed in the chemical shifts recorded in acetone and in acetonitrile are huge, most notably for the signals attributed to the viologens. This significant solvent effect was observed for all the investigated clips. For instance, the signals attributed to the bipyridinium units in **44**⁴⁺ appear between 9.5 and 10 ppm in acetone and between 8.75 and 9.5 in acetonitrile. This behaviour, albeit not fully understood, might result from the existence of supramolecular interactions involving the viologen units and the polyaryl linker (H_m, H_n, H_g and H_h).

Insights into the conformation of these tweezers in solution were provided by 2D-ROESY NMR measurements supported by computational data. The later revealed the existence of a dynamic equilibria between the W- and U-shaped conformers as shown in Figure 107, involving hydrogen bonds between the central nitrogen atom and either H_f or H_i.

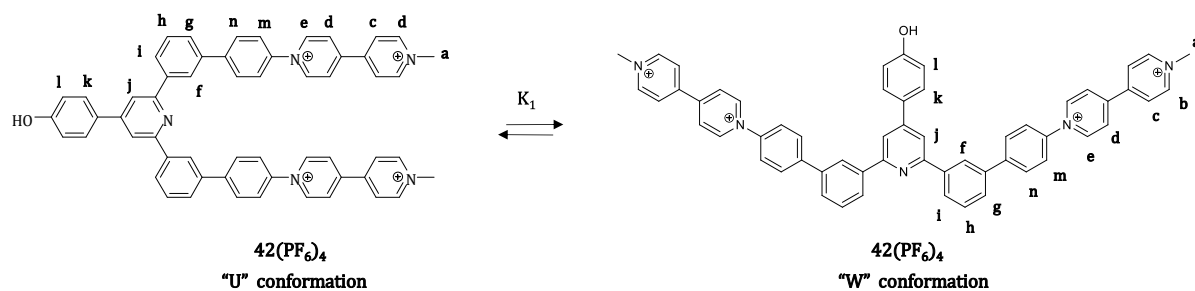


Figure 107 : Chemdraw representation of structural conformation of **42**(PF₆)₄ in solution.

As an example, the ROESY spectra of **42**(PF₆)₄ shows one correlation between H_i and H_j, and other between H_f and H_j, suggesting the existence of both conformations in solution (Figure 108A).

DFT level calculations carried out on **42**⁴⁺ revealed that the energy difference between the W-conformer and the U-conformer is about -3.4 kcal.mol⁻¹ (Figure 108B). This supports the coexistence of both conformations in solution.

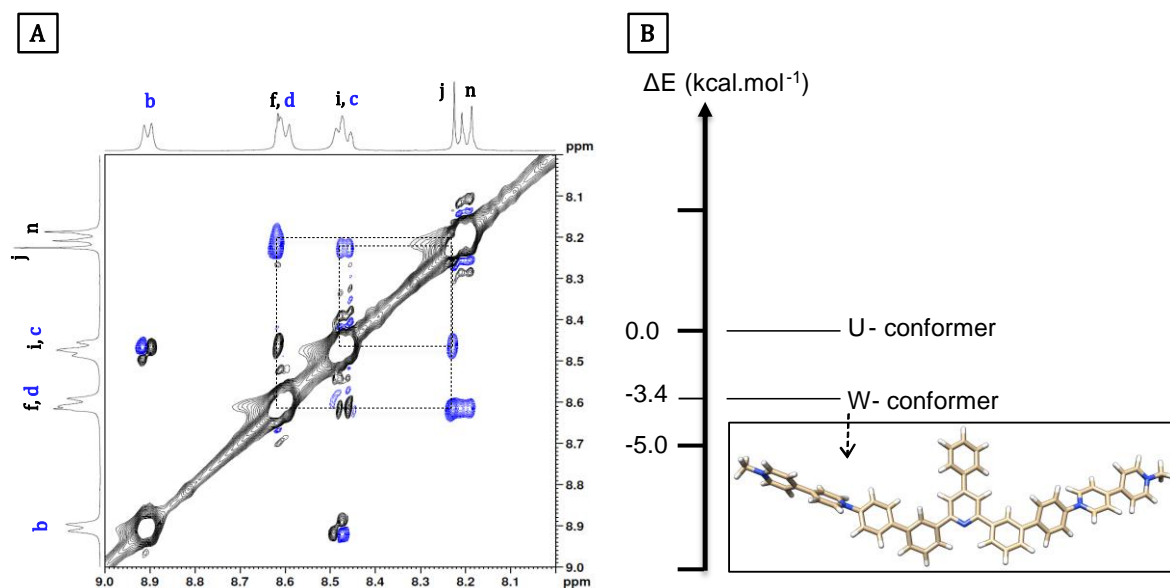


Figure 108: A) ^1H - ^1H ROESY NMR map of $\mathbf{42}(\text{PF}_6)_4$, (5mM, $\text{CD}_3\text{CN}-d_3$), 400 MHz. B) Relative energies calculated (DFT) for the W and U-shaped isomers of $\mathbf{42}(\text{PF}_6)_4$.

III.2.3. Electrochemical Characterization

Electrochemical investigations have been carried out in DMF (0.1 M TBAP) using cyclic voltammetry (CV) and rotating disk electrode (RDE) voltammetry. Potential values are given against a home-made Ag^+/Ag (10^{-2} M) reference electrode. The electrochemical experiments have been conducted at room temperature under an argon atmosphere (glove box) using a conventional three electrode electrochemical cell. A selection of relevant electrochemical data obtained with $\mathbf{38}(\text{PF}_6)_4$, $\mathbf{42}(\text{PF}_6)_4$, $\mathbf{44}(\text{PF}_6)_4$, and $\mathbf{48}(\text{PF}_6)_4$ together with those of the reference compound $\text{MeVMe}(\text{PF}_6)_2$ and $\text{PhVMe}(\text{PF}_6)_2$ are collected in Table 6.

The CV curves of all these compounds were found to exhibit similar features, the most characteristic ones being the two successive reduction waves (noted as E^{1c} and E^{2c} in Table 6) attributed to the two consecutive one-electron reductions of each viologen units ($1e^-/\text{viologen}$) yielding the cation radical and neutral quinonic state $\text{V}^{+\bullet}$ and V^0 , respectively. The peak to peak potential shift ($\Delta E_p = E_{pa} - E_{pc}$) measured on the first viologen-centered reduction waves was systematically plotted as a function of scan rate (25 mV/s to 1000 mV/s) to check the diffusion-limited character of these waves but only the ΔE_p values recorded at 100 mV/s are shown in Table 6.

	$E^{1c}(n, \Delta E_p)$	$E^{2c}(n, \Delta E_p)$	$E^{1c} - E^{2c}$
	$V^{2+}/V^{+•}$	V^{2+}/V^0	(V)
MeVMe(PF ₆) ₂	-0.882 ^b (1,62)	-1.198 ^b (1,60)	0.316
PhVMe(PF ₆) ₂	-0.709 ^b (1,58)	-1.035 ^b (1,58)	0.326
38 (PF ₆) ₄	-0.698 ^b (2,50)	-1.034 ^b (2,55)	0.336
42 (PF ₆) ₄	-0.682 ^b (2,51)	-1,002 ^{c,d}	na
44 (PF ₆) ₄	-0.667 ^b (2,43)	-1,030 ^{c,d}	na
48 (PF ₆) ₄	-0.665 ^b (2,45)	-1,030 ^{c,d}	na

Table 6: Electrochemical data measured by CV in the following conditions: $1 \times 10^{-3} \text{ M}$ in DMF/TBAP (0.1 M, $E(V)$ vs. Ag^+/Ag), at a vitreous carbon working electrode $\varnothing = 3 \text{ mm}$, 298 K, $\nu = 0.1 \text{ V}\cdot\text{s}^{-1}$ (na : Not available / ^b : Half wave potential / ^c : Peak potential / ^d : Adsorption phenomena).

Several conclusions can be drawn from these data. The first viologen-centered reductions are systematically observed as reversible waves with $E_{1/2}$ values ranging from -0.66 to -0.70 V , which happens to be slightly less negative than the -0.71 V measured in the same conditions with the reference compound PhVMe^{2+} . At first sight, the polyaryl spacer thus seems to have only a limited effect on the terminal viologen units.

The $E^{1c}-E^{2c}$ values are similar for all the investigated compounds, which means that the stability domains of the doubly reduced species $\text{X}^{2(+•)}$ ($\text{X} = \mathbf{38}, \mathbf{42}, \mathbf{44}$ and $\mathbf{48}$) are also in the same order of magnitude. This comparison is however made difficult by the existence of adsorption phenomena coupled to formation of the neutral quinonic species.

The ΔE_p values measured on the first reduction waves ($E_{pc} - E_{pa}$) is found to evolve quite significantly with the length of the organic linker introduced between the central 2,6-*bis*(phenyl)pyridine spacer and the viologen units, from the standard 58/60 mV shift measured with the reference compounds MeVMe^{2+} or PhVMe^{2+} , down to a minimum value of 43 mV measured with $\mathbf{44}^{4+}$. As explain in the previous sections, the drop in the ΔE_p value, below the standard 58 mV shift, reveals the existence of a π -dimerization process involving the doubly reduced species ($\text{X}^{2(+•)} \rightarrow [\text{X}^{2+}]_{\text{dim}}$). The trend observed in Table 6 thus suggests that the length of the linker is a key parameter, the lowest ΔE_p value and the most efficient dimerization being presumably achieved with the tweezer featuring the largest linker, *ie* $\mathbf{44}^{4+}$ and $\mathbf{48}^{4+}$.

All these data are thus consistent with the conclusion that the π -dimerization ability of the doubly reduced species $\text{X}^{2(+•)}$ depends on the size and flexibility of the organic linker introduced between the *bis*(phenyl)pyridine spacer and the terminal viologens. The ΔE_p value is here clearly the most suitable/reliable indicator to compare the ability of the viologen-based

cation radicals in $\mathbf{X}^{2(+\bullet)}$ to dimerize and yield the intramolecular dimer noted $[\mathbf{X}^{2+}]_{\text{dim}}$. In any case, the general mechanism detailed in Figure 109 with the shortest compound $\mathbf{38}^{4+}$ applies for all the investigated tweezers. It involves two consecutive viologen-centered one-electron reduction processes (E°_{1-1} and E°_{1-2}) yielding the *mono* and *bis*-cation radical species ($\mathbf{X}^{4+} \rightarrow \mathbf{X}^{3+\bullet} \rightarrow \mathbf{X}^{2(+\bullet)}$). The chemical steps associated to each redox state are the equilibria between the W- and U-shaped isomers (K_1, K_2, K_3). The K_1 and K_2 values are essentially determined by the stability of the *bis*(phenyl)pyridine spacer in both forms (H-bonds between Hs and N) while K_4 (Figure 109A) can be referred to as a dimerization constant whose value is imposed by the ability of both cation radicals in $\mathbf{X}^{2(+\bullet)}$ to dimerize into the dicationic U-shaped complex $[\mathbf{X}^{2+}]_{\text{dim}}$.

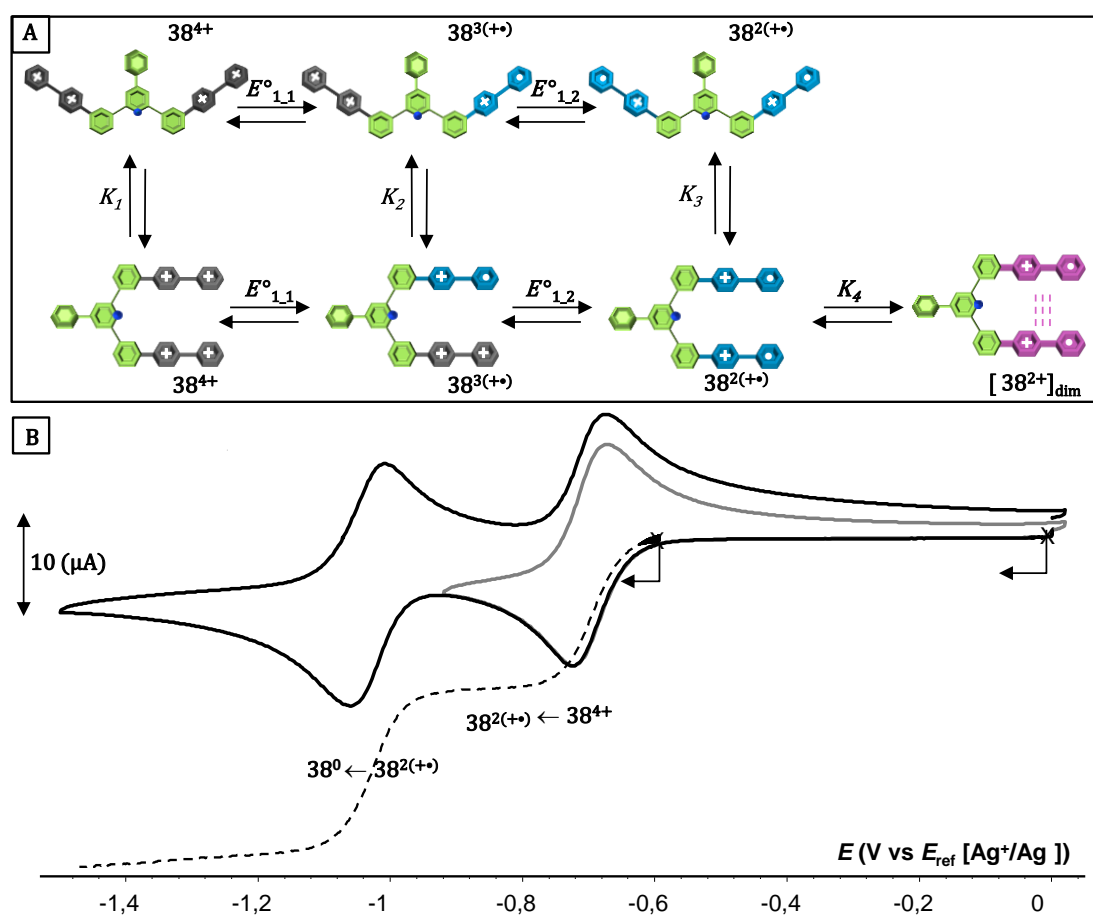


Figure 109: CV curve (solid line) of $\mathbf{38}(\text{PF}_6)_4$ (1×10^{-3} M) recorded in DMF (TBAP 0.1M) using a carbon working electrode ($\varnothing = 3$ mm, E vs. Ag^+/Ag (10^{-2} M), $v = 0.1$ $\text{V} \cdot \text{s}^{-1}$) and rotating carbon disk electrode (dotted line) ($\varnothing = 3$ mm, $v = 0.01$ $\text{V} \cdot \text{s}^{-1}$, 550 rd/min).

The electrochemical signatures of $\mathbf{42}(\text{PF}_6)_4$, $\mathbf{44}(\text{PF}_6)_4$ and $\mathbf{48}(\text{PF}_6)_4$ were found to exhibit similar features (the CV curve of $\mathbf{42}(\text{PF}_6)_4$ is displayed as an example in Figure 110), the most noteworthy being the observation of an intense Gaussian-shaped reoxidation peak associated to the formation of the neutral species \mathbf{X}^0 . Such signal, quite frequently observed with

viologen derivatives, is attributed to the redissolution of neutral X^0 molecules which were physisorbed at the electrode surface during the forward scan. It needs to be mentioned that this adsorption process can be avoided and the reversibility of this reduction wave can be restored by conducting these measurements in less concentrated solutions ≤ 0.1 mM and upon lowering the time scale of the experiments (higher scan rates).

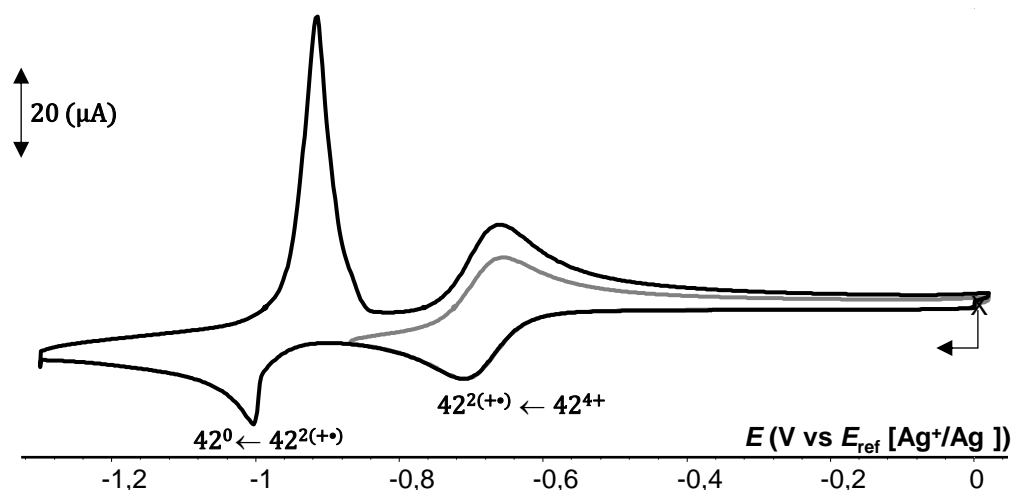


Figure 110: CV curves measured for $42(\text{PF}_6)_4$ at (10^{-3} M) in DMF + TBAP 0.1 M (VC, $\varnothing = 3$ mm, E (V) vs. Ag^+/Ag (10^{-3} M), $v = 0.1$ V s^{-1}).

The main conclusions drawn from these measurements are that the tweezers 38^{4+} , 42^{4+} , 44^{4+} and 48^{4+} are slightly easier to reduce than the reference compounds MeVMe^{2+} and PhVMe^{2+} (Table 6). The first reduction potential increases as the length of the linker increases [$E_{38(\text{PF}_6)_4}^{1c} < E_{42(\text{PF}_6)_4}^{1c} < E_{44(\text{PF}_6)_4}^{1c} \approx E_{48(\text{PF}_6)_4}^{1c}$]. The ΔE_p values follows a similar trend as it decreases as the length of the linker increases to reach 43 mV with $44(\text{PF}_6)_4$. Taken together, these experimental data thus reveal that the distance between both viologens in this systems is too long to enable an efficient intramolecular dimerization ($X^{2(+\bullet)} \leftrightarrow [X^{2+}]_{\text{dim}}$, large K_4). The association between both viologen radicals happens however to be facilitated by the introduction of long and flexible spacers between the viologen and *bis*(phenyl)pyridine core like in $44(\text{PF}_6)_4$. These assumptions have been further supported by spectroelectrochemical and computational chemistry studies.

III.2.4: Spectro-Electrochemical Characterization

Spectroelectrochemistry measurements have been carried out under an argon atmosphere (glove box) in anhydrous DMF (+TBAP, 0.1 M). The latter involved conducting potentiostatic electrolysis of ~ 10 ml solutions of 38^{4+} , 42^{4+} , 44^{4+} and 48^{4+} using a platinum

plate working electrode whose potential was set between -0.85 and -1 V vs. Ag^+/Ag (10^{-2}M), depending on the compounds. Changes in the UV-vis absorption signature were monitored in real time using an all quartz immersion probe introduced in the electrolysis cell.

Preliminary measurements have been carried out with simple viologen derivatives used as references. The exhaustive one-electron reduction of the reference compounds MeVMe^{2+} (0.5 mM) and PhVMe^{2+} (0.2 mM) resulted in the emergence of intense signals attributed to the free, *ie* non-associated, viologen-based cation radicals $\text{MeVMe}^{+\bullet}$ and $\text{PhVMe}^{+\bullet}$, respectively (Figure 111A and B). The significant discrepancies observed between those two spectra recorded in the same experimental conditions suggest that the cation radical is partially delocalized on the adjacent benzene ring. As can be seen in Figure 111A and B, the spectrum of $\text{MeVMe}^{+\bullet}$ features a sharp absorption band centred at 400 nm ($\epsilon = 20,000 \text{ M}^{-1}\cdot\text{cm}^{-1}$) and a much broader signal with multiple shoulders centred at 609 nm ($\epsilon = 8,000 \text{ M}^{-1}\cdot\text{cm}^{-1}$) while that of $\text{PhVMe}^{+\bullet}$ shows a quite broad signal centred at 415 nm ($\epsilon = 19,000 \text{ M}^{-1}\cdot\text{cm}^{-1}$) associated to a series of transitions centered at 617 nm ($\epsilon = 13,000 \text{ M}^{-1}\cdot\text{cm}^{-1}$).

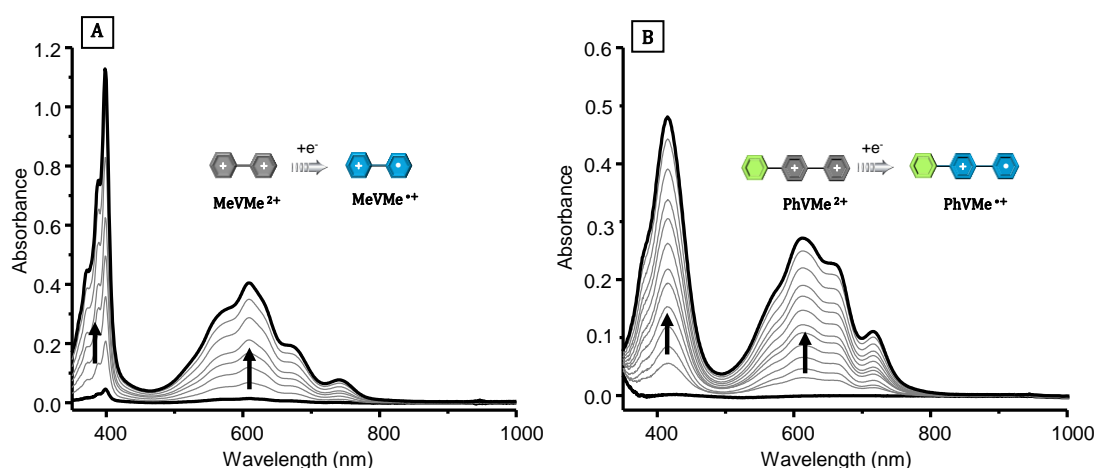


Figure 111: Superposition of UV-vis absorption spectrum of (A) $\text{MeVMe}(\text{PF}_6)_2$ and (B) $\text{PhVMe}(\text{PF}_6)_2$ recorded during the exhaustive one electron reduction in [DMF + 0.1 M TBAP, $l = 1$ mm, $t \approx 30$ min, working electrode = Pt (A : 0.5 mM, 10 mL, $E_{\text{app}} = -1$ V / B : 0.2 mM, 10 mL, $E_{\text{app}} = -0.91$ V)].

Similar measurements have been carried out with $\mathbf{38}(\text{PF}_6)_4$ and $\mathbf{42}(\text{PF}_6)_4$. The one electron reduction of $\mathbf{38}(\text{PF}_6)_4$ ($1e/\text{viologen}$) led to the development of two main absorption signals centered at $\lambda_{\text{max}} = 419$ nm ($\epsilon = 42,600 \text{ M}^{-1}\cdot\text{cm}^{-1}$) and 613 nm ($\epsilon = 30,200 \text{ M}^{-1}\cdot\text{cm}^{-1}$) coming along with a less intense signals centered at 987 nm ($\epsilon = 3,200 \text{ M}^{-1}\cdot\text{cm}^{-1}$) (Figure 112A). For compound $\mathbf{42}(\text{PF}_6)_4$, new absorption bands were seen to develop at 423 nm ($\epsilon = 41,200 \text{ M}^{-1}\cdot\text{cm}^{-1}$), 613 nm ($\epsilon = 24,000 \text{ M}^{-1}\cdot\text{cm}^{-1}$) and 939 nm ($\epsilon = 2,000 \text{ M}^{-1}\cdot\text{cm}^{-1}$) (Figure 112B). In

both cases, the spectra recorded after addition of two electrons/molecule reveal the simultaneous presence of the free unassociated bis-radical $\mathbf{X}^{2(+\bullet)}$ and of the π -dimerized tweezer $[\mathbf{X}^{2+}]_{\text{dim}}$ ($\mathbf{X} = 38$ or 42) in solution. This conclusion is mainly supported by the fact that the absorption bands observed in the visible range (400-800) are similar to those obtained in the same conditions with the reference compound PhVMe^{2+} (dashed curve in Figure 112), while the broad band observed in the near infra-red region is a clear diagnostic signature revealing the formation of viologen based π -dimers. The relative intensity of these signals, particularly the weak intensity of the broad near IR band, also reveal that the dimerization constant is low, ie that equilibrium $\mathbf{X}^{2(+\bullet)} \leftrightarrow [\mathbf{X}^{2+}]_{\text{dim}}$ ($\mathbf{X} = 38$ or 42) is displaced in favour of the non-associated species $\mathbf{X}^{2(+\bullet)}$.

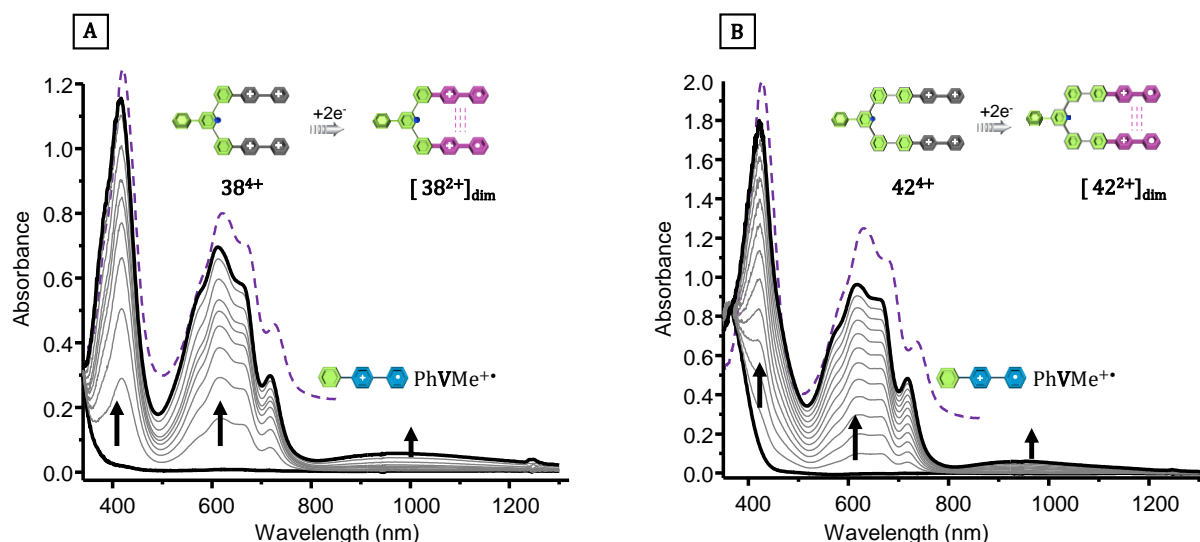


Figure 112: Superposition of UV-Vis absorption spectrum of (A) $38(\text{PF}_6)_4$ and (B) $42(\text{PF}_6)_4$ recorded during the exhaustive two electron reduction in $[\text{DMF} + 0.1 \text{ M TBAP}, 10 \text{ mL}, l = 1 \text{ mm}, t \approx 30 \text{ min}, \text{working electrode} = \text{Pt} (\text{A}:0.2 \text{ mM}, E_{\text{app}} = -0.91 \text{ V}/ \text{B}:0.5 \text{ mM}, 10 \text{ mL}, E_{\text{app}} = -0.85 \text{ V})]$.

A deconvolution of these signals carried out using the signature of $\text{PhVMe}^{+\bullet}$ (free radical) and a suitable propyl linked π -dimer³⁸ as references led to the finding that the relative amount of dimer is larger for $42(\text{PF}_6)_4$ (23%) than for $38(\text{PF}_6)_4$ (11%), which is consistent with the idea that the dimerization requires some flexibility provided by the linker introduced between the viologen and the 2,6-*bis*(phenyl)pyridine spacer. It is worth mentioning that each redox state of the tweezers may adopt either a W- or U-shaped conformation in solution. This applies of course to the \mathbf{X}^{4+} species but also to the doubly reduced non-dimerized species $\mathbf{X}^{2(+\bullet)}$.

The stability of all the species involved in the E_nC_n process shown in Figure 109A has moreover been demonstrated upon checking that the starting material \mathbf{X}^{4+} can be fully

recovered by re-oxidation of the doubly reduced species ($E_{app} = 0$ V) and upon following the advancement of each electrolysis and checking the stability of the reduced species at the electrolysis time scale by RDE measurements (Figure 113A and B).

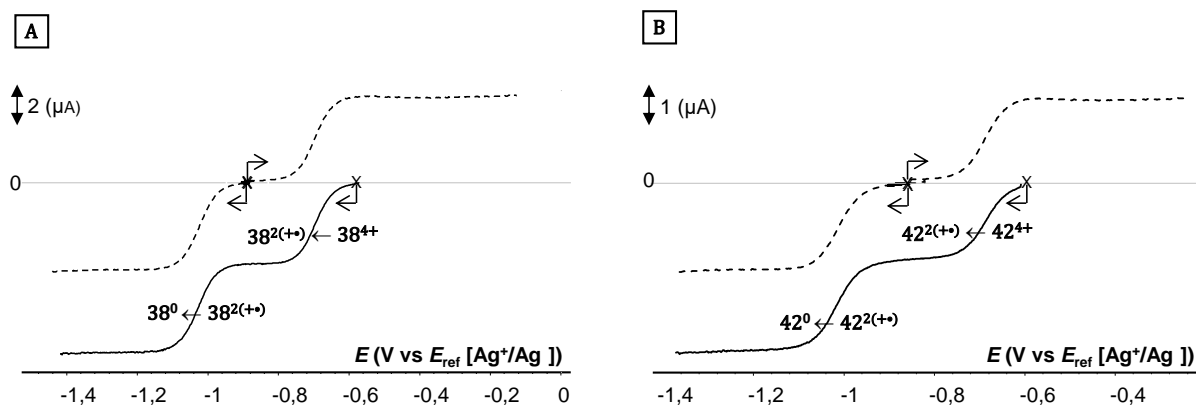


Figure 113: Voltammetric curves of (A) $38(\text{PF}_6)_4$ (0.2 mM) / (B) $42(\text{PF}_6)_4$ (0.1 mM) recorded in DMF (TBAP 0.1M) at a RDE ($\varnothing = 3$ mm, $\nu = 0.01 \text{ V}\cdot\text{s}^{-1}$, 550 rd/min) before electrolysis (solid line) and after electrolysis (dotted line) (1e/viologens).

The presence of free radicals in solution after completion of the electrolysis has been confirmed by ESR measurements carried out at room temperature. As can be seen in Figure 114, the spectra recorded for samples taken after two electron reduction of 38^{4+} and 42^{4+} feature a single signal at $g = 2.00$ attributed to the presence of $S = 1/2$ viologen-based radicals.

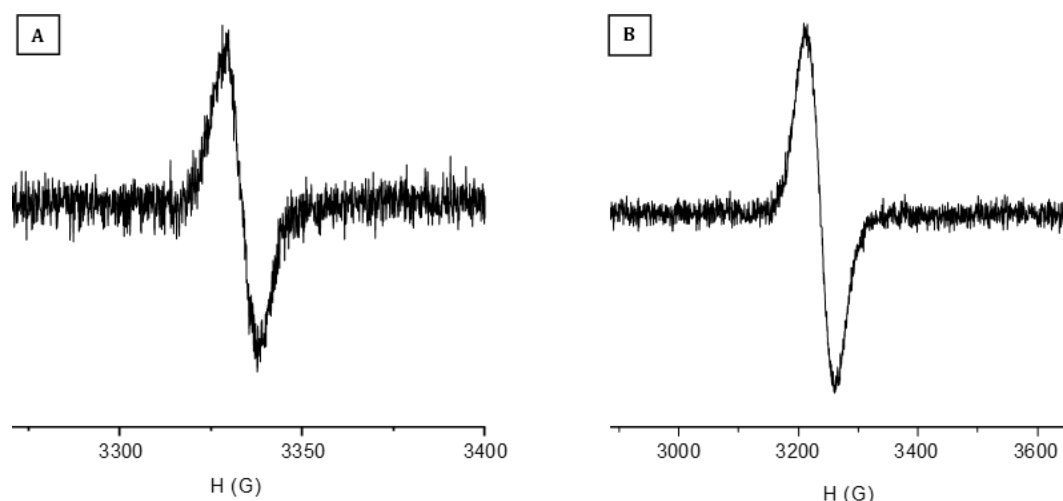


Figure 114: X-band ESR spectra recorded after two electron reduction of (A) 38^{4+} and (B) 42^{4+} (RT, DMF + TBAP (0.1M)).

Similar studies have been conducted with $44(\text{PF}_6)_4$, and $48(\text{PF}_6)_4$, featuring the same 4-ethynylphenyl linkers. The changes in the UV/Vis signature monitored throughout the 2 electron reduction of 44^{4+} and 48^{4+} carried out on platinum at $E_{app} = -0.91$ V are shown in Figure 115. The most significant differences observed between these curves and those

recorded in the same conditions with 38^{4+} and 42^{4+} lie i) in the shape of the band centred at ~ 600 nm, which is now quite different from that of the reference compound $\text{PhVMe}^{+\bullet}$ and ii) in the intensity of the broad band observed in the near IR attributed to the intramolecular dimer $[\text{X}^{2+}]_{\text{dim}}$ ($\text{X} = 44, 48$).

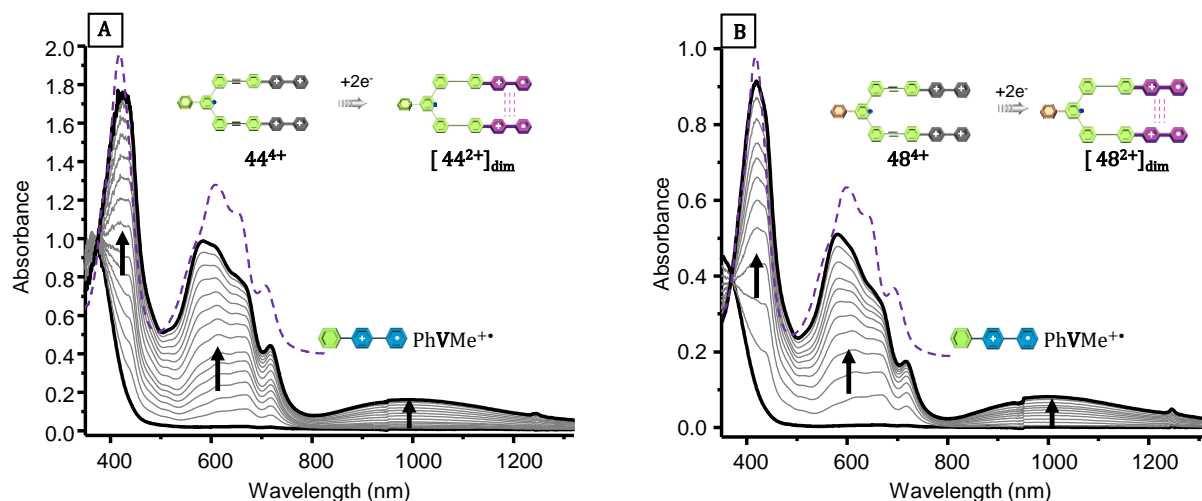


Figure 115: UV-Vis absorption spectra recorded during the exhaustive two electron reduction of (A) $44(\text{PF}_6)_4$ and (B) $48(\text{PF}_6)_4$ in $[\text{DMF} + 0.1 \text{ M TBAP}, 10 \text{ mL}, l = 1 \text{ mm}, t \approx 30 \text{ min}, \text{working electrode} = \text{Pt}$ (A : 0.5 mM , $E_{\text{app}} = -0.91 \text{ V}$ / B : 0.1 mM , 10 mL , $E_{\text{app}} = -0.91 \text{ V}$).

These differences can be readily explained by the fact that the intramolecular dimerization of both viologens in $\text{X}^{2(+\bullet)} \leftrightarrow [\text{X}^{2+}]_{\text{dim}}$ proceeds more efficiently in the most flexible systems ($\text{X} = 44$ and 48) than in the most rigid and shorter analogues ($\text{X} = 38$ and 42). Here again, a deconvolution of these signals led to an estimation of the $[\text{X}^{2+}]_{\text{dim}} / \text{X}^{2(+\bullet)}$ ratio reaching 26% and 28% by the end of the electrolysis of $44(\text{PF}_6)_4$ and $48(\text{PF}_6)_4$, respectively.

It should also be emphasized that the intramolecular nature of the π -dimerization has been systematically checked with concentration-dependent studies revealing that the electrochemical and spectroelectrochemical data recorded with 38^{4+} , 42^{4+} , 44^{4+} and 48^{4+} do not change significantly with concentration. For instance the absorption spectrum recorded after two-electron reduction of a $5 \times 10^{-4} \text{ M}$ DMF solution of 44^{4+} is shown in Figure 116A (black curve) together with those obtained after dilution of the electrolyzed solution down to $2.5 \times 10^{-4} \text{ M}$ and $1 \times 10^{-4} \text{ M}$. Taken together, the shape of the normalized spectra collected at different concentrations and the linear evolution of the absorbance at $\lambda = 990 \text{ nm}$ as function of concentration ($5 \times 10^{-4} \text{ M}$ to $5 \times 10^{-5} \text{ M}$ see Figure 116B) support the conclusion that no intermolecular dimerization occurs in solution in this concentration range. It should also be mentioned that the stability/signature of the reduced species upon dilution was also checked by RDE measurements (see Figure 116C).

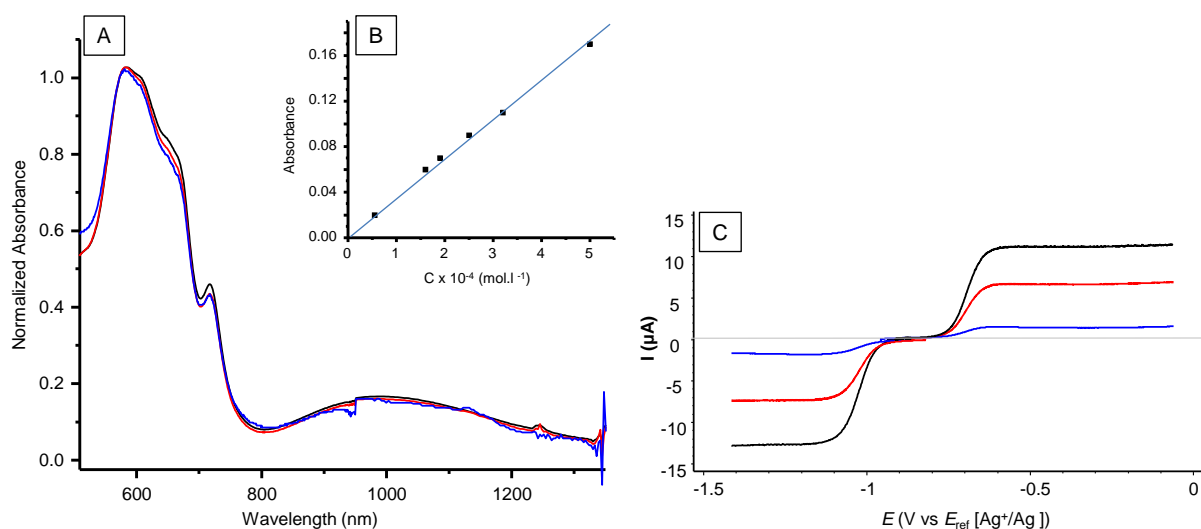


Figure 116: A) Normalized UV-vis absorption spectrum recorded of $44(\text{PF}_6)_4$ as function on concentration. B) Variation of absorption spectrum recorded of $44(\text{PF}_6)_4$ as function of concentration at $\lambda = 990$ nm. C) VRDE curves of $44(\text{PF}_6)_4$ recorded in DMF (TBAP 0.1M) using rotating carbon disk electrode ($\varnothing = 3$ mm, $\nu = 0.01 \text{ V.s}^{-1}$, 550 rd/min) before electrolysis and after electrolysis [black (5×10^{-4} M) / red (2.5×10^{-4} M) / blue (5×10^{-5} M)].

To summarize, all these results support the conclusion that the 2,6-*bis*(phenyl)pyridine spacer is flexible/short enough to promote the intramolecular dimerization of two viologen cation-radicals introduced at the 6th positions of the terminal benzene ring and that the efficiency of the dimerization (K_4 in Figure 109A) depends on the length and flexibility of the organic linkers introduced between the 2,6-*bis*(phenyl)pyridine core and the terminal viologens ($((K_4)_{44,48} > (K_4)_{42} > (K_4)_{38})$).

III.2.5. Computational Analysis

The DFT optimized structures together with the relative energies calculated $[\text{X}^{2+}]_{\text{dim}}$ ($X = 38, 42$ and 44) are shown in Figure 117. The π -dimers formed upon reduction shows two parallel viologen sub-units in $[44^{2+}]_{\text{dim}}$ at a distance of 3.61 Å, while the structure obtained for $[42^{2+}]_{\text{dim}}$ shows a crossed conformation of the viologens at a distance of 3.28 Å and the distance between the the viologen moieties in $[38^{2+}]_{\text{dim}}$ is 4.81 Å. The energetic difference is about 8 kcal.mol⁻¹ between $[38^{2+}]_{\text{dim}}$ and $[42^{2+}]_{\text{dim}}$ in favor of $[42^{2+}]_{\text{dim}}$ (Figure 117A) due to the limited interaction between the viologen moieties in $[38^{2+}]_{\text{dim}}$ where one of the viologen then turns itself to promote few CH- π interactions. This type of interaction triggers $\approx 3\text{--}4$ kcal.mol⁻¹ far less than the π -stacked conformation. Furthermore the energetic difference of $[44^{2+}]_{\text{dim}}$ and $[42^{2+}]_{\text{dim}}$ is similar and the difference is 1.6 kcal.mol⁻¹ between them.

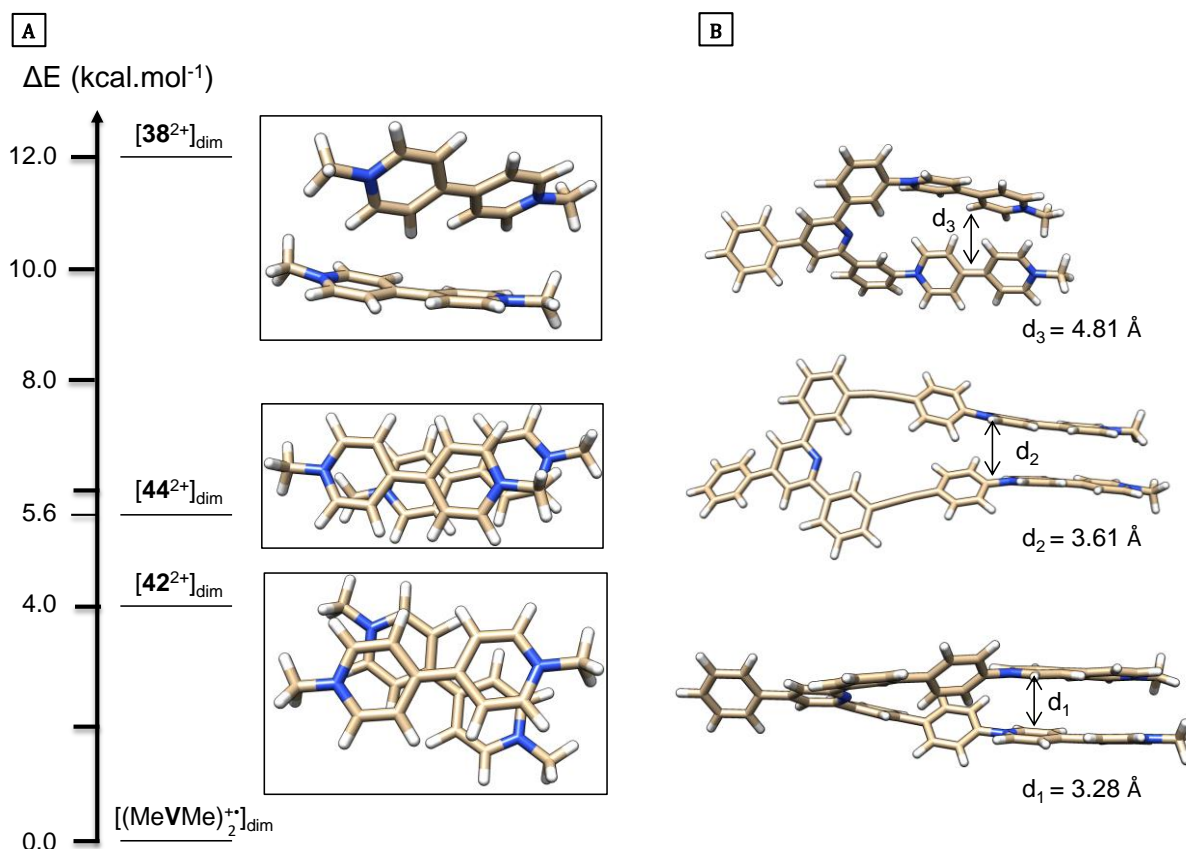


Figure 117: A) Relative energies of the viologen dimer in its geometries in the boxes, reflecting the structural deviation from the “ideal”, not constrained π -stacked dimer. B) DFT optimized structures for the π -dimers formed upon reduction of the viologen units in **38**(PF₆)₄, **42**(PF₆)₄ and **44**(PF₆)₄.

In summary, the DFT calculation support the conclusion that the efficiency of the dimerization depends on the length and flexibility of the organic linkers introduced between the 2,6-*bis*(phenyl)pyridine core and the terminal viologens.

III.2.6. Molecular Recognition Properties

These flexible tweezers feature two cationic viologens and a phenol ring that can potentially be exploited in host-guest processes as an acceptor (A) and donor (D) units, respectively. We first checked the ability of these molecules to self-assemble in solution through a combination of non-directional DA interactions and/or directional hydrogen bonds, for instance between the outer phenol and inner pyridine moieties (O-H...N) (Figure 118A).

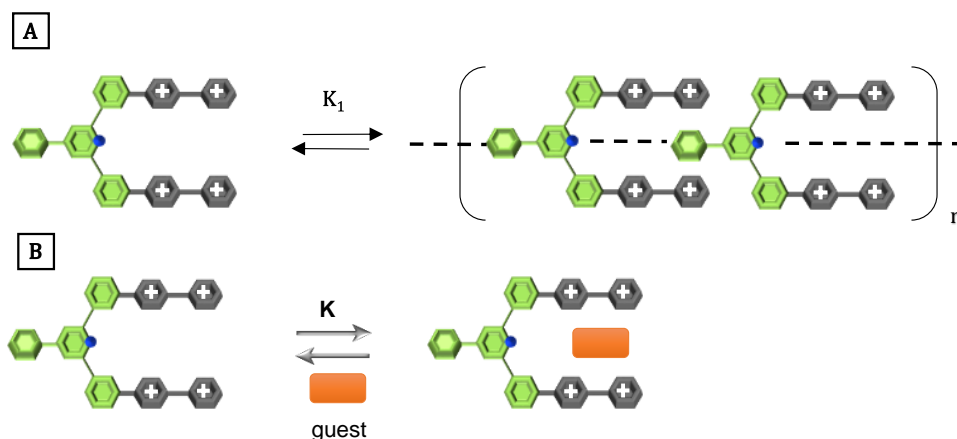


Figure 118: Self-association (A) and host-guest (B) processes considered with 38^{4+} .

The self-association ability of $38(\text{PF}_6)_4$, $42(\text{PF}_6)_4$, and $44(\text{PF}_6)_4$ was mainly assessed from concentration-dependent $^1\text{H-NMR}$ measurements carried out in CH_3CN for $38(\text{PF}_6)_4$ and $42(\text{PF}_6)_4$ and in acetone for $44(\text{PF}_6)_4$. The latter revealed that varying the concentration from $1 \times 10^{-3} \text{ mol.l}^{-1}$ to $5 \times 10^{-3} \text{ mol.l}^{-1}$ has in fact very little impact (less than 0.03 ppm) on all the chemical shifts. The absence of supramolecular interactions in these compounds was further confirmed by UV-vis absorbance measurements showing that the Beer Lambert Law is satisfied for all these compounds over a broad concentration range ($1 \times 10^{-3} \text{ mol.l}^{-1}$ to $5 \times 10^{-6} \text{ mol.l}^{-1}$) (Figure 119).

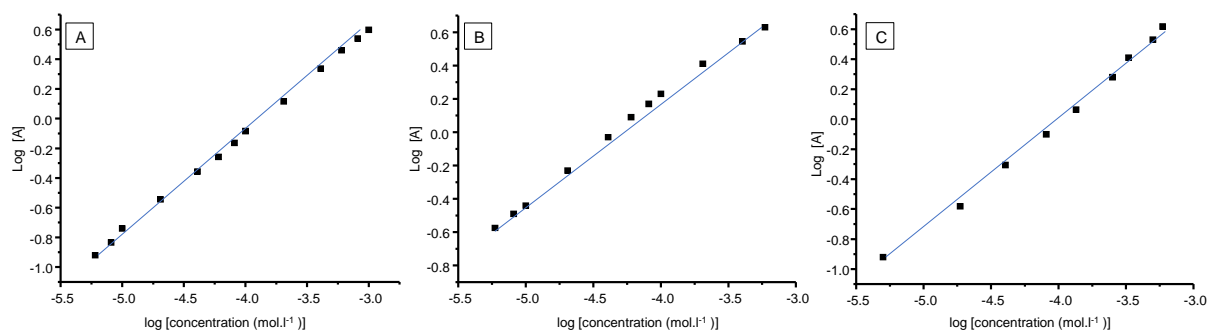


Figure 119: Variation of absorbance (logarithmic scale) measured as function of concentration (logarithmic scale) in CH_3CN . A) $38(\text{PF}_6)_4$, $\lambda = 272 \text{ nm}$, B) $42(\text{PF}_6)_4$, $\lambda = 263 \text{ nm}$, C) $44(\text{PF}_6)_4$, $\lambda = 278 \text{ nm}$.

All these results thus support the conclusion that the self-complexation of $38(\text{PF}_6)_4$, $42(\text{PF}_6)_4$, and $44(\text{PF}_6)_4$ is negligible in acetonitrile. Failure to observe such association can be explained by the existence of dynamic equilibria between the W- and U-shaped conformers and by the weak donor properties of the phenol ring.

We then turned our attention to host-guest processes involving exogenic donors featuring different size, charge and electron-donating properties. Here again the formation of host-guest

complexes has been checked from $^1\text{H-NMR}$ and UV-vis absorbance measurements carried out in organic media. We will detail below the results obtained with $\mathbf{38}(\text{PF}_6)_4$ wherein the viologen units are directly linked to the Ph-Pyr-Ph linker. Among all the donors investigated, pyrene and carbazole have given the best results. The interactions of $\mathbf{38}(\text{PF}_6)_4$ with these guests have first been investigated by $^1\text{H-NMR}$ in deuterated acetonitrile. The host-guest equilibria involved in solution were found to be kinetically fast at the NMR time scale. As can be seen in Figure 120, addition of increasing amounts of guest (pyrene) led to significant upfield shift of the viologen based protons including (H_a) resulting from the establishment of intermolecular DA interactions.

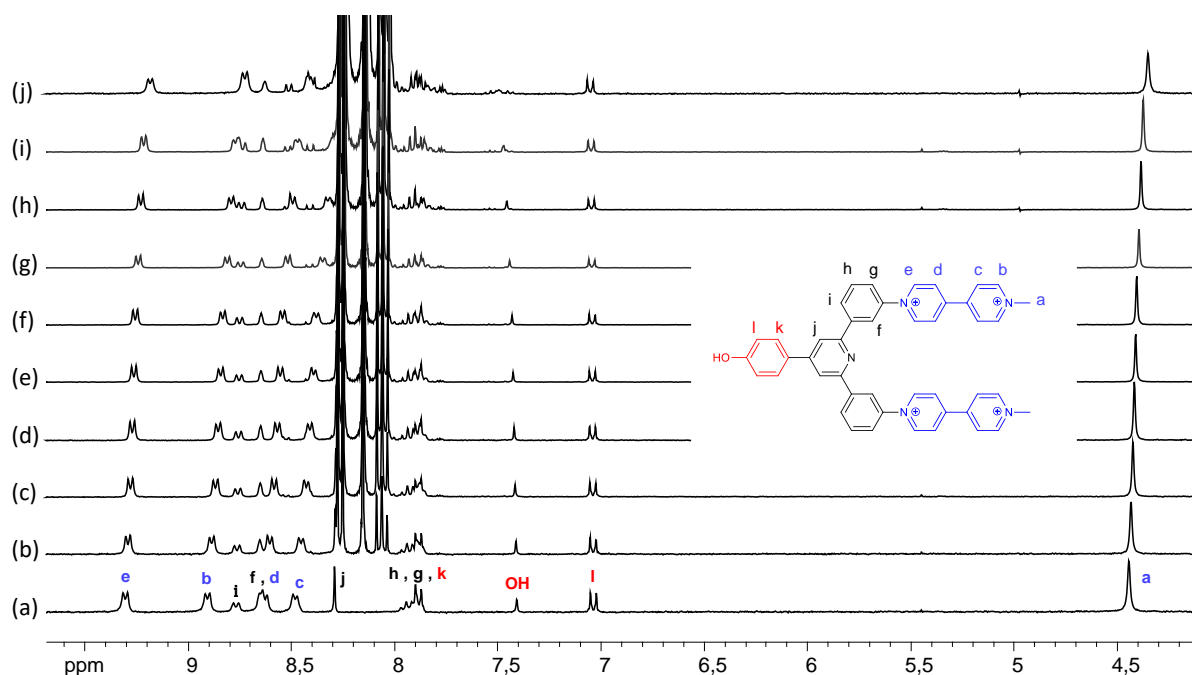


Figure 120: $^1\text{H-NMR}$ spectrum of $\mathbf{38}(\text{PF}_6)_4$ (1mM, $\text{CD}_3\text{CN-}d_3$, 295 K, 300 MHz) during the addition of [Pyrene] (number of equivalents): (a) 0, (b) 4, (c) 8, (d) 12, (e) 16, (f) 20, (g) 30, (h) 40, (i) 50, (j) 60.

The largest shift was observed for the signal attributed to H_c reaching $\Delta\delta = 0.16$ ppm after addition of pyrene in excess, to be compared with the 0.03 ppm shift observed in the same conditions for H_g . The three aromatic signals attributed to the pyrene unit were similarly found to experience an upfield shift of $\Delta\delta = 0.1$ ppm. Similar investigations conducted with carbazole led to similar findings, the most noteworthy one being the 0.2 ppm shift experienced by the signal attributed to H_c . The binding isotherm exhibits however a quite flat shape which makes any quantitative analysis of the associated HG process (stoichiometry/binding constant) difficult (see Figure 121).

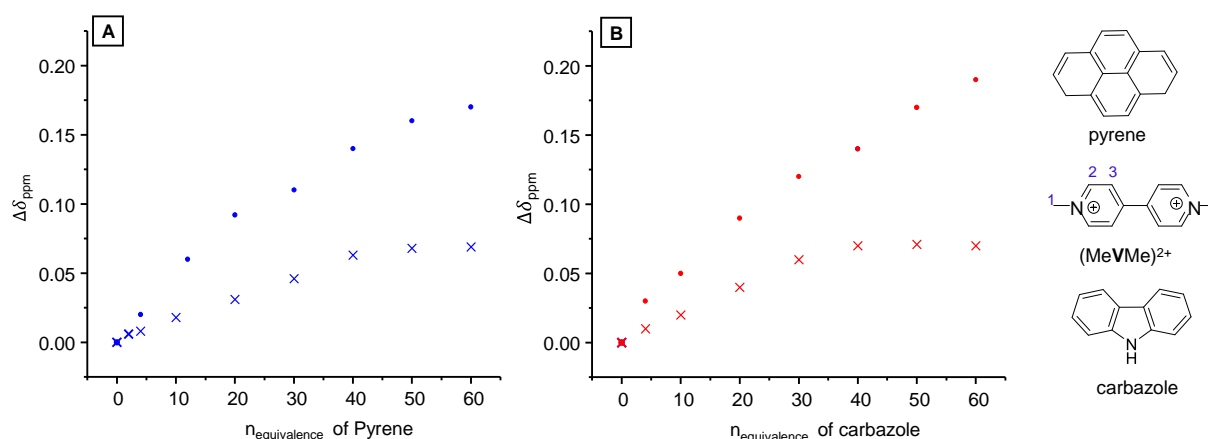


Figure 121: Changes in the chemical shift of H_c in $\mathbf{38}(\text{PF}_6)_4$ (1mM, $\text{CD}_3\text{CN}-d_3$, 295 K, 400 MHz) and H_3 in $\text{MeVMe}(\text{PF}_6)_2$ (2mM, $\text{CD}_3\text{CN}-d_3$, 295 K, 400 MHz) as a function of the amount of added guest (molar equivalents). (•) $\mathbf{38}(\text{PF}_6)_4$ + carbazole / (x) : $\text{MeVMe}(\text{PF}_6)_2$ + carbazole / (•) : $\mathbf{38}(\text{PF}_6)_4$ + pyrene / (x): $\text{MeVMe}(\text{PF}_6)_2$ + pyrene.

Similar experiments have then been carried out with $\text{MeVMe}(\text{PF}_6)_2$ used as a reference acceptor to get insights into the binding mode of $\mathbf{38}^{4+}$ (Figure 122). The ^1H -NMR data collected in the same conditions as above with this simple acceptor are plotted in Figure 121. The progressive addition of pyrene or carbazole resulted in a far more limited upfield shift of the viologen-based signals, the largest shift experienced by the signal attributed to H_3 reaching only $\Delta\delta = 0.07$ ppm in case of and $\Delta\delta = 0.06$ ppm in case of pyrene.

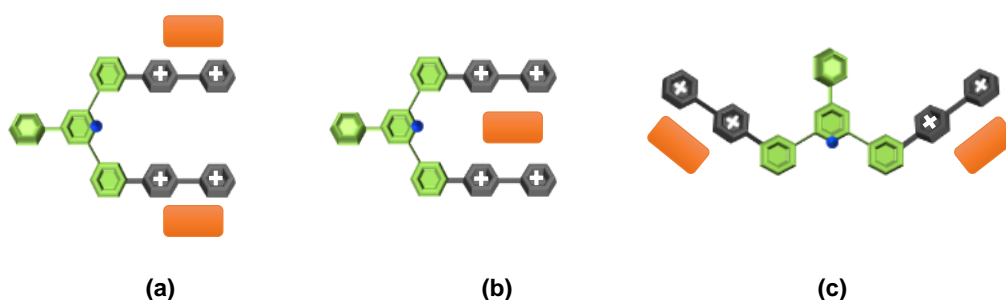


Figure 122 : Schematic representation of the possible forms of donor-acceptor interaction.

All our attempts to further characterize the HG binding process with absorption spectroscopy measurements failed due to the absence of modification observed in the UV-vis signature of $\mathbf{38}^{4+}$ upon addition of increasing amounts of those donor molecules. These preliminary experiments nevertheless revealed that $\mathbf{38}^{4+}$ has only a limited affinity for uncharged aromatic donors in acetonitrile. The differences observed between $\mathbf{38}^{4+}$ and the reference compound MeVMe^{2+} can however only be explained by a tweezer effect leading to the binding of a single guest (D) in between two viologens units (A) ((structure b) in Figure122).

Similar experiments were conducted in DMSO and water with the anionic guests **50**²⁻ and **51**²⁻ respectively, expecting that the targeted HG binding process could be strengthened by electrostatic forces. Here again, the progressive addition of those guests led to an upfield shift of all the viologen-based protons but the most important one was observed for H_d proton, reaching up to $\Delta\delta = 0.076$ ppm (Figure 123A) and $\Delta\delta = 0.075$ ppm (Figure 123B) after addition of only 10 molar equivalents of **50**²⁻ and **51**²⁻, respectively. The amplitude of the shift is here again far more important for **38**⁴⁺ than for the reference MeVMe²⁺ and the shape of the isotherms collected with those guests is consistent with the existence of a much stronger affinity between the tetracationic host and the anionic guests. Fitting those data by Bind fit with a 1/1 binding model led to binding constant estimated to $773\text{M}^{-1} \pm 12$ in DMSO % and $613\text{M}^{-1} \pm 8$ % in D₂O for **50**²⁻ and **51**²⁻, respectively.

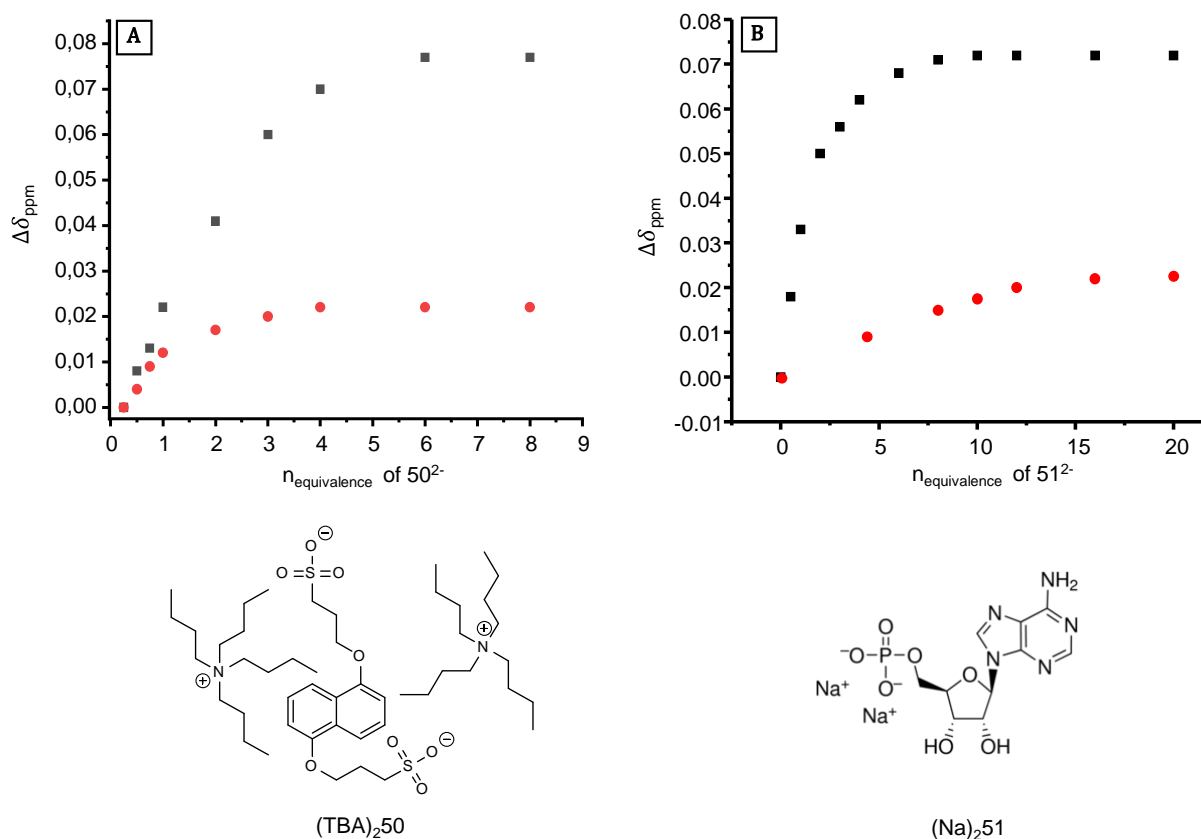


Figure 123: A) Variation of the ¹H-NMR chemical shifts attributed to Hc (■) in **38**(PF₆)₄ (1mM, DMSO-*d*₆, 295 K, 400 MHz) and H₃ (●) in MeVMe(PF₆)₂ (2mM, DMSO-*d*₆, 295 K, 400 MHz) depending on the amount of guest (TBA)₂50 added in molar equivalence. B) Variation of ¹H-NMR chemical shift attributed to Hc (■) in **45**(PF₆)₄ (1mM, D₂O, 295 K, 400 MHz) and H₃ (●) in MeVMe(PF₆)₂ (2mM, D₂O, 295 K, 400 MHz) as a function of molar equivalence of guest (Na)₂51.

The association between **38**⁴⁺ and **50**²⁻ or **51**²⁻ was further investigated by UV-vis absorbance spectroscopy measurements. These studies unfortunately proved fruitful only with **50**²⁻, whose addition to an aqueous solution of the free host **38**⁴⁺ led to a gradual decrease in the intensity of the main adsorption centred at $\lambda = 284$ nm (Figure 124A) at the expense of an

intense signal developing at 258 nm attributed to the guest molecule introduced in excess. These changes were found to come along with a well-defined isosbestic point at 280 nm.

In contrast, the progressive addition of 50^{2-} did not show any significant changes in the UV-vis absorption spectra (Figure 124B). Unfortunately, the observed changes could not be exploited to calculate the binding constants.

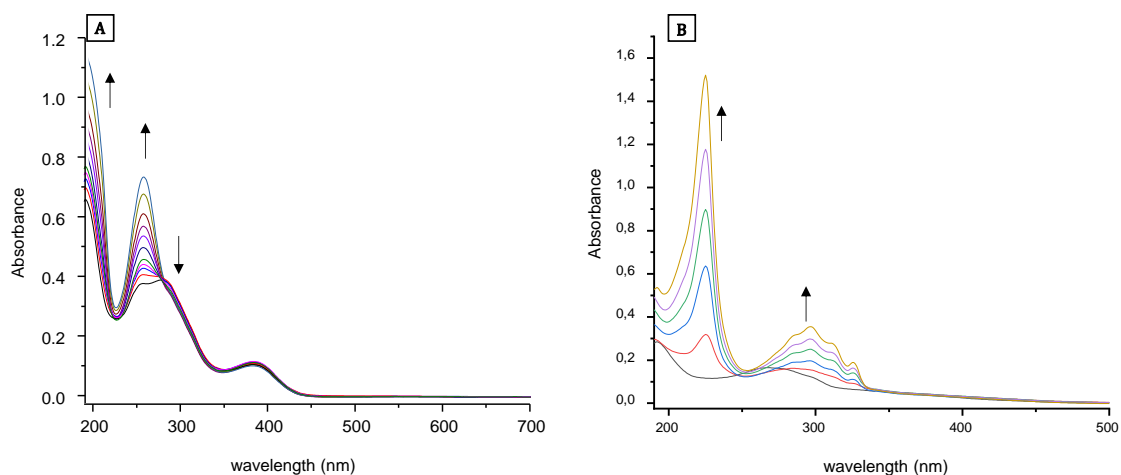


Figure 124: UV-vis absorption spectral changes of $(38(PF_6)_4)$ (1×10^{-4} M) upon addition of A) $(Na)_251$ in water. B) $(TBA)_250$

III.2.7: Conclusion

The 2,6-*bis*(phenyl)pyridine spacer is flexible/short enough to promote the intramolecular dimerization of two viologen unit introduced at the meta position of the terminal phenyl substituents. The efficiency of the dimerization has been shown to depend on the length and flexibility of the organic linkers introduced between the 2,6-*bis*(phenyl)pyridine spacer and the viologens. The binding properties of 38^{4+} have been investigated with different donors in organic and aqueous media. These studies have shown that 38^{4+} has higher affinity toward charged aromatic donors than for uncharged ones as revealed by 1H -NMR and UV-vis absorbance spectroscopy.

III.3. Flexible Tweezers Incorporating a Terpyridine Spacer

Terpyridine has been considered as a flexible linker due its ability to undergo conformational changes ($W \leftrightarrow U$ shapes) triggered by the incorporation of metal ions (Figure 93).^{175, 186} Such metal-induced conformational changes have already been exploited in host-guest chemistry upon decorating terpyridine core with suitable recognition sites.

Our objective was to introduce two viologen units at terminal position of a 2,2',6',2''-terpyridine and investigate the interest of such redox-responsive molecule to the development of switchable molecular and supramolecular systems.

III.3.1: Synthesis of the Targeted Tectons

The multi-step synthesis of the targeted tweezers **54**⁴⁺ and **56**⁴⁺ is represented in Figure 125. It starts with a condensation reaction between 4-Methoxybenzaldehyde and 2-Acetyl-6-bromopyridine to obtain the intermediate **52** in 60 % yield.¹⁸⁷ The latter was subjected to Sonogashira or Suzuki coupling reactions to afford **53** and **55**, respectively. The last step was a Zincke reaction involving **49**²⁺ as key reactant. The targeted compounds **54**⁴⁺ and **56**⁴⁺ feature either a phenyl or a slightly longer ethynyl phenyl linker, respectively.

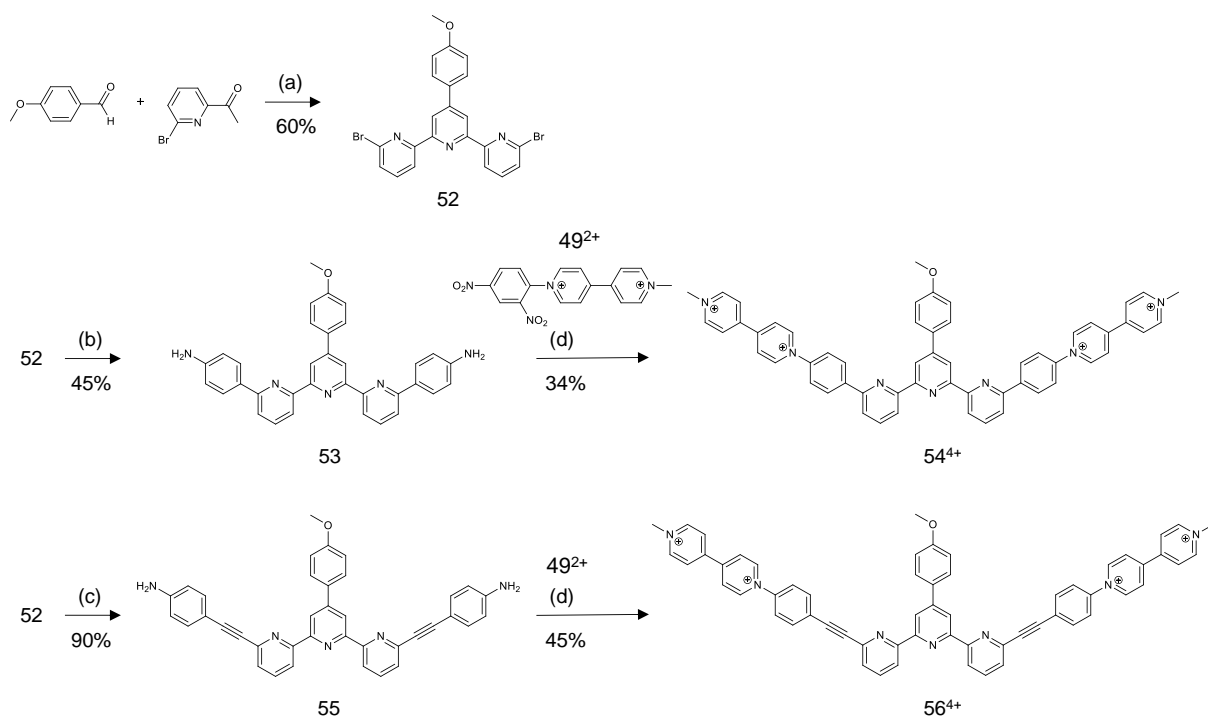


Figure 125: a) NH_4OH , KOH , reflux, 48h; (b) 4-Aminophenylboronic acid pinacol ester, $\text{Pd}(\text{PPh}_3)_4$, K_3PO_4 , THF, reflux; (c) 4-Ethynylaniline, $\text{Pd}(\text{PPh}_3)_2\text{Cl}_2$, CuI , NEt_3 , THF, reflux; (e) **49**(PF_6)₂, EtOH/DMF, 90 °C, 18h.

III.3.2. NMR Characterization

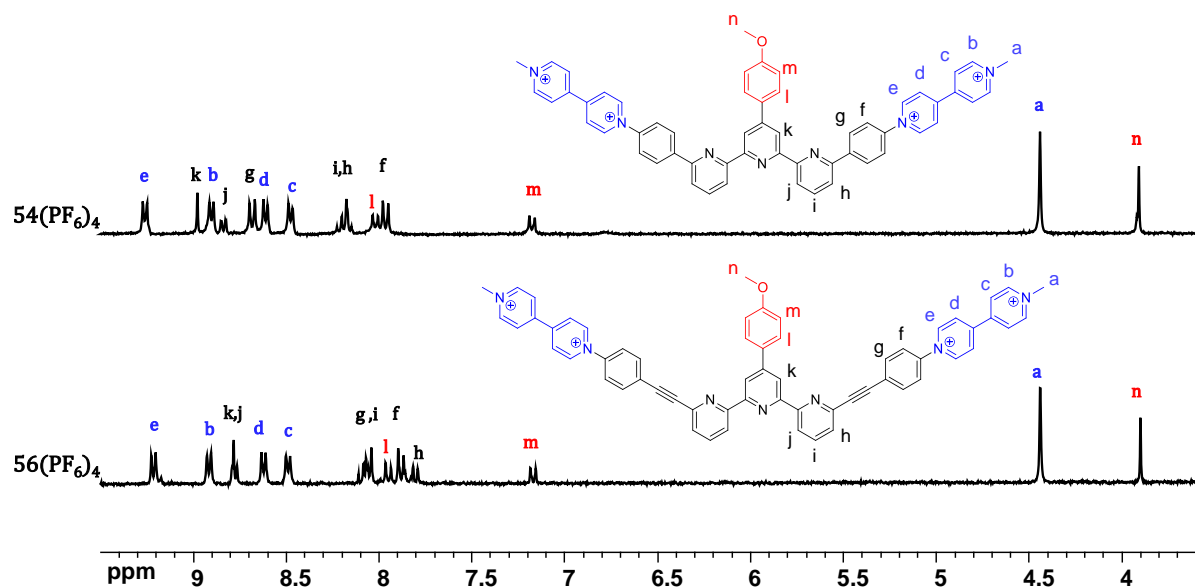


Figure 126: $^1\text{H-NMR}$ spectrum of the viologen based tweezers $\mathbf{54}(\text{PF}_6)_4$ (1 mM, $\text{CD}_3\text{CN-}d_3$) and $\mathbf{56}(\text{PF}_6)_4$ (1 mM, $\text{CD}_3\text{CN-}d_3$), recorded in (295 K, 300 MHz).

The assignments shown in Figure 126 are based on the analyses of 2D spectra (COSY, ROESY). As expected, the chemical shifts and the number of signals observed in the spectra of $\mathbf{54}(\text{PF}_6)_4$ and $\mathbf{56}(\text{PF}_6)_4$ are essentially the same. In the aromatic region, the most deshielded signals are attributed to the hydrogens of the viologen units (H_d , H_e , H_f , H_g). The protons of the terpyridine spacer (H_h , H_i , H_j , H_k) appear as four multiplets between 7.6 and 8.9 ppm while the most shielded signal at 7.2 ppm is attributed to the hydrogen located on the “electron rich” methoxybenzene ring.

Insights into the conformation of those molecules in solution (W- vs. U-shaped isomers) was provided by ROESY measurements revealing the absence of correlation between H_j and H_k . Such results supports the conclusion that these tweezers adopt a W conformation in solution imposed by the electronic repulsion between the nitrogen lone pairs and by hydrogen bonds established between H_j , H_k and the nitrogens of the pyridine rings. This is in accordance with related works described in the literature.¹⁷⁵⁻¹⁷⁶ This has been further supported by DFT calculations (collaboration with Pr. E. Dumont at ENSL) enabling to estimate the energy difference between the W-conformer and the U-conformer to 8.6 kcal.mol⁻¹ (Figure 127).

These experimental and computational data thus suggest that the terpyridine-linked compounds **54**(PF₆)₄ and **56**(PF₆)₄ exist as W-conformers in solution.

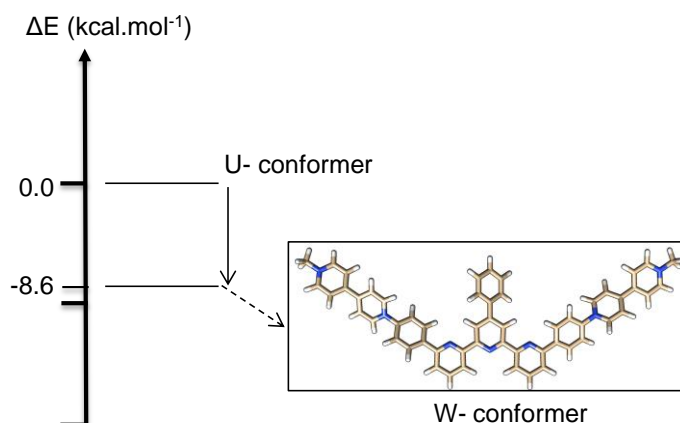


Figure 127: Relative energy difference calculated for **54**(PF₆)₄.

III.3.3. Electrochemical and Spectro-Electrochemical Characterizations

The electrochemical signatures of **54**(PF₆)₄ and **56**(PF₆)₄ have been investigated in DMF using tetra-*n*-butylammonium perchlorate (TBAP) as an electrolyte. Both compounds display similar signatures featuring two consecutive reversible reductions (1e/viologen) in the accessible potential window (Table 7).

	$E^{1c}(n, \Delta E_p)$ $V^{2+}/V^{••}$	$E^{2c}(n, \Delta E_p)$ V^{2+}/V^0	$E^{1c} - E^{2c}$ (V)
MeVMe(PF ₆) ₂	-0.882 ^b (1,62)	-1.198 ^b (1,60)	0.316
PhVMe(PF ₆) ₂	-0.709 ^b (1,58)	-1.035 ^b (1,58)	0.326
38 (PF ₆) ₄	-0.698 ^b (2,50)	-1.034 ^b (2,55)	0.336
42 (PF ₆) ₄	-0.682 ^b (2,51)	-1.002 ^{c,d}	na
44 (PF ₆) ₄	-0.667 ^b (2,43)	-1.030 ^{c,d}	na
48 (PF ₆) ₄	-0.665 ^b (2,45)	-1.030 ^{c,d}	na
54 (PF ₆) ₄	-0.685 ^b (2,44)	-1.044 ^{c,d}	na
56 (PF ₆) ₄	-0.665 ^b (2,50)	-0.956 ^{c,d}	na
(Pd ²⁺)(54 ⁴⁺)(S)	-0.673 ^b (2,63)	-1.013 ^b (2,67)	0.340

Table 7: CV data measured in the following conditions: 1x10⁻³M in DMF/TBAP (0.1 M, E(V) vs. Ag⁺/Ag), at a vitreous carbon working electrode Ø = 3 mm, 298 K, $\nu = 0.1 \text{ V}\cdot\text{s}^{-1}$. (na: Not available / ^b: Half wave potential / ^c: Peak potential / ^d: Adsorption phenomena).

The viologen units are found to be slightly easier to reduce in the alkyne-linked compound **56**⁴⁺(Figure 128) than in **54**⁴⁺, but the potential difference measured between the first and

second reduction processes remains the same (≈ 0.3 V). We found the two electron-reduced species $\mathbf{56}^{(2+\bullet)}$ to be more prone to adsorption than $\mathbf{54}^{(2+\bullet)}$, as revealed on the CV curves by the observation of Gaussian-shaped redissolution peaks on the backward scan. The latter could be however readily circumvented with suitable dilutions (below 3×10^{-4} M) or upon using a platinum as working electrode. Then insights into the ability of the viologen units to form dimers at the reduced state was moreover provided by the low ΔE_p values measured on the first reduction wave. Such conclusion implies that the one electron reduction of both viologens triggers an isomerization of the terpyridine core from the W shape revealed by NMR/computational data to a folded U-shape enabling orbital overlaps between both viologen cation radicals.

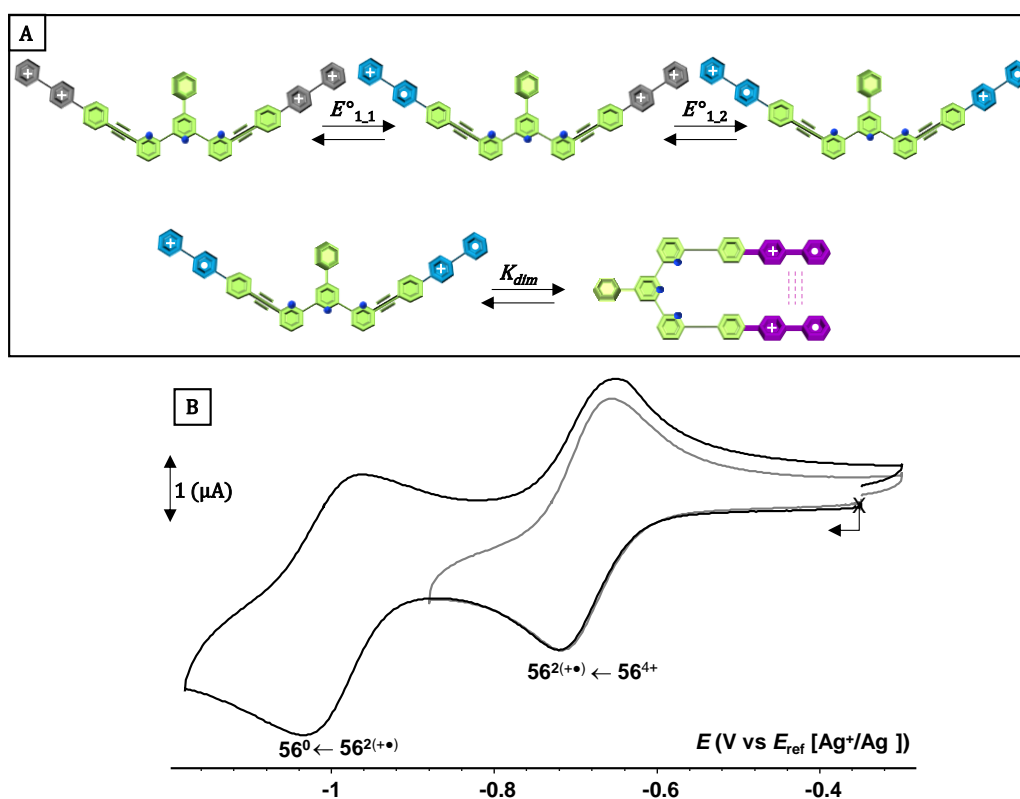


Figure 128: CV curves of $\mathbf{56}(\text{PF}_6)_4$ (5×10^{-4} M) recorded in DMF (TBAP 0.1M) using a platinum working electrode ($\varnothing = 3$ mm, E vs. Ag^+/Ag (10^{-2} M), $\nu = 0.1$ V.s $^{-1}$).

The ability of $\mathbf{54}^{(2+\bullet)}$ and $\mathbf{56}^{(2+\bullet)}$ to form the intramolecular dimers $(\mathbf{54}^{2+})_{\text{dim}}$ and $(\mathbf{56}^{2+})_{\text{dim}}$ in solution has been inferred from absorption spectroscopy measurements. The absorption spectra recorded during an exhaustive reduction (1e/viologen) of $\mathbf{54}(\text{PF}_6)_4$ carried out at in DMF at a platinum electrode led to the appearance of absorption bands centred at 440 nm ($\epsilon = 151000 \text{ M}^{-1} \cdot \text{cm}^{-1}$), 618 nm ($\epsilon = 80000 \text{ M}^{-1} \cdot \text{cm}^{-1}$), 670 nm ($\epsilon = 87500 \text{ M}^{-1} \cdot \text{cm}^{-1}$), 722 nm ($\epsilon = 68700 \text{ M}^{-1} \cdot \text{cm}^{-1}$) and 960 nm ($\epsilon = 2200 \text{ M}^{-1} \cdot \text{cm}^{-1}$) (Figure 129 A). The same experiments

carried out with **56**(PF₆)₄ led to similar changes including new absorption bands appearing at 430 nm ($\epsilon = 52600 \text{ M}^{-1} \cdot \text{cm}^{-1}$), 584 nm ($\epsilon = 25200 \text{ M}^{-1} \cdot \text{cm}^{-1}$), 668 nm ($\epsilon = 25200 \text{ M}^{-1} \cdot \text{cm}^{-1}$), 719 nm ($\epsilon = 15800 \text{ M}^{-1} \cdot \text{cm}^{-1}$) and 951 nm ($\epsilon = 3700 \text{ M}^{-1} \cdot \text{cm}^{-1}$) (Figure 129B).

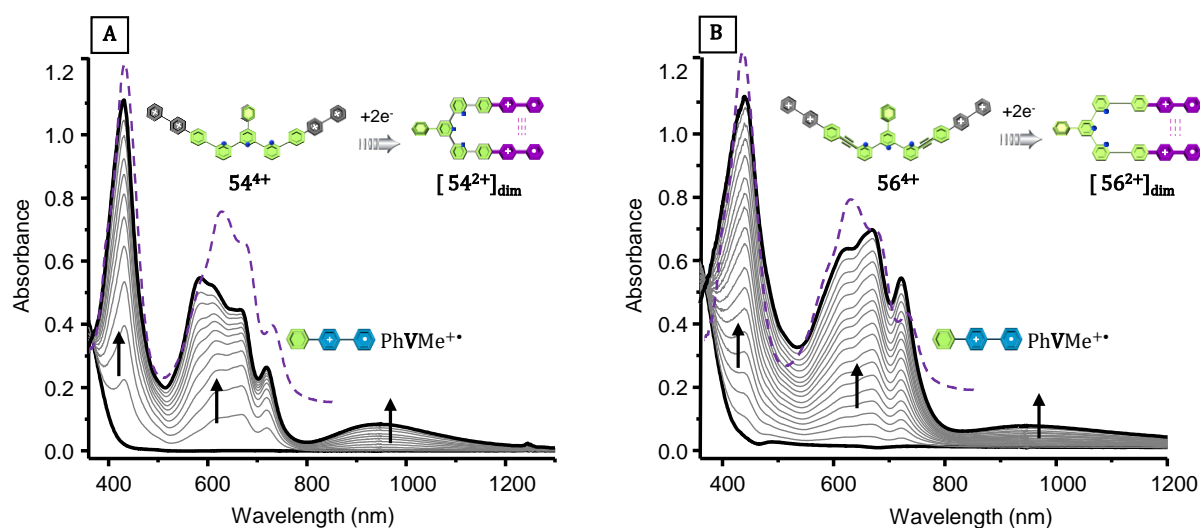


Figure 129: UV-Vis absorption spectra recorded during the exhaustive two electron reduction of (A) **54**(PF₆)₄ and (B) **56**(PF₆)₄ recorded during the exhaustive two electron reduction in [DMF + 0.1 M TBAP, l = 1 mm, t ≈ 30 min, working electrode = Pt (A : 0.16 mM, 10 mL, E_{app} = -0.91 V / B : 0.08 mM, 10 mL, E_{app} = -0.9 V].

Here again, the bands observed in the visible range between 600 nm and 730 nm are attributed to a series of transitions centered on non-dimerized free viologen cation-radical $\text{X}^{2(+\bullet)}$, (X = **54** or **56**) while the diagnostic intense signal developing between 550 and 600 nm and the broad absorption bands at $\lambda > 900 \text{ nm}$ reveals the existence of π -dimerization processes. The intramolecular nature of this dimerization was demonstrated upon checking that the shape of the absorption spectra recorded at the end of the electrolysis is independent on the initial concentration in tweezer ($3 \times 10^{-4} \text{ M}$ to $5.5 \times 10^{-5} \text{ M}$).

The efficiency of the dimerization has been assessed by spectral deconvolution showing that the relative concentration of dimerized species is higher with **54**⁴⁺ (16%) than with **56**⁴⁺ (7%). Such difference can however hardly be explained by flexibility issues as the most rigid tweezer **54**(PF₆)₄ happens to dimerize more efficiently than the most flexible one **56**(PF₆)₄.

Further insights into the structures of the π -dimers formed upon reduction was provided by DFT measurements (collaboration with Pr. E. Dumont at ENSL). The minimized structures shown in Figure 130 bring to light that both viologen sub-units adopt a twisted cofacial arrangement in [**56**²⁺]_{dim} with an interplanar distance d_1 estimated to 3.49 Å. The structure obtained for [**54**²⁺]_{dim} shows a similar twisted arrangement of the viologens, but the absence of ethynyl linker results in a much shorter interplanar distance between both viologen planes

(d_2 estimated to 3.27 Å). The relative energy difference between these two dimers is weak (2.7 kcal.mol⁻¹ in favor of [**54**²⁺]_{dim}) but significant when compared to the overall stabilization energy associated to most viologen-based π -dimerization processes (10-15 kcal mol⁻¹).

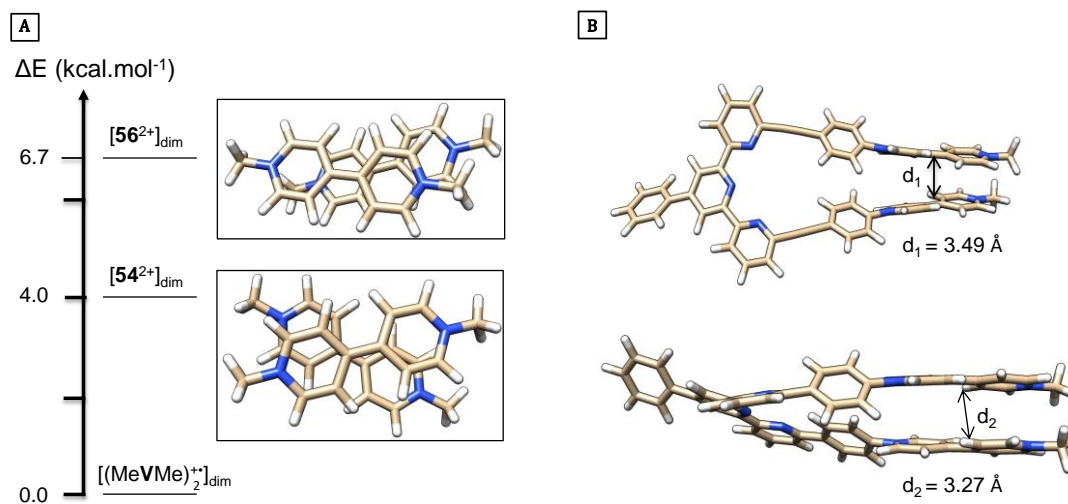


Figure 130: A) Relative energy calculated by DFT for [**54**²⁺]_{dim} and [**56**²⁺]_{dim}. B) DFT optimized structures for the π -dimers formed upon reduction of the viologen units in **54**(PF₆)₄ and **56**(PF₆)₄.

All the results discussed above demonstrate that the terpyridine-based tweezers **54**(PF₆)₄ and **56**(PF₆)₄ adopt in solution a W-shaped conformation locked by a combination of hydrogen-bonds and electrostatic repulsion issues. We have then established on the ground of electrochemical and spectroelectrochemical data that a one electron reduction of both viologen centers triggers a large amplitude conformational change yielding the U-shape isomers stabilized by the intramolecular dimerization of both viologen–cation radicals located on both sides of the terpyridine spacer.

III.3.4. Metallation of the Terpyridine Spacer

Terpyridine ligands have attracted considerable interest due to their ability to coordinate a wide range of metal ions.^{173, 188} Inspired by previous developments on chemically-switchable terpyridine molecular systems,^{176, 186, 189} we have explored the possibility of controlling the W vs. U-shaped conformations of tweezer **54**(PF₆)₄ with suitable metal ions (Figure131).

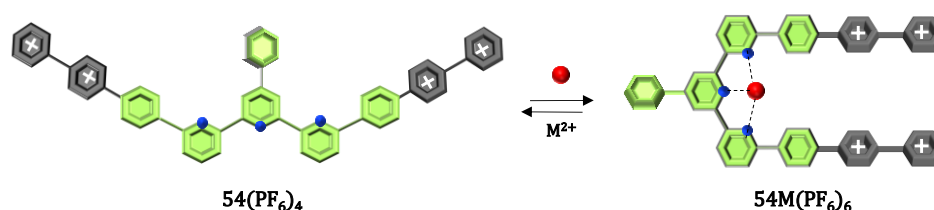


Figure 131: Expected metal triggered conformational changes involving **54**(PF₆)₄ and a suitable metal ion (M²⁺).

Our attention was first focused on the use of Pd^{2+} as a chemical trigger. Complexation was investigated with NMR spectroscopy measurements. As can be seen in Figure 132, the progressive addition of $\text{Pd}(\text{CH}_3\text{CN})_4(\text{BF}_4)_2$ to a solution of $\mathbf{54}(\text{PF}_6)_4$ in deuterated acetonitrile led to the progressive disappearance of the signals attributed to the W-shaped isomer at the expense of new signals attributed to the U-shaped 1:1 (M:L) square planar complex $[(\text{Pd}^{2+})(\mathbf{54}^{4+})\text{S}]$, S being a coordinated solvent molecule (Figure 132).

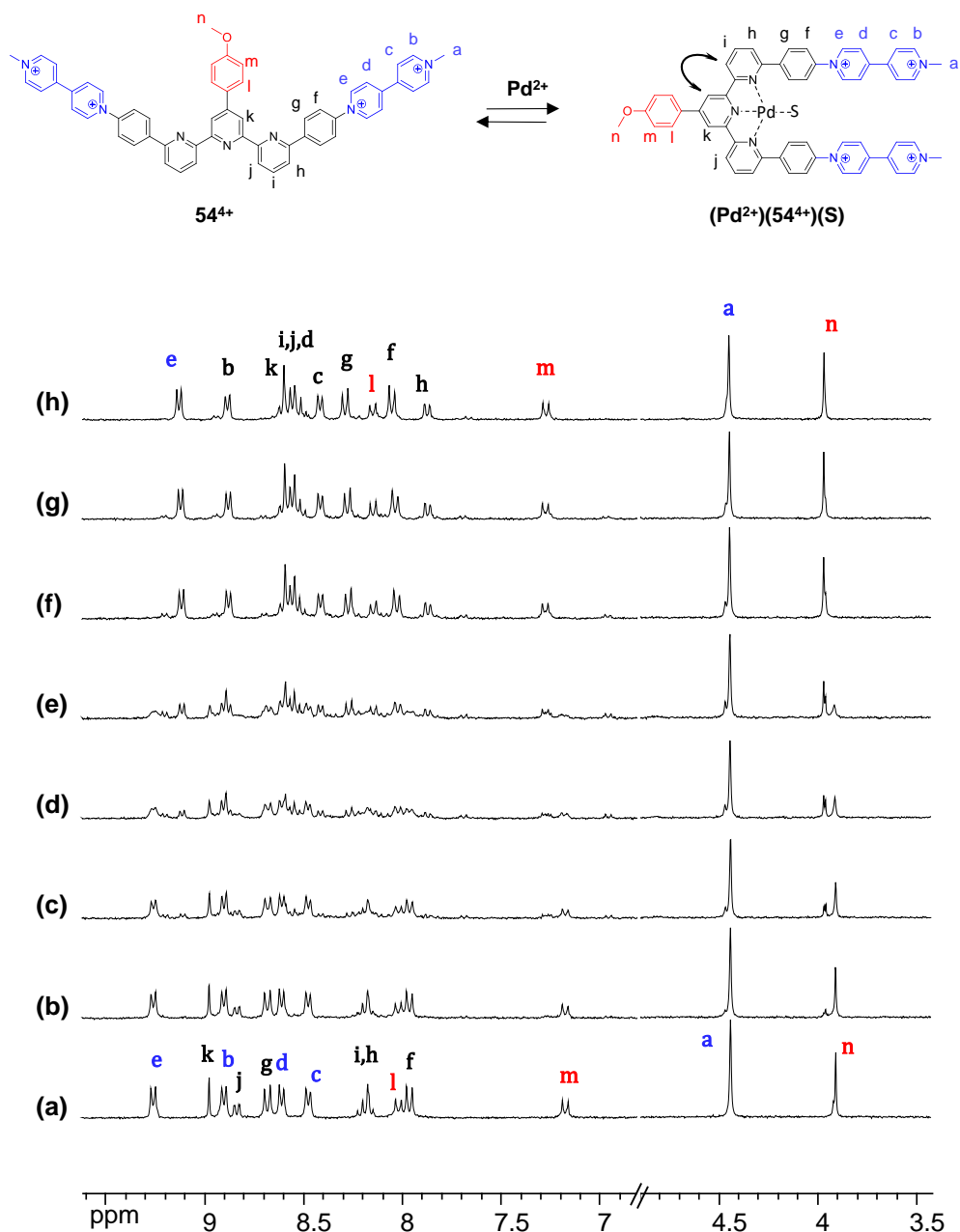


Figure 132: Partial ^1H NMR spectra (300 MHz, $\text{CD}_3\text{CN}-d_3$, 1.0 mM, 295 K) of $\mathbf{54}(\text{PF}_6)_4$ (a) in the absence, and in the presence of (b) 0.25 molar equiv. of $[\text{Pd}(\text{CH}_3\text{CN})_4(\text{BF}_4)_2]$, (c) 0.5 molar equiv. of $[\text{Pd}(\text{CH}_3\text{CN})_4(\text{BF}_4)_2]$, (d) 0.75 molar equiv. of $[\text{Pd}(\text{CH}_3\text{CN})_4(\text{BF}_4)_2]$, (e) 1 molar equiv. of $[\text{Pd}(\text{CH}_3\text{CN})_4(\text{BF}_4)_2]$, (f) 1.5 molar equiv. of $[\text{Pd}(\text{CH}_3\text{CN})_4(\text{BF}_4)_2]$, (g) 2.0 molar equiv. of $[\text{Pd}(\text{CH}_3\text{CN})_4(\text{BF}_4)_2]$ and (h) 8.0 molar equiv. of $[\text{Pd}(\text{CH}_3\text{CN})_4(\text{BF}_4)_2]$.

The isomerization process has an impact on all the signals but the most important changes are observed for the multiplets attributed to H_k and H_j , undergoing upfield shifts of 0.38 ppm and 0.22 ppm, respectively. We also found that the full conversion requires the addition of more than 2 molar equivalents of $\text{Pd}(\text{CH}_3\text{CN})_4(\text{BF}_4)_2$. Most importantly, the formation of a U-shaped isomer was confirmed by ROESY measurements revealing the through space proximity (correlation spot) between H_j and H_k .

Insertion of palladium was also monitored by UV-vis absorption spectroscopy measurements (Figure 131A). The spectrum of the free tweezer $\mathbf{54}(\text{PF}_6)_4$ features one main absorption centred at 263 nm ($\epsilon = 68000 \text{ M}^{-1}\cdot\text{cm}^{-1}$) and two shoulders at 297 and 364 nm. Addition of 0.25 molar equivalents of $\text{Pd}(\text{CH}_3\text{CN})_4(\text{BF}_4)_2$ led to the observation of a new signal at $\lambda = 264$ nm ($\epsilon = 68000 \text{ M}^{-1}\cdot\text{cm}^{-1}$) and of two shoulders at $\lambda = 296$ nm and $\lambda = 364$ nm. Subsequent addition of palladium, up to 8 molar equivalents, was then found to result in significant hyperchromic shifts of these intermediate signals to yield a final spectrum featuring one main absorption centered at 272 nm and two less intense ones at 316 and 384 nm.

Plotting the absorbance at $\lambda = 296$ nm as function of molar equivalence of Pd^{2+} revealed that two major species are formed during the titration experiment: the free tweezer $\mathbf{54}(\text{PF}_6)_4$ that predominates up to $M:L = 1$ and the square-planar palladium complex $[(\text{Pd}^{2+})(\mathbf{54}^{4+})(\text{S})]$ observed as the major species at $M:L > 1$ (Figure 133B).

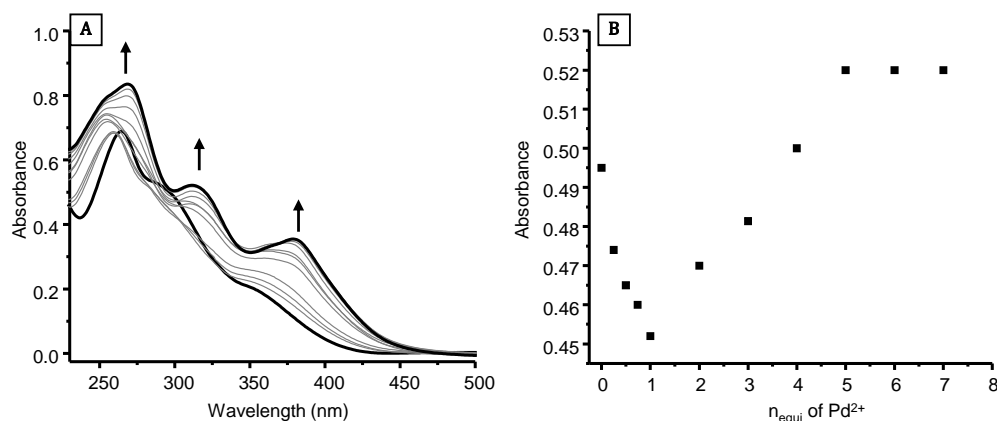


Figure 133: A) UV-Vis spectra of $\mathbf{54}(\text{PF}_6)_4$ ($1 \times 10^{-4} \text{ mol}\cdot\text{l}^{-1}$) in CH_3CN upon addition of increasing amount of $\text{Pd}(\text{CH}_3\text{CN})_4(\text{BF}_4)_2$. B) Changes in the absorption intensity at $\lambda = 296$ nm as a function of the amount of $\text{Pd}(\text{CH}_3\text{CN})_4(\text{BF}_4)_2$ (n_{equi} = number of molar equivalents).

In agreement with previous reports on terpyridine-palladium complexes, the $^1\text{H-NMR}$ and UV-vis spectroscopy data recorded in the presence of an excess metal are attributed to the 1:1 (M:L) square planar palladium complex $(\text{Pd}^{2+})(\mathbf{54}^{4+})(\text{S})$, featuring one single solvent molecule

(S) bound to the palladium center. The intermediate complex formed at low M:L ratio has not yet been identified.

Similar investigations have been conducted using $\text{Zn}(\text{OTf})_2$ as the metal source. Here again, the progressive addition of zinc was found to induce a progressive disappearance of the initial signals attributed to the W-shaped tweezer at the expense of a single set of signals corresponding to the U-Shaped 1:1 (M:L) zinc complex $[(\text{Zn}^{2+})(\mathbf{54}^{4+})(\text{S})_n]$ (Figure 134). The conversion appears almost completed after addition of 1.25 molar equivalent of metal but 2 equivalents were needed to obtain a clean ^1H -NMR of the U-Shaped isomer. The U-shaped conformation of $[(\text{Zn}^{2+})(\mathbf{54}^{4+})(\text{S})_n]$ was confirmed by the observation of correlation between H_j and H_k in the 2D ROESY map recorded after addition of an excess metal.

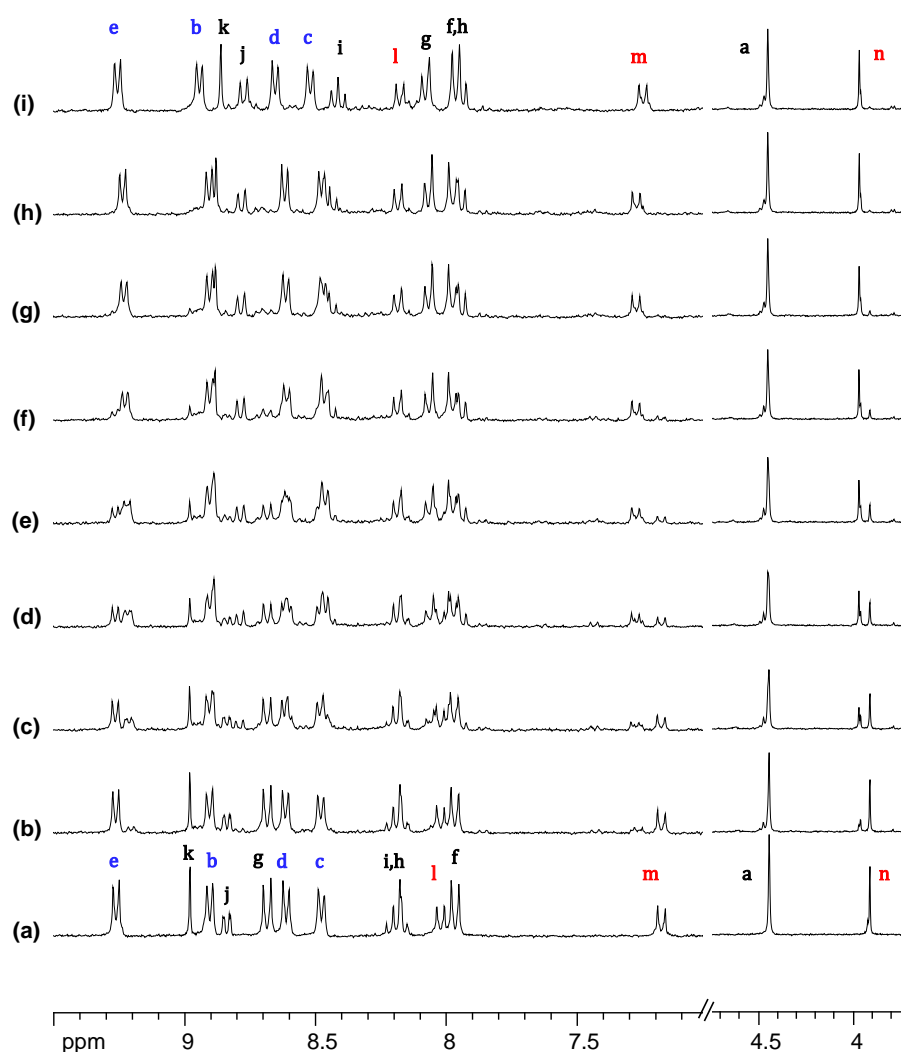


Figure 134: Partial ^1H -NMR spectra (300 MHz, $\text{CD}_3\text{CN}-d_3$, 1.0 mM, 295 K) of $\mathbf{54}(\text{PF}_6)_4$ (a) in the absence, and in the presence of (b) 0.25 molar equiv. of $[\text{Zn}(\text{OTf})_2]$, (c) 0.5 molar equiv. of $[\text{Zn}(\text{OTf})_2]$, (d) 0.75 molar equiv. of $[\text{Zn}(\text{OTf})_2]$, (e) 1 molar equiv. of $[\text{Zn}(\text{OTf})_2]$, (f) 1.25 molar equiv. of $[\text{Zn}(\text{OTf})_2]$, (g) 1.5 molar equiv. of $[\text{Zn}(\text{OTf})_2]$, (h) 2.0 molar equiv. of $[\text{Zn}(\text{OTf})_2]$ and (i) 8.0 molar equiv. of $[\text{Zn}(\text{OTf})_2]$.

The changes observed in the UV–vis absorbance signature upon addition of Zn^{2+} are shown in Figure 135A. This evolution is consistent with the absence of intermediate and with the formation of a single product featuring one main absorption at $\lambda=262$ nm and two intense shoulders at 296 and 344 nm.

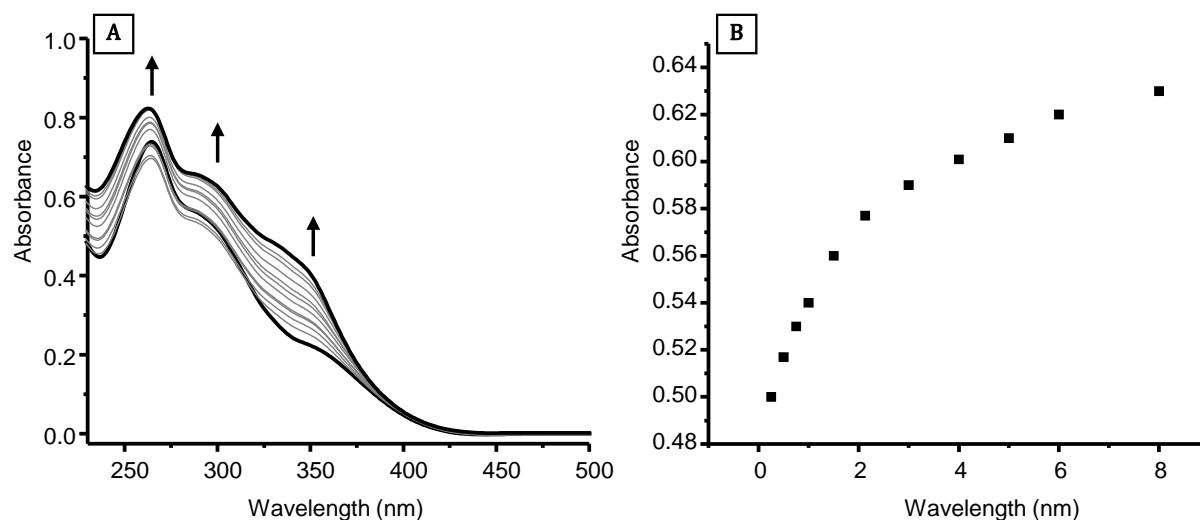


Figure 135: A) UV-vis spectra of $[\mathbf{54}(\text{PF}_6)_4]$ ($1 \times 10^{-4} \text{ mol}\cdot\text{l}^{-1}$) in CH_3CN upon addition of increasing amount of $\text{Zn}(\text{Otf})_2$. B) Changes in the absorption intensity at $\lambda = 295$ nm as a function of the amount of $\text{Zn}(\text{Otf})_2$ (n_{equ} = number of molar equivalents).

III.3.5. Electrochemistry of the Coordination Complexes

The Pd complex $[(\text{Pd}^{2+})(\mathbf{54}^{4+})(\text{S})]$ has been isolated and subjected to electrochemical studies (Figure 136A). One objective was to determine whether the presence of a metal, and the associated U-shape, would promote or hinder the π -dimerization of the viologen radicals.

The CV curve of $[(\text{Pd}^{2+})(\mathbf{54}^{4+})(\text{S})]$ in DMF exhibits two consecutive viologen-centered reduction waves. In terms of potential, the presence of palladium has little effects on the potential values needed to reduce the viologens (Table 7) but it has a significant impact on the shape of the first viologen-centered wave. Formation of the doubly reduced species $[(\text{Pd}^{2+})\mathbf{54}^{2(+\bullet)}(\text{S})]$ indeed appears as a broad quasi-reversible wave featuring a marked shoulder, a result which stands in sharp contrast to the well-defined wave observed with the free ligand. Further characterization of the reduced species by spectroelectrochemical methods revealed that a two electron reduction of $[(\text{Pd}^{2+})(\mathbf{54}^{4+})(\text{S})]$ results in the development of absorption bands centred at 431 nm ($\epsilon = 57500 \text{ M}^{-1}\cdot\text{cm}^{-1}$), 615 nm ($\epsilon = 27600 \text{ M}^{-1}\cdot\text{cm}^{-1}$), 668 nm ($\epsilon = 26900 \text{ M}^{-1}\cdot\text{cm}^{-1}$), 719 nm ($\epsilon = 17500 \text{ M}^{-1}\cdot\text{cm}^{-1}$) and 948 nm ($\epsilon = 4400 \text{ M}^{-1}\cdot\text{cm}^{-1}$). A simple comparison of these data with those collected during the reduction of $\mathbf{54}^{4+}$ alone brings to light the negative impact of the palladium center on the dimerization equilibrium.

The spectrum recorded after two electron reduction of $[(\text{Pd}^{2+})(\mathbf{54}^{4+})(\text{S})]$ indeed reveals that the non-dimerized species $[(\text{Pd}^{2+})(\mathbf{54}^{2(+\bullet)})(\text{S})]$ is the most abundant species in solution and that the π -dimer $[(\text{Pd}^{2+})(\mathbf{54}^{2+})(\text{S})]_{\text{dim}}$ is present in limited quantity (Figure 136B) $|(\text{Pd}^{2+})(\mathbf{54}^{2+})(\text{S})]_{\text{dim}}| / |(\text{Pd}^{2+})(\mathbf{54}^{2(+\bullet)})(\text{S})| \sim 8\%$. These results thus support the conclusion that the palladium center inhibits the π -dimerization of the viologen units, most probably due to the increased rigidity of the molecule and to the presence of a coordinated solvent molecules lying in between both viologens.

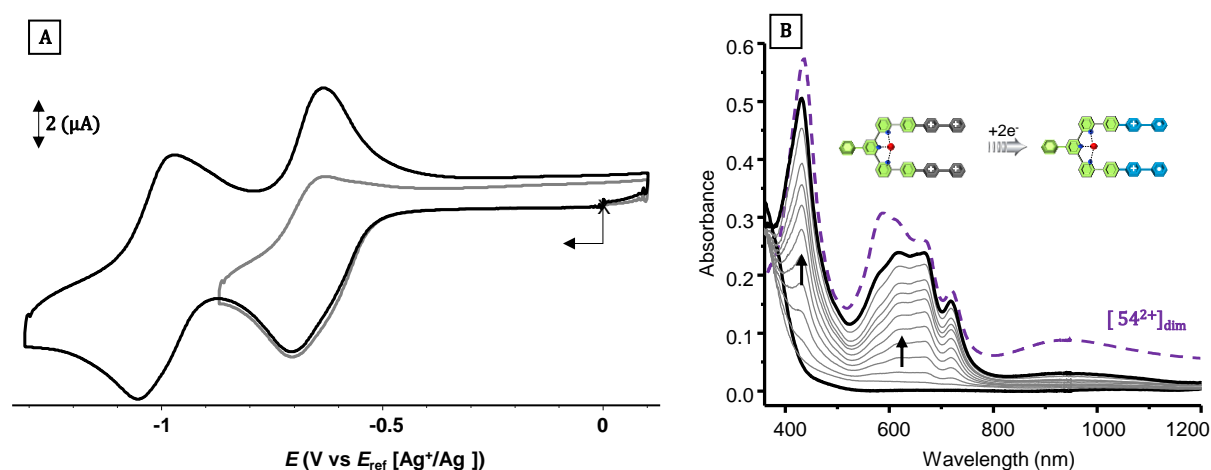


Figure 136: A) CV curve of $[(\text{Pd}^{2+})(\mathbf{54}^{4+})(\text{S})]$ (1×10^{-3} M) recorded in DMF (TBAP 0.1M) using a platinum working electrode ($\varnothing = 3$ mm, E vs. Ag^+/Ag (10^{-2} M), $v = 1 \text{ V}\cdot\text{s}^{-1}$), B) UV-vis absorption spectra recorded during the exhaustive two electron reduction of $[(\text{Pd}^{2+})(\mathbf{54}^{4+})(\text{S})]$ in [DMF + 0.1 M TBAP, $l = 1$ mm, $t \approx 30$ min, working electrode = Pt, $C = 0.11$ mM, 10 mL, $E_{\text{app}} = -0.85$ V].].

Similar investigations carried out on the zinc complex failed due to the apparent dissociation of the complex in DMF. All the data recorded in acetonitrile proved unusable/inconclusive due to the extensive adsorption of the reduced species at the electrode surface.

III.3.6. Conclusion

The terpyridine-based tweezers adopt a W-shaped conformation in solution that is locked by a combination of hydrogen-bonds and electrostatic repulsion forces. It has been established on the ground of electrochemical and spectro-electrochemical data that a one electron reduction of both viologen centers triggers a large amplitude conformational change yielding the U-shaped isomers stabilized by intramolecular dimerization of both viologen–cation radicals located on both sides of the terpyridine spacer. Insertion of a metal ion in the terpyridine spacer also proved to inhibit the π -dimerization of the viologens.

III.4. Rigid Viologen-Based Clips Incorporating Dibenzoacridine Linker

The targeted clips involve a rigid π -conjugated linker, initially introduced by Zimmerman and co-workers,^{166, 190} made of 5 fused aromatic rings. The U-shape of the molecule is blocked and the distance between both terminal attachment points is 7.24 Å. Those features were thought to promote the formation of sandwich-like ADA complexes.

III.4.1. Synthesis of the Targeted Tectons

The multi-step synthesis of the targeted clips is shown in Figure 137. The first step is a Friedel-Craft acylation of bromobenzene yielding **57** in 50% yield.¹⁹¹ The latter was then subjected to a Wolff-Kishner reduction reaction followed by a cyclisation in acidic medium to afford the first key intermediate **59**.¹⁹¹

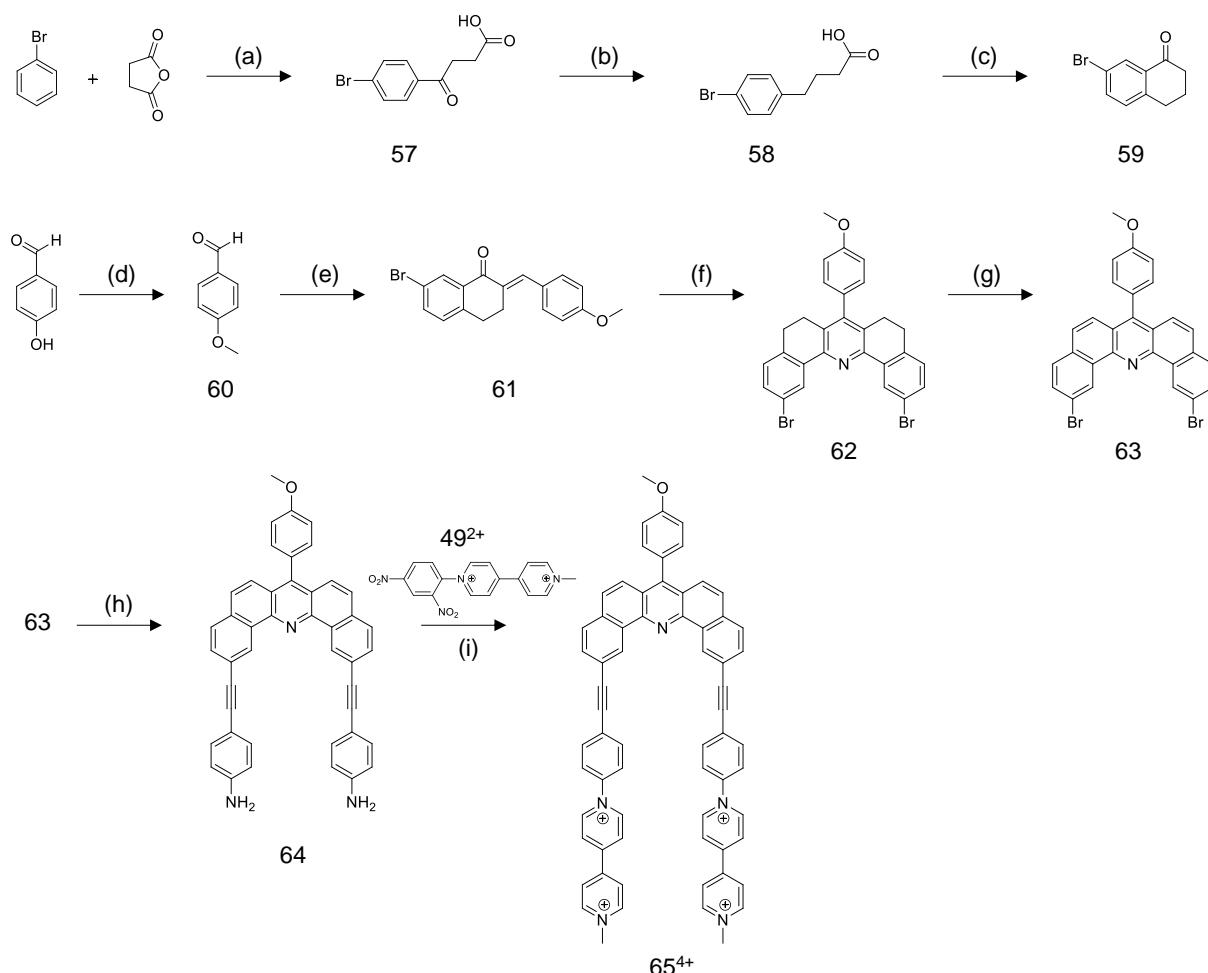


Figure 137: (a) $C_2H_4Cl_2$, $AlCl_3$, reflux, 4h, 48%; (b) $N_2H_4 \cdot H_2O$, KOH , triethyleneglycol, 3h, reflux, 75%; (c) PPA, 90°C, 3h, 72%; (d) K_2CO_3 , CH_3I , DMF, 6h, 75°C, 95%; (e) $NaOH$, **59**, 12h, 79°C, 80%; (f) $BF_3 \cdot Et_2O$, **59**, NH_4OAc -EtOH(3M), 32h, 115°C, 10%; (g) DDQ, dioxane, 24h, 95%; (h) 4-Ethynylaniline, CuI , $Pd(PPh_3)_2Cl_2$, DMF, piperidine, reflux, 24h, 40%; (i) **49**(PF_6)₂, EtOH/ CH_3CN /THF, 70 °C, 18h, 33%.

The second part of this synthesis begins by an alkylation of 4-hydroxybenzaldehyde with iodomethane to obtain compound **60**.¹⁹² The second key intermediate, the α,β -unsaturated ketone **61**, was then obtained through a Claisen-Schmidt condensation involving **59** and **60** as reactants. Reaction of **61** with **59** in boron trifluoride etherate afforded the targeted linker **62** in 10% yield. The four methylenic positions could then be oxidized in the presence of DDQ to obtain the fully conjugated compound **63**. The final steps involved a Sonagashira coupling reaction to introduce two 4-ethynylaniline substituents in compound **63** followed by a Zincke reaction with the viologen derivative **49**²⁺ to obtain the desired clip **65**⁴⁺ as a red powder.

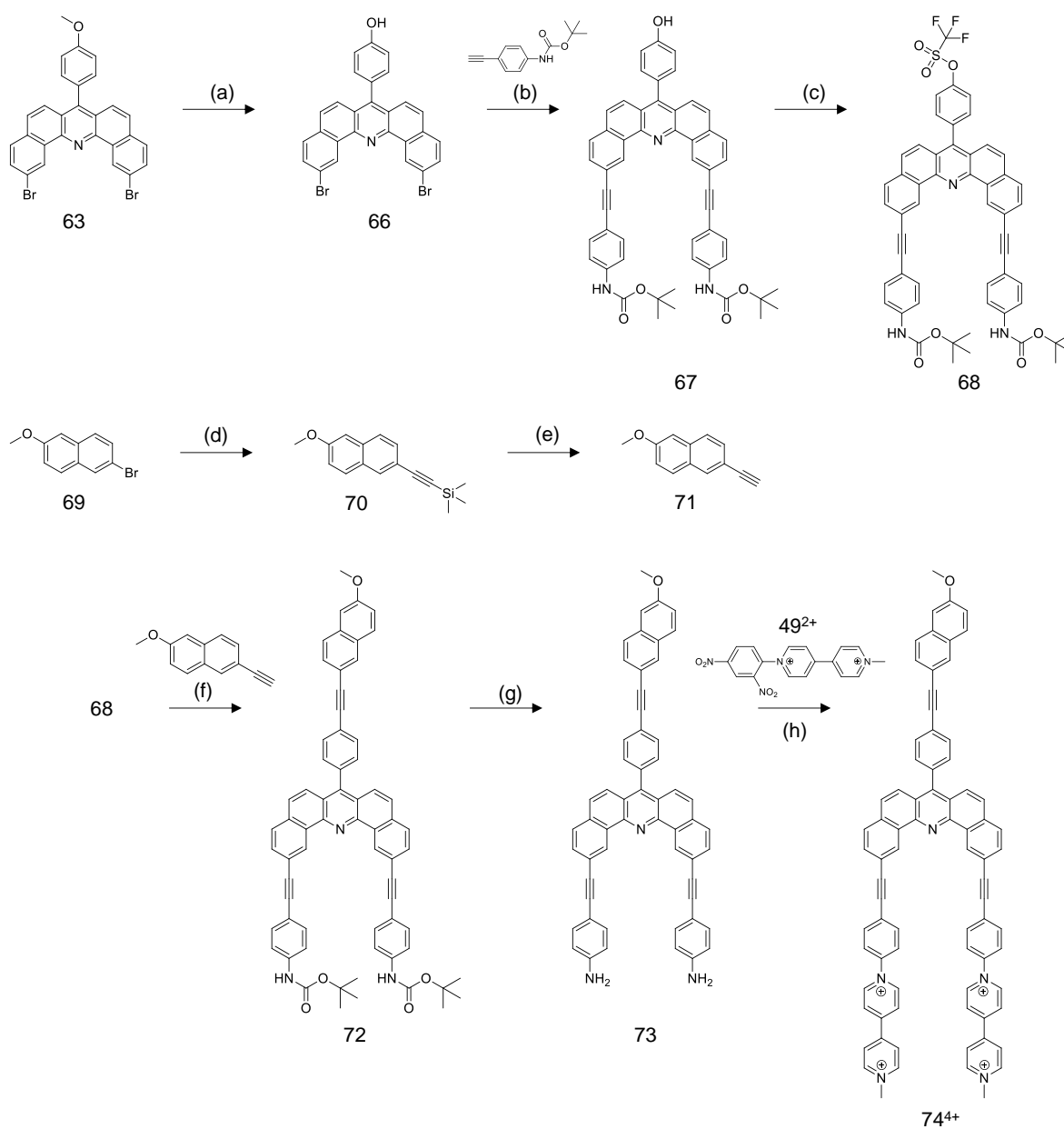


Figure 138: (a) BBr_3 , RT, CH_2Cl_2 , 95%; (b) CuI , $\text{Pd}(\text{PPh}_3)_2\text{Cl}_2$, DMF, piperidine, reflux, 24h, 40%; (c) Trifluoromethanesulfonic anhydride, pyridine, RT, 95%; (d) Ethynyltrimethylsilane, NEt_3 , $\text{Pd}(\text{PPh}_3)_4$, CuI , PPh_3 , THF, RT, 80%; (e) K_2CO_3 , THF/ CH_3OH , RT, 80%; (f) CuI , $\text{Pd}(\text{PPh}_3)_2\text{Cl}_2$, DMF, NEt_3 , reflux, 48h, 70%; (g) TFA, RT, CH_2Cl_2 , 85%; (h) **49**(PF_6)₂, EtOH/ CH_3CN /THF, 70 °C, 18h, 10%.

A methoxybenzene ring has been introduced at the back of the polyaryl spacer to enable its further modification with electron-donor groups. This strategy has been validated with the synthesis of **74**⁴⁺, bearing a methylnaphthalene substituent (Figure 138). The first step relies on the use of BBr₃ to remove the methoxy group in **63** and afford the phenol-appended compound **66**. Then, the latter was submitted to a Sonagashira coupling reactions with Boc-protected 4-ethynylaniline to yield **67** in 40% yield. Introduction of a triflate group on the phenol moiety was subsequently achieved at RT in *ca* 95% yield using pyridine and trifluoromethanesulfonic anhydride as key reactants.

Introduction of the naphthalene substituent was then achieved from a palladium-assisted coupling reaction between **68** and the ethynyl methoxy-naphthalene **71**¹⁹³ obtained in two steps from the commercially-available 2-Bromo-6-methoxynaphthalene. The Boc protecting group in **72** was finally removed in acidic conditions and the bis-aniline **73** was reacted with the “activated” viologen derivative **49**²⁺ to yield the targeted clip **74**(PF₆)₄ isolated as a red solid.

The most challenging and difficult step turned out to be the purification of **74**(PF₆)₄ which could in part be achieved by column chromatography on silica gel using mixtures of polar solvents and salts.

Formation of all the compounds discussed above was confirmed by 1D and 2D-NMR analyses supported by low and high resolution mass spectrometry data. Compound **67** could be further characterized at the solid state by X-ray diffraction analysis conducted on monocrystals grown in acetone by slow evaporation.

Selected side and top views of this species are shown in Figure 139. All the aromatic rings involved in the dibenzoacridine spacer and in the viologen-based arms lie more or less within the same plane. This doesn't include the methoxy phenyl substituent which is found tilted by an angle of 50.31° relatively to the dibenzoacridine plane. The distance measured between the upper and lower attachment points on the dibenzoacridine spacer is $d_1=7.089$ Å, but the flexibility of the alkyne fragment results in a significant inward bending of the Boc-protected arms $d_2=6.50$ Å (Figure 139B). Another interesting feature supporting the idea that such molecule might be prone to aggregation in solution, is the quite short interplanar distances of 4.04 Å measured between two different molecules within the crystal (Figure 139C).

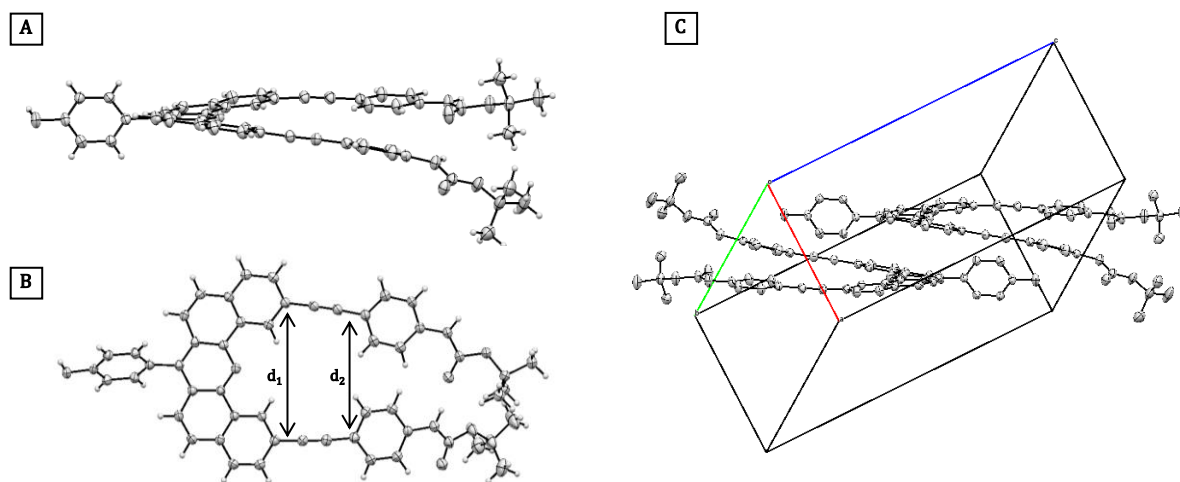


Figure 139 : Side (A) and Top (B) views of **67** and partial overview of the crystal lattice (C).

III.4.2. $^1\text{H-NMR}$ Characterization

A full attribution of the $^1\text{H-NMR}$ spectra of **65**(PF₆)₄ recorded in deuterated acetonitrile, together with a series of spectra revealing the effect of concentration are shown in Figure 140. At 1mM, the hydrogen atoms located on the viologen units appear as four doublets ($J = 6.4$ and 7.7 Hz) observed between 8.4 and 9.5 ppm. The most deshielded signal at about 10 ppm is attributed to both H_h protons which are most probably hydrogen-bonded to the same nitrogen atom of the central pyridine. The other hydrogen atoms located on the conjugated spacer (H_i-H_l) resonate in a more standard range, *ie* between 7.6 and 8.4 ppm, together with the signals attributed to the aromatic protons of the methoxybenzene group (H_n-H_m).

As can be seen in Figure 140, significant changes could be observed upon increasing the concentration of **65**(PF₆)₄ from 1 to 10 mM. All the signals undergo upfield shifts except those attributed to H_m and H_a, undergoing a downfield shift of about 0.03 ppm and 0.01ppm, respectively. The signals attributed to the viologen unit experience only little shifts, reaching 0.03 ppm at 10mM. The most significant shifts, from 0.1 to 0.25 ppm, are observed for the signals attributed to the dibenzoacridine moiety (H_h, H_i, H_j,H_k,H_l). In the case of (H_k, H_i) the shift of 0.1 ppm comes along with a drastic change in multiplicity, from the doublet observed at 1mM to a singlet at 10 mM. All these results thus suggest the existence of a concentration-induced aggregation phenomena leading to the formation of “self-assembled” architectures most likely stabilized though van der Waals interactions involving the planar π -conjugated dibenzoacridine fragments.

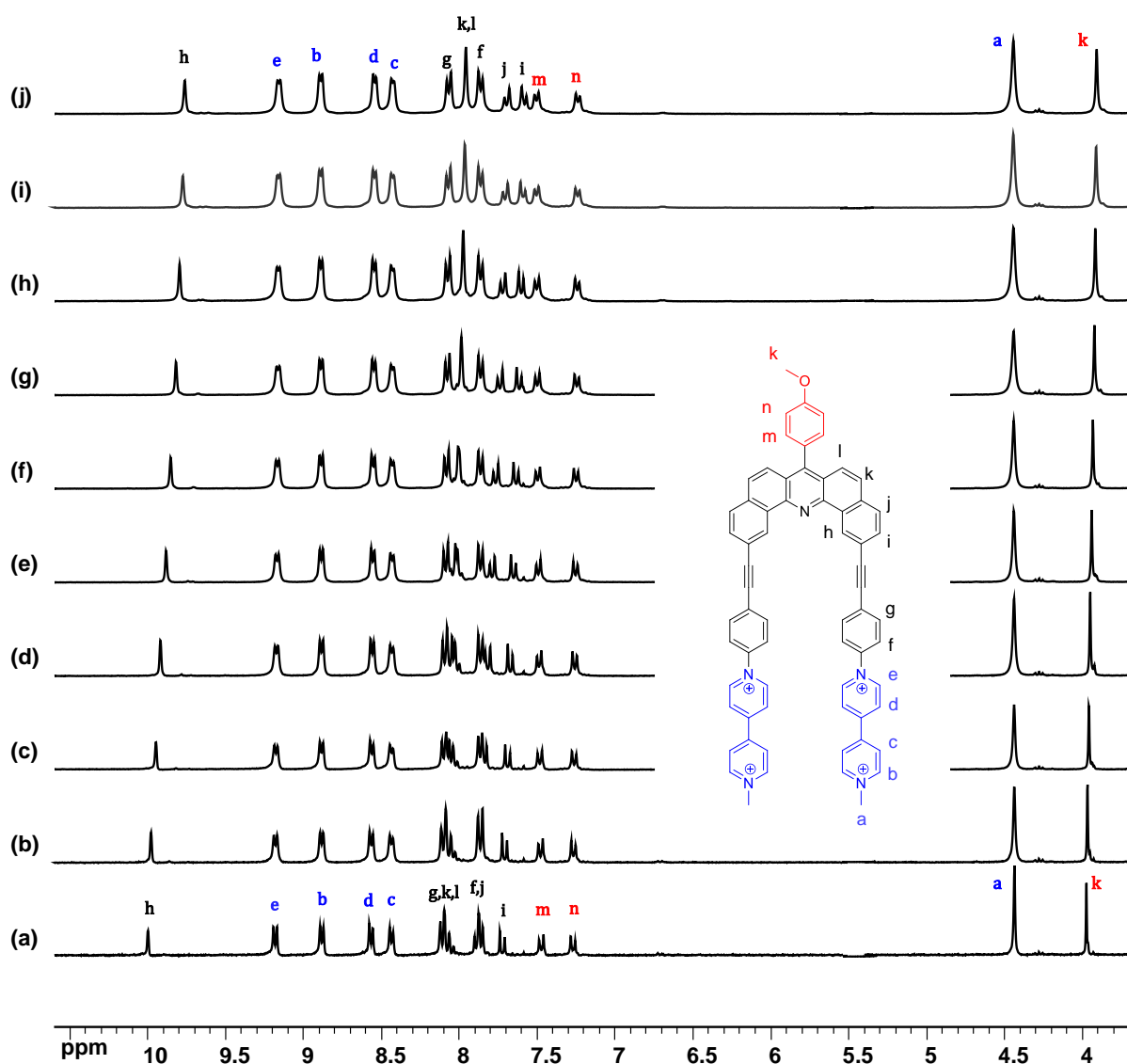


Figure 140: $^1\text{H-NMR}$ spectrum of $65(\text{PF}_6)_4$ recorded at different concentrations, (a) 1m, (b) 2mM, (c) 3mM, (d) 4mM, (e) 5mM, (f) 6mM, (g) 7mM, (h) 8mM, (i) 9mM, (j) 10mM ($\text{CD}_3\text{CN-d}_3$, 295 K, 300 MHz).

We were keen to conduct similar concentration-dependent experiments with $74(\text{PF}_6)_4$, featuring a much better π -donor on the back of the clip. The unusual broadness of all the signals and the low solubility of this compounds in most organic solvent has unfortunately greatly limited these investigations and did not allow us to draw clear-cut conclusions. Preliminary experiments nevertheless revealed the existence of strong concentration and solvent effects, mostly revealed by the large amplitude shifts of all the broad, unfortunately not yet attributed, signals observed in the $^1\text{H-NMR}$ spectrum of $74(\text{PF}_6)_4$. These results are nevertheless consistent with the ability of this molecule to self-assemble in solution. Further investigations will be needed to confirm these assumptions.

III.4.3. Electrochemical and Spectro-electrochemical Characterizations

Electrochemical measurements have been carried out in DMF (0.1 M TBAP) at room temperature under an argon atmosphere.

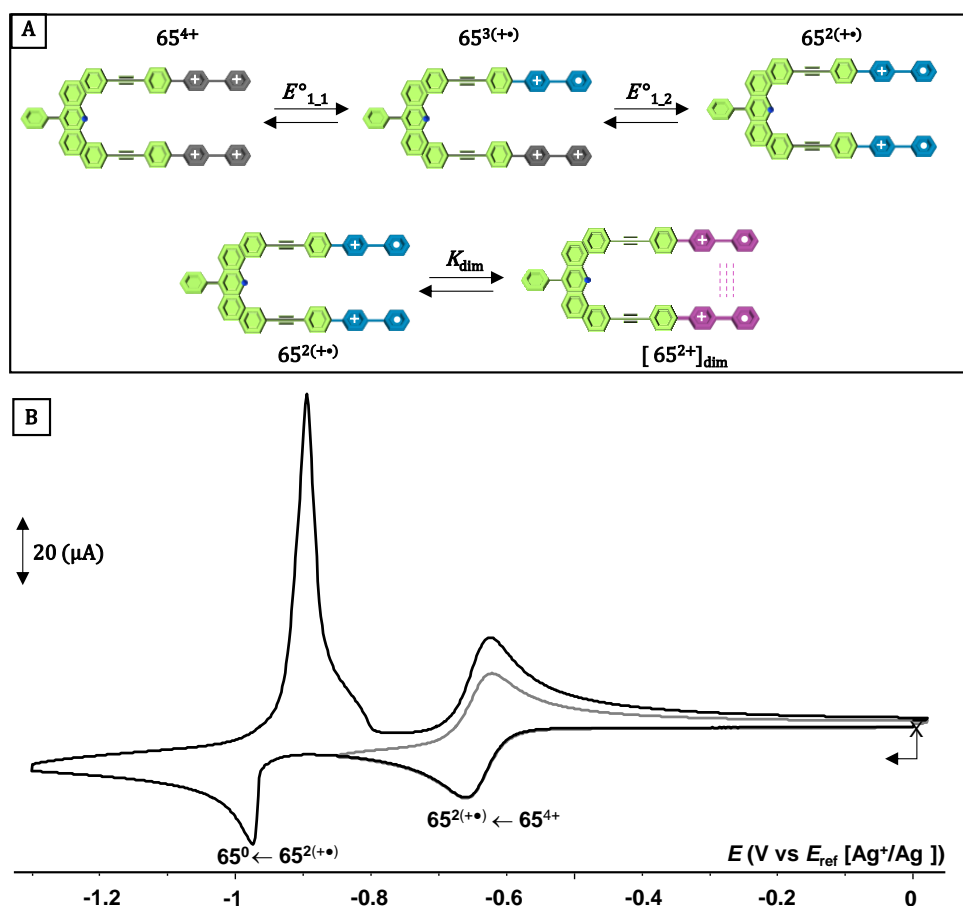


Figure 141: CV curves of $65(PF_6)_4$ (1×10^{-3} M) recorded in DMF (TBAP 0.1M) using a carbon working electrode ($\varnothing = 3$ mm, E vs. Ag^+/Ag (10^{-2} M), $v = 0.1$ V.s $^{-1}$).

As expected, the CV curves recorded for $65(PF_6)_4$ and $74(PF_6)_4$ exhibit similar features (see relevant values collected in Table 8). It includes two consecutive viologen-centered reduction waves, observed between -600 and -1000 mV, attributed to the successive formation of bis(radical-cation) and neutral quinonic species (Figure 141). We also found the fully reduced neutral species 65^0 and 74^0 to get readily adsorbed/desorbed at/from the electrode surface (see Gaussian-shaped signal in Figure 141). In terms of potential, the presence of a naphthalene substituent has little effect on the position of the first reduction wave. It has conversely a significant impact on the ΔE_p value, going from 38 mV measured with 65^{4+} up to 44 mV with 74^{4+} . Apart from being different, these low values also suggest the existence of π -dimerization

processes coupled to the formation of the bisradicals **65**^{2(+•)} and **74**^{2(+•)}. From a structural point of view, these result were rather unexpected when considering the great rigidity of the dibenzoacridine spacer and the quite large distance between both viologen-containing arms.

	$E^{1c}(n, \Delta E_p)$	$E^{2c}(n, \Delta E_p)$	$E^{1c} - E^{2c}$
	$V^{2+}/V^{••}$	V^{2+}/V^0	(V)
MeVMe(PF ₆) ₂	-0.882 ^b (1,62)	-1.198 ^b (1,60)	0.316
PhVMe(PF ₆) ₂	-0.709 ^b (1,58)	-1.035 ^b (1,58)	0.326
38 (PF ₆) ₄	-0.698 ^b (2,50)	-1.034 ^b (2,55)	0.336
42 (PF ₆) ₄	-0.682 ^b (2,51)	-1,002 ^{c,d}	na
44 (PF ₆) ₄	-0.667 ^b (2,43)	-1,030 ^{c,d}	na
48 (PF ₆) ₄	-0.665 ^b (2,45)	-1,030 ^{c,d}	na
54 (PF ₆) ₄	-0.685 ^b (2,44)	-1,044 ^{c,d}	na
56 (PF ₆) ₄	-0.665 ^b (2,45)	-0,956 ^{c,d}	na
65 (PF ₆) ₄	-0.640 ^b (2,38)	-0,973 ^{c,d}	na
74 (PF ₆) ₄	-0.642 ^b (2,44)	-0,990 ^{c,d}	na

Table 8: CV data measured in the following conditions: 1×10^{-3} M in DMF/TBAP (0.1 M, $E(V)$ vs. Ag^+/Ag), at a vitreous carbon working electrode $\varnothing = 3$ mm, 298 K, $v = 0.1$ V·s⁻¹. (na : Not available / ^b : Half wave potential / ^c : Peak potential / ^d : Adsorption phenomena).

The spectroscopic imprints of the electrogenerated species provided further insights into the nature and efficiency of the electron-triggered dimerization process. The electrochemical reduction of **65**⁴⁺ carried out at $E_{app} = -0.85$ V led to the development of new bands centered at 586 nm ($\epsilon = 18000$ M⁻¹.cm⁻¹), 723 nm ($\epsilon = 5500$ M⁻¹.cm⁻¹) and 1016 nm ($\epsilon = 3000$ M⁻¹.cm⁻¹). As already discussed in the previous sections, this spectroscopic signature, and most notably the band at 586 and 1016 nm are clear experimental evidences supporting the formation of π -dimerized species in solution (Figure 142A). The intramolecular nature of the dimerization was then established with additional measurements showing that the optical response recorded after electrolysis is independent of the tweezer's concentration (10^{-4} to 5×10^{-5} M). The observed EEC processes also proved fully reversible at the electrolysis time scale, as revealed by the fact that the initial spectroscopic and electrochemical signatures of **65**⁴⁺ could be fully recovered by reoxidation at $E_{app} = 0V$.

Studying tweezer **74**(PF₆)₄ in the same experimental conditions led to similar results and conclusions. A bulk electrolysis of **74**(PF₆)₄ carried out on platinum at $E_{app} = -0.85$ V led to the development of intense bands centered at 596 nm ($\epsilon = 21000$ M⁻¹.cm⁻¹), 720 nm ($\epsilon = 11000$ M⁻¹.cm⁻¹) and 1017 nm ($\epsilon = 4500$ M⁻¹.cm⁻¹) (Figure 142B). Here again the EEC process

was found to be fully reversible at the electrolysis time scale and the signature recorded after completion of the reduction (1e/viologen) was found to be independent of concentration (10^{-4} to 5×10^{-5} M). The shape of the spectrum recorded after addition of 2 electrons also happened to be similar to that recorded in the same conditions with $\mathbf{65}^{4+}$, which indicates that the naphthalene donor has a limited influence on the ratio between the dimerized and non-dimerized species in solution, the latter being estimated to $|(\mathbf{65}^{2+})_{\text{dim}}|/|\mathbf{65}^{2(+\bullet)}| = 28\%$ and $|(\mathbf{74}^{2+})_{\text{dim}}|/|\mathbf{74}^{2(+\bullet)}| = 24\%$ by deconvolution.

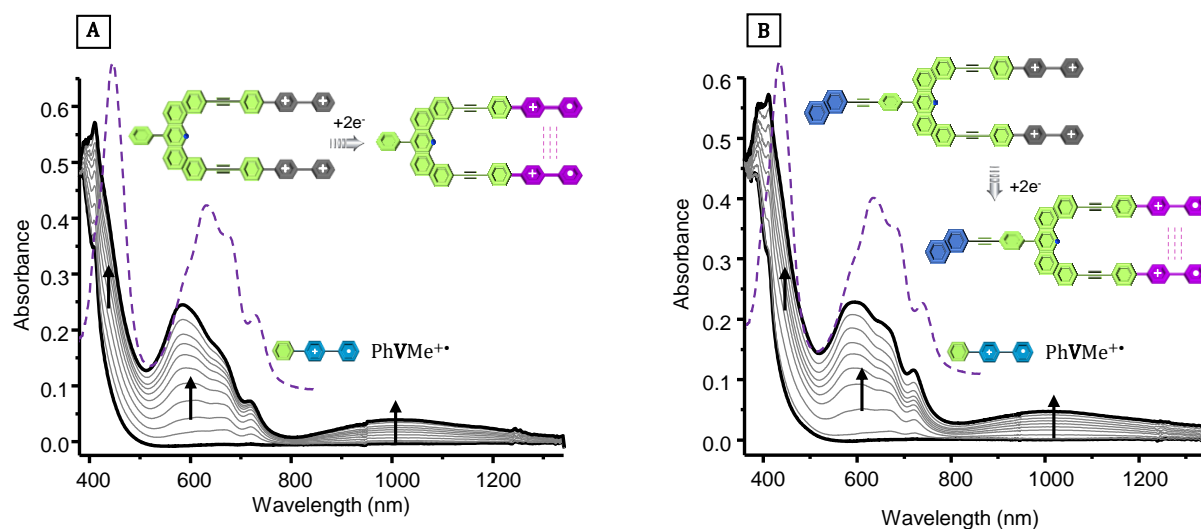


Figure 142: Superposition of UV-vis spectra recorded during the exhaustive reduction (one electron per viologen subunit) of A) $\mathbf{65}(\text{PF}_6)_4$ and B) $\mathbf{74}(\text{PF}_6)_4$ [Pt, 1.4×10^{-4} mol l $^{-1}$, DMF + TBAP 0.1 M, $l = 1$ mm $E_{\text{app}} = -0.85$ V].

III.4.4. Computational Analysis

The influence of the rigidity of the spacer on the π -dimerization process has been confirmed by density functional theory analysis (DFT). The optimized structure of $\mathbf{65}(\text{PF}_6)_4$ shows two overlapped viologen sub-units at a distance of 4.06 Å (Figure 143).

This structure confirms the ability of such a rigid molecule to twist sufficiently that allows both viologen cation radicals to come together at a suitable distance. As observed with the flexible tweezers, the dimerized species involves both viologens arranged in a quiet staggered conformation resulting in a partial orbital overlap. Furthermore, the calculation revealed the difference between $(\mathbf{65}^{2+})_{\text{dim}}$ and the reference isolated $(\text{MeVMe})_{\text{dim}}^{+\bullet}$ is 8.6 kcal.mol $^{-1}$.

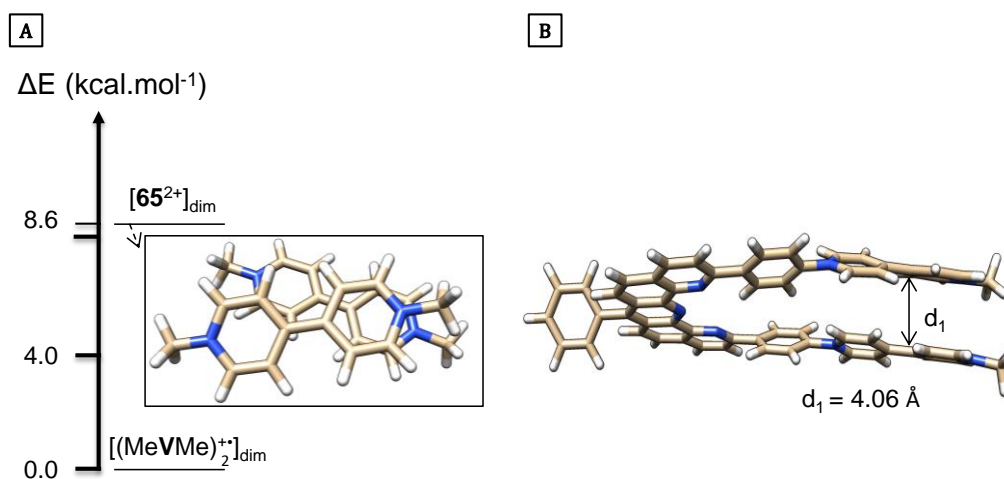


Figure 143: A) Relative energy calculated by DFT for $[\text{65}^{2+}]_{\text{dim}}$. B) DFT optimized structures for the π -dimers formed upon reduction of the viologen units in $\text{65}(\text{PF}_6)_4$.

III.4.5. Conclusion

As a conclusion the electrochemical and spectro-electrochemical data collected with $\text{65}(\text{PF}_6)_4$ and $\text{74}(\text{PF}_6)_4$ support the conclusion that, despite an apparent rigidity imposed by the dibenzoacridine spacer, these molecule are flexible enough to promote the intramolecular dimerization between the electrogenerated viologen-based cation radicals $\text{X}^{2(+\bullet)} \rightarrow (\text{X}^{2+})_{\text{dim}}$ (with X = 72 and 82) and that the presence of an anthracene donor has little impact on the dimerization process.

Chapter IV: Viologen Based Redox Responsive Coordination Polymer

IV.1. Introduction

Self-assembly is a unique spontaneous process allowing to organize, without external constraints, a set of disordered molecular units. It has proved extremely useful over the past decades to give access to highly complex structures from very simple building blocks. In addition, the labile/weak nature of non-covalent connections endow the resulting dynamic assemblies with numerous fascinating properties making them perfect candidates for the development of responsive materials.^{74, 194-195} It includes the ability to undergo assembly/disassembly processes under specific conditions, to adapt to their environment with changes in shape and size or to spontaneously repair structural damages.¹⁹⁶⁻¹⁹⁸

One strategy that has been used to expand the application scope of self-assembled systems relies on the use of metal ions as building elements. The so-called “metal-driven self-assembly approach” has indeed been explored since the early nineties with many transition metals to give access to a wide range of metal-ligand assemblies with interesting properties for applications in various research fields ranging from catalysis to material science.¹⁹⁹⁻²⁰¹ Fujita was a pioneer in this field in showing that the well-defined and highly predictable square planar coordination scheme of Pd²⁺ together with the lability of the Pd-L bonds are very suitable characteristics for the construction of dynamic self-assembled supramolecular systems.²⁰²⁻²⁰³ These innovative contributions have since then led to major developments motivated by the need to access ever more complex assemblies and by the desire to control/exploit their responsive character. The properties and potential applications of stimuli-responsive metal-ligand assemblies have indeed attracted the attention of many chemists over the past decade, leading to the discovery of new “smart” molecular materials capable of modifying one or more of their properties in response to an external stimulus, such as pH, light or to the addition of a chemical species.^{188, 204} Due to conceptual, technical or synthetic locks, much less progresses have been achieved with systems capable to respond to an electrical stimulation, the only approach explored so far relying on a change in the redox state of the metal centers to trigger large scale reorganizations affecting the whole assembly.

The research activity carried out in our group over the past decade has mainly fallen within the scope of molecular metamorphism, where the self-assembled materials undergo large scale structural modifications under the effect of redox stimulus.

Recent achievements include, a bipyridinium-based redox-responsive molecular hinge functionalized by two different self-complementary unit on both ends: a metalloporphyrin

featuring an available binding site on one end and a coordinating group on the other side (Figure 144).³⁹

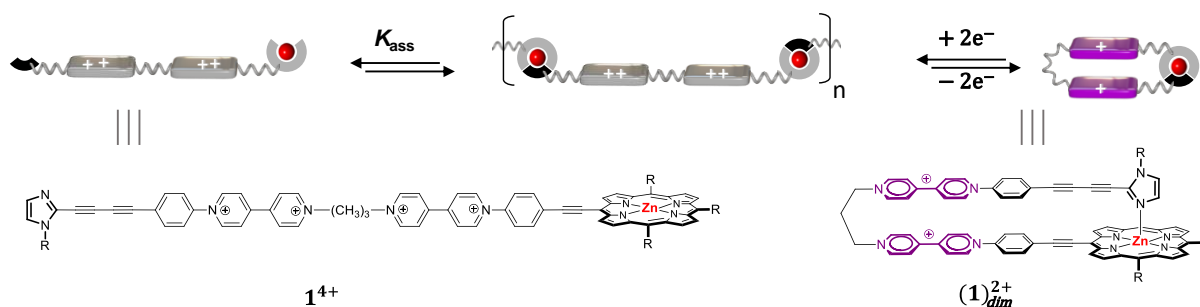


Figure 144: Redox-responsive porphyrin-based molecular tweezers. 39

It has been shown that the monomer adopts in the ground state an elongated conformation enabling the formation of self-assembled coordination oligomers and polymers which dissociates upon reduction due to the intramolecular dimerization process supported with the self-coordination of the monomer.

The same redox responsive hinge has been further employed to achieve control over the organization of ditopic molecular tectons within a palladium-based self-assembled system. (Figure 145).³⁸ Here the hinge that is made of two 4,4'-bipyridinium units linked through a propylene linker functionalized at both end by two identical bidentate ligands. In the presence of a suitable metal ion, these organic tectons self-assemble in solution to form coordination polymers, and their reduction triggers the folding of the hinge and a dissociation of the polymer.

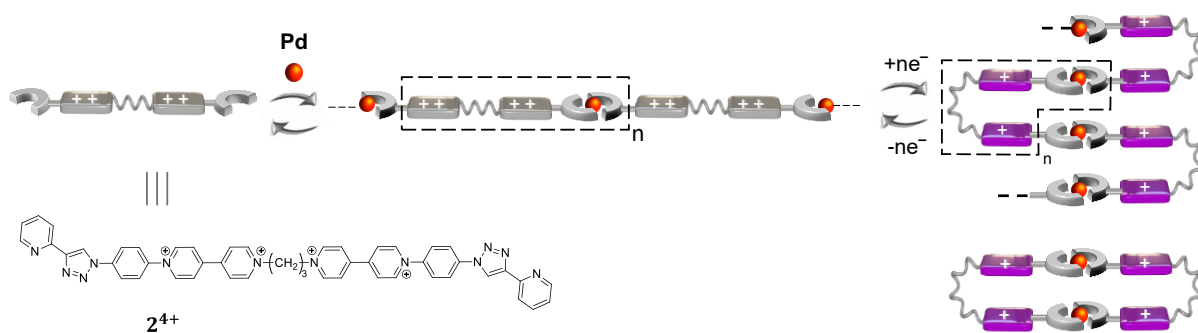


Figure 145: Electro-mechanical folding modifying the association and/or the organisation of tectons within metal-ligand assemblies. 38

As a follow-up to these recent contributions, we will report in the following paragraphs on the formation of discrete palladium-ligand assemblies and coordination polymers whose

structure/size/organization can be tuned with an electrical input. This results are in line with the work carried out by Christophe Kahlfuss (PhD 2012-2015) at ENSL. Our work consisted in pursuing, reproducing and finalizing preliminary studies initiated by Christophe Kahlfuss at the end of his PhD. The basic concept underlying this novel approach is illustrated in Figure 146 with simple sketches. The idea was to introduce two carefully selected metal coordinating units on both sides of a 4,4'-bipyridinium unit so as to enable its self-association in the presence of palladium to form either discrete macrocyclic architectures or coordination polymers. Based on all the knowledge accumulated in recent years in our group on palladium assemblies,³⁸ we considered that the type of assembly (discrete vs. polymeric assemblies) could be determined by a careful design of the coordination unit (denticity, topicity, steric hindrance...) together with a rigorous choice of the palladium source, and more specifically the number and the relative position (*cis* or *trans*) of the available binding sites on the palladium center. It was also anticipated that a dissociation of the self-assembled polymers or a contraction of the discrete coordination rings could be actuated by a suitable electrical stimulation of the assemblies leading to a change in the redox state of the bipyridiniums, from their dicationic state to their cation radical state, and to the coupled formation of π -dimerized coordination rings.

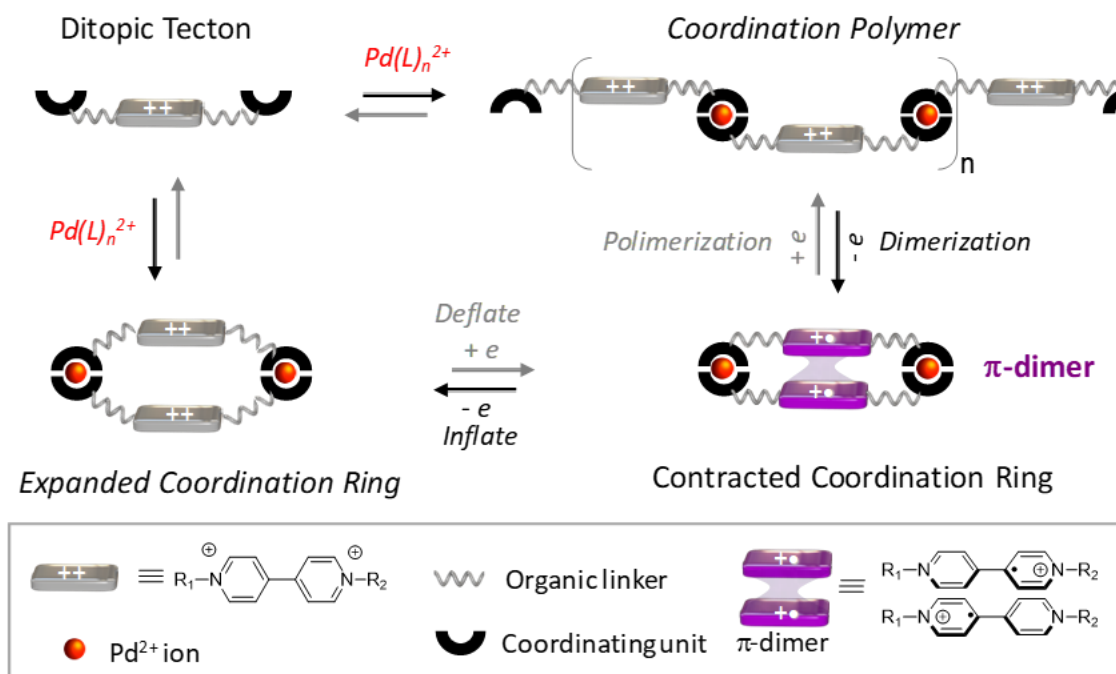


Figure 146: Targeted redox-switchable coordination polymers and discrete macrocyclic assemblies based on viologen unit.

In the following sections, we will report on the self-assembling ability of the bisimidazole-tethered viologen 6^{2+} (Figure 147) in the presence of *cis*-, *trans*- or un-protected palladium (II)

centers yielding either macrocyclic coordination rings or coordination polymers. Then, the electron-triggered dissociation of the coordination polymers or the contraction of the discrete self-assembled rings will be discussed based on spectroscopic, (spectro-) electrochemical and computational data.

IV.1.2. Synthesis of the Targeted Tecton

The synthesis of the target tecton was previously described in thesis of Dr. Christophe Kahlfuss. The synthesis described in Figure 147 is actually the result of an improvement of the previously reported procedure, where the starting point is the iodination of the methyl imidazole. Then the resulting compound **3** was subjected to Sonagashira cross-coupling reaction with ethynylaniline to give compound **4**. The latter was reacted with the activated viologen 5^{2+} to afford 6^{2+} in 38% yield.

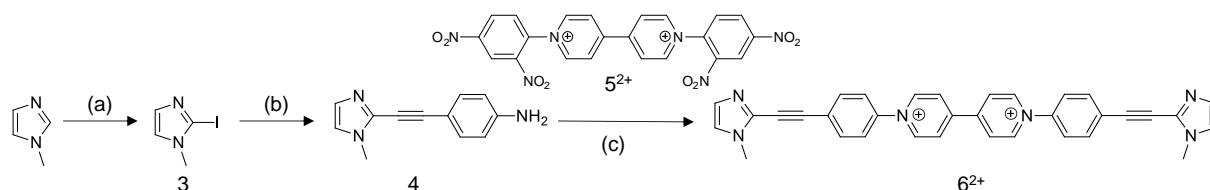


Figure 147: (a) *n*-Buli, I₂, reflux, 4h, 48%; (b) 4-Ethynylaniline, CuI, Pd(PPh₃)₂Cl₂, THF, NEt₃, reflux, 24h, 87%; (c) **5**(PF₆)₂, EtOH/CH₃CN 70 °C, 18h, 38%.

IV.1.3. ¹H-NMR Characterization

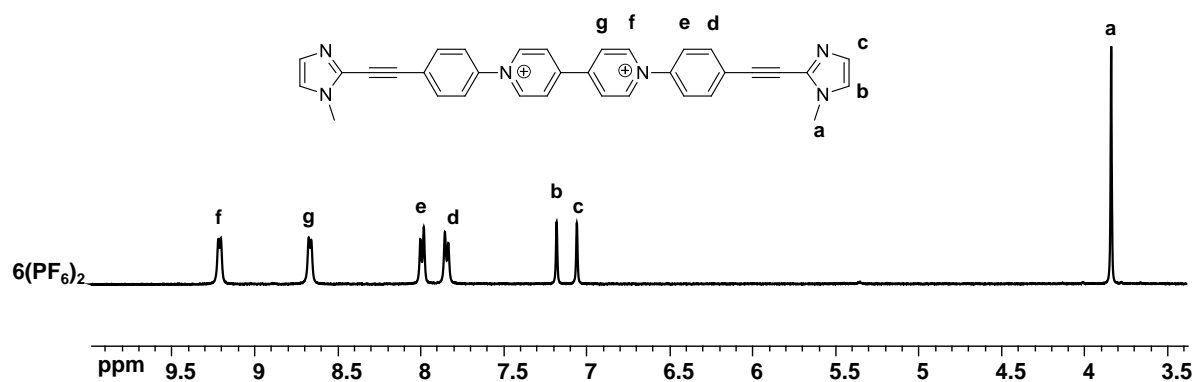


Figure 148: ¹HNMR spectrum of **6**(PF₆)₂ (1mM, CD₃CN-*d*₃, 295 K, 400 MHz).

The protons attributed to viologens resonate in the form of two doublets between 8.65 and 9.19 ppm. The protons of phenyl denoted as H_d and H_e appear at 7.83 ppm and 7.98 ppm. The two singlets at 7.05 ppm and 7.17 ppm that are assigned as H_b and H_c are attributed to the protons of the imidazole cycle, while the singlet at 3.83 corresponds to the protons of the methyl group.

IV.1.4. Complexation with Palladium

Complexation of 6^{2+} with Pd(II) has been thoroughly investigated by NMR spectroscopy, electrochemistry and by spectro-electrochemistry using *cis*-[Pd(en)(NO₃)₂], *trans*-[Pd(CH₃CN)₂(Cl)₂] or [Pd(CH₃CN)₄(BF₄)₂] as sources of partially (*cis*- or *trans*-) or fully un-protected metal centers (en : ethylenediamine). In the two first cases, only the *cis* and *trans* positions occupied by weakly binding nitrate and acetonitrile ligands are kinetically labile and thus prone to ligand exchange, while the four positions of *tetrakis*(acetonitrile)palladium(II) are potentially available for binding.

Selected ¹H-NMR spectra collected with a millimolar solution of 6^{2+} in DMSO-*d*₆ in the presence of increasing amounts of *cis*-protected [Pd(en)(NO₃)₂] are shown in Figure 149.

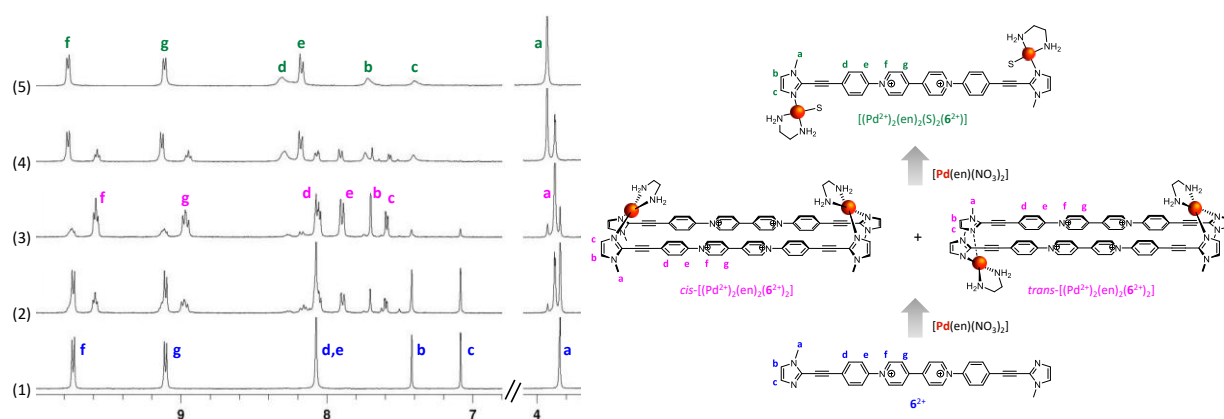


Figure 149: Partial ¹H-NMR spectra (400 MHz, DMSO-*d*₆, 1.0 mM, 293 K) of $6(\text{PF}_6)_2$ in the absence (1), and in the presence of (2) 0.5 molar equiv. of [Pd(en)(NO₃)₂], (3) 1.0 molar equiv. of [Pd(en)(NO₃)₂], (4) 10 molar equiv. of [Pd(en)(NO₃)₂] and (5) 200 molar equiv. of [Pd(en)(NO₃)₂].

The kinetics of the ligand exchange processes occurring in solution upon addition of metal are slow with respect to the NMR time scale. As expected, coordination of the imidazole rings to Pd(II) leads to a significant shift of the signals attributed to H_b and H_c. The chemical shift of the singlet attributed to the protons of the methyl substituent (H_a) proved to be one of the most valuable and direct diagnostic tool for analyzing the metal binding processes and for identifying the most abundant species formed at given metal/ligand ratios (M:L). Addition of sub-stoichiometric amounts of metal ions ($0 < \text{M:L} < 1$) was found to induce the progressive disappearance of the initial signal resonating at 3.84 ppm at the expense of two very close singlets of equal intensities centered at 3.87 and 3.88 ppm, which suggests the formation of two species featuring similar structures. This assumption is supported by the observation of similar low field shift and splitting affecting the signal attributed to H_c on the imidazole ring, while H_b appears in the form of a singlet. Another important conclusion drawn from these

data is that complexation of palladium occurs simultaneously on both sides of the ligands, as proved by the fact that no signal corresponding to a "free" imidazole ring is observed in the signature of the two symmetrical species developing over the course of the titration experiment up to M:L = 1. The NMR spectra recorded in the presence of one molar equivalent of Pd²⁺ also reveal that 19% of the ligand remains uncomplexed. Further addition of Pd(II) (1 < M:L) led to disappearance of these intermediate signals at the expense of a new set of signals, reaching a maximum intensity after addition of palladium in large excess, attributed to the metal-saturated complex [(Pd²⁺)₂(en)₂(S)₂(6²⁺)] (with S = Solvent).

The array of spectra depicted in Figure 149 thus reveals that the solution contains four different species present in equilibrium over a wide range of concentration: the free ligand 6²⁺, two intermediate symmetric isomers and the final metal-saturated complex [(Pd²⁺)₂(en)₂(S)₂(6²⁺)] (with S = Solvent). The eight protons of the viologen units (H_f and H_g) are interestingly found to resonate at similar frequencies in the free ligand and in the final product obtained after addition of palladium in excess. This however proved not true for the signals attributed to the hydrogen atoms located on the phenyl (+ 0.1 and + 0.2 ppm) and imidazole rings (+ 0.3 ppm) undergoing significant downfield shifts upon formation of the 2:1 (M:L) complex [(Pd²⁺)₂(en)₂(S)₂(6²⁺)]. Further investigations carried out in DMF-*d*₇ moreover led to similar results (Figure 150).

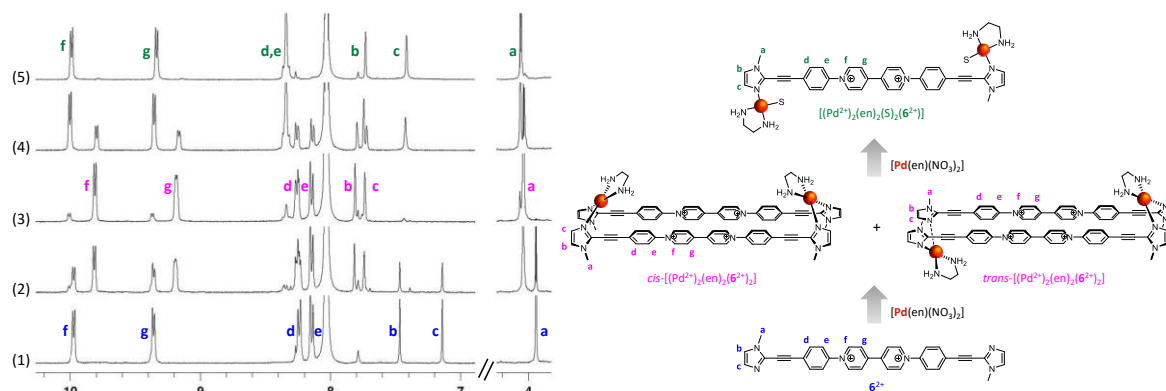


Figure 150: ¹H-NMR spectrum of 6(PF₆)₂ (1 mM, DMF-*d*₇, 295 K, 400 MHz) in the absence (1), and in the presence of (2) 0.5 molar equiv. of [Pd(en)(NO₃)₂], (3) 1.0 molar equiv. of [Pd(en)(NO₃)₂], (4) 10 molar equiv. of [Pd(en)(NO₃)₂] and (5) 200 molar equiv. of [Pd(en)(NO₃)₂].

The well-defined shape of all the signals observed throughout the titration experiment are moreover clear experimental evidences supporting the formation of isolated species rather than oligomers and polymers. This conclusion was further confirmed by DOSY NMR measurements, showing that the calculated diffusion coefficient remains unchanged upon dilution of the sample from 1.0 mM to 0.5 mM, demonstrates that the bis-imidazole ligand 6²⁺

is not involved in the formation of coordination polymers, but rather in the entropy-driven formation of discrete complexes. The ^1H - and DOSY-NMR data discussed above rather support the conclusion that the box-shaped isomers noted $\text{cis}[(\text{Pd}^{2+})_2(\text{en})_2(\mathbf{6}^{2+})_2]$ and $\text{trans}[(\text{Pd}^{2+})_2(\text{en})_2(\mathbf{6}^{2+})_2]$ in Figure 149 are formed in the early stage of the titration ($0 < \text{M:L} < 1$) with a maximum concentration reached at $\text{M:L} = 1$, each being distinguished on the ^1H -NMR spectrum with specific signals for protons H_a and H_c . This conclusion implies that the electrostatic repulsion between two dicationic viologen units is not large enough to prevent the formation of such a box-shaped macrocyclic structure wherein two positively charged viologens end up adopting a cofacial arrangement. Formation of such discrete metalacyclic compounds is further supported by a significant shielding of the viologen-based signals H_f and H_g upon metalation. As previously established by Crowley et al. with constrained bis-pyridinium derivatives,²⁰⁵ these shifts can indeed be attributed to the spatial proximity and van der Waals interactions occurring between both viologens in both the cis - and $\text{trans}[(\text{Pd}^{2+})_2(\text{en})_2(\mathbf{6}^{2+})_2]$ isomers. Subsequent addition of Pd(II) led to a dissociation of both [2:2] metallacyclic isomers in favour of the metal-saturated [2:1] complex $[(\text{Pd}^{2+})_2(\text{en})_2(\text{S})_2(\mathbf{6}^{2+})]$, which becomes predominant only after addition of 10 equiv. of $[\text{Pd}(\text{en})(\text{NO}_3)_2]$ ($10 < \text{M:L}$). At $\text{M:L} = 10$ the ratio between the macrocyclic and metal-saturated complexes ($[(\text{Pd}^{2+})_2(\text{en})_2(\text{S})_2(\mathbf{6}^{2+})]:[(\text{Pd}^{2+})_2(\text{en})_2(\mathbf{6}^{2+})_2]$) could be estimated to 1:4 from the integration of specific ^1H -NMR signals.

A similar study was then conducted with $\text{trans}[\text{Pd}(\text{CH}_3\text{CN})_2(\text{Cl})_2]$ used as a trans -protected metal source. As can be seen in Figure 151, addition of this metal salt to a millimolar solution of $\mathbf{6}^{2+}$ was found to result in the disappearance of the initial singlets/multiplets at the expense of new sets of signals. The changes observed throughout the titration are consistent with the successive formation of three main species whose relative concentration evolves with the M:L ratio. In particular, the singlet centered at 3.94 ppm attributed to the N-methyl substituents of the free ligand $\mathbf{6}^{2+}$ (H_a) sees its intensity gradually decreases at the expense of one main signal developing at 3.97 ppm and reaching its maximum intensity at $\text{M:L} = 1$ (Figure 151, spectrum 3). The initial signal of the imidazole ring (H_b and H_c) undergoes similar changes with a progressive disappearance at the expense of two novel deshielded signals. Analogous changes are observed in the aromatic domain with the development of two novel shielded signals attributed to the viologen subunit (H_f and H_g) in a 1:1 (M:L) adduct. Further addition of metal salt then leads to the emergence of a new sets of signals reaching maximum intensities as $\text{M:L} \geq 10$ (Figure 151, spectrum 5). The spectrum of the final complex displays two doublets at

9.39 and 10.00 ppm attributed respectively to H_g and H_f, one AB quartet at 8.27 and 8.33 ppm corresponding to the hydrogen atoms located on the phenyl rings (H_d and H_e), and two singlets at 7.28 and 7.58 ppm attributed to the protons of the imidazole ring (H_b and H_c). No significant modifications of the ¹H-NMR spectra could be observed upon further addition of trans-[Pd(CH₃CN)₂(Cl)₂].

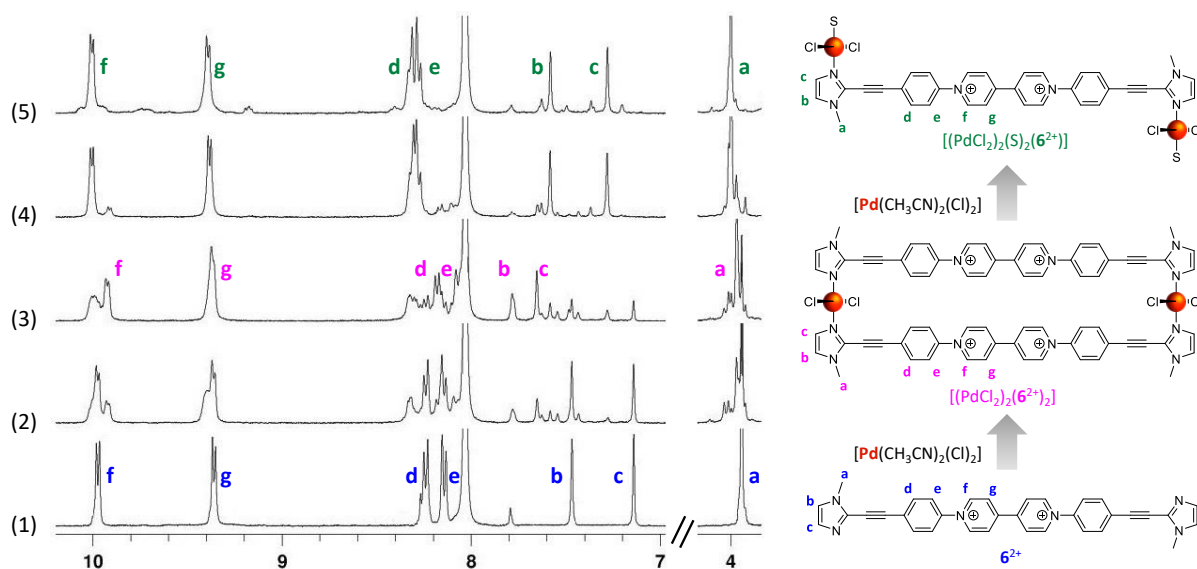


Figure 151: Partial ¹H-NMR spectra (400 MHz, DMF-*d*₇, 1.0 mM, 293 K) of **6**(PF₆)₂ (1) in the absence, and in the presence of (2) 0.5 molar equiv. of [Pd(CH₃CN)₂(Cl)₂], (3) 1.0 molar equiv. of [Pd(CH₃CN)₂(Cl)₂], (4) 2.0 molar equiv. of [Pd(CH₃CN)₂(Cl)₂], (5) 10 molar equiv. of [Pd(CH₃CN)₂(Cl)₂].

Contrarily to what was observed with cis-[Pd(en)(NO₃)₂], the spectra recorded in the presence of trans-[Pd(CH₃CN)₂(Cl)₂] displays a series of non-identified weakly intense signals suggesting the formation of side products most probably resulting from kinetic issues in line with the known trans-effect affecting the lability of metal-ligand bonds in chlorinated square planar complexes.²⁰⁶

The data discussed above nevertheless clearly indicate that the three main species shown in Figure 151 are formed successively with increasing M:L ratio. A careful analysis of the signals assigned to the protons of the imidazole (H_a, H_b and H_c) and the viologen units (H_f and H_g) indeed reflects that the symmetric and discrete complexes [(PdCl₂)₂(**6**²⁺)₂] and [(PdCl₂)₂(S)₂(**6**²⁺)] are the main species in solution at M:L = 1 and M:L ≥ 2, respectively. In mixtures involving sub-stoichiometric amounts of trans-[Pd(CH₃CN)₂(Cl)₂] (M:L < 1), the box-shaped [(PdCl₂)₂(**6**²⁺)₂] complex and the free ligand **6**²⁺ are the main species in solution while subsequent addition of Pd(II), up to 2 equiv., leads to the exclusive formation of the 1:2 (M:L) complex [(PdCl₂)₂(S)₂(**6**²⁺)] featuring two trans-coordinated chlorine ligands on each palladium centers. Here again, the high field shift of the viologen-based H_f signal (−0.05

ppm) observed upon formation of the box-shaped $[(\text{PdCl}_2)_2(\mathbf{6}^{2+})_2]$ complex is attributed to the spatial proximity between both viologens in the macrocyclic structure. The trans- versus cis-coordination modes imposed for $\mathbf{6}^{2+}$ by the chlorine and ethylene diamine ligands leads however to major structural differences between the box-shaped $[(\text{PdCl}_2)_2(\mathbf{6}^{2+})_2]$ and $[(\text{Pd}^{2+})_2(\text{en})_2(\mathbf{6}^{2+})_2]$ complexes, which includes the distance and relative arrangement between both viologen units.

All the data presented above support the conclusion that discrete complexes rather than polymers are formed in solution from mixtures of $\mathbf{6}^{2+}$ and *cis*- $[\text{Pd}(\text{en})(\text{NO}_3)_2]$ or *trans*- $[\text{Pd}(\text{CH}_3\text{CN})_2(\text{Cl})_2]$.

Formation of coordination polymers was conversely observed when using $[\text{Pd}(\text{CH}_3\text{CN})_4](\text{BF}_4)_2$ as the metal source, featuring four "available" binding positions around the Pd center (Figure 152).

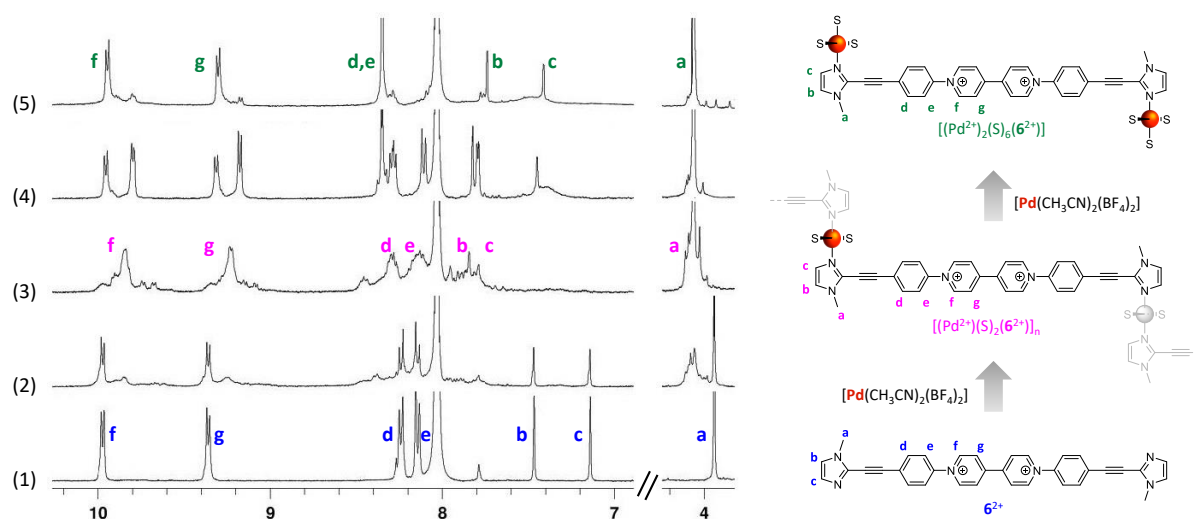


Figure 152: Partial ^1H -NMR spectra (400 MHz, $\text{DMF-}d_7$, 1.0 mM, 293 K) of $\mathbf{6}(\text{PF}_6)_2$ (1) in the absence, and in the presence of (2) 0.5 equiv. of $[\text{Pd}(\text{CH}_3\text{CN})_4](\text{BF}_4)_2$, (3) 1.0 equiv. of $[\text{Pd}(\text{CH}_3\text{CN})_4](\text{BF}_4)_2$, (4) 10 equiv. of $[\text{Pd}(\text{CH}_3\text{CN})_4](\text{BF}_4)_2$, (5) 200 equiv. of $[\text{Pd}(\text{CH}_3\text{CN})_4](\text{BF}_4)_2$.

Addition of this non-protected metal salt to a millimolar solution of $\mathbf{6}^{2+}$ indeed led to the progressive disappearance of all the signals attributed to $\mathbf{6}^{2+}$ in favor of a series of very broad and weakly intense signals observed until addition of palladium in excess (Figure 152), which is compatible with the existence of multiple equilibria involving various coordination polymers/oligomers. Well resolved NMR signals, characteristic of smaller and defined assemblies, could only be observed again after addition of an excess of about 5 equiv. of palladium. In the presence of a large excess of $[\text{Pd}(\text{CH}_3\text{CN})_4](\text{BF}_4)_2$, the protons of the

pyridinium rings get ultimately shifted at 9.29 and 9.93 ppm while the protons of the imidazole ring are seen to resonate at 7.43 and 7.76 ppm (Figure 152).

The formation of coordination polymers or oligomers in the conditions described above has been further confirmed from DOSY-NMR measurements carried out in DMSO-*d*₆ at different M:L ratio. As can be seen in Figure 153A, addition of [Pd(CH₃CN)₄](BF₄)₂ to a 1 mM solution of **6**²⁺ was found to result in a significant drop of the diffusion coefficient going from 157 μm².s⁻¹ down to 85 μm².s⁻¹ after addition of 1 equiv. of Pd(II). Subsequent addition of Pd(II) then led to an increase of the diffusion coefficient up 125 μm².s⁻¹ reached for M:L = 5. Similarly, the diffusion coefficient calculated for a 1:1 (M:L) ratio was found to decrease with increasing concentration, as expected for a concentration dependent self-assembly process (Figure 153B). The broadness of the DOSY NMR signals also suggest a rather large polydispersity in the investigated mixtures. All these data thus support the conclusion that the largest oligomers are formed at M:L = 1 and that every deviation from that stoichiometry lead to the displacement of the equilibria in favor of shorter assemblies.

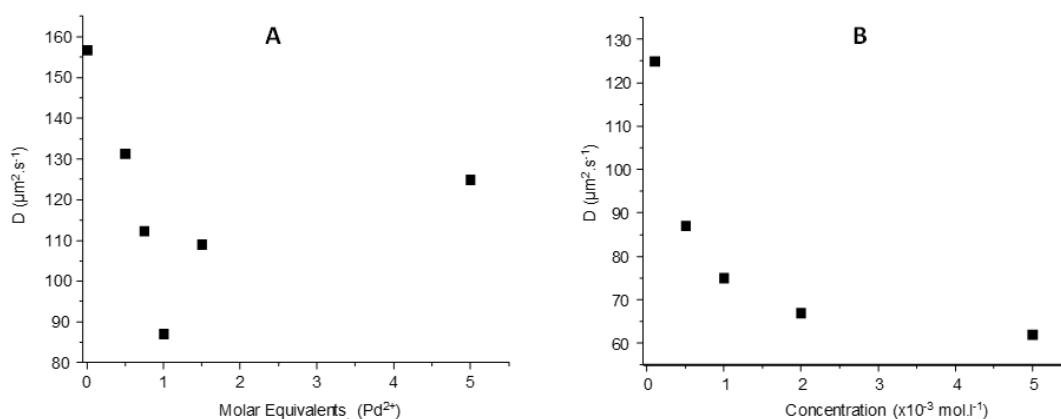


Figure 153: Average diffusion coefficient for **6**(PF₆)₂ recorded as function of the number of molar equivalent of [Pd(CH₃CN)₄](BF₄)₂, measured by DOSY-NMR (400 MHz, DMSO-*d*₆, 1.0 mM, 293 K).

IV.1.5. Electrochemical Characterization

The free ligand **6**²⁺ has been studied by cyclic voltammetry (CV) in DMF. Selected curves are shown in Figure 154. The curve recorded at a glassy carbon working electrode at 100 mV/s exhibits two reversible reduction waves at $[E_{1/2^1}]_1 = 545$ mV ($\Delta E_p^1 = 63$ mV, $\nu = 0.1$ V.s⁻¹) and $[E_{1/2^2}]_2 = 769$ mV ($\Delta E_p^2 = 59$ mV, $\nu = 0.1$ V.s⁻¹) corresponding to the successive formation of the radical cation **6**⁺ and of the neutral quinonic species **6**⁰. One key information extracted from these preliminary measurements, and more specifically from the rather limited amplitude of the $\Delta E_{1/2}$ value ($[E_{1/2^2}]_1 - [E_{1/2^2}]_2 = 224$ mV) and from the standard ΔE_p^1 value

($|E_{pc}^1 - E_{pa}^1| = 59$ mV) measured on the first reduction wave is that the electrogenerated cation radicals $6^{+\bullet}$ do not interact in solution in these experimental conditions.

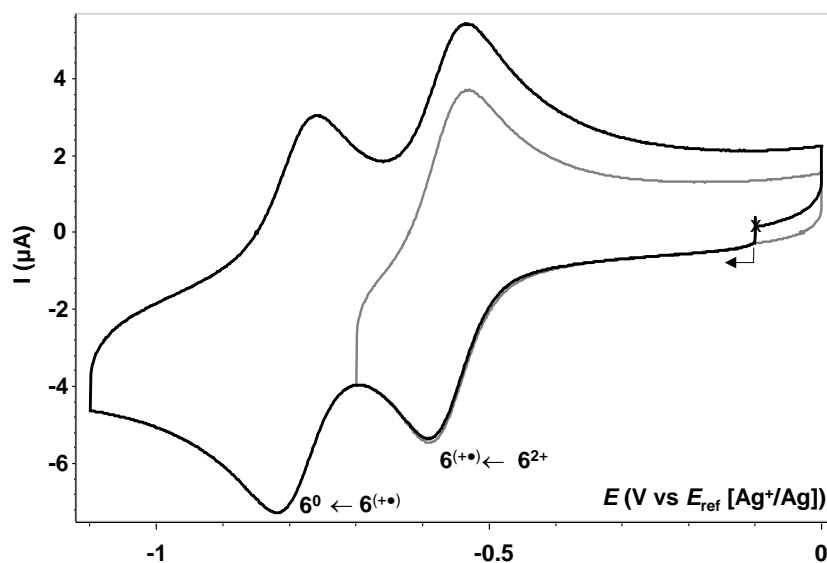


Figure 154: Voltammograms recorded for $6(\text{PF}_6)_2$ (0.4 mM, DMF+TBAP 0.1 M, VC, $\varnothing = 3$ mm, E vs Ag^+/Ag 10^{-2} M, $\nu = 0.1$ V s^{-1}).

The complexation of 6^{2+} with palladium has been similarly studied by electrochemical methods. Selected CV curves recorded at different M:L ratio with *cis*-protected $[\text{Pd}(\text{NO}_3)_2(\text{en})]$ as the palladium source are shown in Figure 155. These data reveal that the addition of 1 molar equivalent of metal (M:L = 1) leads to a major shift of the first viologen-centered reduction wave towards less negative potential ($E_{1/2} = -0.399$ V, $\Delta E_{1/2} = +150$ mV) and to a large decrease of the peak to peak potential shift going from 59 mV (M:L = 0) to 38 mV (M:L = 1). It also led to a less important shift of the second reduction potential towards more negative values ($\Delta E_{1/2} = -50$ mV). As discussed in the previous sections, these changes support the conclusion that the presence of Pd^{2+} promotes an efficient π -dimerization of the electrogenerated viologen-based cation radicals. This assumption is moreover fully consistent with our analyses of the $^1\text{H-NMR}$ titration data which have led to the identification of the metallacyclic complexes *cis*- or *trans*- $[(\text{Pd}^{2+})_2(\text{en})_2(6^{2+})_2]$ (Figure 156) as the main species in solution at M:L = 1, the pre-organization and spatial proximity between both viologen sub-units held in a cofacial arrangement by two Pd(II) hinges being perfectly suited to promote the electron-triggered formation (1e/viologen) of the intramolecular π -dimer $[(\text{Pd}^{2+})_2(\text{en})_2(6^+)_{\text{dim}}]$ (Figure 156). The CV curve recorded at M:L = 1 also suggest that the *cis*- and *trans*-isomers exhibit similar electrochemical behavior, which is not surprising given the great similarity between the environments of the viologens in both macrocyclic compounds. Another major

finding is that the reduction of the free ligand is hardly observed on the CV curve recorded at M:L = 1, a fact which contrasts with the NMR data discussed above revealing that 19% of the ligand remains uncomplexed in these experimental conditions. Failure to observe such wave attributed to the reduction of the free ligand ($\mathbf{6}^{2+}/\mathbf{6}^{+}$) can be explained by the dynamic nature of the electrochemical and chemical equilibria involved in solution (see in Figure 156 the K_{1-6} and K_{dim} constants corresponding to a wide range of complexation, reduction/oxidation and π -dimerization processes). As can be seen in Figure 155A, the first wave at ~ -0.4 V corresponds to the two electron reduction of the metallacyclic compound $[(\text{Pd}^{2+})_2(\text{en})_2(\mathbf{6}^{2+})_2]$ ($[E^0]_{1b}$ and $[E^0]_{2b}$ in Figure 156) yielding the doubly reduced complex $[(\text{Pd}^{2+})_2(\text{en})_2(\mathbf{6}^{+})_2]$ which is readily transformed at the CV time scale into the intramolecular dimer $[(\text{Pd}^{2+})_2(\text{en})_2(\mathbf{6}^+)_{dim}]$ (K_{dim} in Figure 156). Our explanation of the electrochemical signature recorded at M:L = 1 results from this series of events triggered at the early stage of the scanning experiment, the most important one being the effective π -dimerization process $[(\text{Pd}^{2+})_2(\text{en})_2(\mathbf{6}^+)_{dim}] \rightarrow [(\text{Pd}^{2+})_2(\text{en})_2(\mathbf{1}^+)_{dim}]$ leading, at the CV time scale, to a displacement of the initial complexation equilibrium (K_I in Figure 156) and thus to the consumption of the free ligand $\mathbf{6}^{2+}$.

Further addition of *cis*-[Pd(NO₃)₂(en)] led to the observation of two different reduction waves centered at $E_{1/2} = -0.532$ V ($\Delta E_p = 72$ mV) and at $E_{1/2} = -0.410$ V ($\Delta E_p = 27$ mV). The CV curve recorded at M:L = 10 is shown in Figure 155A. The first reduction at $E_{1/2} = -0.410$ V (could be readily attributed to the EEC process involving the two electron reduction of $[(\text{Pd}^{2+})_2(\text{en})_2(\mathbf{6}^{2+})_2]$ and its subsequent π -dimerization to yield $[(\text{Pd}^{2+})_2(\text{en})_2(\mathbf{6}^+)_{dim}]$ ($[E^0]_{1b}$, $[E^0]_{2b}$, K_{dim} in Figure 156), while the second and more intense wave at $E_{1/2} = -0.532$ V ($\Delta E_p = 72$ mV) could be attributed to the one-electron reduction of the bimetallic complex $[(\text{Pd}^{2+})_2(\text{en})_2(\text{S})_2(\mathbf{6}^{2+})]$ ($[E^0]_{1c}$ in Figure 156). Observation of both signals is here in agreement with the ¹H-NMR data depicted in Figure 149 allowing to estimate the concentration ratio $[(\text{Pd}^{2+})_2(\text{en})_2(\text{S})_2(\mathbf{6}^{2+})] : [(\text{Pd}^{2+})_2(\text{en})_2(\mathbf{6}^{2+})_2]$ to 1:4 at M:L = 10.

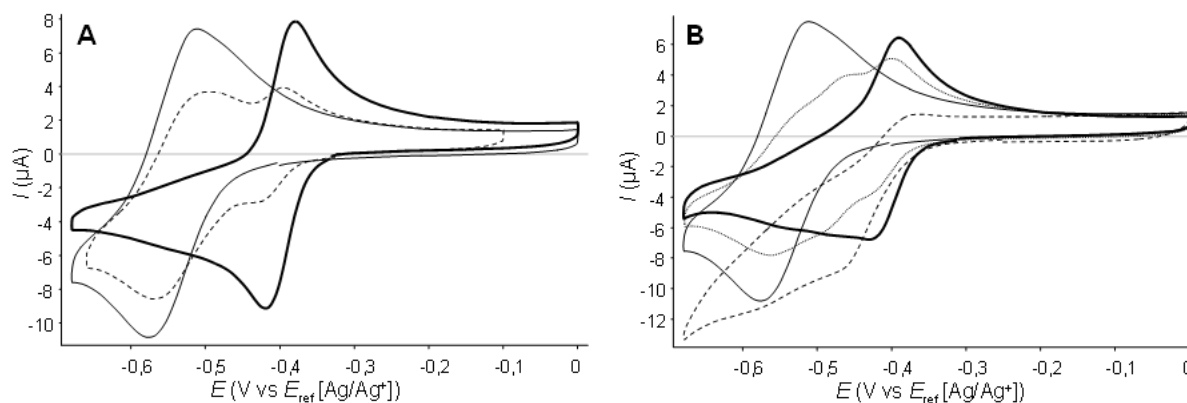


Figure 155: Voltammograms recorded for $\mathbf{6}(\text{PF}_6)_2$ (0.4 mM, DMF+TBAP 0.1 M) in the presence of A) $\text{cis-}[\text{Pd}(\text{NO}_3)_2(\text{en})]$: 0 eq. (full line), 1 eq. (bold line) and 10 eq. (dashed line) and B) $\text{trans-}[\text{Pd}(\text{Cl})_2(\text{CH}_3\text{CN})_2]$: 0 eq. (full line), 0.4 eq. (dotted line), 1 eq. (bold line) and 3 eq. (dashed line) (VC, $\varnothing = 3$ mm, E vs. Ag^+/Ag 10^{-2} M, $\nu = 0.1$ V s^{-1}).

Similar measurements have been carried out using the *trans*-protected palladium source $[\text{Pd}(\text{Cl})_2(\text{CH}_3\text{CN})_2]$ as a reactant.

Addition of 1 molar equivalent of this metal salt to an electrolytic solution of $\mathbf{6}^{2+}$ in DMF (0.4 mM) led to a large shift of the first reduction wave towards less negative potential values ($\Delta E_{1/2} = +135$ mV, $E_{1/2} = -0.411$ V) coming along with a significant decrease of the ΔE_p value reaching 41 mV at M:L = 1 and $\nu = 100$ mV/s Figure 155B). As already discussed with the *cis*-protected metal salt, these changes can be seen as unambiguous experimental evidences demonstrating that the complexation of $\mathbf{6}^{2+}$ with $\text{trans-}[\text{Pd}(\text{Cl})_2(\text{CH}_3\text{CN})_2]$ promotes the intramolecular π -dimerization of the electrogenerated viologen cation radicals within the intramolecular macrocyclic complex $[(\text{Pd}^{2+})_2(\text{Cl})_2(\mathbf{6}^+)_2]_{\text{dim}}$.

Further addition of $\text{trans-}[\text{Pd}(\text{Cl})_2(\text{CH}_3\text{CN})_2]$ (the curve recorded at M:L = 3 is shown in Figure 155B) was conversely found to result in the observation of ill-defined irreversible signals at $E < -0.4$ V. From the NMR data discussed above, we know that the main species in solution at M:L = 3 is the bimetallic complex $[(\text{Pd}^{2+})_2(\text{Cl})_2(\mathbf{6}^{2+})]$. The reduction wave observed as a dashed line in Figure 155B is thus potentially attributed to the one electron reduction of the single viologen unit involved in this metal saturated complex. The unusual shape of this signal is however not clearly understood, one possible explanation supported by the observation of a deposit onto the electrode being that the "free" metal salt, present in solution at M:L > 2, gets reduced /physisorbed at the electrode in this potential range.

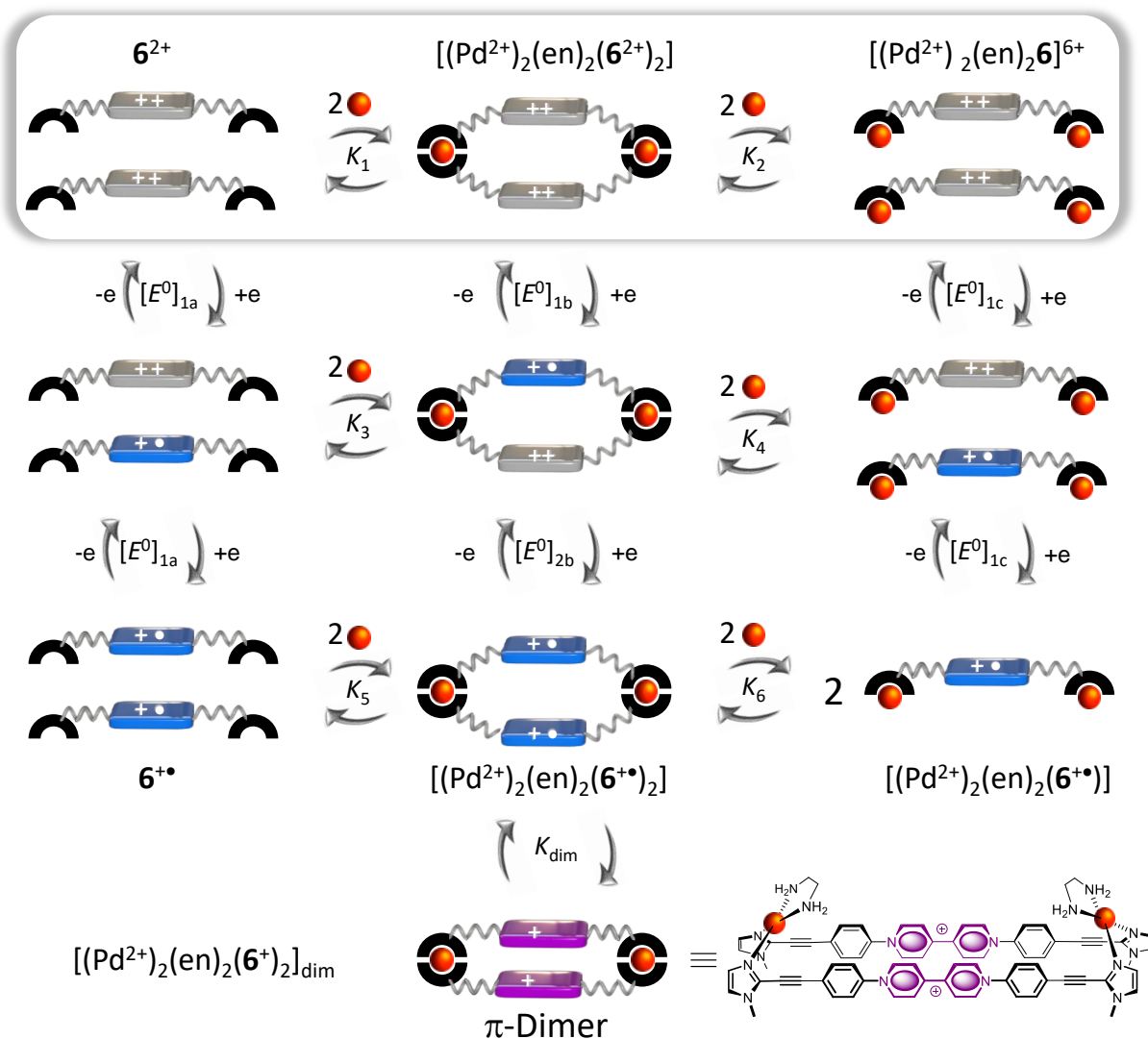


Figure 156: Schematic representation of the chemical and electrochemical reactions and equilibria involving 6^{2+} and of *cis*-[Pd(NO₃)₂(en)]. Each Electrochemical steps (E) represented in this mechanism are mono-electronic.

A closer look at the well-defined CV data collected at M:L = 1 with the *cis*- and *trans*-protected metal salts nevertheless enables to compare the dimerization ability of both viologen units incorporated in macrocyclic complexes *cis*-[(Pd²⁺)₂(en)₂(6²⁺)₂] and *trans*-[(Pd²⁺)₂(Cl)₂(6²⁺)₂] (Figure 156). Both compounds are clearly prone to dimerization and the similar drop in the ΔE_P values (38 vs. 41) and potential shifts $\Delta E_{1/2}$ (+155 vs +135) measured in the presence of *cis*-[Pd(en)(NO₃)₂] and *trans*-[Pd(CH₃CN)₂(Cl)₂] suggest that similar dimers (arrangement, orbital overlap, interplanar distance) are formed with the *cis* or *trans*-protected metallic hinges.

Further insights into the arrangements of the oxidized and reduced forms of these macrocyclic complexes have been provided by computational analyses. The DFT minimized structures of

the oxidized and two-electron reduced species obtained at M:L = 1 are shown in Figure 157. These structures reveal that *i*) Both viologens stand at the same distance from each other (3.46 Å) in the *cis* and *trans* protected dimers $cis-[(Pd^{2+})_2(en)_2(6^+)_2]_{dim}$ and $trans-[(Pd^{2+})_2(Cl)_2(6^+)_2]_{dim}$ and that *ii*) the *trans*-configuration of the PdCl₂ hinge enforces a twist of 36° between the viologen axis leading to a partial and quite limited overlap between both viologen cation radicals, while the *cis*-protected palladium hinge allows both viologens to lie perfectly aligned which results in a much more extensive orbital overlap.

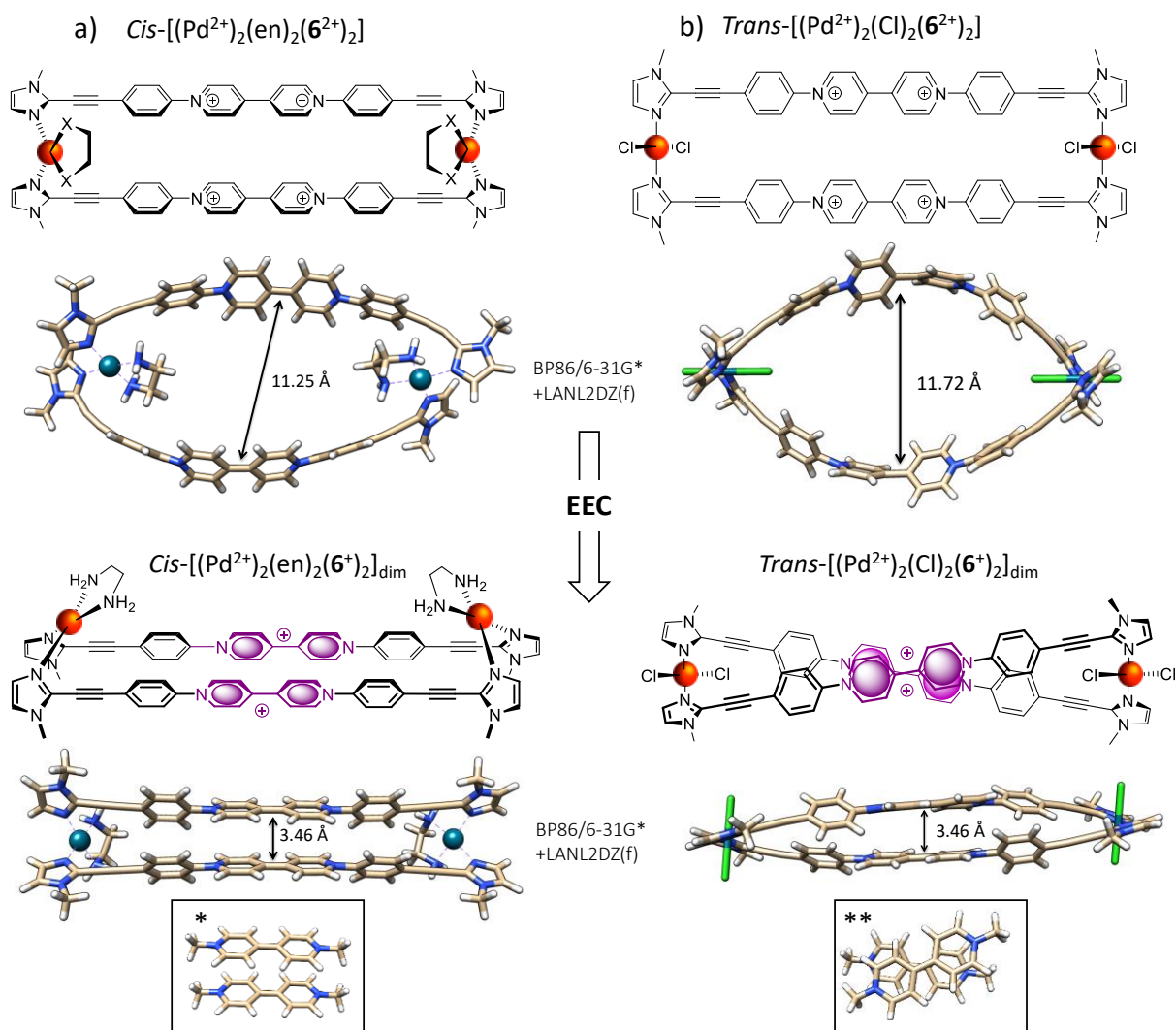


Figure 157: Schematic representation and DFT-minimized structures corresponding to the macrocyclic complexes formed at M:L=1 with a) $cis-[Pd(en)_2(NO_3)_2]$ and b) $trans-[Pd(Cl)_2(CH_3CN)_2]$ and to the corresponding π -dimers formed upon reduction of the viologen units (one electron per viologen). Enlarged top-views showing the relative position between both viologen cation radicals in the dimeric forms appear below in boxes marked with one or two stars.

The calculated structures depicted in Figure 157, and most notably the great difference observed between the structures of the oxidized species $cis-[(Pd^{2+})_2(en)_2(6^{2+})_2]$ and of the doubly reduced π -dimerized compound $cis-[(Pd^{2+})_2(en)_2(6^+)_2]_{dim}$, bring to light the existence of a reversible “inflating/deflating” process associated to the electron transfer centered on the

viologen units. At the oxidized state, the “inflated” oval-shaped form is imposed by electrostatic repulsive forces occurring within the highly positively charged ($z=+8$) complex $cis\text{-}[(\text{Pd}^{2+})_2(\text{en})_2(\mathbf{6}^{2+})_2]$. Deflation of this structure is then triggered by the one-electron reduction of both viologens and by the coupled dimerization of the resulting π -radicals to yield a square shaped intramolecular dimer. From a quantitative perspective, the deflation associated to electron transfer results in a large drop in the size of the inner cavity from 11.3 down to 3.46 Å (Figure 157a). A similar fully reversible electron-triggered “inflating/deflating” process is involved with the *trans* protected palladium hinge where the inner dimension changes from 11.7 Å to 3.46 Å upon stimulation (Figure 157b).

CV measurements carried out in the presence of the palladium salt $[\text{Pd}(\text{CH}_3\text{CN})_4]^{2+}$ brought to light the ability of the “non-protected” palladium center to promote the dimerization of $\mathbf{6}^{\bullet+}$. This effect is mainly revealed on the curve recorded at M:L = 1 through the large positive shift of the first reduction wave associated to a small negative shift of the second reduction wave (Figure 158). These changes were also found to come along with a significant broadening of the first reduction wave associated to a loss of its reversible character. Based on our analyses of the NMR data collected at this M:L ratio (see Figure 152 and Figure 153), this unexpected shape of the first viologen-centered reduction wave observed at ca -0.5 V was attributed to the presence of many different assemblies/oligomers in solution exhibiting slightly different local environments around the viologens units.

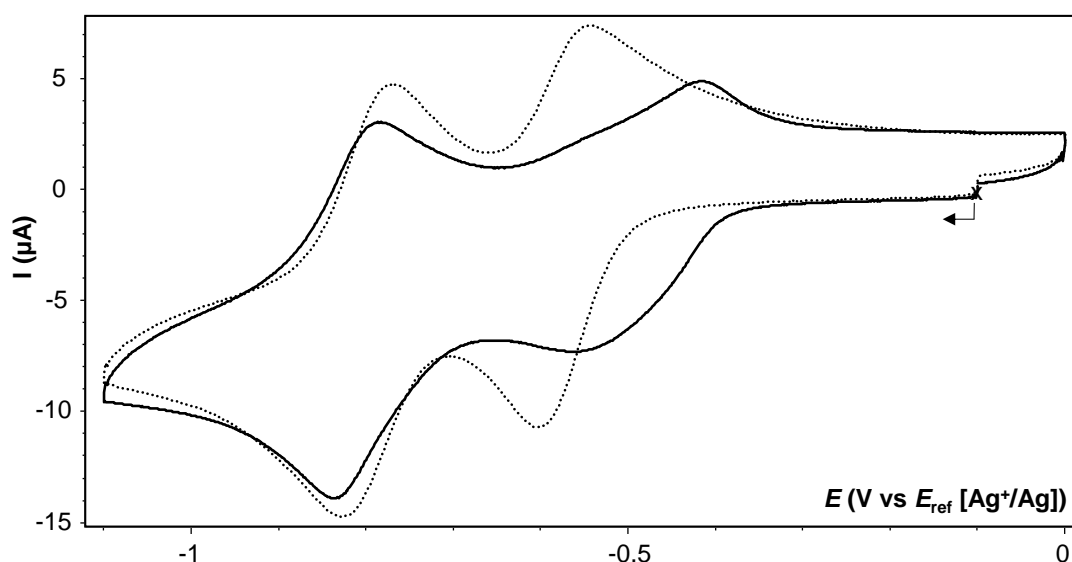


Figure 158: Cyclic voltammograms recorded for $\mathbf{6}(\text{PF}_6)_2$ (1 mM, DMF+TBAP 0.1 M) in the presence of A) $\text{Pd}(\text{ACN})_4(\text{BF}_4)_2$: 0 eq. (dotted line), 1 eq. (full line) (VC, $\varnothing = 3$ mm, E vs. Ag^+/Ag 10^{-2} M, $\nu = 0.1$ V s^{-1}).

All the electrochemical data discussed above support the conclusion that the intramolecular dimerization is highly favored in the presence of one molar equivalent of Palladium(II), which is consistent with the formation of macrocyclic square-shaped 2:2 complexes initially proposed on the ground of NMR data.

IV.1.6. Spectro-Electrochemical Measurements

The conclusion reached from the CV data recorded with *cis*-[Pd(en)₂(NO₃)₂], *trans*-[Pd(Cl)₂(ACN)₂] and Pd(ACN)₄(BF₄)₂ have been further confirmed by spectro-electrochemical measurements which involved regularly recording absorption spectra over time during the potentiostatic reduction of selected complexes.

Initial measurements have been carried out in the absence of metal, with the free ligand only. The exhaustive bulk reduction of **6**²⁺ (10 ml at 0.4 mM in electrolytic DMF, $E_{app} = -0.67$ V, one electron by viologen subunit) led to a decrease in the intensity of the absorption band centered at 305 nm (19200 M⁻¹.cm⁻¹) at the expense of new signals developing at $\lambda_{max} = 668$ nm (17700 M⁻¹.cm⁻¹), 728 nm (19800 M⁻¹.cm⁻¹) and 468 nm (20500 M⁻¹.cm⁻¹) (molar extinction coefficients have been calculated from the final spectrum, shown in Figure 159A as a dashed curve, recorded after completion of the electrolysis). The stability of **6**^{+•} at the electrolysis time scale was checked with coulometric and RDE measurements and upon checking that the initial electrochemical and spectroscopic signatures can be fully recovered by back-electrolysis (re-oxidation at 0V). The signature recorded after completion of the one-electron reduction is thus attributed to the “isolated” cation radical **6**^{+•} and the absence of signal in the near IR region confirms that no π -dimers are formed in these experimental conditions (0.4 to 1.0 mM in DMF).

Similar measurements have then been carried in the presence of 1 molar equiv. of *cis*-[Pd(NO₃)₂(en)]. As can be seen in Figure 159A, the exhaustive one-electron reduction of a 1:1 (M:L) mixture at $E_{app} = -0.67$ V led to the progressive development of a new set of absorption bands centered at $\lambda_{max} = 457$ nm (46400 M⁻¹.cm⁻¹), 614 nm (29100 M⁻¹.cm⁻¹), 651 nm (28800 M⁻¹.cm⁻¹) and 1000 nm (4500 M⁻¹.cm⁻¹). In agreement with the conclusion drawn above from CV data, the spectrum recorded after completion of the electrolysis exhibits typical features revealing the palladium assisted π -dimerization of **6**^{+•}, including the broad absorption band observed in the NIR region and the blue shift of the intense bands observed in the visible range. This new set of signals observed in Figure 159A and the well-defined isosbestic point

at 400 nm are thus fully consistent with the conclusion that the intramolecular dimer $cis-[(Pd^{2+})_2(en)_2(6^+)_{2}]_{dim}$ is generated in solution by reduction of the box-shaped metallocyclic 2:2 (M:L) complex $-cis-[(Pd^{2+})_2(en)_2(6^{2+})_2]$. As frequently seen with viologen-based dimers, the equilibria between the dimerized and non-dimerized forms (K_{dim} in Figure 158) is revealed in Figure 159A by the shoulder at about 730 nm attributed to the bis-radical $cis-[(Pd^{2+})_2(en)_2(6^{\bullet})_2]$, incorporating two non-interacting viologen-based cation radicals. Taken together, the weak intensity of this shoulder, the large intensity of the near IR band and the CV data discussed above support the idea that the dimerization equilibrium is strongly displaced towards the π -dimerized species.

Carrying out similar spectroelectrochemistry measurements in the presence of 1 equiv. of $trans-[Pd(Cl)_2(CH_3CN)_2]$ lead to the appearance of the same absorption bands centered at 457 nm ($45300 M^{-1}.cm^{-1}$), 611 nm ($29500 M^{-1}.cm^{-1}$), 648 nm ($26700 M^{-1}.cm^{-1}$) and at 1000 nm ($5800 M^{-1}.cm^{-1}$) (Figure 159B). At first sight, the great similarities observed between the SEC curves recorded with the *cis*- and *trans*-protected metal ions suggest that the bulk reduction of both mixtures leads to the same π -dimers.

We also discovered that the exhaustive reduction of 6^{2+} performed in the presence of only 0.5 equiv. of $trans-[Pd(Cl)_2(CH_3CN)_2]$ leads to the exact same set of signals. As can be seen in Figure 155B, the CV curves recorded in sub-stoichiometric conditions (M<L) exhibit three different waves attributed to successive reduction of the 2:2 (M:L) macrocyclic compound $trans-[(PdCl_2)_2(6^{2+})_2]$ followed by that of an intermediate compound that we assume to be a 1:2 (M:L) complex featuring two ligands bound to a single metal ion, and of the free ligand 6^{2+} . It needs to be mentioned that the formation of a 1:2 (M:L) intermediate complex at the electrode interface stills remains speculative as such species could not be observed on the 1H -NMR spectra recorded in sub-stoichiometric conditions. As a matter of fact, the proposed attribution mostly relies on previous investigations showing that the electron-triggered intramolecular π -dimerization of 2:1 (M:L) palladium complexes results in a positive shift of the first viologen-centered reduction wave of only +60 to 100 mV. Such limited stabilization effect is thus in good agreement with the intermediate position of the wave observed at *ca.* – 0.5 V in Figure 155B, attributed to a 2:1 (M:L), wherein the viologens are more easily reduced than in the free ligand but harder to reduce than in the macrocyclic 2:2 complex.

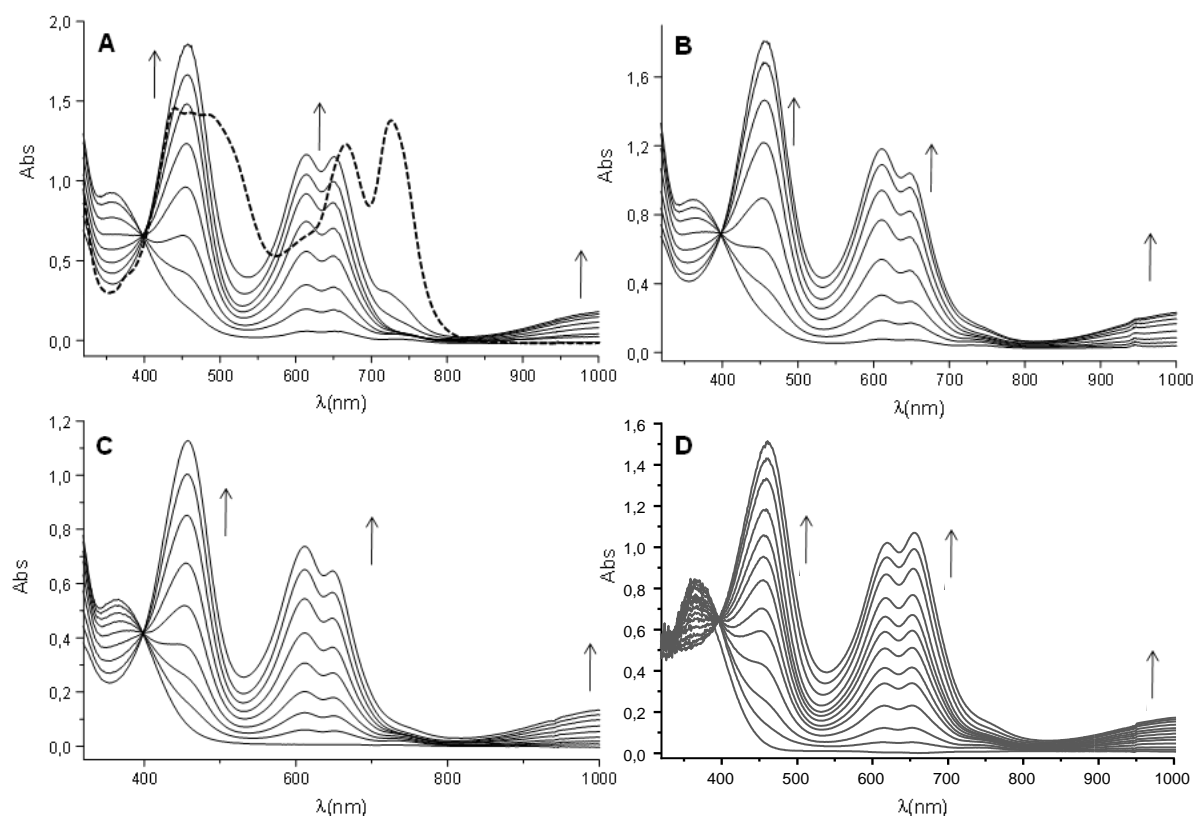


Figure 159: Superposition of the UV-vis spectra recorded during the exhaustive reduction (1 electron per viologen sub-unit) of 6^{2+} A) alone (dashed line), and in the presence of A) *cis*-[Pd(NO₃)₂(en)] (1 eq.; full line), B) *trans*-[Pd(Cl)₂(CH₃CN)₂] (1 eq.), C) *trans*-[Pd(Cl)₂(CH₃CN)₂] (0.5 eq.) and D) [Pd(CH₃CN)₄](BF₄)₂ (1 eq.) (DMF + 0,1 M TBAP, $E_{app} = -0.67$ V, 0,4 mM, 15 mL, $l = 1$ mm, $t \approx 30$ min, Pt).

The UV-vis spectra recorded during the exhaustive reduction of 6^{2+} (0.4 mM in electrolytic DMF, $E_{app} = -0.67$ V, one electron per viologen subunit) in the presence of [Pd(CH₃CN)₄](BF₄)₂ are shown in Figure 159D. Here again, a clean isosbestic point is observed at 400 nm and the signals developing upon reduction of the viologen centers are the same as those observed with *cis*-[Pd(NO₃)₂(en)] and *trans*-[Pd(Cl)₂(CH₃CN)₂]. It includes absorption bands at 466 nm (47200 M⁻¹.cm⁻¹), 621 nm (30800 M⁻¹.cm⁻¹) and 661 nm (35200 M⁻¹.cm⁻¹), as well as a broad absorption band centered at $\lambda_{max} = 1025$ nm (4900 M⁻¹.cm⁻¹). The full reversibility of the phenomena involved in solution was demonstrated by checking that the initial signature of the sample can be recovered by reoxidation at $E_{app} = 0$ V. These results are thus compatible with a palladium-assisted formation of π -dimerized species looking very much like those formed in the presence of *cis*-[Pd(NO₃)₂(en)] and *trans*-[Pd(Cl)₂(CH₃CN)₂]. It is to be mentioned that the relatively “high” intensity of the absorption band at 661 nm and of the shoulder at 730 nm suggest a more important concentration of non-associated radical comparatively to what was observed with *cis*-[Pd(NO₃)₂(en)] and *trans*-[Pd(Cl)₂(CH₃CN)₂].

Taken together, the $^1\text{H-NMR}$, CV and SEC results discussed above clearly demonstrate that the palladium ions promote the π -dimerization of the electrochemically generated viologen-based cation radical through the formation of highly preorganized metalacyclic architectures obtained by self-assembly of two metal ions and two imidazole-tipped ditopic ligands. The key experimental data supporting the idea that all the equilibria involved in solution are displaced in favor of intramolecular macrocyclic dimers noted $[(\text{Pd}^{2+})(\text{X})_2(\mathbf{6}^+)_2]_{\text{dim}}$ (X = en, Cl⁻ or ACN) are i) a major shift of the reduction potential towards less negative values, which results from a large stabilization of the electrogenerated radicals through π -dimerization, ii) a drop of the ΔE_p value down to almost 30 mV measured in the presence of palladium, iii) the inability of the free ligand to dimerize in palladium free solutions and from, iv) the observation of diagnostic spectroscopic signatures revealing the near quantitative formation of π -dimerized species featuring identical, if not very similar, structures.

One major result of our investigations is indeed the striking similarities observed between the spectra recorded after reduction of $\mathbf{6}^{2+}$ in the presence of *cis*-[Pd(NO₃)₂(en)] and *trans*-[Pd(Cl)₂(CH₃CN)₂]. Such results were quite unexpected since the spectral signature of π -dimers is known to mostly depend on the relative distance/orbital overlap between the two radicals and on their relative spatial arrangement. The DFT minimized structures of *cis*-[(Pd²⁺)₂(en)($\mathbf{6}^{2+}$)₂] and *trans*-[(PdCl₂)₂($\mathbf{6}^{2+}$)₂] and of the corresponding π -dimers *cis*-[(Pd²⁺)₂(en)($\mathbf{6}^+$)₂]_{dim} and *trans*-[(PdCl₂)₂($\mathbf{6}^+$)₂]_{dim} are shown in Figure 157. These model clearly bring to light the great structural differences imposed by the stereochemistry of the palladium center. At the oxidized state, the *cis* or *trans* coordination scheme of the inorganic spacer results in a slightly different distance between both viologens (11.3 vs 11.7 Å, see Figure 157). The *cis* /*trans* effects are in fact found to be far more important at the reduced state; ie between the π -dimerized structures *cis*-[(Pd²⁺)₂(en)($\mathbf{6}^+$)₂]_{dim} and *trans*-[(PdCl₂)₂($\mathbf{6}^+$)₂]_{dim}, wherein the conformations of the molecules are imposed by two different constraints : i) the stereochemistry of the metal center and ii) the proximity (π interplanar distance) required to achieve an orbital overlap between both viologen cation radicals involved in the complex. In the case of *trans*-[(PdCl₂)₂($\mathbf{6}^+$)₂]_{dim}, bringing the viologen radicals at a closer distance can only be achieved through a twisting of the macrocycle yielding a figure eight conformation with limited orbital overlaps between the π -radicals. The situation is very different for the *cis*-protected linkers as the dimerization is greatly facilitated by the conformation of the molecule enabling to bring both viologen cation radicals at suitably close distance while keeping a perfectly aligned co-facial arrangement. The major differences (interplanar distance, twist

angle) observed between the calculated π -dimerized structures of cis - $[(Pd^{2+})_2(en)(\mathbf{6}^+)_2]_{dim}$ and $trans$ - $[(PdCl_2)_2(\mathbf{6}^+)_2]_{dim}$ are thus not compatible with the nearly identical absorption spectra shown in Figure 159A and B. This inadequacy between structural feasibility and experimental data led us to suspect the existence of a stabilizing $trans \rightarrow cis$ isomerization coupled to the electron transfer centered on the $trans$ protected compound $trans$ - $[(PdCl_2)_2(\mathbf{6}^+)_2]$, the improved stability of the cis -dimer being the driving force of the reorganization or the $trans$ -dimer (Figure 160).

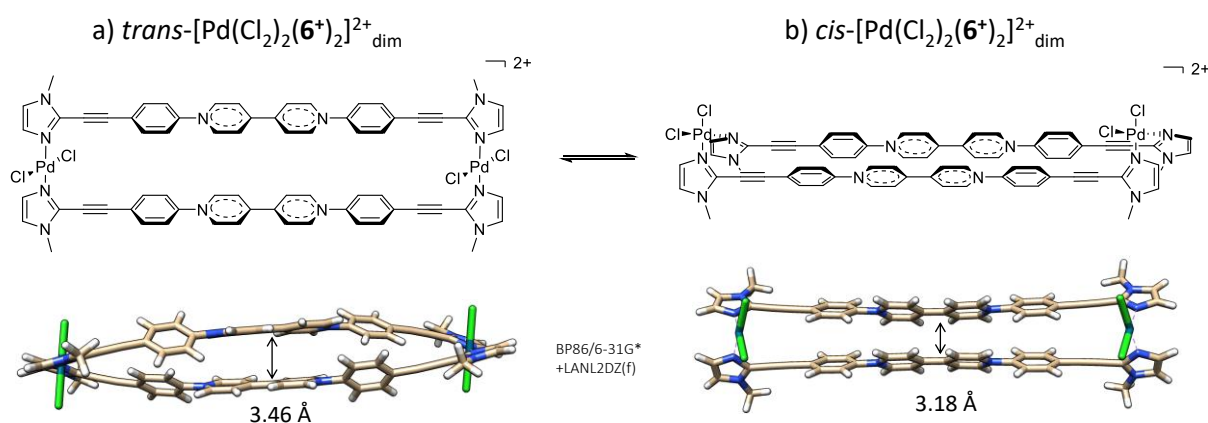


Figure 160: Optimized geometries for the cis - $[(PdCl_2)_2(\mathbf{6}^+)_2]_{dim}^{2+}$ and $trans$ - $[(PdCl_2)_2(\mathbf{6}^+)_2]_{dim}^{2+}$ complexes, at the DFT/M06-2X/6-31G(d)+LANL2DZ(f) level of theory.

The influence of the geometry around the palladium center during the π -dimerization process has been studied on the model species cis - $[(PdCl_2)_2(\mathbf{6}^+)_2]_{dim}^{2+}$ and $trans$ - $[(PdCl_2)_2(\mathbf{6}^+)_2]_{dim}^{2+}$. Their geometry has been studied by density functional theory (DFT) at the M06-2X/6-31G(d)+LANL2DZ(f) level of theory (Figure 160). The optimized structure of cis - $[(PdCl_2)_2(\mathbf{6}^+)_2]_{dim}^{2+}$ shows two parallel viologen sub-units at a distance of ca. 3.18 Å, while the structure obtained for $trans$ - $[(PdCl_2)_2(\mathbf{6}^+)_2]_{dim}^{2+}$ shows a crossed conformation that allows the viologens to stand with a slightly higher spacing (3.46 Å, twist angle 33.2°). The boxes embedding induces a deviation from the reference stacking distance (3.3 Å), either with a slightly compression for the cis isomer or a twisted and more “open” form for the $trans$ isomer. Their energetic difference amounts to -3.2 kcal.mol⁻¹ in favor of the cis isomer, which corroborates the $trans \rightarrow cis$ isomerization hypothesized on the ground of experimental data.

IV.1.7. Conclusion

As a conclusion, we have developed a metal-induced self-assembly strategy promoting the π -dimerization of simple viologen-based tectons at room temperature and in standard concentration ranges. Our investigations revealed that discrete box-shaped 2:2 (M:L) macrocycles are formed in solution in the presence of *cis*-[Pd(en)(NO₃)₂] and *trans*-[Pd(CH₃CN)₂(Cl)₂] and that the structure/geometry of the self-assembled product is determined by the relative position of the non-exchangeable ligands (*cis*-ethylenediamine *vs* *trans*-dichloride) initially bound to the metal. Use of a “non-protected” metal source, *ie tetrakis*(acetonitrile)Pd featuring four available/exchangeable binding sites, was conversely found to enable the formation of coordination polymers/oligomers reaching a maximum size at M:L = 1.

On the ground of detailed spectroscopic and electrochemical data supported by computational calculations, we have established that all the investigated palladium-based inorganic hinges (*cis*-, *trans*- or *un*-protected) promote an effective intramolecular π -dimerization of the electrogenerated viologen cation radicals involved in the macrocyclic or polymeric assemblies. From a structural point of view, the reduction and re-oxidation of both viologen units involved in the discrete 2:2 (M:L) assemblies result in a reversible “inflating/deflating” of the macrocyclic structure associated to a large modification in the size of the inner cavity going from ~11.3 to 3.5 Å.

We have also established that the one electron reduction of the viologen units present in different metal:ligand mixtures leads to the formation of the same intramolecular π -dimer, regardless of the initial environment around the metallic precursor (*cis*-, *trans*- or *un*-protected) and of the relative ratio between metal and ligand initially introduced in solution. In line with this finding, all the experimental and computational data discussed above suggest that the electrical stimulation of the macrocyclic assembly formed with *trans*-[Pd(CH₃CN)₂(Cl)₂] triggers a *trans* → *cis* isomerization of the coordinated ligands.

Dissociation of the coordination polymers/oligomers formed in the presence of *tetrakis*(acetonitrile)palladium(II) was also achieved upon reduction of the viologen units involved in the organic tectons, the driving force of the disassembling process being here again the formation of (2:2) (M:L) box-shape π -dimers.

General Conclusion

The aim of this thesis is to develop redox switchable molecular or supramolecular systems whose properties can be modulated by structural rearrangements. This task has been achieved through the introduction of viologen moieties into the skeleton of these systems, where it can benefit from the π -dimerization process that occurs between the viologen units at the cation-radical state.

In this prospect, the first part reports the formation of supramolecular assemblies involving Cucurbit[8]uril (CB[8]) cavitands and viologen based tectons as building elements. The driving force of the self-assembly process is the π -dimerization of the viologen cation radicals introduced at the porphyrin and tetraphenyl ethylene platforms. The reversible association of the redox-responsive tecton with CB[8] to form self-assembled architectures in solution mainly under redox-stimulation, has been established on the ground of spectroscopic, electrochemical, spectro-electrochemical and computational data.

The second part reports the development of viologen-based tweezers and clips of various sizes and flexibilities. In this aspect, tweezers incorporating 2,6-*bis*(phenyl)pyridine as a spacer have shown to exist in two different conformations in solution. These tweezers are flexible/short enough to promote the intramolecular π -dimerization of the viologen units introduced at the meta position of the terminal phenyl substituents and the efficiency of the dimerization is found to depend on the length and flexibility of the organic linkers introduced between the spacer and the viologens. The binding properties of one of the 2,6-*bis*(phenyl)pyridine based tweezer **38**⁴⁺ has higher affinity toward charged aromatic donors than for uncharged ones. Whereas, Tweezers incorporating terpyridine as a spacer exist solely in W-shaped conformation in solution and the one electron reduction of the viologens triggers the conformational change into U-shaped isomers that are stabilized by intramolecular dimerization of both viologen-cation radicals located on both sides of the terpyridine spacer. In addition to that the presence of a metal ion in the terpyridine spacer proved to inhibit the π -dimerization of the viologens. Finally, clips incorporating dibenzoacridine as a spacer have shown to form intramolecular π -dimer between the viologens despite of its imposed rigidity.

The last part discusses about the metal-induced self-assembly strategy that is used to promote the π -dimerization of viologen-based radicals at room temperature and in standard concentration ranges. Discrete box-shaped 2:2 (M:L) macrocycles or coordination polymers

are formed in solution by self-assembly of a viologen-based ditopic-ligand with cis-[Pd(en)(NO₃)₂], trans-[Pd(CH₃CN)₂(Cl)₂] or [Pd(CH₃CN)₄(BF₄)₂]. Changing the redox state of the bipyridium units involved in the tectons, from their dicationic state to their radical cation state, results in a reversible “inflation/deflation” of the discrete 2:2 (M:L) macrocyclic assemblies associated to a large modification in the size of their inner cavity. Viologen-centered electron transfer is also used to trigger a dissociation of the coordination polymers formed with tetrakis(acetonitrile)Pd(II), the driving force of the disassembling process being the formation of discrete box-shaped 2:2 (M:L) assemblies stabilized by π -dimerization of both viologen cation radicals.

As perspectives, we believe that the work in this thesis will be a great source of inspiration for the development of redox-responsive dynamic supramolecular assemblies involving π -dimerization as actuation forces which can open new approaches toward the creation of redox responsive smart materials.

V: Experimental Part

V.1. General Synthesis

V.1.1. Solvents and Reagents

DMSO (Aldrich, 99.9%), methanol (VWR, pure), ethanol (Carlo Erba, puro), acetonitrile (VWR, HPLC grade), methylene chloride (Carlo Erba, puro), chloroform (Carlo Erba, puro), cyclohexane (Sigma Aldrich, 98.8%) and pentane (Sigma Aldrich, 95%) were purchased and used as received. THF was dried over alumina and triethylamine was distilled over KOH and argon. Water was purified by reverse osmometry with an Elga Purelab purification system (5 M Ω .cm). The organic and inorganic reagents used in the procedures described below were purchased from Aldrich, Acros, Alfa Aesar or TCI and were used without further purification.

V.1.2. Apparatus and Spectroscopic Characterizations

¹H-NMR and ¹³C-NMR spectra were recorded at room temperature on Bruker Avance 300 or 400 MHz spectrometers. ¹H chemical shifts were referenced to residual solvent peaks. Coupling constants values (J) are given in hertz and chemical shifts (δ) in ppm. The abbreviations used are: s = singlet, d = doublet, t = triplet, m = multiplet and br = broad.

Diffusion experiments were performed using the bipolar pulse longitudinal eddy current delay (BPPLIED) pulse sequence. Sine shaped pulse field gradient were used with a length $\delta = 1.5$ ms and the gradient intensity was linearly incremented over 20 or 30 experiments. After each gradient pulse a 200 μ s delay was used as a recovery delay. The diffusion time Δ was chosen between 1200 and 2000 μ s. The DOSY spectra were obtained by applying an Inverse Laplace Transform (ILT) along the diffusion axis, using the Gifa algorithm embedded into the commercial software NMRnotebook (NMRTEC, Illkirch). Standard NMR tubes ($\varnothing = 5$ mm) were used for DOSY experiments performed in DMSO while Norell S300 tubes ($\varnothing = 3$ mm) were used with acetonitrile to limit the effects of convection.

UV-vis spectra were recorded on a MCS 500 or MCS 601 UV-NIR Zeiss spectrophotometer using conventional quartz cells or all-quartz immersion probes (Hellma Inc.).

Mass spectrometry measurements were carried out at the “Centre commun de spectrométrie de masse-Lyon 1” mass spectrometry facility with a MicrOTOFQ II(Bruker) using electrospray ionization (ESI).

X-Ray diffraction analyses were carried out at the “Centre de Diffraction Henri Longchambon-Lyon 1”. A suitable crystal $0.71 \times 0.53 \times 0.31 \text{ mm}^3$ was selected and mounted on a nylon loop in perfluoroether oil on an by Xcalibur, Atlas, Gemini ultra-diffractometer. The crystal was kept at a steady $T = 150.01(10) \text{ K}$ during data collection. The structure was solved with the **ShelXT** (Sheldrick, 2015) structure solution program using the Intrinsic Phasing solution method and by using **Olex2** (Dolomanov et al., 2009) as the graphical interface. The model was refined with version 2018/3 of **ShelXL** (Sheldrick, 2015) using Least Squares minimisation.

ESR X-band spectra were recorded on a Bruker EMX, equipped with the ER-4192 ST Bruker cavity.

V.2. Electrochemical studies

V.2.1. Solvents and Electrolytes

Acetonitrile (Acros Organics, extra-dry with molecular sieves, water < 0.005%), dimethylformamide (Sigma Aldrich, extra-dry with molecular sieves, water < 0.01%) were degassed using Freeze-Pump-Thaw procedure and were used for the spectroelectrochemical studies. The electrolyte tetra-*n*-butylammonium perchlorate (TBAP, Fluka puriss.) was purchased and used without further purification

V.2.2. Apparatus and Spectroelectrochemical Characterization

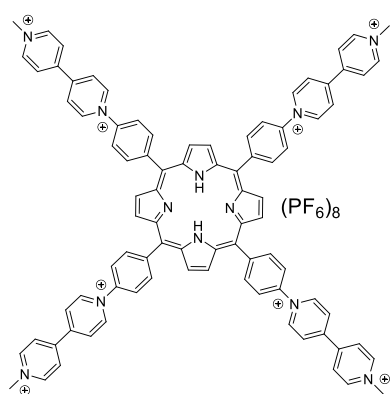
Cyclic voltammetry (CV) and voltammetry with rotating disc electrodes (RDE) were recorded using a SP300 Bilogic potentiostat. The analytical studies were conducted under an argon atmosphere (glove box or argon stream) in a standard one-compartment, three-electrodes electrochemical cell. Tetra-*n*-butylammonium was used as supporting electrolytes (0.1 M). An automatic ohmic drop compensation procedure was systematically performed when using cyclic voltammetry. Vitreous carbon ($\varnothing = 3 \text{ mm}$) working electrodes (CH Instruments) were polished with 1 mm diamond paste before each recording. Standard sweep rates of 0.01 and 0.1 V s^{-1} were used in CV and RDE experiments. Voltamperometry with a rotating disk electrode (RDE) was carried out with a radiometer (CTV101 radiometer analytical) equipment at a rotation rate of 500 rad min^{-1} using a glassy carbon RDE tip ($\varnothing = 3 \text{ mm}$).

Spectroelectrochemical measurements were carried out at room temperature under an argon atmosphere (glove box or argon stream) in a standard one-compartment, three-electrodes electrochemical cell with a biologic SP300 potentiostat coupled to an MCS 500 or MCS 601 UV-NIR Zeiss spectrophotometer using 1 or 10 mm all-quartz Helmma immersion probes. Electrolyses were conducted at room temperature using platinum plates (10 cm²) working electrodes and a large piece of carbon felt as a counter-electrode isolated from the electrolytic solution through an ionic bridge. AgNO₃/Ag (CH Instruments, 10⁻² M + TBAP 10⁻¹ M in CH₃CN) was used as a reference electrode.

V.3. Synthetic procedures

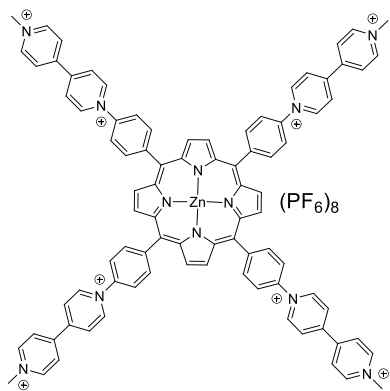
All reagents were either obtained commercially and used as received without any further purification or synthesized according to literature procedures.

V.3.1. Synthetic procedures related to chapter II



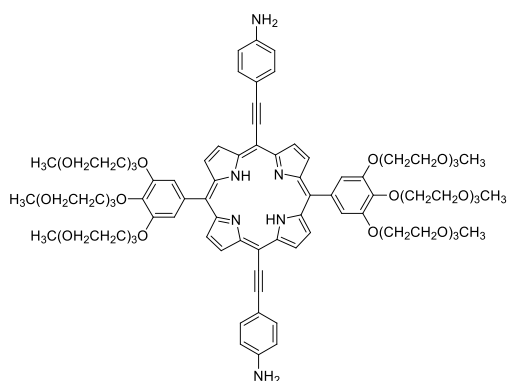
Synthesis of **11H₂(PF₆)₈**: To a stirred solution of 10Cl₂¹⁰⁴ (206 mg, 0.5 mmol) in ethanol and water (50 mL, 2:1) **8**²⁰⁷ (67 mg, 0.1 mmol) was added. The reaction was refluxed for 18 h, then concentrated under reduced pressure. Purification by flash chromatography on silica gel (CH₃CN/H₂O/sat. aq. KNO₃: 12/7/7) and anion exchange using an aqueous saturated KPF₆ solution, gave **11H₂(PF₆)₈** (71 mg, 29%) as a violet solid.

¹H NMR (CD₃CN, 400 MHz): δ = -2.78 (s, 2H), 4.48 (s, 12H), 8.24 (d, 8H, J = 8.2 Hz), 8.58 (d, 8H, J = 6.3 Hz), 8.64 (d, 8H, J = 8.2 Hz), 8.78 (d, 8H, J = 6.5 Hz), 8.96 (d, 8H, J = 6.3 Hz), 9.08 (s, 8H), 9.54 ppm (d, 8H, J = 6.5 Hz). Abs (DMF) : 418 nm (ε=100000 M⁻¹.cm⁻¹), 516 nm (ε=5087.7 M⁻¹.cm⁻¹), 553 nm (ε=2175.4 M⁻¹.cm⁻¹), 592 nm (ε=1298.2 M⁻¹.cm⁻¹), 648 nm (ε=982.4 M⁻¹.cm⁻¹).



Synthesis of **11Zn(PF₆)₈**: To a stirred solution of **10Cl₂**¹⁰⁴ (206 mg, 0.5 mmol) in ethanol and water (50 mL, 2:1) **9**²⁰⁸ (74 mg, 0.1 mmol) was added. The reaction was refluxed for 18 h, then concentrated under reduced pressure. Purification by flash chromatography on silica gel (CH₃CN/H₂O/sat. aq. KNO₃: 12/7/7) and anion exchange using an aqueous saturated KPF₆ solution, gave **11Zn(PF₆)₈** (81 mg, 32%) as a violet solid.

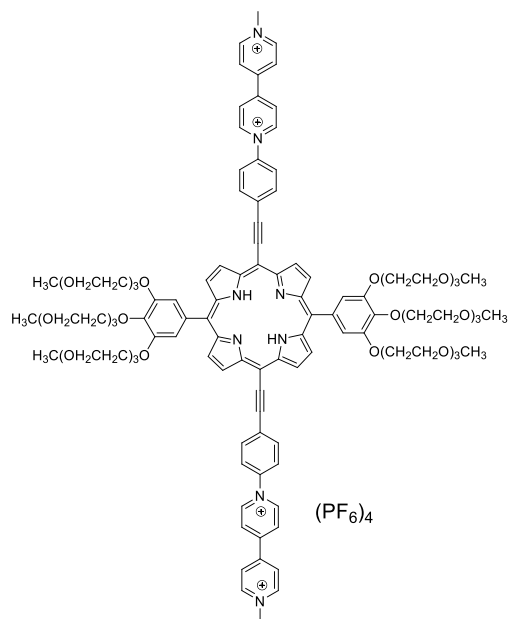
¹H NMR (CD₃CN, 400 MHz): δ = 4.48 (s, 12H), 8.21 (d, 8H, J = 7.7 Hz), 8.57 (d, 8H, J = 5.4 Hz), 8.62 (d, 8H, J = 7.7 Hz), 8.77 (d, 8H, J = 5.6 Hz), 8.97 (d, 8H, J = 5.4 Hz), 9.04 (s, 8H), 9.55 ppm (d, 8H, J = 5.6 Hz). Abs (DMF): λ = 426 nm (ε=266666 M⁻¹.cm⁻¹), 561 nm (ε=1736.8 M⁻¹.cm⁻¹), λ = 606 nm (ε=10701.7 M⁻¹.cm⁻¹).



Synthesis of **15** : To a stirred solution of **14**¹³⁴ (2.8 g, 1.74 mmol) in THF (20 mL), 4-Ethynylaniline (0.51 g, 4.39 mmol) with triethylamine (14 mL) was added. Then the mixture was deoxygenated by freeze-pump-thaw cycles and purged with argon gas. Then triphenyl arsine (0.26 g, 0.87 mmol) with Pd₂(dba)₃ (143 mg, 0.157 mmol) was introduced and allowed the mixture to stir at 50 °C in the dark for 24

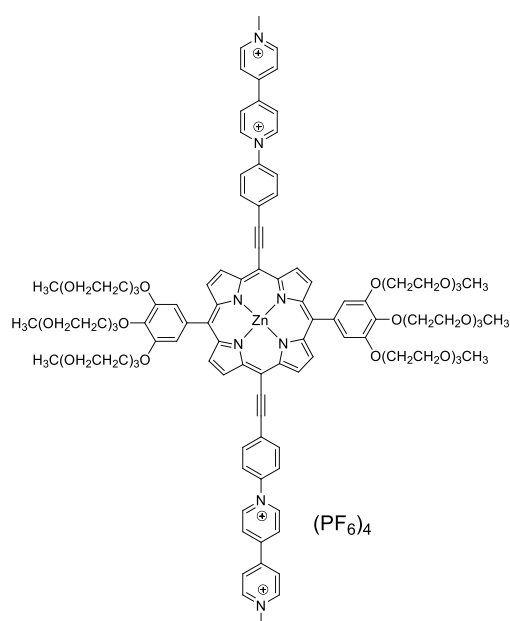
h. Then the crude mixture was washed with brine. The organic layer separated and dehydrated by anhydrous sodium sulphate. Then the solution was evaporated under reduced pressure and the crude material was subjected to chromatography column on silica gel using ethyl methanol/ dichloromethane 0.3 : 9.7 as an eluent to give **15** (2.6 g, 90%).

¹H NMR (300 MHz, CDCl₃) δ 9.63 (d, J = 4.7 Hz, 4H), 8.84 (d, J = 4.7 Hz, 4H), 7.84 (d, J = 8.3 Hz, 4H), 7.45 (s, 4H), 6.86 (d, J = 8.3 Hz, 4H), 4.51 (m, 4H), 4.32 (m, 8H), 4.05 – 3.89 (m, 17H), 3.81-3.73 (m, 12H), 3.64 – 3.61 (m, 13H), 3.54 – 3.51 (m, 9H), 3.42 (s, 6H), 3.38 – 3.35 (m, 10H), 3.22 (s, 11H), -1.85 (s, 2H). HR-MS (ESI⁺) calc. for [M+3H]³⁺ m/z = 555.9419; found m/z = 555.9423.



Synthesis of **17H₂(PF₆)₄**: To a stirred solution of **16(PF₆)₂**¹⁰⁴ (1.1 g, 1.8 mmol in EtOH/CH₃CN (2:1,60 mL) **15** (1 g, 0.6 mmol)) was introduced. The resulting mixture was allowed to stir at 70 °C for 18h. After completion of the reaction, the mixture was evaporated under reduced pressure and the crude product was subjected to chromatography on silica gel using acetonitrile/water/saturated aqueous KNO₃ (6:2:2) as eluent. A final counter-ion metathesis using a saturated aqueous KPF₆ solution afforded **17H₂(PF₆)₄** (0.88 g, 58%) as a green powder.

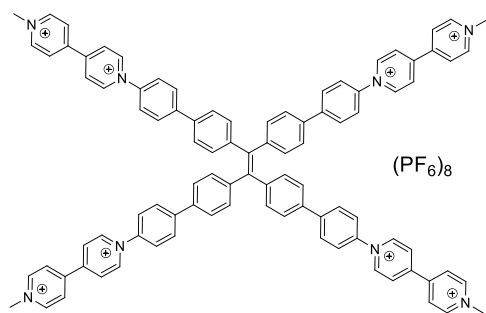
¹H NMR (400 MHz, DMSO) δ 9.92 (d, J = 4.4 Hz, 4H), 9.83 (d, J = 6.5 Hz, 4H), 9.35 (d, J = 6.4 Hz, 4H), 9.08 (d, J = 4.4 Hz, 4H), 9.03 (d, J = 6.5 Hz, 4H), 8.93 (d, J = 6.4 Hz, 4H), 8.63 (d, J = 8.4 Hz, 4H), 8.28 (d, J = 8.4 Hz, 4H), 7.62 (s, 4H), 4.49 (s, 6H), 3.10-4.42 (m, 90H), -2.06 (s, 2H). HR-MS (ESI⁺) calc. for [M]⁴⁺ m/z = 493.7372; found m/z = 493.7376. Abs (DMF): λ =452 nm (ε=162162 M⁻¹.cm⁻¹), λ =607 nm (ε=77477 M⁻¹.cm⁻¹) and λ =695 nm (ε=52252 M⁻¹.cm⁻¹).



Synthesis of **17Zn(PF₆)₄**: To a solution of **17H₂(PF₆)₄** (0.125 g, 0.48 mmol) in acetonitrile (20 ml), Zn(OAc)₂ (90 mg, 0.048 mmol) was introduced then the mixture was stirred at room temperature for 16 h in a dark environment. Then the mixture was evaporated under reduced pressure and KPF₆ was added and the precipitate was collected by filtration to afford **17Zn(PF₆)₄** in quantitative yield.

¹H NMR (400 MHz, DMSO) δ 9.83 (m, 8H), 9.35 (d, J = 6.3 Hz, 4H), 9.02 (m, 8H), 8.93 (d, J = 6.3 Hz, 4H), 8.57 (d, J = 8.4 Hz, 4H), 8.25 (d, J = 8.4

Hz, 4H), 7.52 (s, 4H), 4.49 (s, 6H), 3.15-4.42 (m, 90H). HR-MS (ESI⁺) calc. for [M]⁴⁺ m/z = 509.2156; found m/z = 509.2145. Abs (DMF) : $\lambda = 451$ nm ($\epsilon = 103614$ M⁻¹.cm⁻¹) and $\lambda = 670$ nm ($\epsilon = 48192$ M⁻¹.cm⁻¹).

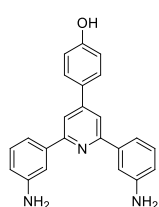


Synthesis of 21(PF₆)₈ : To a solution of **16(PF₆)₂**¹⁰⁴ (2.6 g, 3.90 mol) in EtOH/CH₃CN (1:1,250 mL), **20** (0.38 g, 0.54 mmol)) was added. The resulting mixture was allowed to stir at 70 °C for 18h. After completion of the reaction, the mixture was evaporated under reduced pressure and the crude product was subjected to column chromatography on

silica using acetonitrile/water/saturated aqueous potassium nitrate (6:2:2) as eluent. A final counter-ion metathesis using a saturated aqueous potassium hexafluorophosphate solution afforded **21(PF₆)₈** (0.54 g, 40%) as a brown powder.

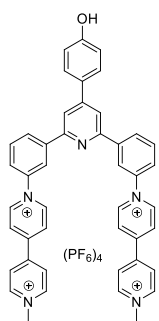
¹H NMR (400 MHz, CD₃CN) δ (ppm): 9.17 (d, J = 6.7 Hz, 8H), 8.88 (d, J = 6.7 Hz, 8H), 8.57 (d, 6.7 Hz, 8H), 8.46 (d, 6.7 Hz, 8H), 7.98 (d, J = 7.2 Hz, 8H), 7.83 (d, J = 7.2 Hz, 8H), 7.66 (d, J = 8.1 Hz, 8H), 7.37 (d, J = 8.1 Hz, 8H), 4.42 (s, 12H). ¹³C NMR (101 MHz, CD₃CN) δ (ppm): 151.03, 149.80, 147.13, 145.97, 144.47, 144.32, 141.99, 141.55, 137.39, 132.51, 129.26, 127.78, 127.50, 127.43, 125.54, 49.23. HR-MS (ESI⁺) calc. for [M]⁸⁺ m/z = 164.5769; found m/z = 164.5773.

V.3.2. Synthetic procedures related to chapter III



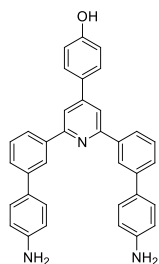
Synthesis of 37: In a 250 mL round-bottomed flask equipped with a reflux condenser and a dropping funnel, **36**¹⁸⁵ (5 g, 12 mmol) is suspended with palladium on carbon 10% (0.1 g) in a mixture of ethanol (30 mL) and dimethylformamide (DMF, 5 mL). Then mixture was warmed and hydrazine monohydrate 80% (10 mL) in ethanol (15 mL) was added dropwise over a period of 1 hour through a dropping funnel, while keeping the temperature at about 70°C. After 4 hours, the mixture was filtered while hot to remove Pd/C, then solution was evaporated under reduced pressure and the crude material was subjected to chromatography column on silica gel using ethyl acetate/dichloromethane 1:1 as an eluent to give **37** (3 g, 70%) as a pure white powder.

^1H NMR (400 MHz, Acetone) δ (ppm): 7.93 (s, 2H), 7.81 (d, $J = 8.7$ Hz, 2H), 7.66 – 7.62 (m, 2H), 7.51 (d, $J = 7.7$, 2H), 7.20 (t, $J = 7.7$ Hz, 2H), 7.04 – 6.99 (d, $J = 8.7$ Hz, 2H), 6.79 – 6.73 (m, 2H), 4.74 (broad s, 4H). ^{13}C NMR (101 MHz, Acetone) δ (ppm): 158.57, 157.49, 149.37, 148.69, 140.63, 130.09, 129.08, 128.48, 116.86, 115.92, 115.58, 114.98, 113.17. HR-MS (ESI $^+$) calc. for $[\text{M}+\text{H}]^+$ $m/z = 354.1601$; found $m/z = 354.1594$.



Synthesis of **38(PF₆)₄**: To a solution of **49(PF₆)₂**¹⁰⁴ (747mg, 1.18 mmol) in EtOH/CH₃CN (1:1,16 mL), **37** (200 mg, 0.56 mmol)) was added. The resulting mixture was allowed to stir at 70°C for 18h. After completion of the reaction, the mixture was evaporated under reduced pressure and the crude product was subjected to column chromatography on alumina using acetonitrile/water/saturated aqueous potassium nitrate (6:2:2) as eluent. A final counter-ion metathesis using a saturated aqueous potassium hexafluorophosphate solution afforded **38(PF₆)₄** (0.28 g, 40%) as a pure light yellow powder.

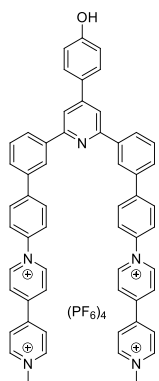
^1H NMR (400 MHz, CD₃CN)) δ (ppm): 9.30 (d, $J = 6.9$ Hz, 4H), 8.91 (d, $J = 6.6$ Hz, 4H), 8.77 (d, $J = 7.6$ Hz, 2H), 8.67 (m, 2H), 8.62 (d, $J = 6.9$ Hz, 4H), 8.48 (d, $J = 6.6$ Hz, 4H), 8.29 (s, 2H), 7.92 (t, $J = 7.6$ Hz, 2H), 7.88(d, $J = 8.6$ Hz, 2H), 7.41 (s, 1H), 7.04 (d, $J = 8.6$ Hz, 2H), 4.44 (s, 6H). ^{13}C NMR (101 MHz, CD₃CN)) δ (ppm): 159.34, 155.59, 151.49, 151.42, 149.93, 147.18, 146.37, 143.55, 142.16, 131.69, 131.08, 129.52, 127.80, 127.57, 125.69, 123.73, 118.53, 116.64, 117.91, 30.47. HR-MS (ESI $^+$) calc. for $[\text{M}]^{4+}$ $m/z = 165.8244$; found $m/z = 165.8242$.



Synthesis of **41**: To a stirred solution of **40**¹⁸⁵ (0.4 g, 0.83 mmol) and 4-Aminophenylboronic acid pinacol ester (0.54g, 2.49 mmol) in tetrahydrofuran (THF, 100mL), Pd(PPh₃)₄ (0.19 g, 0.16 mmol) and K₃PO₄ (0.12 g, 0.24 mmol) were added. The mixture was then refluxed for 24h, then the solution was evaporated under reduced pressure and the crude material was subjected to chromatography column on silica gel using ethyl acetate/dichloromethane 3:7 as an eluent to give **41** (0.38 g, 92%) as a pure white powder.

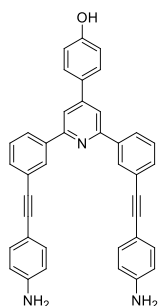
^1H NMR (400 MHz, Acetone)) δ (ppm): 8.72 (s, 1H), 8.55 (s, 2H), 8.21 (d, $J = 7.5$ Hz, 4H), 7.92 (d, $J = 8.2$ Hz, 2H), 7.66 (d, $J = 7.7$ Hz, 2H), 7.55 (dd, $J = 7.5, 5.8$ Hz, 6H), 7.03 (d, $J =$

8.2 Hz, 2H), 6.81 (d, J = 8.4 Hz, 4H), 4.79 (s, 4H). ^{13}C NMR (101 MHz, Acetone) δ (ppm): 158.63, 157.23, 149.98, 148.27, 141.88, 140.11, 129.82, 129.27, 129.02, 128.72, 127.68, 126.47, 124.60, 124.55, 116.11, 115.87, 114.65. HR-MS (ESI⁺) calc. for $[\text{M}+\text{H}]^+$ m/z = 502.2226; found m/z = 506.2232.



Synthesis of **42**(PF₆)₄: To a solution of 1-(2,4-dinitrophenyl)-1'-methyl-[4,4'-bipyridine]-1,1'-diium hexafluorophosphate **49**(PF₆)₂¹⁰⁴ (312mg, 0.49 mmol) in EtOH/CH₃CN (1:1,80 mL), **41** (120 mg, 0.23 mmol) was added. The resulting mixture was allowed to stir at 70°C for 18h. After completion of the reaction, the mixture was evaporated under reduced pressure and the crude product was subjected to column chromatography on alumina using acetonitrile/water/saturated aqueous potassium nitrate (6:2:2) as eluent. A final counter-ion metathesis using a saturated aqueous potassium hexafluorophosphate solution afforded **42**(PF₆)₄ (0.13 g, 52%) as a yellow powder.

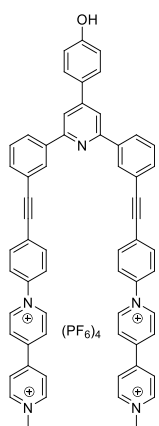
^1H NMR (400 MHz, CD₃CN) (ppm): 9.24 (d, J = 6.4 Hz, 4H), 8.90 (d, J = 6.4 Hz, 4H), 8.65 – 8.57 (m, 6H), 8.47 (t, J = 6.4 Hz, 6H), 8.25 – 8.14 (m, 6H), 7.91 (t, J = 8.3 Hz, 8H), 7.75 (t, J = 7.8 Hz, 2H), 7.41 (s, 1H), 7.06 – 6.98 (m, 2H), 4.44 (s, 6H). ^{13}C NMR (101 MHz, CD₃CN) (ppm): 207.44, 159.00, 157.39, 150.73, 149.88, 147.17, 146.08, 145.08, 141.12, 139.54, 130.33, 130.19, 129.85, 129.48, 128.73, 128.33, 127.80, 127.55, 126.53, 125.56, 117.90, 117.64, 116.48, 49.27. HR-MS (ESI⁺) calc. for $[\text{M}]^{4+}$ m/z = 203.8401; found m/z = 203.8394.



Synthesis of **43**: A dry flask (100 mL) was charged with **40**¹⁸⁵ (1 g, 2.09 mmol), 4-Ethynylaniline (1.2 g, 10.2 mmol), piperidine (3 mL), Pd(PPh₃)₂Cl₂ (150 mg, 0.213 mmol), CuI (47mg, 0.429 mmol) and THF (100 mL). Then the mixture was heated at 54°C for 20 h. After cooling, the mixture was washed with water, then the solid was dissolved in DCM and purified by column chromatography through silica (EA/ dichloromethane = 1/9), affording compound **43** (0.4 g, 34%) as yellow powder.

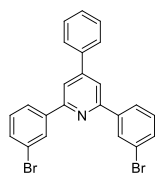
^1H NMR (400 MHz, Acetone) δ (ppm): 8.51 (s, 2H), 8.39 – 8.26 (m, 2H), 8.21 (s, 2H), 7.96 (d, J = 8.6 Hz, 2H), 7.62 – 7.49 (m, 4H), 7.32 (d, J = 8.5 Hz, 4H), 7.05 (d, J = 8.6 Hz, 2H),

6.71 (d, $J = 8.5$ Hz, 4H), 5.07 (s, 4H). ^{13}C NMR (101 MHz, Acetone) δ 158.64, 156.70, 150.10, 149.33, 139.82, 132.78, 131.50, 129.54, 129.40, 128.89, 128.76, 126.37, 124.66, 116.43, 115.78, 114.04, 110.15, 91.15, 86.49. HR-MS (ESI⁺) calc. for $[\text{M}+\text{H}]^+$ $m/z = 554.2227$; found $m/z = 554.2224$.



Synthesis of **44(PF₆)₄**: To a solution of **49(PF₆)₂**¹⁰⁴ (238mg, 0.49 mmol) in EtOH/CH₃CN (1:1,80 mL), **43** (100 mg, 0.18 mmol)) was added. The resulting mixture was allowed to stir at 70°C for 18h. After completion of the reaction, the mixture was evaporated under reduced pressure and the crude product was subjected to column chromatography on alumina using acetonitrile/water/saturated aqueous potassium nitrate (6:2:2) as eluent. A final counter-ion metathesis using a saturated aqueous KPF₆ solution afforded **44(PF₆)₄** (0.07g, 27%) as a brown powder.

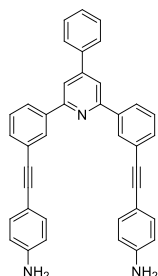
^1H NMR (400 MHz, Acetone, 3mM) δ (ppm): 9.75 (d, $J = 6.4$ Hz, 4H), 9.45 (d, $J = 6.4$ Hz, 4H), 9.07 (d, $J = 6.4$ Hz, 4H), 8.95 (d, $J = 6.4$ Hz, 4H), 8.80 (s, 1H), 8.57 (s, 2H), 8.49 (d, $J = 7.4$ Hz, 2H), 8.26 (s, 2H), 8.14 (d, $J = 8.4$ Hz, 4H), 8.05 (d, $J = 8.4$ Hz, 4H), 7.96 (d, $J = 8.2$ Hz, 2H), 7.76 (d, $J = 7.2$ Hz, 2H), 7.69 (d, $J = 7.4$ Hz, 2H), 7.06 (d, $J = 8.2$ Hz, 2H), 4.79 (s, 6H). ^{13}C NMR (101 MHz, Acetone) δ 159.15, 156.33, 150.96, 150.60, 149.47, 147.12, 145.90, 142.17, 140.16, 133.58, 132.36, 130.20, 129.27, 129.11, 128.74, 128.13, 127.36, 127.01, 125.21, 122.68, 116.85, 116.10, 92.78, 87.33, 67.21, 48.45. HR-MS (ESI⁺) calc. for $[\text{M}]^{4+}$ $m/z = 215.8401$; found $m/z = 215.8401$.



Synthesis of **46**: A 500 mL round-bottomed flask was charged with **45** (2.4 g, 22 mmol), **39** (8.75 g, 44 mmol), ammonium acetate (10.7 g, 0.13 mol) and glacial acetic acid (50 mL). The mixture was refluxed for 18 hours. Then the solution was evaporated under reduced pressure and the crude material was subjected to chromatography column on silica gel using pentane/dichloromethane 4:6 as an eluent to give **46** (4 g, 80%) as a pure white powder.

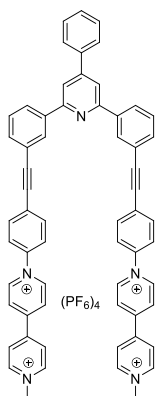
^1H NMR (400 MHz, Acetone) δ (ppm): 8.56 (t, $J = 1.6$ Hz, 2H), 8.38 (d, $J = 7.8$ Hz, 2H), 8.29 (s, 2H), 8.09 – 7.99 (m, 2H), 7.69 (dd, $J = 7.9, 0.9$ Hz, 2H), 7.56 (ddd, $J = 12.5, 11.2, 4.8$ Hz, 5H). ^{13}C NMR (101 MHz, Acetone) δ (ppm): 155.62, 150.76, 141.60, 138.21, 132.15, 130.74,

129.97, 129.33, 129.05, 127.57, 125.95, 122.64, 117.56. HR-MS (ESI⁺) calc. for [M+H]⁺ m/z = 463.9644; found m/z = 463.9647.



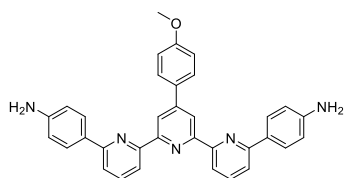
Synthesis of **47**: A dry flask (100 mL) was charged with **46** (0.6 g, 1.29 mmol), 4-Ethynylaniline (0.75 g, 6.45 mmol), piperidine (2 mL), Pd(PPh₃)₂Cl₂ (73 mg, 0.103 mmol), CuI (23mg, 0.206 mmol) and THF (50 mL). The mixture was degassed by nitrogen bubbling for 3 min and then heated at 90°C for 20 h. After cooling, the mixture was washed with water, then the solid was dissolved in DCM and purified by column chromatography through silica (EA/dichloromethane = 1/9), affording compound **47** (0.48 g, 65%) as yellow powder.

¹H NMR (400 MHz, Acetone) δ(ppm): 7.93 (s, 2H), 7.83 – 7.79 (m, 2H), 7.65 – 7.62 (m, 2H), 7.51 (dd, J = 7.7, 1.0 Hz, 2H), 7.20 (t, J = 7.7 Hz, 2H), 7.03 – 7.00 (m, 2H), 6.79 – 6.74 (m, 2H), 4.74 (s, 4H). ¹³C NMR (101 MHz, Acetone) δ(ppm): 164.28, 158.56, 157.49, 152.54, 149.36, 148.69, 140.63, 130.09, 129.08, 128.76, 128.47, 118.99, 116.85, 115.91, 115.58, 114.97, 114.15, 113.16, 112.21.



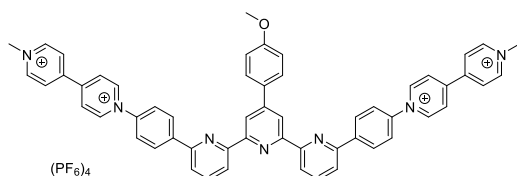
Synthesis of **48(PF₆)₄**: To a solution of **49(PF₆)₂**¹⁰⁴ (460mg, 0.74 mmol) in EtOH/CH₃CN (1:1,40 mL), **47** (200 mg, 0.37 mmol)) was added. The resulting mixture was allowed to stir at 70°C for 18h. After completion of the reaction, the mixture was evaporated under reduced pressure and the crude product was subjected to column chromatography on alumina using acetonitrile/water/saturated aqueous potassium nitrate (4:4:2) as eluent. A final counter-ion metathesis using a saturated aqueous KPF₆ solution afforded **48(PF₆)₄** (0.21 g, 45%) as a pure yellow powder.

¹H NMR (400 MHz, CD₃CN) δ(ppm): 9.17 (d, J = 4.5 Hz, 4H), 8.89 (d, J = 6.4 Hz, 4H), 8.58 (d, J = 6.4 Hz, 4H), 8.52 (s, 2H), 8.50 – 8.38 (m, 6H), 8.19 (s, 2H), 7.98 (dd, J = 10.8, 5.1 Hz, 6H), 7.83 (d, J = 8.6 Hz, 4H), 7.75 (d, J = 7.7 Hz, 2H), 7.72 – 7.50 (m, 5H), 4.43 (s, 6H). ¹³C NMR (101 MHz, CD₃CN) δ(ppm): 156.87, 151.35, 151.20, 149.82, 147.15, 146.03, 142.26, 140.42, 138.73, 134.02, 132.96, 130.82, 130.05, 129.95, 129.80, 128.81, 128.01, 127.84, 127.53, 125.59, 123.20, 118.35, 93.30, 87.85, 67.87, 25.83. HR-MS (ESI⁺) calc. for [M]⁴⁺ m/z = 211.8413; found m/z = 211.8409.



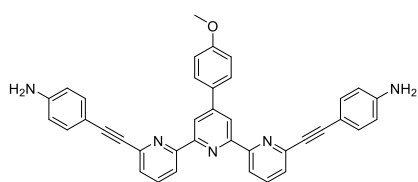
Synthesis of **53**: In a 250 mL round-bottomed flask equipped with a reflux condenser, **52**¹⁸⁷ (1g, 2.01 mmol), Pd(PPh₃)₄ (0.46 g, 0.4 mmol), 4-Aminophenylboronic acid pinacol ester (1.32g, 6.02 mmol) and K₃PO₄ (1.2 g, 6.02 mmol) were dissolved in tetrahydrofuran (THF, 50 mL). The mixture was then refluxed for 24, then the solution was evaporated under reduced pressure and the crude material was subjected to chromatography column on silica gel using ethyl acetate/dichloromethane 2:8 as an eluent to give **53** (0.95 g, 90%) as a pure white powder.

¹H NMR (400 MHz, Acetone) δ(ppm): 8.93 (s, 2H), 8.55 (dd, J = 7.7, 0.7 Hz, 2H), 8.11 – 8.03 (m, 4H), 7.97 (dd, J = 12.3, 4.4 Hz, 4H), 7.86 (dd, J = 7.7, 0.7 Hz, 2H), 7.18 (d, J = 8.8 Hz, 2H), 6.86 – 6.78 (d, 4H), 4.98 (s, 4H), 3.92 (s, 3H). ¹³C NMR (101 MHz, Acetone) δ(ppm): 160.87, 156.76, 156.46, 155.36, 149.86, 149.68, 137.57, 130.99, 128.42, 127.88, 127.63, 118.71, 117.84, 117.82, 114.68, 114.20, 54.71. HR-MS (ESI⁺) calc. for [M+H]⁺ m/z = 522.2288; found m/z = 522.2287.



Synthesis of **54(PF₆)₄**: To a stirred solution of **49(PF₆)₂**¹⁰⁴ (600mg, 0.95 mmol) in EtOH/DMF (1:1,55 mL), **53** (250 mg, 0.47 mmol)) was added. The resulting mixture was allowed to stir at 90°C for 18h. After completion of the reaction, the mixture was evaporated under reduced pressure and the crude product was subjected to column chromatography on alumina using acetonitrile/water/saturated aqueous potassium nitrate (4:3:3) as eluent. A final counter-ion metathesis using a saturated aqueous potassium hexafluorophosphate solution afforded **54(PF₆)₄** (0.3 g, 45%) as a yellow powder.

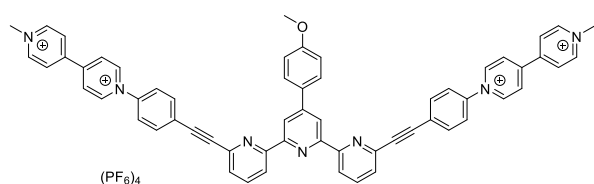
¹H NMR (400 MHz, CD₃CN)) δ(ppm): 9.26 (d, J = 6.8 Hz, 4H), 8.97 (s, 2H), 8.90 (d, J = 6.8 Hz, 4H), 8.83 (d, J = 7.6 Hz, 2H), 8.68 (d, J = 8.6 Hz, 4H), 8.61 (d, J = 6.8 Hz, 4H), 8.47 (d, J = 6.8 Hz, 4H), 8.24 – 8.12 (m, 4H), 7.99 (dd, J = 21.6, 8.6 Hz, 6H), 7.17 (d, J = 8.7 Hz, 2H), 4.44 (s, 6H), 3.91 (s, 3H). ¹³C NMR (101 MHz, CD₃CN)) δ(ppm): 161.53, 156.54, 156.43, 154.50, 151.23, 150.63, 149.93, 147.18, 146.10, 145.84, 143.19, 139.26, 131.05, 129.62, 129.28, 127.83, 127.54, 125.58, 122.04, 121.50, 118.87, 115.12, 55.78, 49.27. HR-MS (ESI⁺) calc. for [M]⁴⁺ m/z = 207.8414; found m/z = 207.8414.



Synthesis of **55**: A dry flask (100 mL) was charged with a mixture of **52**¹⁸⁷ (0.5 g, 1 mmol), 4-Ethynylaniline (0.471 g, 4 mmol), triethylamine (80mL), Pd(PPh₃)₂Cl₂ (141 mg, 0.2 mmol), CuI (44mg, 0.4 mmol) and THF (160 mL).

Then the mixture was heated at 54°C for 20 h. After cooling, the mixture was washed with water, then the solid was dissolved in DCM and purified by column chromatography through silica using dichloromethane as an eluent, affording compound 55 but not pure and seems to decompose on silica.

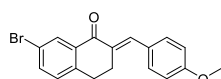
¹H NMR (300 MHz, Acetone) δ 8.79 (s, 2H), 8.68 (d, *J* = 7.9 Hz, 2H), 8.02 – 7.93 (m, 4H), 7.62 (d, *J* = 7.6 Hz, 2H), 7.38 (d, *J* = 8.5 Hz, 4H), 7.19 (d, *J* = 8.8 Hz, 2H), 6.73 (d, *J* = 8.6 Hz, 4H), 5.16 (s, 4H), 3.91 (s, 3H). HR-MS (ESI⁺) calc. for [M+H]⁺ *m/z* = 570.2288; found *m/z* = 570.2289.



Synthesis of **56(PF₆)₄**: To a stirred solution **49(PF₆)₂**¹⁰⁴ (600mg, 0.369 mmol) in EtOH/DMF(1:1,55 mL), **55** (100 mg, 0.175 mmol) was added. The resulting mixture was

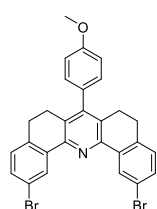
allowed to stir at 90 °C for 18h. After completion of the reaction, the mixture was evaporated under reduced pressure and the crude product was subjected to column chromatography on alumina using acetonitrile/water/saturated aqueous potassium nitrate (7:2:1) as eluent. A final counter-ion metathesis using a saturated aqueous potassium hexafluorophosphate solution afforded **56(PF₆)₄** (0.05 g, 34%) as a yellow powder.

¹H NMR (300 MHz, CD₃CN) δ 9.21 (d, *J* = 6.8 Hz, 4H), 8.91 (d, *J* = 6.6 Hz, 4H), 8.78 (m,4H), 8.62 (d, *J* = 6.8 Hz, 4H), 8.49 (d, *J* = 6.6 Hz, 4H), 8.05 – 7.49 (m, 14H), 7.17 (d, *J* = 8.6 Hz, 2H), 4.44 (s, 6H), 3.90 (s, 3H). ¹³C NMR (101 MHz, CD₃CN) δ(ppm):161.63, 156.96, 155.96, 151.51, 150.49, 149.82, 147.22, 146.22, 143.08, 142.75, 142.48, 138.48, 135.14, 134.48, 130.68, 129.07, 128.74, 128.01, 127.74, 125.67, 121.87, 115.87, 92.25, 86.70, 55.84, 49.77. HR-MS (ESI⁺) calc. for [M]⁴⁺ *m/z* = 219.8416; found *m/z* = 219.8421.

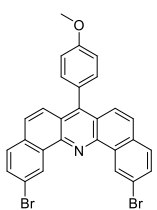


Synthesis of **61**: In a stirred solution of **59**¹⁹¹ (1g, 4.44 × 10⁻³ moles) in

ethanol (25 ml), **60**¹⁹² (0.604g, 4.44×10^{-3} moles) and NaOH (8M, 36 ml) were introduced in the reaction mixture. After that the reaction was refluxed at 79°C for 1 hour, then it was left to stir at room temperature overnight. The product was collected by filtration and wash with water to obtain pure **61** (1.3g, 80%). ¹H NMR (300 MHz, CDCl₃) δ (ppm): δ 8.24 (d, *J* = 2.1 Hz, 1H), 7.85 (s, 1H), 7.59 (dd, *J* = 8.1, 2.1 Hz, 1H), 7.43 (d, *J* = 8.7 Hz, 2H), 7.14 (d, *J* = 8.1 Hz, 1H), 6.96 (d, *J* = 8.7 Hz, 2H), 3.86 (s, 3H), 3.13 (dd, *J* = 9.0, 3.9 Hz, 2H), 2.98 – 2.77 (m, 2H). ¹³C NMR (400 MHz, CD₃CN) δ (ppm): δ 186.73, 160.93, 143.29, 137.30, 136.43, 135.58, 133.92, 132.62, 131.31, 130.55, 128.80, 120.75, 114.65, 55.66, 28.47, and 27.40. HR-MS (ESI⁺) calc. for [M+H]⁺ *m/z* = 343.0328; found *m/z* = 343.0326.

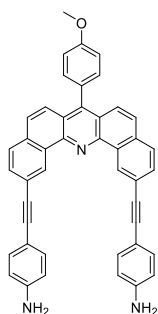


Synthesis of **62**: In a volumetric flask (10 ml) dried under argon compounds **59**¹⁹¹ (0.1g, 2.92×10^{-4} moles), **61** (0.065g, 2.92×10^{-4} moles) were introduced, then BF₃.Et₂O (0.73g, 5.17×10^{-3} moles) was added which resulted a brown colored mixture. The reaction was then slowly heated to 115 °C and the temperature was maintained for 8 h. Then the solution was cooled to 0 °C and carefully added ammonium acetate-ethanol solution (4.9 mL, 3.00 M) to it over 45 min. The mixture was then refluxed for 24 h. Then it was cooled to room temperature. After that the solvent were removed under reduced pressure, 100 mL water was added, and the sample was extracted into methylene chloride. The organic extract was dried over magnesium sulfate and filtered, and removed at reduced pressure. The residue was subjected to column chromatography on silica gel (petroleum ether/dichloromethane, 60:40) to obtain **62** (16mg, 10%). ¹H NMR (300 MHz, CDCl₃) δ (ppm): δ 8.64 (d, *J* = 2.1 Hz, 2H), 7.43 (dd, *J* = 8.0, 2.1 Hz, 2H), 7.07 (dt, *J* = 22.8, 8.7 Hz, 6H), 3.89 (s, 3H), 2.94 – 2.49 (m, 8H). ¹³C NMR (400 MHz, CDCl₃) δ (ppm): δ 159.18, 149.04, 137.07, 136.57, 131.57, 129.96, 129.79, 129.15, 128.18, 121.06, 114.09, 55.35, 27.61, 25.69. HR-MS (ESI⁺) calc. for [M+H]⁺ *m/z* = 546.0065; found *m/z* = 546.0063.



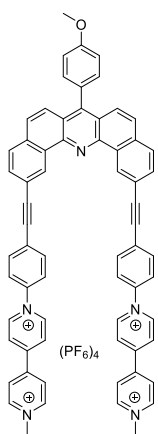
Synthesis of **63**: A 100 ml flask equipped with a condenser was flame dried under a continuous stream of argon. The flask was charged with **62** (0.2 g, 0.366 mmol) dissolved in hot anhydrous 1,4-dioxane (15 ml). To the hot solution 2,3-dichloro-5,6-dicyano-1,4-benzoquinone (DDQ) (0.16 g, 0.73 mmol) was added. Upon addition, the color of the reaction immediately became brown-red. The reaction was refluxed for a period of 24 h. The reaction was poured into 100

mL of a saturated Na₂CO₃ solution. This was warmed to 65 °C. Then the precipitate was collected and washed with water to obtain the desired compound in a quantitative yield as white powder. ¹H NMR (400 MHz, CD₂Cl₂) δ 9.92 (d, *J* = 2.0 Hz, 2H), 7.96 – 7.82 (m, 4H), 7.70 (q, *J* = 9.2 Hz, 4H), 7.44 (d, *J* = 8.7 Hz, 2H), 7.22 (d, *J* = 8.7 Hz, 2H), 4.00 (s, 3H). ¹³C NMR (400 MHz, CDCl₃) δ 159.90, 146.42, 144.47, 133.22, 132.21, 131.94, 131.72, 129.47, 127.94, 127.84, 126.73, 124.63, 124.60, 121.48, 114.05, 55.44. HR-MS (ESI⁺) calc. for [M+H]⁺ *m/z* = 541.9750; found *m/z* = 541.9743.



Synthesis of 64: A dry flask (100 mL) was charged with a mixture of **63** (0.3 g, 0.554 mmol), 4-Ethynylaniline (0.324 g, 2.77 mmol), piperidine (0.6 mL), Pd (PPh₃)₂Cl₂ (31 mg, 0.044 mmol), CuI (10 mg, 0.088 mmol) and DMF (50 mL). Then the mixture was heated at 90°C for 20 h. After cooling, the mixture was washed with water, then the solid was dissolved in DCM and purified by column chromatography through silica using (EtOAc/dichloromethane, 40:60) as an eluent, affording compound **64** (130mg, 40%) as brown yellow powder.

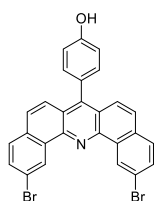
¹H NMR (300 MHz, CD₂Cl₂) δ 10.01 (s, 2H), 7.92 (dd, *J* = 14.9, 8.3 Hz, 4H), 7.82 – 7.42 (m, 10H), 7.22 (d, *J* = 8.3 Hz, 2H), 6.74 (d, *J* = 8.3 Hz, 4H), 4.00 (br s, 7H). ¹³C NMR (400 MHz, acetone) δ 149.33, 144.73, 133.15, 132.96, 132.76, 132.44, 131.83, 131.73, 130.98, 128.59, 128.38, 128.25, 127.95, 127.20, 124.83, 124.42, 123.10, 119.84, 114.16, 110.29, 92.17, 87.33. HR-MS (ESI⁺) calc. for [M+H]⁺ *m/z* = 616.2383; found *m/z* = 616.2373.



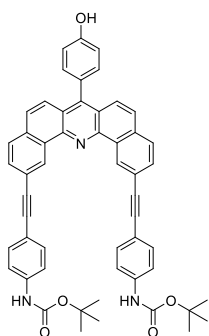
65(PF₆)₄: To a stirred solution of **49(PF₆)₂**¹⁰⁴ (250 mg, 0.4 mmol) in EtOH/CH₃CN/THF(1:1:1, 21 mL), **64** (100 mg, 0.162 mmol)) was added. The resulting mixture was allowed to stir at 70°C for 18h. After completion of the reaction, the precipitate was collected and subjected to column chromatography on alumina using acetonitrile/water/saturated aqueous potassium nitrate (7:2:1) as eluent. A final counter-ion metathesis using a saturated aqueous potassium hexafluorophosphate solution afforded **65(PF₆)₄** (0.1 g, 33%) as a red powder.

¹H NMR (300 MHz, CD₃CN) δ 10.00 (s, 2H), 9.18 (d, *J* = 6.7 Hz, 4H), 8.88 (d, *J* = 6.7 Hz, 4H), 8.57 (d, *J* = 6.7 Hz, 4H), 8.43 (d, *J* = 6.7 Hz, 4H), 8.09 (t, *J* = 8.4 Hz, 8H), 7.87 (t, *J* = 8.0 Hz, 6), 7.72 (d, *J* = 9.2 Hz, 2H), 7.47 (d, *J* = 8.5 Hz, 2H), 7.27 (d, *J* = 8.4 Hz,

2H), 4.43 (s, 6H), 3.97 (s, 3H). ^{13}C NMR (400 MHz, acetone) δ 160.60, 151.36, 149.86, 147.44, 147.17, 146.03, 145.41, 142.27, 134.47, 134.19, 132.56, 132.35, 132.02, 129.27, 128.67, 128.22, 127.97, 127.80, 127.64, 127.52, 126.08, 125.59, 125.17, 121.42, 114.75, 94.27, 88.66, 68.10, 49.50. HR-MS (ESI⁺) calc. for $[\text{M}]^{4+}$ $m/z = 231.3445$; found $m/z = 231.3440$.

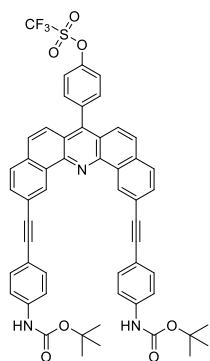


Synthesis of 66: In a round bottom flask, **63** (180 mg, 0.331 mmol) was dissolved in 50 ml dry CH_2Cl_2 at room temperature. 1 mL BBr_3 solution (1.0 M in CH_2Cl_2) was then added dropwise at -78°C . The reaction mixture was allowed to warm to room temperature overnight. It was then washed with 10% aqueous HCl and extracted with CH_2Cl_2 . The organic layer was washed with brine and dried over MgSO_4 . Then the solution was evaporated under reduced pressure to obtain the desired compound in a quantitative yield as a red powder. ^1H NMR (400 MHz, CD_2Cl_2) δ 9.87 (s, 2H), 7.85 (dt, $J = 24.5, 5.1$ Hz, 4H), 7.66 (dd, $J = 22.4, 9.3$ Hz, 4H), 7.34 (d, $J = 8.4$ Hz, 2H), 7.10 (d, $J = 8.4$ Hz, 2H). ^{13}C NMR (400 MHz, CDCl_3) δ 156.03, 146.33, 144.49, 133.24, 132.23, 131.96, 131.92, 129.50, 128.04, 127.95, 126.79, 124.61, 121.49, 115.50. HR-MS (ESI⁺) calc. for $[\text{M}+\text{H}]^+$ $m/z = 527.9593$; found $m/z = 527.9604$.



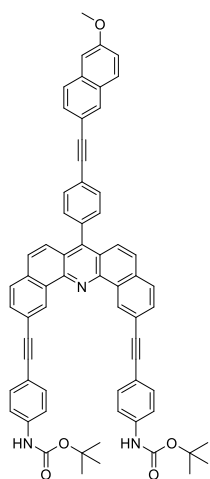
Synthesis of 67: A dry flask (100 mL) charged with a mixture of **66** (0.35 g, 0.661 mmol), tert-butyl (4-ethynylphenyl) carbamate (0.71 g, 3.3 mmol), piperidine (0.6 mL), $\text{Pd}(\text{PPh}_3)_2\text{Cl}_2$ (37 mg, 0.052 mmol), CuI (12 mg, 0.16 mmol) and DMF (50 mL) was heated at 90°C for 20 h. After cooling, the mixture was washed with water, then the solid was dissolved in DCM and purified by column chromatography through silica using (dichloromethane /Pentane; 9:1) as an eluent, affording compound **67** as a yellow powder.

^1H NMR (400 MHz, Acetone) δ 9.98 (s, 2H), 8.82 (s, 1H), 8.52 (s, 2H), 8.05 (d, $J = 8.2$ Hz, 2H), 7.99 – 7.84 (m, 4H), 7.70 (q, $J = 8.9$ Hz, 10H), 7.42 (d, $J = 8.4$ Hz, 2H), 7.20 (d, $J = 8.4$ Hz, 2H), 1.54 (s, 18H). ^{13}C NMR (400 MHz, Acetone) δ 157.86, 152.71, 146.92, 144.87, 140.27, 133.19, 132.32, 131.78, 131.72, 131.27, 128.34, 128.32, 127.08, 126.60, 124.89, 124.54, 122.30, 118.26, 116.72, 115.62, 90.73, 88.99, 79.73, 27.72. HR-MS (ESI⁺) calc. for $[\text{M}+\text{H}]^+$ $m/z = 802.3264$; found $m/z = 802.3275$.



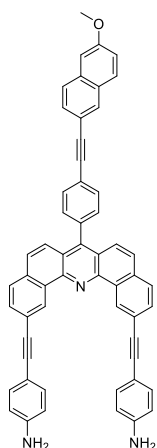
Synthesis of **68**: In a round bottom flask, **67** (10 mg, 0.012 mmol) was dissolved in 10 ml dry pyridine. Trifluoromethanesulfonic anhydride (4.2 μ l, 0.024 mmol) was slowly added at 0°C. The resultant mixture was stirred at 0°C for another 30 min, and then the reaction was warmed to room temperature. The mixture was kept at room temperature for 2 days. After that, the mixture was poured into 200 ml cold water, and was extracted by dichloromethane and evaporated under reduced pressure. The crude product was subjected to column chromatography on silica gel (petroleum ether/dichloromethane, 30:70) to obtain **68** as a yellow powder in a quantitative yield.

^1H NMR (400 MHz, THF) δ 10.81 (br s, 1H), 9.94 (s, 2H), 8.56 (s, 2H), 7.97 (d, J = 8.2 Hz, 2H), 7.88 (dd, J = 31.3, 8.2 Hz, 2H), 7.80 (d, J = 9.2 Hz, 2H), 7.73 (q, J = 8.8 Hz, 5H), 7.59 (s, 7H), 7.49 (d, J = 9.2 Hz, 2H), 1.53 (s, 18H). ^{13}C NMR (400 MHz, Acetone) δ 152.51, 149.90, 144.96, 144.08, 140.33, 137.02, 132.97, 132.68, 132.11, 131.69, 131.40, 128.25, 128.01, 127.61, 123.88, 123.75, 122.78, 121.85, 117.83, 116.65, 91.05, 88.81, 79.24, 27.70. ^{19}F NMR (282 MHz, Acetone) δ -74.03.



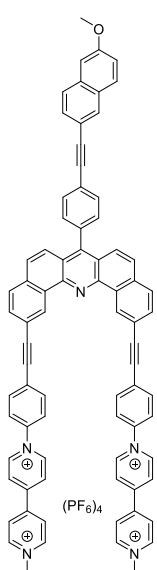
Synthesis of **72**: A dry flask (100 mL) was charged with a mixture of **68** (0.08 g, 0.085 mmol), **71**¹⁹³ (25 mg, 0.128 mmol), NEt_3 (10 mL), $\text{Pd}(\text{PPh}_3)_2\text{Cl}_2$ (4.8 mg, 6.86 μ mol), CuI (0.4 mg, 6.86 μ mol) and DMF (10 mL). Then the mixture was heated at 90°C for 48 h. After cooling, the mixture was washed with water, then the solid was dissolved in DCM and purified by column chromatography through silica using (dichloromethane/pentane; 8:2) as an eluent, affording compound **72** as a light yellow powder.

^1H NMR (400 MHz, THF) δ 9.95 (s, 2H), 8.56 (s, 2H), 8.06 (s, 1H), 7.97 (d, J = 8.2 Hz, 2H), 7.91 – 7.76 (m, 8H), 7.59 (q, J = 8.2 Hz, 13H), 7.26 (d, J = 2.3 Hz, 1H), 7.18 (dd, J = 8.9, 2.5 Hz, 1H), 3.91 (s, 2H), 1.53 (s, 18H). ^{13}C NMR (400 MHz, Acetone) δ 158.85, 152.53, 145.50, 144.98, 140.37, 136.24, 134.59, 133.06, 132.71, 132.11, 131.76, 131.61, 131.26, 130.69, 129.12, 128.66, 128.62, 128.34, 127.95, 127.30, 126.86, 124.18, 123.95, 123.88, 122.63, 119.44, 117.85, 117.76, 116.70, 105.70, 90.92, 88.86, 88.30, 79.24, 78.27, 54.88, 27.84.



Synthesis of **73**: To a stirred solution of **72** (50 mg, 0.051 mmol) in dichloromethane (30 mL), TFA (1.5 mL) was added at 0°C. Then mixture was allowed to stir at room temperature for 3 hour. After evaporation a saturated aqueous solution of sodium bicarbonate was added and the subsequent mixture was extracted three times with dichloromethane. The organic layer was washed with brine, dried (Na₂SO₄) and evaporated under reduced pressure. Then subjected to chromatography column on silica gel using dichloromethane/pentane (8:2) as an eluent to afford compound **73** as a yellow powder.

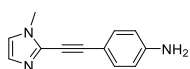
¹H NMR (400 MHz, Acetone) δ 9,94(s, 2H), 8.16 (s, 1H), 8.07 (d, *J* = 8.3 Hz, 2H), 7.93 (m, 7H), 7.64 (m, 8.1 Hz, 6H), 7.46 (d, *J* = 8.3 Hz, 4H), 7,3 (s, 1H), 7.24 (d, *J* = 8.4 Hz, 1H), 6.78 (d, *J* = 8.2 Hz, 4H), 5,13(s, 4H), 3,97(s, 3H). HR-MS (ESI⁺) calc. for [M+H]⁺ m/z = 766.2853; found m/z = 766.2858.



Synthesis of **74(PF₆)₄**: A solution of **49(PF₆)₂**¹⁰⁴ (184 mg, 0.294 mmol) was dissolved in EtOH/CH₃CN/THF(1:1:1,21 mL) then **73** (90 mg, 0.117 mmol) was added. The resulting mixture was allowed to stir at 70 °C for 18h. After completion of the reaction, the precipitate was collected and washed with dichloromethane to afforded and purified on silica using pressure to obtain **74(PF₆)₄** (66 mg, 10%) as an orange powder.

¹H NMR (400 MHz, DMSO) δ 9.95 (s, 2H), 9.44 (d, *J* = 6.95 Hz, 4H), 9.31 (d, *J* = 6.2 Hz, 4H), 8.94 (d, *J* = 6.95 Hz, 4H), 8.86 (d, *J* = 6.95 Hz, 4H), 8.3 – 7.98 (m, 16H), 7.98 – 7.85 (m, 4H), 7.81 (d, *J* = 8.8 Hz, 1H), 7.64 (m, 2H), 7.53 (d, *J* = 8.8 Hz, 1H), 7.40 (s, 1H), 7.25 (d, *J* = 6.7 Hz, 1H), 4.47 (s, 6H), 3.91 (s, 3H). HR-MS (ESI⁺) calc. for [M]⁴⁺ m/z = 268.8557; found m/z = 268.8553.

V.3.3. Synthetic procedures related to chapter IV



Synthesis of **4** : To a stirred, degassed solution of 4-ethynylaniline (117 mg, 1.0 mmol), **3**²⁰⁹ (208 mg, 1.0 mmol), copper(I) iodide (9.5 mg, 5 mol %), triethylamine (4 mL) and tetrahydrofuran (16 mL), bis(triphenylphosphine)palladium(II) dichloride (70 mg, 10 mol %) was added. The reaction mixture was stirred for 18 h at 60 °C

and subsequently concentrated under reduced pressure. Purification by flash chromatography on silica gel (ethyl acetate/cyclohexane: 1/1) gave **4** (172 mg, 87%) as a yellow solid.

^1H NMR (300 MHz, CDCl_3): δ 3.76 (s, 3H), 3.78 (br s, 2H), 6.63 (d, 2H, $J = 8.4$ Hz), 6.90 (s, 1H), 7.06 (s, 1H), 7.36 (d, $J = 8.4$ Hz, 2H). ^{13}C NMR (100 MHz, CDCl_3): $\delta = 33.7, 66.8, 84.9, 93.7, 111.1, 114.8$ (2C), 121.4, 129.7, 133.3 (2C), 147.5. HR-MS (ESI $^+$): calc. for $\text{C}_{12}\text{H}_{12}\text{N}_3$ $[\text{M}+\text{H}]^+$ 198.1031, found 198.1030.



Synthesis of **6(PF₆)₂**: To a stirred solution of **5(PF₆)₂**¹⁰⁴ (78 mg, 0.1 mmol) in ethanol (10 mL) and acetonitrile (10 mL), **4** (43 mg, 0.22 mmol) was added. The reaction mixture was stirred for 6 h at 80 °C and subsequently concentrated under reduced pressure. Purification by flash chromatography on silica gel (acetonitrile/water/saturated aqueous potassium nitrate: 100/15/2.5) and anion exchange using an aqueous saturated KPF_6 solution, gave **6(PF₆)₂** (31 mg, 38%) as an orange solid.

^1H NMR (400 MHz, $\text{DMSO}-d_6$): δ 3.84 (s, 6H), 7.08 (d, 2H, $J = 0.9$ Hz), 7.42 (d, 2H, $J = 0.9$ Hz), 8.07 (s, 8H), 9.10 (d, 4H, $J = 7.0$ Hz), 9.74 (d, 4H, $J = 7.0$ Hz). ^{13}C NMR (100 MHz, CDCl_3): δ 32.2, 83.5, 90.7, 124.2, 126.1, 127.1, 128.4, 130.7, 132.1, 134.4, 143.0, 146.6, 151.4. HR-MS (ESI $^+$): calc for $\text{C}_{34}\text{H}_{26}\text{N}_6^{2+}$ $[\text{M}-2\text{PF}_6]^{2+}$ 259.1109, found 259.1112.

References

- 1) Wang, S.; Xu, Z.; Wang, T.; Xiao, T.; Hu, X. Y.; Shen, Y. Z.; Wang, L. *Nat Commun* **2018**, *9* (1), 1737.
- 2) Rothmund, P. W. *Nature* **2006**, *440* (7082), 297-302.
- 3) Hunter, C. A.; Sanders, J. K. M. *J. Am. Chem. Soc* **1990**, *112* (14), 5525-5534.
- 4) Franco Cozzi; Francesco Ponzini; Rita Annunziata; Mauro Cinquini; Siegel, J. S. *Angew. Chem. Int. Ed. Engl.* **1995**, *34*, 1019-1020.
- 5) Christopher A. Hunter; Jeremy K. M. Sanders; Godfrey S. Beddard; Evans, S. *J. Chem. Soc., Chem. Commun.* **1989**, 1765-1767.
- 6) Amabilino, D. B.; Stoddart, J. F., Self-assembly and macromolecular design. In *Pure Appl. Chem.*, 1993; Vol. 65, p 2351.
- 7) Fahrenbach, A. C.; Bruns, C. J.; Cao, D.; Stoddart, J. F. *Acc. Chem. Res* **2012**, *45* (9), 1581-1592.
- 8) Lü, J.-M.; Rosokha, S. V.; Kochi, J. K. *J. Am. Chem. Soc.* **2003**, *125* (40), 12161-12171.
- 9) Yu, Z.; Tetard, L.; Zhai, L.; Thomas, J. *Energy Environ. Sci.* **2015**, *8* (3), 702-730.
- 10) Capdevila-Cortada, M.; Novoa, J. J. *Chem. Eur. J* **2012**, *18* (17), 5335-5344.
- 11) Yakushi, K.; Nishimura, S.; Sugano, T.; Kuroda, H.; Ikemoto, I. *Acta Cryst. B* **1980**, *36* (2), 358-363.
- 12) Rosokha, S. V.; Kochi, J. K. *J. Am. Chem. Soc.* **2007**, *129* (4), 828-838.
- 13) Fuhrhop, J. H.; Wasser, P.; Riesner, D.; Mauzerall, D. *J. Am. Chem. Soc.* **1972**, *94* (23), 7996-8001.
- 14) van Haare, J. A. E. H.; Groenendaal, L.; Havinga, E. E.; Janssen, R. A. J.; Meijer, E. W. *Angew. Chem. Int. Ed.* **1996**, *35* (6), 638-640.
- 15) Bird, C. L.; Kuhn, A. T. *Chem. Soc. Rev.* **1981**, *10* (1), 49-82.
- 16) Iordache, A.; Kannappan, R.; Métay, E.; Duclos, M.-C.; Pellet-Rostaing, S.; Lemaire, M.; Milet, A.; Saint-Aman, E.; Bucher, C. *Org. Biomol. Chem.* **2013**, *11* (26), 4383-4389.
- 17) Michaelis, L.; Hill, E. S. *J. Gen. Physiol.* **1933**, *16* (6), 859-873.
- 18) Mortimer, R. J. *Chem. Soc. Rev.* **1997**, *26* (3), 147-156.
- 19) Ding, J.; Zheng, C.; Wang, L.; Lu, C.; Zhang, B.; Chen, Y.; Li, M.; Zhai, G.; Zhuang, X. *J. Mater. Chem. A* **2019**, *7* (41), 23337-23360.
- 20) Sakano, T.; Ito, F.; Ono, T.; Hirata, O.; Ozawa, M.; Nagamura, T. *Thin Solid Films* **2010**, *519* (4), 1458-1463.

- 21) Ito, F.; Nagamura, T. *J. Photochem. Photobiol* **2007**, *8* (4), 174-190.
- 22) Müller, E.; Bruhn, K. A. *Chem. Ber.* **1953**, *86* (9), 1122-1132.
- 23) Kosower, E. M.; Cotter, J. L. *J. Am. Chem. Soc.* **1964**, *86* (24), 5524-5527.
- 24) Iordache, A.; Oltean, M.; Milet, A.; Thomas, F.; Baptiste, B.; Saint-Aman, E.; Bucher, C. *J. Am. Chem. Soc.* **2012**, *134* (5), 2653-2671.
- 25) Torrance, J. B.; Scott, B. A.; Welber, B.; Kaufman, F. B.; Seiden, P. E. *Phys. Rev. B* **1979**, *19* (2), 730-741.
- 26) Gionis, V.; Ficket, O.; Izumi, M.; Garrigou-Lagrange, C.; Amiell, J.; Papavasseliou, G.; Delhaes, P. *Chem. Lett.* **1991**, *20* (5), 871-874.
- 27) Evans, A. G.; Evans, J. C.; Baker, M. W. *J. Am. Chem. Soc.* **1977**, *99* (18), 5882-5884.
- 28) Geraskina, M. R.; Buck, A. T.; Winter, A. H. *J. Org. Chem.* **2014**, *79* (16), 7723-7727.
- 29) Bockman, T. M.; Kochi, J. K. *J. Org. Chem.* **1990**, *55* (13), 4127-4135.
- 30) Femoni, C.; Iapalucci, M. C.; Longoni, G.; Tiozzo, C.; Wolowska, J.; Zacchini, S.; Zazzaroni, E. *Chem. Eur. J* **2007**, *13* (23), 6544-6554.
- 31) Ko, Y. H.; Kim, E.; Hwang, I.; Kim, K. *Chem. Commun.* **2007**, 1305-1315.
- 32) Lee, J. W.; Samal, S.; Selvapalam, N.; Kim, H.-J.; Kim, K. *Acc. Chem. Res.* **2003**, *36*, 621-630.
- 33) Hirayama, F. *J. Chem. Phys.* **1965**, *42*, 3163.
- 34) Kannappan, R.; Bucher, C.; Saint-Aman, E.; Moutet, J.-C.; Milet, A.; Oltean, M.; Méta, E.; Pellet-Rostaing, S.; Lemaire, M.; Chaix, C. *New J. Chem.* **2010**, *34* (7), 1373-1386.
- 35) Iordache, A.; Retegan, M.; Thomas, F.; Royal, G.; Saint-Aman, E.; Bucher, C. *Chem. Eur. J* **2012**, *18* (25), 7648-7653.
- 36) Iordache, A.; Retegan, M.; Thomas, F.; Royal, G.; Saint-Aman, E.; Bucher, C. *Chem. Eur. J.* **2012**, *18*, 7648 – 7653.
- 37) Nambu, Y.; Yamamoto, K.; Endo, T. *J. Chem. Soc., Chem. Commun.* **1986**, (7), 574-576.
- 38) Kahlfuss, C.; Gibaud, T.; Denis-Quanquin, S.; Chowdhury, S.; Royal, G.; Chevallier, F.; Saint-Aman, E.; Bucher, C. *Chem. Eur. J* **2018**, *24* (49), 13009-13019.
- 39) Kahlfuss, C.; Denis-Quanquin, S.; Calin, N.; Dumont, E.; Garavelli, M.; Royal, G.; Cobo, S.; Saint-Aman, E.; Bucher, C. *J. Am. Chem. Soc.* **2016**, *138* (46), 15234-15242.
- 40) Imabayashi, S.-i.; Kitamura, N.; Tokuda, K.; Tazuke, S. *Chem. Lett.* **1987**, *16* (5), 915-918.
- 41) Imabayashi, S.-I.; Kitamura, N.; Tazuke, S.; Tokuda, K. *J. Electroanal. Chem* **1988**, *243* (1), 143-160.
- 42) Watanabe, T.; Honda, K. *J. Phys. Chem.* **1982**, *86* (14), 2617-2619.

- 43) Furue, M.; Nozakura, S.-i. *Chem. Lett.* **1980**, 9 (7), 821-824.
- 44) Flanagan, J. B.; Margel, S.; Bard, A. J.; Anson, F. C. *J. Am. Chem. Soc.* **1978**, 100 (13), 4248-4253.
- 45) Richardson, D. E.; Taube, H. *Inorg. Chem* **1981**, 20 (4), 1278-1285.
- 46) Furue, M.; Nozakura, S.-i. *Bull. Chem. Soc. Jpn.* **1982**, 55 (2), 513-516.
- 47) Deronzier, A.; Galland, B.; Vieira, M. *Electrochim. Acta* **1983**, 28 (6), 805-811.
- 48) Bruinink, J. J. *Electrochem. Soc.* **1977**, 124 (12), 1854.
- 49) Atherton, S. J.; Tsukahara, K.; Wilkins, R. G. *J. Am. Chem. Soc.* **1986**, 108 (12), 3380-3385.
- 50) Passon, M.; Ruff, A.; Schuler, P.; Speiser, B.; Leis, W. *J Solid State Electrochem.* **2015**, 19 (1), 85-101.
- 51) Geraskina, M. R.; Dutton, A. S.; Juetten, M. J.; Wood, S. A.; Winter, A. H. *Angew. Chem. Int. Ed.* **2017**, 56 (32), 9435-9439.
- 52) Iordache, A.; Oltean, M.; Milet, A.; Thomas, F.; Saint-Aman, E.; Bucher, C. *J. Am. Chem. Soc.* **2012**, 134, 2653-2671.
- 53) Kahlfuss, C.; Métay, E.; Duclos, M.-C.; Lemaire, M.; Milet, A.; Saint-Aman, E.; Bucher, C. *Chem. Eur. J.* **2014**, 21, 2090 – 2106.
- 54) Kahlfuss, C.; Métay, E.; Duclos, M.-C.; Lemaire, M.; Oltean, M.; Milet, A.; Saint-Aman, E.; Bucher, C. *C. R. Chim.* **2014**, 17 (6), 505-511.
- 55) Iordache, A.; Kanappan, R.; Métay, E.; Duclos, M.-C.; Pellet-Rostaing, S.; Lemaire, M.; Milet, A.; Saint-Aman, E.; Bucher, C. *Org. Biomol. Chem.* **2013**, 11, 4383-4389.
- 56) Kahlfuss, C.; Milet, A.; Wytko, J. A.; Weiss, J.; Saint-Aman, E.; Bucher, C. *to be published*.
- 57) Geuder, W.; Hünig, S.; Suchy, A. *Tetrahedron* **1986**, 42 (6), 1665-1677.
- 58) Neta, P.; Richoux, M.-C.; Harriman, A. *J. Chem. Soc., Faraday Trans. 2* **1985**, 81 (9), 1427-1443.
- 59) Wang, Y.; Frasconi, M.; Stoddart, J. F. *ACS Cent. Sci.* **2017**, 3 (9), 927-935.
- 60) Liu, Z.; Nalluri, S. K. M.; Stoddart, J. F. *Chem. Soc. Rev.* **2017**, 46 (9), 2459-2478.
- 61) Stoddart, J. F. *Angew. Chem. Int. Ed.* **2017**, 56 (37), 11094-11125.
- 62) Li, H.; Fahrenbach, A. C.; Dey, S. K.; Basu, S.; Trabolsi, A.; Zhu, Z.; Botros, Y. Y.; Stoddart, J. F. *Angew. Chem. Int. Ed.* **2010**, 49 (44), 8260-8265.
- 63) Li, S.; Purdy, W. C. *Chem. Rev.* **1992**, 92 (6), 1457-1470.
- 64) Saenger, W.; Jacob, J.; Gessler, K.; Steiner, T.; Hoffmann, D.; Sanbe, H.; Koizumi, K.; Smith, S. M.; Takaha, T. *Chem. Rev.* **1998**, 98 (5), 1787-1802.

- 65) Hedges, A. R. *Chem. Rev.* **1998**, 98 (5), 2035-2044.
- 66) Sabadini, E.; Cosgrove, T.; Egídio, F. d. C. *Carbohydr. Res.* **2006**, 341 (2), 270-274.
- 67) Adar, E.; Degani, Y.; Goren, Z.; Willner, I. *J. Am. Chem. Soc.* **1986**, 108 (16), 4696-4700.
- 68) Diaz, A.; Quintela, P. A.; Schuette, J. M.; Kaifer, A. E. *J. Phys. Chem.* **1988**, 92 (12), 3537-3542.
- 69) Kaifer, A. E.; Quintela, P. A.; Schuette, J. M. In *The Interactions of Surfactant Viologens with Cyclodextrins*, United States-Japan Seminar on Host-Guest Chemistry, Dordrecht, 1989//; Gokel, G. W.; Koga, K., Eds. Springer Netherlands: Dordrecht, 1989; pp 107-115.
- 70) Yasuda, A.; Kondo, H.; Itabashi, M.; Seto, J. *J. Electroanal. Chem* **1986**, 210 (2), 265-275.
- 71) Behrend, R.; Meyer, E.; Rusche, F. *Justus Liebigs Ann. Chem.* **1905**, 339 (1), 1-37.
- 72) Zhao, Y.; Huang, Y.; Zhu, H.; Zhu, Q.; Xia, Y. *J. Am. Chem. Soc.* **2016**, 138 (51), 16645-16654.
- 73) Gutsche, C. D.; Dhawan, B.; No, K. H.; Muthukrishnan, R. *J. Am. Chem. Soc.* **1981**, 103 (13), 3782-3792.
- 74) Correia, H. D.; Chowdhury, S.; Ramos, A. P.; Guy, L.; Demets, G. J.-F.; Bucher, C. *Polym. Int.* **2019**, 68 (4), 572-588.
- 75) Lagona, J.; Mukhopadhyay, P.; Chakrabarti, S.; Isaacs, L. *Angew. Chem. Int. Ed.* **2005**, 44 (31), 4844-4870.
- 76) Cintas, P. *J. Incl. Phenom. Mol. Recognit. Chem.* **1994**, 17 (3), 205-220.
- 77) Lee, J. W.; Samal, S.; Selvapalam, N.; Kim, H.-J.; Kim, K. *Acc. Chem. Res* **2003**, 36 (8), 621-630.
- 78) Nkrumah, A. Design, Synthesis, and Characterization of Dynamic Metallo-Supramolecular Polymers Stabilized by Non-Covalent Interactions. Ohio University Honors Tutorial College, 2013.
- 79) Buschmann, H.-J.; Cleve, E.; Jansen, K.; Wego, A.; Schollmeyer, E. *Mater. Sci. Eng. C* **2001**, 14 (1), 35-39.
- 80) Liu, S.; Zavalij, P. Y.; Isaacs, L. *J. Am. Chem. Soc.* **2005**, 127 (48), 16798-16799.
- 81) Kim, K.; Selvapalam, N.; Oh, D. H. *J. Incl. Phenom. Macrocycl. Chem.* **2004**, 50 (1), 31-36.
- 82) Masson, E.; Ling, X.; Joseph, R.; Kyeremeh-Mensah, L.; Lu, X. *RSC Adv.* **2012**, 2 (4), 1213-1247.

- 83) Jeon, Y. J.; Kim, H.; Jon, S.; Selvapalam, N.; Oh, D. H.; Seo, I.; Park, C.-S.; Jung, S. R.; Koh, D.-S.; Kim, K. *J. Am. Chem. Soc.* **2004**, *126* (49), 15944-15945.
- 84) Kim, H.-J.; Jeon, W. S.; Ko, Y. H.; Kim, K. *Proc. Natl. Acad. Sci.* **2002**, *99* (8), 5007.
- 85) Kim, H.-J.; Heo, J.; Jeon, W. S.; Lee, E.; Kim, J.; Sakamoto, S.; Yamaguchi, K.; Kim, K. *Angew. Chem. Int. Ed.* **2001**, *40* (8), 1526-1529.
- 86) Jeon, W. S.; Kim, H.-J.; Lee, C.; Kim, K. *Chem. Commun.* **2002**, (17), 1828-1829.
- 87) Cram, D. J. *Angew. Chem. Int. Ed.* **1986**, *25* (12), 1039-1057.
- 88) Lehn, J.-M. *Science* **1993**, *260*, 1762+.
- 89) Cram, D. J. *Angew. Chem. Int. Ed.* **1988**, *27* (8), 1009-1020.
- 90) Schubert, U. S.; Eschbaumer, C. *Angew. Chem. Int. Ed.* **2002**, *41* (16), 2892-2926.
- 91) Sallé, M.; Canevet, D.; Balandier, J.-Y.; Lyskawa, J.; Trippé, G.; Goeb, S.; Le Derf, F. *Phosphorus Sulfur Silicon Relat. Elem.* **2011**, *186* (5), 1153-1168.
- 92) Al Kobaisi, M.; Bhosale, S. V.; Latham, K.; Raynor, A. M.; Bhosale, S. V. *Chem. Rev.* **2016**, *116* (19), 11685-11796.
- 93) Blanco-Gómez, A.; Cortón, P.; Barravecchia, L.; Neira, I.; Pazos, E.; Peinador, C.; García, M. D. *Chem. Soc. Rev.* **2020**, *49* (12), 3834-3862.
- 94) Li, X.-F.; Yu, S.-B.; Yang, B.; Tian, J.; Wang, H.; Zhang, D.-W.; Liu, Y.; Li, Z.-T. *Sci. China Chem.* **2018**, *61* (7), 830-835.
- 95) Lee, J. W.; Kim, K.; Choi, S.; Ko, Y. H.; Sakamoto, S.; Yamaguchi, K.; Kim, K. *Chem. Commun.* **2002**, (22), 2692-2693.
- 96) Kim, K.; Kim, D.; Lee, J. W.; Ko, Y. H.; Kim, K. *Chem. Commun.* **2004**, (7), 848-849.
- 97) Ko, Y. H.; Kim, K.; Kang, J.-K.; Chun, H.; Lee, J. W.; Sakamoto, S.; Yamaguchi, K.; Fetting, J. C.; Kim, K. *J. Am. Chem. Soc.* **2004**, *126* (7), 1932-1933.
- 98) Yin, Z.-J.; Wu, Z.-Q.; Lin, F.; Qi, Q.-Y.; Xu, X.-N.; Zhao, X. *Chin. Chem. Lett.* **2017**, *28* (6), 1167-1171.
- 99) Wang, Y.; Cheng, T.; Sun, J.; Liu, Z.; Frascioni, M.; Goddard, W. A.; Stoddart, J. F. *J. Am. Chem. Soc.* **2018**, *140* (42), 13827-13834.
- 100) Grunder, S.; McGrier, P. L.; Whalley, A. C.; Boyle, M. M.; Stern, C.; Stoddart, J. F. *J. Am. Chem. Soc.* **2013**, *135* (47), 17691-17694.
- 101) Zhan, T.-G.; Zhou, T.-Y.; Lin, F.; Zhang, L.; Zhou, C.; Qi, Q.-Y.; Li, Z.-T.; Zhao, X. *Org. Chem. Front.* **2016**, *3* (12), 1635-1645.
- 102) Zhang, X.; Nie, C.-B.; Zhou, T.-Y.; Qi, Q.-Y.; Fu, J.; Wang, X.-Z.; Dai, L.; Chen, Y.; Zhao, X. *Polym. Chem.* **2015**, *6* (11), 1923-1927.
- 103) Cheng, W.-C.; Kurth, M. J. *Org. Prep. Proced. Int* **2002**, *34* (6), 585-608.

- 104) Constantin, V.-A.; Cao, L.; Sadaf, S.; Walder, L. *Phys. Status Solidi B* **2012**, *249* (12), 2395-2398.
- 105) Bardelang, D.; Udachin, K. A.; Leek, D. M.; Ripmeester, J. A. *CrystEngComm* **2007**, *9* (11), 973-975.
- 106) Lagona, J.; Mukhopadhyay, P.; Chakrabarti, S.; Isaacs, L. *Angew. Chem., Int. Ed. Engl.* **2005**, *44*, 4844-4870.
- 107) Masson, E.; Raeisi, M.; Kotturi, K. *Isr. J. Chem.* **2018**, *58* (3-4), 413-434.
- 108) Ammar, F.; Savéant, J. M. *J. Electroanal. Chem* **1973**, *47* (1), 115-125.
- 109) Kahlfuss, C.; Saint-Aman, E.; Bucher, C. *Organic Redox Systems* **2016**, 39-88.
- 110) Kadish, K. M.; Shiue, L. R.; Rhodes, R. K.; Bottomley, L. A. *Inorg. Chem* **1981**, *20* (4), 1274-1277.
- 111) Kahlfuss, C.; Saint-Aman, E.; Bucher, C., Redox-controlled intramolecular motions triggered by π -dimerization and π merization processes. In *Organic Redox Systems: Synthesis, Properties, and Applications*, Nishinaga, T., Ed. John Wiley and sons: New-York, 2016; pp 39-88.
- 112) Lu, J.-M.; Rosokha, S. V.; Kochi, J. K. *J. Am. Chem. Soc.* **2003**, *125*, 12161-12171.
- 113) Jeon, W. S.; Kim, H. J.; Lee, C.; Kim, K. *Chem. Commun.* **2002**, (17), 1828-1829.
- 114) Mayhew, S. G. *Eur. J. Biochem.* **1978**, *85* (2), 535-547.
- 115) Iordache, A.; Oltean, M.; Milet, A.; Thomas, F.; Baptiste, B.; Saint-Aman, E.; Bucher, C. *J. Am. Chem. Soc.* **2012**, *134*, 2653-2671.
- 116) Neta, P. *J. Phys. Chem.* **1981**, *85* (24), 3678-3684.
- 117) Kalyanasundaram, K. *J. Photochem. Photobiol. A* **1988**, *42* (1), 87-109.
- 118) Baral, S.; Neta, P.; Hambright, P. *Radiat. Phys. Chem. (1977)* **1984**, *24* (2), 245-255.
- 119) Harriman, A. *Journal of Photochemistry* **1985**, *29* (1), 139-150.
- 120) Bonnet, R.; Ridge, R. J.; Land, E. J.; Sinclair, R. S.; Tait, D.; Truscott, T. G. *J. Chem. Soc., Faraday Trans.* **1982**, *78* (1), 127-136.
- 121) Harel, Y.; Meyerstein, D. *J. Am. Chem. Soc.* **1974**, *96* (9), 2720-2727.
- 122) Harriman, A.; Richoux, M. C.; Neta, P. *J. Phys. Chem.* **1983**, *87* (24), 4957-4965.
- 123) Abou-Gamra, Z. M.; Guindy, N. M. *Spectrochim. Acta A* **1989**, *45* (12), 1207-1210.
- 124) Fang, Y.; Gorbunova, Y. G.; Chen, P.; Jiang, X.; Manowong, M.; Sinelshchikova, A. A.; Enakieva, Y. Y.; Martynov, A. G.; Tsivadze, A. Y.; Bessmertnykh-Lemeune, A.; Stern, C.; Guillard, R.; Kadish, K. M. *Inorg. Chem.* **2015**, *54* (7), 3501-3512.
- 125) Ishida, M.; Nakahara, K.; Sakashita, R.; Ishizuka, T.; Watanabe, M.; Uno, H.; Osuka, A.; Furuta, H. *J Porphy. Phthalocyanines* **2014**, *18* (10n11), 909-918.

- 126) Wilson, G. S.; Peychal-Heiling, G. *Anal. Chem.* **1971**, *43* (4), 545-550.
- 127) Lanese, J. G.; Wilson, G. S. *J. Electrochem. Soc.* **1972**, *119* (8), 1039-1043.
- 128) Mahesh, M.; Murphy, J. A.; LeStrat, F.; Wessel, H. P. *Beilstein J. Org. Chem.* **2009**, *5*, 1.
- 129) Kahlfuss, C.; Gibaud, T.; Denis-Quanquin, S.; Chowdhury, S.; Royal, G.; Chevallier, F.; Saint-Aman, E.; Bucher, C. *Chem. Eur. J.* **2018**, *24* (49), 13009-13019.
- 130) Abdul-Hassan, W. S.; Roux, D.; Bucher, C.; Cobo, S.; Molton, F.; Saint-Aman, E.; Royal, G. *Chem. Eur. J.* **2018**, *24* (49), 12961-12969.
- 131) Nagamura, T.; Takeyama, N.; Matsuo, T. *Chem. Lett.* **1983**, 1341-1344.
- 132) Nagamura, T.; Takeyama, N.; Matsuo, T. *Chem. Lett.* **1983**, *12* (9), 1341-1344.
- 133) Kahlfuss, C.; Métyay, E.; Duclos, M.-C.; Lemaire, M.; Oltean, M.; Milet, A.; Saint-Aman, É.; Bucher, C. *C. R. Chim.* **2014**, *17* (6), 505-511.
- 134) Morisue, M.; Morita, T.; Kuroda, Y. *Org. Biomol. Chem.* **2010**, *8* (15), 3457-3463.
- 135) Chowdhury, S.; Nassar, Y.; Guy, L.; Frath, D.; Chevallier, F.; Dumont, E.; Ramos, A. P.; Demets, G. J.-F.; Bucher, C. *Electrochim. Acta* **2019**, *316*, 79-92.
- 136) Dixon, D. W.; Steullet, V. *J. Inorg. Biochem.* **1998**, *69* (1), 25-32.
- 137) Kano, K.; Takei, M.; Hashimoto, S. *J. Phys. Chem.* **1990**, *94* (5), 2181-2187.
- 138) Kubát, P.; Lang, K.; Procházková, K.; Anzenbacher, P. *Langmuir* **2003**, *19* (2), 422-428.
- 139) Kano, K.; Minamizono, H.; Kitae, T.; Negi, S. *J. Phys. Chem. A* **1997**, *101* (34), 6118-6124.
- 140) Kano, K.; Fukuda, K.; Wakami, H.; Nishiyabu, R.; Pasternack, R. F. *J. Am. Chem. Soc.* **2000**, *122* (31), 7494-7502.
- 141) Procházková, K.; Zelinger, Z.; Lang, K.; Kubát, P. *J. Phys. Org. Chem.* **2004**, *17* (10), 890-897.
- 142) Pasternack, R. F.; Huber, P. R.; Boyd, P.; Engasser, G.; Francesconi, L.; Gibbs, E.; Fasella, P.; Cerio Venturo, G.; Hinds, L. d. *J. Am. Chem. Soc.* **1972**, *94* (13), 4511-4517.
- 143) Rehm, D.; Weller, A. *Isr. J. Chem.* **1970**, *8* (2), 259-271.
- 144) Rehm, D.; Weller, A. *Berichte der Bunsengesellschaft für physikalische Chemie* **1969**, *73* (8-9), 834-839.
- 145) Dancil, K.-P. S.; Hilario, L. F.; Khoury, R. G.; Mai, K. U.; Nguyen, C. K.; Weddle, K. S.; Shachter, A. M. *J. Heterocycl. Chem.* **1997**, *34* (3), 749-755.
- 146) Liu, Y.; Diercks, C. S.; Ma, Y.; Lyu, H.; Zhu, C.; Alshmimri, S. A.; Alshihri, S.; Yaghi, O. M. *J. Am. Chem. Soc.* **2019**, *141* (1), 677-683.

- 147) Banerjee, M.; Emond, S. J.; Lindeman, S. V.; Rathore, R. *J. Org. Chem.* **2007**, *72* (21), 8054-8061.
- 148) Uhlenheuer, D. A.; Petkau, K.; Brunsveld, L. *Chem. Soc. Rev.* **2010**, *39* (8), 2817-2826.
- 149) Stupp, S. I.; Palmer, L. C. *Chem. Mater.* **2014**, *26* (1), 507-518.
- 150) Meeuwissen, J.; Reek, J. N. H. *Nature Chemistry* **2010**, *2* (8), 615-621.
- 151) Hardouin-Lerouge, M.; Hudhomme, P.; Sallé, M. *Chem. Soc. Rev.* **2011**, *40* (1), 30-43.
- 152) Schrader, T.; Bitan, G.; Klärner, F.-G. *Chem. Commun.* **2016**, *52* (76), 11318-11334.
- 153) Leblond, J.; Petitjean, A. *ChemPhysChem* **2011**, *12* (6), 1043-1051.
- 154) Blake, J. F.; Jorgensen, W. L. *J. Am. Chem. Soc.* **1990**, *112* (20), 7269-7278.
- 155) Zhu, Z.; Cardin, C. J.; Gan, Y.; Colquhoun, H. M. *Nature Chemistry* **2010**, *2* (8), 653-660.
- 156) Klärner, F.-G.; Kahlert, B. *Acc. Chem. Res* **2003**, *36* (12), 919-932.
- 157) Chen, C. W.; Whitlock, H. W. *J. Am. Chem. Soc.* **1978**, *100* (15), 4921-4922.
- 158) Užarević, K.; Halasz, I.; Đilović, I.; Bregović, N.; Rubčić, M.; Matković-Čalogović, D.; Tomišić, V. *Angew. Chem. Int. Ed.* **2013**, *52* (21), 5504-5508.
- 159) Colquhoun, H. M.; Zhu, Z.; Williams, D. J. *Org. Lett.* **2003**, *5* (23), 4353-4356.
- 160) Pérez, E. M.; Capodilupo, A. L.; Fernández, G.; Sánchez, L.; Viruela, P. M.; Viruela, R.; Ortí, E.; Bietti, M.; Martín, N. *Chem. Commun.* **2008**, (38), 4567-4569.
- 161) Fernández, G.; Pérez, E. M.; Sánchez, L.; Martín, N. *Angew. Chem. Int. Ed.* **2008**, *47* (6), 1094-1097.
- 162) Koshland Jr, D. E. *Angew. Chem. Int. Ed.* **1995**, *33* (23-24), 2375-2378.
- 163) Korenaga, T.; Kosaki, T.; Kawauchi, Y.; Ema, T.; Sakai, T. *J. Fluor. Chem.* **2006**, *127* (4), 604-609.
- 164) Zimmerman, S. C.; VanZyl, C. M.; Hamilton, G. S. *J. Am. Chem. Soc.* **1989**, *111* (4), 1373-1381.
- 165) Zimmerman, S. C.; VanZyl, C. M. *J. Am. Chem. Soc.* **1987**, *109* (25), 7894-7896.
- 166) Zimmerman, S. C.; Wu, W.; Zeng, Z. *J. Am. Chem. Soc.* **1991**, *113* (1), 196-201.
- 167) Sommer, R. D.; Rheingold, A. L.; Goshe, A. J.; Bosnich, B. *J. Am. Chem. Soc.* **2001**, *123* (17), 3940-3952.
- 168) Zimmerman, S. C., Rigid molecular tweezers as hosts for the complexation of neutral guests. In *Supramolecular Chemistry I — Directed Synthesis and Molecular Recognition*, Canceill, J.; Chambron, J. C.; Collet, A.; Dietrich-Buchecker, C.; Durst, H. D.; Dutasta, J. P.; Kohnke, F. H.; Lozach, B.; Mathias, J. P.; Misumi, S.; Sauvage, J. P.; Stoddart, J. F.;

- Tomalia, D. A.; Zimmerman, S. C., Eds. Springer Berlin Heidelberg: Berlin, Heidelberg, 1993; pp 71-102.
- 169) Kim, D.; Lee, S.; Gao, G.; Seok Kang, H.; Ko, J. *J. Organomet. Chem.* **2010**, *695* (1), 111-119.
- 170) Lobert, M.; Bandmann, H.; Burkert, U.; Büchele, U. P.; Podsadlowski, V.; Klärner, F.-G. *Chem. Eur. J* **2006**, *12* (6), 1629-1641.
- 171) Constable, E. C., The Coordination Chemistry of 2,2':6',2''-Terpyridine and Higher Oligopyridines. In *Advances in Inorganic Chemistry*, Emeléus, H. J., Ed. Academic Press: 1986; Vol. 30, pp 69-121.
- 172) Petitjean, A.; Khoury, R. G.; Kyritsakas, N.; Lehn, J.-M. *J. Am. Chem. Soc.* **2004**, *126* (21), 6637-6647.
- 173) Ulrich, S.; Lehn, J.-M. *Chem. Eur. J* **2009**, *15* (23), 5640-5645.
- 174) Linke-Schaetzl, M.; Anson, C. E.; Powell, A. K.; Buth, G.; Palomares, E.; Durrant, J. D.; Balaban, T. S.; Lehn, J.-M. *Chem. Eur. J* **2006**, *12* (7), 1931-1940.
- 175) Doistau, B.; Benda, L.; Cantin, J.-L.; Chamoreau, L.-M.; Ruiz, E.; Marvaud, V.; Hasenknopf, B.; Vives, G. *J. Am. Chem. Soc.* **2017**, *139* (27), 9213-9220.
- 176) Doistau, B.; Rossi-Gendron, C.; Tron, A.; McClenaghan, N. D.; Chamoreau, L.-M.; Hasenknopf, B.; Vives, G. *Dalton Trans.* **2015**, *44* (18), 8543-8551.
- 177) Shinkai, S.; Nakaji, T.; Ogawa, T.; Shigematsu, K.; Manabe, O. *J. Am. Chem. Soc.* **1981**, *103* (1), 111-115.
- 178) Irie, M.; Kato, M. *J. Am. Chem. Soc.* **1985**, *107* (4), 1024-1028.
- 179) Fathalla, M.; Jayawickramarajah, J. *Eur. J. Org. Chem.* **2009**, *2009* (35), 6095-6099.
- 180) Leblond, J.; Gao, H.; Petitjean, A.; Leroux, J.-C. *J. Am. Chem. Soc.* **2010**, *132* (25), 8544-8545.
- 181) Azov, V. A.; Gómez, R.; Stelten, J. *Tetrahedron* **2008**, *64* (8), 1909-1917.
- 182) Skibiński, M.; Gómez, R.; Lork, E.; Azov, V. A. *Tetrahedron* **2009**, *65* (50), 10348-10354.
- 183) Cotellet, Y.; Hardouin-Lerouge, M.; Lemasson, E.; Morille, Y.; Canevet, D.; Legoupy, S.; Hudhomme, P. *Chem. Commun.* **2020**, *56* (20), 3077-3080.
- 184) Fu, T.; Han, Y.; Ao, L.; Wang, F. *Organometallics* **2016**, *35* (17), 2850-2853.
- 185) Shabanian, M.; Kang, N.; Liu, J.; Wagenknecht, U.; Heinrich, G.; Wang, D.-Y. *RSC Adv.* **2014**, *4* (45), 23420-23427.
- 186) Doistau, B.; Tron, A.; Denisov, S. A.; Jonusauskas, G.; McClenaghan, N. D.; Gontard, G.; Marvaud, V.; Hasenknopf, B.; Vives, G. *Chem. Eur. J* **2014**, *20* (48), 15799-15807.

- 187) He, Y.-J.; Tu, T.-H.; Su, M.-K.; Yang, C.-W.; Kong, K. V.; Chan, Y.-T. *J. Am. Chem. Soc.* **2017**, *139* (11), 4218-4224.
- 188) McConnell, A. J.; Wood, C. S.; Neelakandan, P. P.; Nitschke, J. R. *Chem. Rev.* **2015**, *115* (15), 7729-7793.
- 189) Isla, H.; Srebro-Hooper, M.; Jean, M.; Vanthuyne, N.; Roisnel, T.; Lunkley, J. L.; Muller, G.; Williams, J. A. G.; Autschbach, J.; Crassous, J. *Chem. Commun.* **2016**, 52 (35), 5932-5935.
- 190) Zimmerman, S. C.; Saionz, K. W. *J. Am. Chem. Soc.* **1995**, *117* (3), 1175-1176.
- 191) Heller, D. P.; Goldberg, D. R.; Wu, H.; Wulff, W. D. *Can. J. Chem.* **2006**, *84* (10), 1487-1503.
- 192) Córdova, A.; Janda, K. D. *J. Am. Chem. Soc.* **2001**, *123* (34), 8248-8259.
- 193) Hachiya, S.; Asai, K.; Konishi, G.-i. *Tetrahedron Letters* **2013**, *54* (14), 1839-1841.
- 194) Yan, X.; Wang, F.; Zheng, B.; Huang, F. *Chem. Soc. Rev.* **2012**, *41* (18), 6042-6065.
- 195) Xue, M.; Yang, Y.; Chi, X.; Yan, X.; Huang, F. *Chem. Rev.* **2015**, *115* (15), 7398-7501.
- 196) Yan, Q.; Feng, A.; Zhang, H.; Yin, Y.; Yuan, J. *Polym. Chem.* **2013**, *4* (4), 1216-1220.
- 197) Yang, X.; Yu, H.; Wang, L.; Tong, R.; Akram, M.; Chen, Y.; Zhai, X. *Soft Matter* **2015**, *11* (7), 1242-1252.
- 198) Häring, M.; Díaz, D. D. *Chem. Commun.* **2016**, 52 (89), 13068-13081.
- 199) Leininger, S.; Olenyuk, B.; Stang, P. J. *Chem. Rev.* **2000**, *100* (3), 853-908.
- 200) De, S.; Mahata, K.; Schmittel, M. *Chem. Soc. Rev.* **2010**, *39* (5), 1555-1575.
- 201) Croué, V.; Goeb, S.; Sallé, M. *Chem. Commun.* **2015**, 51 (34), 7275-7289.
- 202) Fujita, M.; Ibukuro, F.; Hagihara, H.; Ogura, K. *Nature* **1994**, *367* (6465), 720-723.
- 203) Fujita, M.; Tominaga, M.; Hori, A.; Therrien, B. *Acc. Chem. Res.* **2005**, *38* (4), 369-378.
- 204) Li, W.; Kim, Y.; Li, J.; Lee, M. *Soft Matter* **2014**, *10* (29), 5231-5242.
- 205) Crowley, J. D.; Steele, I. M.; Bosnich, B. *Chem. Eur. J.* **2006**, *12* (35), 8935-8951.
- 206) Pinter, B.; Van Speybroeck, V.; Waroquier, M.; Geerlings, P.; De Proft, F. *Phys. Chem. Chem. Phys.* **2013**, *15* (40), 17354-17365.
- 207) Karimipour, G.; Kowkabi, S.; Naghiha, A. *Braz. Arch. Biol. Technol.* **2015**, *58*, 431-442.
- 208) Prabhavathi, G.; Yamuna, R.; Jafer, A. C. *J. Organomet. Chem.* **2018**, *861*, 219-229.
- 209) Satake, A.; Shoji, O.; Kobuke, Y. *J. Organomet. Chem.* **2007**, *692* (1), 635-644.